23rd Annual

Alberta Biomedical Engineering Conference

Program and Proceedings



October 21-22, 2022



October 21-22, 2022

PROGRAM COMMITTEE

CONFERENCE ORGANIZERS

Co-Chairs	University of Alberta	Dan Romanyk Karyne Rabey
	University of Calgary	Roman Krawetz Michael Kallos
	University of Saskatchewan	Emily McWalter
Student Co-Chairs	University of Alberta	Timothy Gadzella Ramin Fathian
	University of Calgary	Tiffany Dang Karson Fitzsimons
	University of Saskatchewan	Amanda Zimmerling

ABSTRACT REVIEWERS

University of Alberta
Albert Vette
Dan Romanyk
Daniel Graf
Karyne Rabey
Lindsey Westover
Rica Sharma

University of Calgary
Amir Nezhad
Brent Edwards
Colin Dalton
Ethan MacDonald
John Bertram
Lauren Burt
Roman Krawetz
Sarah Manske
Steven Boyd
Zahra Abbasi

University of Saskatchewan
Daniel Chen
Dean Chapman
Emily McWalter
Julia Montgomery
Steve Machtaler

University of Lethbridge
Jon Doan

KEYNOTE SPEAKERS

Jim Boire	**President and Founder** RMD Engineering
Adrian Lai	**Senior Research Scientist, Product Innovation Team** lululemon
Deanna Burgart	**Senior Instructor, Department of Chemical and Petroleum Engineering** Schulich School of Engineering, University of Calgary **Teaching Chair, Integrating Indigenous Knowledge in Engineering**

INDUSTRY SPEAKERS

Efram Violato	**Research Associate** NAIT
Julia Montgomery	**Associate Professor, Department of Large Animal Clinical Sciences** University of Saskatchewan
Rob Henderson	**President and CEO** BioTalent Canada
Sergey Gasilov	**Senior Scientist** Canadian Light Source

STUDENT TRAINEES

University of Alberta	Timothy Gadzella Ramin Fathian	
University of Calgary	Tiffany Dang Karson Fitzsimons Kelsie Volek	Conference Student Co-Chairs
University of Saskatchewan	Amanda Zimmerling	
	Amanda Zimmerling Arya Subramanian Daphne Kaketsis Jessica Corpuz Karson Fitzsimons Manmeet Dhiman Mozhgan Sabz Natasha Bzowey Ramin Fathian Samantha Leech Thomas Lijnse Tiffany Dang Timothy Gadzella	Session Chairs

THANK YOU TO JULIANA CYR AND ALL VOLUNTEERS WHO HELPED WITH THE ORGANIZATION AND PLANNING OF OUR CONFERENCE!

THANK YOU TO OUR SPONSORS

UNIVERSITY OF CALGARY
Biomedical Engineering

UNIVERSITY OF CALGARY
FACULTY OF KINESIOLOGY

UNIVERSITY OF SASKATCHEWAN

UNIVERSITY OF ALBERTA

Gold Sponsors

BioTalent™/MC Canada

Igniting the bio-economy's brainpower
Catalyseur de l'intelligence en bioéconomie

Silver Sponsors

RMD GROUP OF COMPANIES

McCAIG INSTITUTE FOR BONE AND JOINT HEALTH

Alberta Children's HOSPITAL RESEARCH INSTITUTE

Bronze Sponsors

LIBIN CARDIOVASCULAR INSTITUTE

EDGE scientific

NAIT CENTRE FOR ADVANCED MEDICAL SIMULATION

Canadian Light Source | Centre canadien de rayonnement synchrotron

UNIVERSITY OF CALGARY | NSERC CRSNG

We-TRAC CREATE Training Program

REPRODUCTION AND REGENERATIVE MEDICINE Research Group

PROGRAM

FRIDAY			
3:00 – 3:10 pm		**Welcoming Remarks** – Student Co-Chairs	
		Keynote Speaker	
3:10 – 3:55 pm		Chair: Amanda Zimmerling, Karson Fitzsimons	
		Jim Boire President and Founder, RMD Engineering	
Podium Presentations & 3MT, Group 1			
4:00 – 5:00 pm		Session Chairs: Manmeet Dhiman, Jessica Corpuz	
Volek, Kelsie		A High Throughput Vascularized Lung-on-a-chip to Characterize the Fibroproliferative Stage of Acute Respiratory Distress Syndrome (ARDS)	In Person
Lawson, Ireland		Collagenase for Cerebral Palsy: Passive Force Production and Collagen Content	In Person
Vega, Fernando		Towards a Non-invasive Method for Screening Alzheimer's Disease: Image Translation to Estimate Amyloid-Beta Positron from Structural MRI	In Person
Malinovksa, Julia		Reprogramming of fibroblast cells to human induced pluripotent stem cells in a stirred suspension bioreactor	In Person
Yousef Zadeh, Fatemeh		Muscle pain modulates electroencephalography signals	Online
Nazari, Simin		Interactions of Reverse Dipole Moment Zwitterionic Materials with Human Serum Proteins towards Hemocompatible Dialysis Membranes	Online
Podium Presentations & 3MT, Group 2			
5:15 – 6:15 pm		Session Chairs: Thomas Lijnse, Arya Subramanian	
Chen, Amanda		Altered forearm crutch length changes shoulder and scapular kinematics	Online

Yeung, Ho Lam		Isn't research 'fun' when trying to speed your supervisor's Window's Matlab 'RNA-Squiggle' analysis using multi-threaded CPU's, GPU's and a third party Linux GIT download?	Online
Kalaga, Riya		Effect of Prebiotic Fibre Supplementation on Macrophage Infiltration in Adipose Tissue of Obese Rats	In Person
Rueda Montes, Mateo		Measuring Localized Trabecular Bone Loss Using HR-pQCT Images of Human Knees Following ACL Injury	In Person
Cho, Lydia		Following the migraine cycle in children and youth using magnetic resonance spectroscopy	In Person
6:30 – 9:00 pm		Reception and Interlab Scavenger Hunt Awards	

SATURDAY			
7:00 – 8:00 am		**Breakfast**	
Podium Presentations, Group 3			
8:00 – 9:30 am		Session Chairs: Mozhgan Sabz, Natasha Bzowey	
Smith, Ainsley		Evaluating critical care patient muscle density and cross-sectional area loss using computed tomography internal calibration	In Person
De Wet, Robyn		Replicating Patient-Specific Orthodontic Treatment on an In Vitro Orthodontic Simulator Mechanical Tester	In Person
Zimmerling, Amanda		Tensile Properties of 3D Printed Alginate Tissue Scaffolds	In Person
Dhiman, Manmeet		Delamination Strength and Stiffness in the Annulus Fibrosus from Adult Spinal Deformity Patients	In Person
Fernandez, Eleonora		Texture analysis of bovine meniscus T2* maps	In Person
Nichols, Alexander		Modeling a Robotic Hand in a Virtual Reality Environment	In Person
Mirkiani, Soroush		Intraspinal Microstimulation Implants Based on Microcoils	In Person
Shin, Joonhwan		Multi-axis robotic 3D bioprinting using the FRESH method	In Person

9:30 – 10:00 am		**Coffee Break**
		Keynote Speaker
10:00 – 11:00 am		Chair: Ramin Fathian, Tiffany Dang
		Adrian Lai Senior Research Scientist, Product Innovation Team
11:00 – 12:30 pm		**Poster Session 1**
12:30 – 1:30 pm		**Lunch Break**
Industry Panel		
1:30 – 2:30 pm		Chair: Timothy Gadzella, Amanda Zimmerling
		Efram Violato Research Associate, NAIT **Julia Montgomery** Associate Professor, Department of Large Animal Clinical Sciences, University of Saskatchewan **Rob Henderson** President and CEO, BioTalent Canada **Sergey Gasilov** Senior Scientist, Canadian Light Source
2:30 – 3:00 pm		**Coffee Break**
3:00 – 4:30 pm		**Poster Session 2**
		Keynote Speaker
4:30 – 5:30 pm		Chair:
		Deanna Burgart Senior Instructor, Department of Chemical and Petroleum Engineering, Schulich School of Engineering, University of Calgary Teaching Chair, Integrating Indigenous Knowledge in Engineering

Podium Presentations, Group 4			
5:40 – 7:00 pm		Session Chairs: Samantha Leech, Daphne Kaketis	
Smith, Hannah		The effect of a 3-week delayed prebiotic fibre intervention on muscle integrity in rat vastus lateralis in a diet-induced obesity model	In Person
Bzowey, Natasha		Articular Cartilage T2 Relaxation Time Decreases in Regions of Loaded Contact in Cadaver Knees	In Person
O'Sullivan, Carly		Effect of high and low epidural spinal cord stimulation and intraspinal microstimulation on cFos positive neuron distribution	In Person
Maalouf, Elissa		EEG Channel and Sampling Rate Reduction for Brain Computer Interfaces	In Person
Kabarchuk, Natasha		Ex-Vivo Heart Perfusion Flow Meter	In Person
Jar, Chester		Measuring Dental Implant Stability with the Advanced System for Implant Stability Testing (ASIST)	In Person
Munro, Emily		Using Machine Learning to Discover Genetic Effects on Brain Aging in the UK Biobank	In Person
Kang, Hellen		Using a Vascularized 3D Lung-on-a-Chip to Characterize HIF-1α-Dependent Immune Responses During Pneumococcal Pneumonia	In Person
7:00 pm		**Closing Remarks – Conference Co-Chairs**	
7:05 – 8:30 pm		**Dinner**	
9:00 pm		**Conference Social** Elk & Oarsman, Banff	

KEYNOTE SPEAKERS



Jim Boire

President and Founder, RMD Engineering

Jim Boire is a Journeyman Machinist by trade and has a Bachelor of Science in Mechanical Engineering from the University of Saskatchewan (1996). Jim has been a project management professional (PMP) since 2017. During the Covid 19 pandemic, Jim lead the team that developed Canada's only self-funded Emergency Use Ventilator that was Certified by Health Canada and sold to the province of Saskatchewan. Jim also founded the company One Health Medical Technologies that was certified as Saskatchewan's only medical device manufacturer – all in 8 months!

Prior to Starting RMD Engineering in 2001, Jim was a manufacturing Engineer in Saskatoon, and then moved to Regina to work as a maintenance and process engineer for Mosaic Belle Plain, and finally a maintenance engineer for SaskPower. RMD has grown from 3 Employees and 1200 square feet, to over 85 employees, and a recently expanded 100,000 square foot engineering and manufacturing facility in Saskatoon. The company designs and builds custom equipment for Aero space, Synchrotrons, utilities, agriculture, and many other unique areas where process and engineering challenges exist. Jim is very proud to have been born and raised in Saskatchewan, and to call the province home.



Deanna Burgart

Senior Instructor, Department of Chemical and Petroleum Engineering, Schulich School of Engineering, University of Calgary
Teaching Chair, Integrating Indigenous Knowledge in Engineering

Deanna Burgart is a Cree Dene Irish-Canadian Senior Instructor and Teaching Chair in the Schulich School of Engineering focused on weaving Indigenous knowledge into engineering. She brings over 20 years of experience in energy and pipelines and is passionate about the United Nations Sustainable Development Goals and United Nations Declaration of Rights of Indigenous People. She helps STEM (Science, Technology, Engineering and Math) focused organizations and educators operationalize Indigenous inclusion in their work.

She is the co-founder and co-president of IndigeSTEAM, a non-profit focused on creating a community of support and outreach for Indigenous youth, students, and professionals in STEM through the integration of art, culture and Indigenous wisdom. Deanna can be found online at www.indigeneering.com.



Adrian Lai

Senior Research Scientist, Product Innovation Team, lululemon

Adrian Lai is a Senior Research Scientist on the Product Innovation Team at lululemon. Originally from Sydney, Australia, he graduated with degrees in Mechatronics (BS) and Biomedical Engineering (MS) from the University of New South Wales before completing his PhD in Mechanical Engineering at the University of Melbourne. Adrian's academic research has spanned vehicle safety (helmets, incapacitation systems), musculoskeletal modelling, human clinical and performance testing and in-vivo vertebrate muscle physiology.

Adrian's diverse background, particularly in biomedical engineering and continuous desire to learn, has shaped how he integrates ideas, research and insights that are integrate to his role at lululemon; to shape, surprise and engineer delight into future products by going beyond classic R&D techniques blending mind and body.

INDUSTRY PANELISTS



Rob Henderson
President and CEO, BioTalent Canada

Rob Henderson is President and CEO of BioTalent Canada. Since joining the company in 2011, BioTalent Canada has grown to become the talent driver behind life-changing science in Canada. Over the past several years, BioTalent Canada has produced comprehensive evidence-based resources—Labour Market Intelligence reports, National Compensation Guides, National Occupational Standards—that the industry relies on to build successful teams.

The company has also developed programs and services that bridge the gap between employers to job seekers and placed over 5,000 Canadians in new careers across Canada. In 2021, BioTalent Canada itself was designated as one of Canada's Top 50 workplaces in Canada for less than 50 employees.



Efrem Violato
Research Associate, NAIT

Efrem Violato has a background in Social-Cognitive and Educational Psychology with a focus on health professional education and training, specifically simulation, group performance, and assessment. His role within the Northern Alberta Institute of Technology Centre for Advanced Medical Simulation covers diverse responsibilities including supporting the Alberta Innovates Health Innovation Platform Partnership at CAMS. Efrem helps Innovators and Small-Medium Enterprises design and conduct simulation-based usability testing for medical devices, including digital health technologies.



Julia Montgomery

Associate Professor, University of Saskatchewan

Dr. Julia Montgomery is an Associate Professor in the Department of Large Animal Clinical Sciences at the Western College of Veterinary Medicine, University of Saskatchewan (USask) and a faculty member of the USask Biomedical Engineering Division, as well as the USask Respiratory Research Centre. Dr. Montgomery' s appointment includes clinical service in large animal internal medicine (LAIM), teaching and research. Her research program focuses on clinically applied research in equine internal medicine (equine asthma, equine metabolic syndrome, laminitis prevention) and testing innovative technologies for the advancement of both animal and human health and well-being. Dr. Montgomery received her veterinary degree from the School of Veterinary Medicine Hannover, Germany, and holds a PhD from the University of Prince Edward Island (UPEI). She completed her Large Animal Internal Medicine residency at the Atlantic Veterinary College, UPEI, and is a Diplomate of the American College of Veterinary Internal Medicine, Specialty of LAIM. Dr. Montgomery has extensive experience in collaborating with industry on several biomedical engineering projects in support of animal and human health.



Sergey Gasilov

Senior Scientist, Canadian Light Source

Sergey Gasilov is a Senior Scientist at the Canadian Light Source, specializing in the development of instruments and techniques for hard X-ray imaging and microtomography. Sergey completed his MSc work at the Moscow Engineering Physics Institute, and during his PhD he worked in Russia, Italy, and Japan on X-ray imaging with laser-plasma-driven X-ray sources. After that, Sergey worked on the development of phase-contrast techniques for biomedical imaging at the Ludwig Maximilian University in Germany, and the European Synchrotron Radiation Facility, in France. In 2018, Sergey became responsible for the Biomedical Imaging and Therapy beamlines at the Canadian Light Source.

POSTERS

Poster Session 1		
11:00 – 12:30 pm		
Acddeh, Abdoljalil	1	Challenges of Respiratory Signals Measurement in fMRI Studies
Iwasyk, Alexander	3	Opportunistic 3D Modelling of Clinical CT for a Subject-Specific Assessment of Fracture Risk
Koshyk, Andrew	7	Development of a Discrete Element Model to Evaluate Contact Stress in the Equine Metacarpophalangeal Joint
Bugbird, Annabel	9	What factors drive bone phenotyping – does resolution play a significant role?
Sekhon, Armaan	11	Measuring sarcomere dynamics following fluorescent labelling of α-actinin and myomesin structural proteins
Al-Shimari, Banin	13	The role of the subtalar and ankle joints to maintain stability while walking on uneven surfaces
Matheson, Bryn	15	Using deep learning to augment osteoporosis screening
Betancourt Lee, Catherine	17	Microneedle Array Load Factors
Tiessen, Chris	19	The Effect of Hold Time on Mechanical Properties of Myofibrils Stretched Passively due to Immunoglobulin Domain Unfolding and Refolding
Keen, Christopher	21	Using Artificial Intelligence to Predict Tumour Recurrence Based on PET-CT Images
Gye, Daniel	23	Preliminary Compression Testing of Aramid-Epoxy Braided composites for use in Prosthetics
Stewart, Dean	25	Directional cues in context affect perceptions and kinematics for manual materials handling
Gysel, Emilie	27	The influence of culturing conditions on the proteome of human induced pluripotent stem cells
Smith, Emily	29	RED-S Risk and Bone Mineral Density Changes in Long Track Speed Skaters
Roberts, Erin	31	Effect of Hydrodynamic Properties on Mesenchymal Stromal Cell Expansion on Microcarriers
Bessa, Guilherme	33	A comparative study between a Newtonian and non-Newtonian droplet impact in a liquid pool
MacDuff, Hannah	35	Validating a markerless motion capture system for sit to stand testing
Han, Ian	37	Serum Metabolite Predictors of Preterm Birth in Primigravida

Kuri, J. Carlos	39	Fluorometric Aptasensor; evaluation of stability and comparison to standard ELISA assay
Tu, Jean	41	Tibial acceleration is not a valid surrogate measure for predicting musculoskeletal loads
Corpuz, Jessica May	43	Proteoglycan 4's impact on the intervertebral discs
Ellis, Joshua	45	Effects of forearm crutch length on latissimus dorsi activity during swing-through gait
Le, Kathy	47	The Use of Electromyography as a Novel Assessment Tool in Multiple Sclerosis
Wallich, Mackenzie	49	Decision Support Using Accelerometry and Machine Learning
Soleymani, Mahshid	51	The impact of data normalization and plane view in deep learning methods for classifying disease subtypes in multiple sclerosis using brain magnetic resonance imaging scans
Law, Maria	53	A Machine Learning Study on Rural-Urban Differences Among Older Drivers
Stibbards-Lyle, Maya	55	Fluid shear stress and involution: Implications for postpartum breast cancer
Palizi, Mehrdad	57	Sex estimation by linear classification of statistical shape models (hemipelvis and talus)
Kerr McNutt, Morgan	59	Development of a Brain Controlled Robot for Paralympic Sport
Sabz, Mozhgan	61	High-Flow and Low-Flow Oxygen Delivery by Nasal Cannula Evaluated in Neonatal and Adult Airway Replicas
Kenny, Olivia	63	Developing methodology to monitor tendon strain within the equine forelimb
Wadodkar, Payal Parekh, Verdant	65	Designing fully automated smart vertical farming systems with the assistance of sensors as a solution to socio-economic problems
Steele, Racheal	67	Cerebral blood flow and magnetic susceptibility are reduced in the bacterial lipopolysaccharide (LPS) mouse model of inflammation
Derafshi, Reihaneh	69	Investigating the common driving routes and destinations among older adults
Chauvet, Robert	71	Blast Injury Prevention Device Finite Element Simulation
Heschl, Samantha	73	The effect of Proteoglycan 4 on disc integrity and functionality
Patwary, Sammy	75	Sorting the Stay
Price, Sarah	77	An Algorithm to Improve the Accuracy of Microwave Breast Imaging: Validation and Testing
Schadan, Sydney	79	Stimulation-dependent quantification of trunk muscle responses to single-pulse epidural spinal stimulation

Vandenberg, Tod	81	Development of a Finite Element Model to Examine the Response of the Advanced System for Implant Stability Testing (ASIST) in Dental Implants
Muresan, Tudor	83	Effects of Cyclic Loading Interruption on Bovine Cortical Bone
Ohazukosi, Uche	85	Investigating the effect of normobaric oxygen therapy in the experimental autoimmune encephalomyelitis (EAE) mouse model of MS
Wang, Xun	87	A Dynamic Procedure to Detect Maximum Voluntary Contraction in Lower Back
Iffath, Fariha	89	Analysis of Human Musical Cognitive Preferences.
Ma, Hilda	91	The Link Between Oxygen Consumption Rate and In Vitro Chondrogenesis for Cartilage Tissue Engineering
Hamidreza Heidary, Seyed	93	Design And Implementation of a Smart Bicycle for Knee Osteoarthritis Rehabilitation
Ayooluwakiitan, Okesanya Sumaya, Soufi	95	A Validation Study of Markerless Motion Capture Using Sit-to-Stand Tests
Muhammed, Rania	97	The Correlation Between Behavioural and Physiological Changes in the CNS in the EAE Mouse Model of Multiple Sclerosis
Poster Session 2		
3:00 – 4:30 pm		
Stahl, Alana	2	Examination of Bone Turnover Biomarkers in Ovariectomized Cynomolgus Monkeys Associated with Antiresorptive Treatment
Morrison, Alida	4	Quantifying and visualizing regional bone changes in the knee following an ACL tear
Angulo, Ana Gloria	6	Bone fatigue properties across different dimensional scales following bisphosphonate treatment in ovariohysterectomized rabbits
Das, Anik	8	Introducing Unsupervised ML Technique to Children's Brain MR Imaging
Demong, Anthony	10	Using Robotics to Automate the Fabrication of Cannulae
Murani, Arman	12	The effect of a 3-week delayed prebiotic fiber intervention on fat infiltration in vastus lateralis muscles of female Sprague-Dawley rats
Abraham, Brett	14	The expansion of human skin-derived Schwann cells in stirred suspension bioreactors to improve cellular production for clinically relevant quantities of cells.
dos Santos Figueredo Junior. Carlos Alberto	16	Ultrasound imaging of the periodontium
Gupta, Chetan	18	Developing Smart-Traps to Observe Physiological Stress Responses in Wild-Caught Rodents

Alexander, Christina	20	Physical activity monitor validation study in youth and young adults
Tsui, Christopher	22	Evaluating glial cell response to functional microelectrode implants in vitro
Kaketsis, Daphne	24	Validating in-vivo HR-pQCT bone remodeling measurements in knee osteoarthritis
Desai, Dhairya	26	Investigating sarcomere length non-uniformity and repeatability in immunofluorescent labelled skeletal rabbit psoas muscles
Dittmer, Emily	28	Using wearable fitness trackers to predict intrapersonal activity and sleep outcomes with supervised machine learning
Bangsboll, Emily	30	Kinematic Comparison of Cervical Vertebrae Following Total Disc Arthroplasty
Shahidi, Faezehsadat	32	Session-Based Recommender Systems and Hyper Parameter Optimization for Machine Learning of Administrative Data
Bugler, Hanna	34	Deep Learning Model for Frequency and Phase Correction of MR Spectroscopy MEGA-PRESS Data
Booth, Heather	36	Effect of Protein Supplementation on the Isolation of Exosomes Derived from Human Cancer Cells
Vandergaag, Isabella	38	Validation of knee joint space width and quadriceps angle using EOS imaging
Cooper, Jackson	40	Geometric Correction of Fluoroscopic Imaging Systems by Self-Calibrating Bundle Adjustment
Holloway, Jenna	42	Determining Strategies to Produce a Low-Cost Media for Human Induced Pluripotent Stem Cell Expansion in Vertical-Wheel® Bioreactors
Feddema, Joshua	44	Simulation Analysis for the Development of ECMO Cannula
Laketic, Katarina	46	Blood Metallomic Signatures Associated with Pregnancy Smoking Exposure
Qian, Linna	48	Development of a Remote Health and Activity Monitoring Assessment Tool with Ultra-Wide-Band Tracking
Ead, Maha	50	Investigating the Use of PCU as a Talus Bone Implant Coating
Boucher Hoglin, Mairi	52	Investigation of axial rigidity of Kevlar tubular braided composites for cardiovascular catheter application
Masoomikhanghah, Maryam	54	in vivo changes in articular cartilage and meniscus UTE-T2* with load in osteoarthritis
McLennan, Cael	56	Analyzing Gait Adaptations to Surgically Induced Fractures in Young and Old Mice
Thatcher, Michael	58	A biomechanical comparison of two modern suture techniques for arthroscopic rotator cuff repair

Hassan, Mostafa	60	Evaluating CNN with a cross-validation approach to classify adolescent idiopathic scoliosis (AIS) severity
Meulenbroek, Nathan	62	Experimental Directivity Detection with Individual Biaxial Ultrasound Transducers
Annaa, Osman Jakpa	64	Using Deep Learning and Interpretable AI to Predict Outcomes in Medical Data
Faridi, Pouria	66	Real-time Smart Switching in Home-based Lower-limb Exoskeletons
Sheronick, Raneem	68	Multiphase Computed Tomography Perfusion Maps Predict Penumbra Volume in Patients with Acute Ischemic Stroke
Kakavand, Reza	70	A Novel Combination of Neural Networks and Statistical Shape Modelling for Automatic Knee Joint Geometry Construction from MRI
Pommot Berto, Rodrigo	72	Reducing GABA-edited Magnetic Resonance Spectroscopy Scan Times with Deep Learning
Leech, Samantha	74	Tissue effects on neurochemical quantification using single voxel magnetic resonance spectroscopy
Vestrum, Sarah	76	Sensitivity-Enhanced Patch Antenna Sensor for Distant Hydration Monitoring Applications
Abdollahi, Sorosh	78	Creating super-repellent bacterial nanocellulose membranes with tunable properties
Bader, Taylor	80	Do Mechanical and Structural Differences in Degenerated Intervertebral Discs Result in Degenerative Scoliosis and Spondylolisthesis?
Heisser, Torri	82	Does Botox-Induced Paraspinal Muscle Weakness Result in Osteoarthritic Changes in Facet Joints?
Santos, Tyler	84	Understanding Robotic Gait Trainers Usage Data for Children with Mobility Disorders
Nguyen, Vivian	86	Running with Varying Stiffness Across Different Shoes Affect Lower Limb Biomechanics
Khoz, Zahra	88	Development and Validation of a Depth-Dependent Transversely Isotropic Finite Element Model of Cartilage: Cross-Validation and Comparison with Fibril-Reinforced Poroelastic Approach
Waungana, Tadiwa	90	Imaging characteristics of a weight-bearing, cone beam computed tomography system
Otoo, Baaba	92	Chondrocyte deformations during cyclic loading
Luong, Peter	94	Optimizing Printed Circuit Board Parameters for ACET Micropumps
Haider, Kazim	96	Rapid Fabrication of Metal Microneedle Arrays

A High Throughput Vascularized Lung-on-a-chip to Characterize the Fibroproliferative Stage of Acute Respiratory Distress Syndrome (ARDS)

Kelsie Volek[1] and Mark R. Gillrie[2]
[1]Schulich School of Engineering, University of Calgary; [2]Cumming School of Medicine, University of Calgary

Introduction

Acute Respiratory Distress Syndrome (ARDS) is a form of respiratory failure caused by lung tissue damage. This condition often requires mechanical lung ventilation due to severe lung failure. The fibroproliferative stage of ARDS is a serious consequence of this disease, often leading to death [1]. Major limitations in our ability to understand fibroproliferative ARDS exist as it cannot be modeled in animals due to restrictions of prolonged ventilation. The aim of this study is to generate a high throughput vascularized human lung-on-a-chip model to characterize fibroproliferative ARDS.

Methods

The computer program SolidWorks was used to design a mold for a high throughput lung-on-a-chip device that contained 16 'lungs'. When the design was complete, the mold was 3D printed and tested. The mold was used to make the lung-on-a-chip device, using PDMS and cover glass. In the device endothelial cells (HUVEC) and fibroblast cells (nhLF) were cocultured and mixed with thrombin and fibrinogen, then injected together into the central channel of the PDMS 'lungs'. The polymerization of fibrin allowed the cells to be suspended in a 3D matrix. The HUVEC cells underwent a vasculogenesis process, during which they formed vessels. After three days epithelial cells (H441) were placed on top of the endothelial cells to form an air-liquid interface. The 'lungs' were induced with five different compounds known to cause fibrosis to mimic different types of ARDS. The 'lungs' were immunofluorescently labelled for fibrotic markers and imaged on an inverted Leica Sp8 confocal microscope.

Results

Only one fibrotic condition showed significant lung tissue and vasculature damage, when compared to a negative control. This condition was induced with Poly IC, a double stranded RNA agonist that mimics viral infections (including SARS-COV2), commonly seen in patients that develop ARDS [2]. These 'lungs' appeared to have vessels that were destroyed, and this was confirmed by quantifying certain vessel properties including tube area, skeleton length, and number of branches. All three of these properties showed significant reductions in Poly IC 'lungs'. Two known fibrotic markers (collagen I and alpha smooth muscle actin) were also quantified using immunofluorescence and they were found to significantly decrease in the Poly IC conditions compared to the negative controls.

Conclusions

Poly IC was the only fibrotic agonist seen to cause severe physical changes to this lung-on-a-chip model. The fibrotic markers hypothesized to increase in the fibrotic conditions decreased in the Poly IC induced 'lungs', suggesting that there is crosstalk occurring between the different cell types present in this *in vitro* model. Results suggest that 2D cell culture and mouse models alone will not be sufficient in properly characterizing ARDS. Future experiments will be performed to explore mechanisms of airway fibrosis. Fully integrated vascular flow and ventilation will need to be incorporated into this model to understand effects of post-inflammatory fibrosis on blood vessel function and tissue mechanical properties.

References

[1] Burnham et al., 2013, The fibroproliferative response in acute respiratory distress syndrome: Mechanisms and clinical significance, European Respiratory Journal, 43(1), 276–285.

[2] Gan et al., 2018, TLR3 regulated poly I:C-induced neutrophil extracellular traps and acute lung injury partly through p38 Map Kinase, Frontiers in Microbiology, 9.

Collagenase for Cerebral Palsy: Passive Force Production and Collagen Content

Ireland Lawson, Venus Joumaa, Ruth Seerattan, Tim Leonard, Walter Herzog
Human Performance Lab, Faculty of Kinesiology, University of Calgary

Introduction

Cerebral Palsy (CP) is a neuromotor condition causing muscle stiffness and physical impairments [1]. It has been suggested that the CP muscle stiffness is caused by an increase in the collagen content of the extracellular matrix [2]. Current treatments for CP include surgical lengthening of spastic muscles and botulinum toxin-A (Botox) injections. There are serious drawbacks to these treatments. Surgical lengthening of muscles is highly invasive and Botox injections only provides relief for a limited time. Therefore, there is a need for an effective intervention to combat CP muscle stiffness with little detrimental side effects.

Collagenase is a naturally produced enzyme which breaks down collagen. It has been hypothesized that a decrease in the extracellular collagen content of spastic muscles using collagenase may decrease the passive stiffness, and thus may help in restoring normal muscle function. The objective of our study is to determine the effect of collagenase incubation on passive force and total collagen content in muscle samples isolated from children with CP.

Methods

CP muscle samples (n=11) were incubated in either collagenase (350 Units/mL for up to 1hr, experimental group) or saline (control group) solutions, tested for passive force before and after incubation using a series of stress-relaxation tests at strain magnitudes of 1, 2.5, 5 and 7.5%, and then stained and analyzed for their collagen content.

Results

Peak and steady state passive force were decreased by 49±16% in the experimental group following incubation in collagenase (Figure 1). There was no difference in the amount of collagen between the experimental and control group samples.

Discussion

The decrease in passive force following collagenase incubation provides support for the potential use of collagenase as an alternative treatment to muscle stiffness in children with CP. We hypothesize that the collagenase cleaved collagen fibrils and connections between fibrils thus reducing passive force in the experimental samples while preserving the total collagen content.

References

1. Howard JJ, Graham K, Shortland AP. Developmental Medicine & Child Neurology. 2021;64(3):289–95.
2. Booth CM, Cortina-Borja MJ, Theologis TN. Developmental Medicine and Child Neurology. 2001;43(05):314.

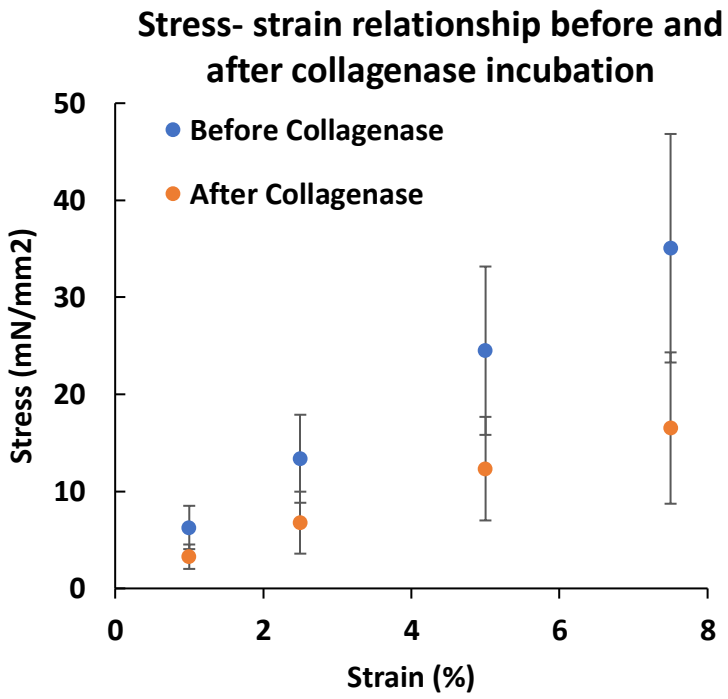


Figure 1: Stress-strain relationship of the passive force before (blue) and after (orange) incubation in collagenase at tissue strains of 1%, 2.5%, 5% and 7.5%.

Towards a Non-invasive Method for Screening Alzheimer's Disease: Image Translation to Estimate Amyloid-Beta Positron from Structural MRI

Fernando Vega, AbdolJalil Addeh, Ahmed Elmenshawi, M. Ethan MacDonald
Departments of Electrical & Software Engineering, Biomedical Engineering and Radiology,
Hotchkiss Brain Institute, University of Calgary, AB, Canada

Introduction: Alzheimer's Disease (AD) is the most prevalent cause of dementia, with an estimated economic burden of $305 Billion in 2020 [1]. By the time that AD is clinically diagnosed, the patient is already experiencing neuronal loss and brain atrophy. Amyloid-beta is a key molecule that is widely believed to be the root cause of AD pathophysiology [2]. Over the last 15-years, amyloid-beta targets have gained significance with the use of PET tracers, however, PET imaging has some disadvantages such as: cost, invasiveness, radiation exposure and advanced tracers are not available in all jurisdictions [3]. Structural MRI is about 10-times cheaper and can aid to assess AD as well by targeting structural changes and atrophy driven by AD [4]. Currently, MRI does not provide the valuable molecular information as PET does, however, this would be possible by building image translation models that yield synthetic PET images from MRI relying on the known relationship that amyloid-beta burden and brain atrophy.

Methods: Pairs of MRI and PET images from the Open Access of Imaging Studies (OASIS-3) database were preprocessed by brain extraction, and registration to the Montreal Neurological Institute (MNI) template for both MRI and PET images, 2D slice splitting in the axial plane, and normalization. A Generative Adversarial Network (GAN) architecture was implemented to conduct image translation with python using the pytorch deep learning library. A custom loss function was implemented that masks the image during training to penalize information outside of the brain. Finally, the model was used with 335 unseen MRI images to generate synthetic PET images that were evaluated with their paired original PET image with Structural Similarity Index Metric (SSIM).

Results: Figure 1 shows two examples of the structural MRI, PET, synthetic PET images, the difference between the synthetic PET and real PET and the SSIM score.

Conclusions: The results are encouraging and effectively enable the screening of AD with MRI. The estimation of pixel intensity still requires improvement, future research will address this problem by implementing a more complex model architectures, such as 3D GAN models.

References

1. Wong, et al., Economic burden of Alzheimer disease and managed care considerations. Am J Manag Care, 2020.
2. Hampel, et al., The Amyloid-β Pathway in Alzheimer's Disease. Molecular Psychiatry, 2021.
3. Marti-Climent, et al., Effective dose estimation for oncological and neurological PET/CT procedures. EJNMMI Res, 2017.
4. Buxton, et al., Introduction to functional magnetic resonance imaging : principles and techniques. 2009.

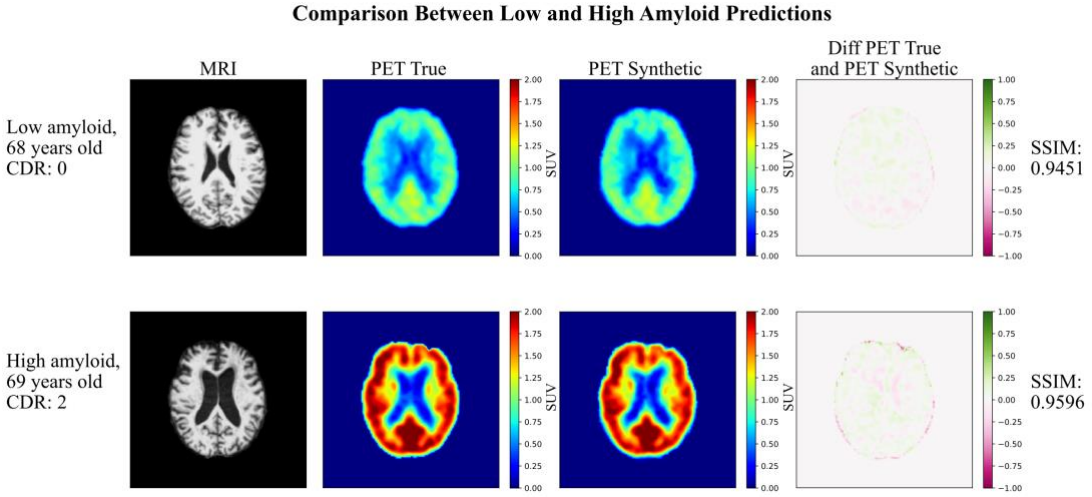


Figure 1.- Two subjects with low and high beta-amyloid respectively, left image is MRI image, the center-left is true PET image, the center-right is synthetic PET, and the right is difference map between true and synthetic PET

Reprogramming of fibroblast cells to human induced pluripotent stem cells in a stirred suspension bioreactor

Julia Malinovska[1,2], Alexandra M. Kozlov[3], Dean H. Betts[3], Robert C. Cumming[3], Michael S. Kallos[1,2]
1 - Pharmaceutical Production Research Facility, University of Calgary, Canada
2 - Department of Biomedical Engineering, University of Calgary, Canada
3 - Department of Biology, The University of Western Ontario, Canada

Introduction

The regenerative medicine field is increasingly focused on the use of human induced pluripotent stem cells (hiPSCs) for cell therapy, drug screening, and disease modelling [1]. These cells are made through reprogramming somatic cells (fibroblasts) and have the ability to self-renew and develop into almost any cell type[2]. Various approaches for reprogramming are available however, challenges with large scale manufacturing, virus integration into the genome and low efficiency are present [3]. The creation of a bioprocess is vitally important to obtain a clinically relevant number of hiPSCs but there exists a gap between the reprogramming and expansion stages which needs to be addressed first.

Methods

Fibroblasts are anchorage dependent cells, therefore a microcarrier screening will be performed to select the optimal microcarrier type to support growth in suspension. Brightfield images and Confocal fluorescent images with a Nucleic Acid stain will be taken to observe cell attachment. Viability and growth kinetics will be assessed using a Nucleocounter NC-200. Reprogramming in suspension will be performed using the Sendai Virus CytoTune™-iPS 2.0 (Invitrogen, A16517) kit in 10mL stirred suspension bioreactors. Pluripotency of generated cells will be validated using alkaline phosphatase (AP) live staining and immunocytochemistry.

Results

The microcarrier screening showed an optimal performance of the collagen coated microcarrier (Corning, 3786). Initial results demonstrating the impact of a dynamic culture and shear force were also obtained through inducing a dynamic environment during reprogramming using a shaker plate. Compared to static, the dynamic culture reduced the time it takes to form colonies and produced larger colony sizes as seen in Figure 1.

Conclusions

Clinical applications require scale-up to achieve a large number of cells. This project aims to conduct reprogramming in a stirred suspension bioreactor to close the gap between reprogramming and expansion. The ability to reprogram somatic cells in a dynamic culture would increase reprogramming efficiency and advance the development of an hiPSC bioprocess.

References

[1] M. Ohnuki and K. Takahashi, “Present and future challenges of induced pluripotent stem cells.”
2] J. S. Kim, H. W. Choi, S. Choi, and J. T. Do, “Reprogrammed Pluripotent Stem Cells from Somatic Cells,” Int. J. Stem Cells, vol. 4, no. 1, p. 1, 2011.
[3] M. S. Rao and N. Malik, “Assessing iPSC reprogramming methods for their suitability in translational medicine,” *J. Cell. Biochem.*, vol. 113, no. 10, pp. 3061–3068, Oct. 2012.

Figures

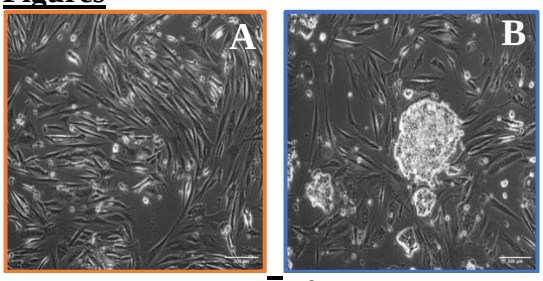


Figure 1: Comparison of cell colonies on Day 15 seeded at 60,000 cells / well of a 6 well plate in static (A) and shaken (B).

Muscle pain modulates electroencephalography signals

Fatemeh Yousef Zadeh, Connor Maxey, Kent Hecker, Andrea Protzner, Saied Jalal Aboodarda
University of Calgary, Alberta, Canada

Introduction

Prior investigations have postulated that muscle pain can alter brain activity patterns and this alteration can be detected by electroencephalogram (EEG) frequency band signals(Sun et al., 2021; Zis et al., 2022) . However, these studies have used thermal, electrical, or cold exposure-induced pain that do not simulate deep muscle pain induced by muscle injuries or high-intensity exercise. Accordingly, in this research, we applied experimental pain induced by a combination of blood occlusion and electrical stimulation to investigate if deep muscle pain can modulate EEG signals. We hypothesize that muscle pain can alter brain activity in the somatosensory and somatomotor areas of the brain and the alpha, beta and gamma frequency EEG signals can monitor these alterations.

Methods

Twenty-one healthy participants undertook two experimental conditions in a crossover repeated measure experimental study while EEG signals were continuously recorded from the scalp using a 32 channels EEG system according to 10-20 system at 500 Hz. During the first condition (fixation), participants were asked to look at a black spot placed 150 cm in front of them and the visual gaze remained relatively still for 4 min and 15 s. In the second condition (pain), a rapid cuff inflator was used to occlude the left femoral artery innervating the thigh for two bouts of 2 min at 300 mmHg while there was a 15 s occlusion release between the two bouts. During the entire 4:15 min of pain intervention, 10 Hz electrical stimulus was applied to occluded thigh muscles. Thereafter, the electrical stimulation and occlusion were stopped, and the participants were asked to do fixation for another 4:15 min. This process was repeated twice, and the pain level was recorded right before each fixation period. Visual analogue scale (VAS) was used to measure the subjective pain level.

All data processing was performed using Matlab (The Mathworks Inc., Natick, MA). Based on previous studies (Sun et al., 2021), EEG signals were band-pass filtered (0.1–55 Hz) to remove signal drift and line noise after visually inspecting the signal for large artifacts. Independent Component Analysis (ICA) was performed to reject components associated with EMG and eye movements using EEGLAB13.2.2b (Delorme and Makeig 2004). Eventually, the clean data was analyzed in different frequency domains through fast-Fourier transformation.

Results

Perceived pain reduced alpha power in the left and right fronto-central cortex (channels: F3, FC5, FC1, and F4, FC2, FC6 clustered), and in the left and right centro-parietal cortex (channels: CP5, CP1, P3 and CP2, CP6, P4 clustered) compared to fixation ($F=62.74$; $P< 0.001$). Similar results were observed in beta band in the four mentioned clusters ($F=86.3$; $P<0.001$). Regarding the pain-induced cortical gamma alterations, the pain effect was only observed in the two clusters in fronto-central cortex (channels: F3, FC5, FC1, and F4, FC2, FC6 clustered) ($F=10.27$; $P< 0.0026$).

Conclusions

Overall, the results suggest that the experimental muscle pain induced by blood flow occlusion and electrical stimulation could alter the brain activity signals in fronto-central and centro-parietal clusters in alpha and beta EEG bands, contrary to gamma which only shows the pain effect in the fronto-central cluster.

References

Sun, G., Wen, Z., Ok, D., Doan, L., Wang, J., & Chen, Z. S. (2021). Detecting acute pain signals from human EEG. *J Neurosci Methods*, *347*, 108964. https://doi.org/10.1016/j.jneumeth.2020.108964

Zis, P., Liampas, A., Artemiadis, A., Tsalamandris, G., Neophytou, P., Unwin, Z., Kimiskidis, V. K., Hadjigeorgiou, G. M., Varrassi, G., Zhao, Y., & Sarrigiannis, P. G. (2022). EEG Recordings as Biomarkers of Pain Perception: Where Do We Stand and Where to Go? *Pain Ther*, *11*(2), 369-380. https://doi.org/10.1007/s40122-022-00372-2

Interactions of Reverse Dipole Moment Zwitterionic Materials with Human Serum Proteins towards Hemocompatible Dialysis Membranes

Simin Nazari[1] and Amira Abdelrasoul[1,2]*

****amira.abdelrasoul@usask.ca***

[1]Division of Biomedical Engineering, University of Saskatchewan, 57 Campus Drive, Saskatoon, Saskatchewan, S7N 5A9, Canada.

[2]Department of Chemical and Biological Engineering, University of Saskatchewan, 57 Campus Drive, Saskatoon, Saskatchewan, S7N 5A9, Canada.

Introduction

Molecular docking has received a lot of attention for its powerful ability to understand the interaction between ligand-protein complexes, in recent years[1]. Molecular docking allows designing new antifouling compounds in addition to assessing the effect of various parameters like dipole orientation[2,3]. Zwitterionic (ZW) structures have been introduced as an important class of biomimetic to enhance antifouling properties of various surfaces, including medical devices[4]. A zwitterion is a molecule that includes both cationic and anionic parts and is characterized by dipole moment due to its electrostatic nature; however, the influence of the dipole orientation on fouling property has not studied so far. Therefore, this study aimed to investigate the effect of dipole orientation on ZW materials interactions with human serum proteins towards hemocompatible dialysis membranes.

Methods

2-methacryloyloxyethyl phosphorylcholine (MPC) and choline phosphate monomer (MBP) zwitterions were used to study the effect of opposite dipole orientation in ZWs on their interactions affinity via molecular docking. The 3D X-ray structures of human serum proteins were downloaded from RCSB protein data bank and all of the crystallography ligands, ions and water molecules, were removed from the protein backbone. The ligand structures have been created using ChemDraw software and the minimization of molecular structures has been performed. Molecular docking of human serum proteins with ZW materials was performed with AutoDock vina software version 4.0.

Results

For the first time, computational docking has been used to comprehensively analyze the impact of ZWs dipole orientation on interactions affinity. Computational docking using Auto Dock Vina provides useful data on binding sites and interaction patterns that are the important factors interactions and adsorption of the proteins to the ZW materials. The results demonstrated that zwitterionic materials have unique behavioral pattern that is affected by ZW conformations that alter electrostatic interactions. Docking studies analysis showed that the MPC had higher affinity energies than MBP of for all the ligand-proteins interactions indicating that the dipole orientation affected the optimized structures as well as protein-ligand interactions that directly influence on ZW hemocompatibility.

Conclusions

Protein-ligand interactions of different dipole orientation ZWs have been thoroughly investigated using molecular docking. MBP showed lower affinity energy in attaching to all examined proteins compared to MPC, displaying better antifouling compound and distinctive behavior as a result of their dipole moments.

References

(1) Daneshamouz, S.; Saadati, S.; Abdelrasoul, A. *Structural Chemistry* **2022**, *33*, 1133.

(2) Saadati, S.; Eduok, U.; Westphalen, H.; Abdelrasoul, A.; Shoker, A.; Choi, P.; Doan, H.; Ein-Mozaffari, F.; Zhu, N. *Materials Today Communications* **2021**, *29*, 102928.

(3) Westphalen, H.; Saadati, S.; Eduok, U.; Abdelrasoul, A.; Shoker, A.; Choi, P.; Doan, H.; Ein-Mozaffari, F. *Scientific reports* **2020**, *10*, 1.

(4) Nazari, S.; Abdelrasoul, A. *Biomedical Engineering Advances* **2022**, 100026.

Altered forearm crutch length changes shoulder and scapular kinematics

Amanda L. Chen, BSc[1], Gregor Kuntze, PhD[2], Janet L. Ronsky, PhD[1], Ranita H.K. Manocha, MD, MSc[3]
[1]Department of Mechanical and Manufacturing Engineering, University of Calgary, Calgary, Alberta, Canada
[2]Faculty of Kinesiology, University of Calgary, Calgary, Alberta, Canada
[3]Division of Physical Medicine & Rehabilitation, University of Calgary, Calgary, Alberta, Canada

Introduction

Forearm crutches (FC) are commonly prescribed to help individuals with impairment of one or both legs mobilize [1]. FCs result in weight-bearing through the hands, wrists, and forearms. FC use has been associated with rare injuries to the upper limb nerves and bones, and improper crutch length may increase the risk of such injuries [2]. The aim of this investigation was to explore the effects of forearm crutch length on upper limb kinematics to better understand upper limb injury risk with crutch-walking. It was hypothesized that longer crutches would increase scapular upward rotation, shoulder extension, shoulder abduction, elbow flexion, and wrist ulnar deviation, and that shorter crutches would have the opposite effect.

Methods

15 healthy males (mean±SD: age 24.5±5.8 years, BMI 24.9±2.4 kgm^{-2}) with no prior crutch experience were fitted with FCs for 3 length conditions: standard fit [3]; 5cm longer than standard; and 5cm shorter than standard. Participants were instructed on single-limb swing-through gait (STG) and walked across an 8x2 m raised walkway. Whole body and crutch kinematics were recorded using a 10-camera motion capture system (Motion Analysis, USA; 120Hz) for fifteen trials per length condition. The order of crutch length tested was randomized [4]. Joint angles were computed in Visual 3D (C-Motion, USA) and then normalized to the STG gait cycle. Statistical analyses were conducted in MATLAB (v2021a, Mathworks, USA). The effects of crutch length on joint angles at initial crutch contact (IC) and joint range of motion (ROM) were analyzed using multivariate analysis (Hotelling's T2, $\alpha = 0.025$) and simultaneous confidence intervals (CI).

Results

Significant effects of crutch length on joint angles at IC were found for both the long-standard ($p < 0.001$) and short-standard ($p < 0.001$) length comparisons. Crutch length did not affect joint ROM throughout the gait cycle. At crutch initial contact, the long crutch condition produced greater scapular upwards rotation (mean difference [97.5% CI]: -4.7 [-6.1, -3.2]˚), shoulder abduction (-3.5 [-5.8, -1.2]˚) , shoulder extension (-3.4 [-5.8, -0.9]˚ and elbow flexion (4.7 [2.0, 7.5]˚) compared to the standard crutch condition. The short crutch condition produced greater scapular downwards rotation (3.6 [2.3, 4.9]˚), shoulder adduction (2.0 [0.3, 3.7]˚) and shoulder flexion (3.2 [0.4, 6.0]˚) compared to the standard crutch length. There was no effect of crutch length on wrist radial/ulnar deviation.

Conclusions

Altering FC length changed downward/ upward scapular rotation and shoulder adduction/abduction and flexion/extension at crutch initial contact during crutch-assisted swing-through gait in healthy novice male crutch users. In contrast to previous literature [5], the long crutch condition increased shoulder abduction, which could increase compressive forces in the glenohumeral joint and cause shoulder pain [6]. Further research on how altered upper limb kinematics correlate with injury risk with forearm crutches is necessary. In addition, the impacts of altered crutch length in long-term users who tend to use forearm crutches would be important to understand.

References

[1] Rasouli & Reed, 2020. *J Biomech*. 98: 109489.
[2] Manocha et al., 2021. *PM&R*. 13: 1176-1192.
[3] Potter & Wallace, 1990. *BMJ*. 301: 1037-1039.
[4] Urbaniak & Plous. Research randomizer (version 4.0). 2013.
[5] Sherif et al., 2016. *Int J Ind Ergon*. 53: 59-66.
[6] Crosbie et al., 1992. *Aust J Physiother*. 38: 261-266.

Isn't research 'fun' when trying to speed your supervisor's Window's Malab 'RNA-Squiggle' analysis using multi-threaded CPU's, GPU's and a third-party Linux GIT download?

Ho Lam Yeung[1], Michael Smith[2]
[1] Mitacs Globalink Research Intern, Biomedical Engineering Programme, University of Hong Kong, Hong Kong
[2] Department of Electrical and Software Engineering, University of Calgary, Canada

Introduction

Figure 1 shows part of a noisy-ensemble of 'squiggles' resulting after analysing the picoamperage signals generated as nucleotides pass through the nanopores of the new USB-based Oxford MinION sequencer [1]. Data pruning and the dynamic Barycentre Averaging (*DBA*) algorithm must be used for generating a consensus as standard averaging approaches fail because misreads distort the squiggles unevenly in time. This research was to speed the overall code work path, finally allowing each member of the ensemble to vote on the consensus's validity using a multi-threaded *GPU DBA* variant [2].

Methods

Headers were discriminated by the huge difference in standard deviation from the RNA data, see Fig.1. Hundreds of squiggle data streams were examined to determine their stretching/ shrinking distortions along the time axis. The result of recursive statistical computation of differences in means and standard deviations between the amplitudes, density, and length of a stream, local neighbors, and the ensemble was the basis of rejecting a data stream. To assess the optimization, times were compared for standard Matlab functions, the multi-threaded *CPUs* protocol, *parfor loop*, and *gpuArray* functions in which ensemble array was moved to *GPU* memory for fast, parallelized computation. As the current third-party *DBA* implemented continuously calling the MatLab's inefficient native dynamic time warping *dtw* function, a custom Linux C++ *"OpenDBA"* that used the NVIDIA *CUDA* units was ported to a Window's environment.

Results

The efficiency and accuracy of the optimized code were assessed on a simplified squiggle model, an array of random numbers with designated mean and standard deviation. Using MatLab's multi-threaded *parfor loop* approach was inefficient when calculating mean and standard deviation on the large ensemble array. *gpuArray* was slightly optimized compared to the standard MatLab, an advantage trimmed by the process of moving the ensemble array overhead back and forth from the GPU. Moving the *Linux-based OpenDBA* to the Windows platform and linking to MatLab was more difficult than anticipated and the work is continuing.

Conclusions

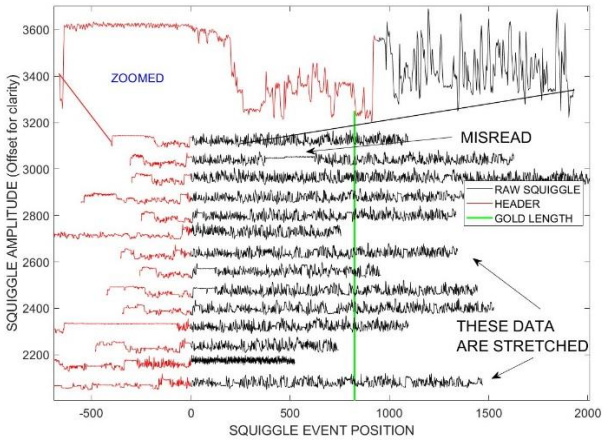
No further research on optimizing multi-threaded CPU and *GPU* computation is planned for the one-time pruning of data. To achieve an optimized *DBA GPU* process, these choices are suggested, (i) continual porting the *Linux-based OpenDBA* to Windows, and linking with to Matlab. or (ii) moving all research onto a *Linux* platform.

References

[1] Smith, M., et al. "Improved step-current signal consensus by combining DTWA with ensemble voting," *Public Library of Science*, vol. 17, no. 9, pp. 1009350-e1009350, 2021.

[2] Gordon, P., "nodrogluap/OpenDBA: GPU-accelerated Dynamic Time Warp (DTW) Barycenter Averaging," 2022. [Online]. Available: https://github.com/nodrogluap/OpenDBA.

Figures



Squiggles have a noisy header (red) to be removed, and an almost random main body (black) with multi-misreads and duplications.

Effect of Prebiotic Fibre Supplementation on Macrophage Infiltration in Adipose Tissue of Obese Rats

Riya Kalaga[1], Nada Abughazaleh[2], Ruth-Anne Seerattan[3], Walter Herzog[3]
[1]Faculty of Arts and Science, University of Toronto, [2]Department of Biomedical Engineering, University of Calgary, [3]Human Performance Laboratory, Faculty of Kinesiology, University of Calgary

Introduction

Obesity is a chronic health issue that is associated with a state of low-grade inflammation with progressive immune cell infiltration into adipose tissues[1]. Adipose tissue inflammation is a major driving force for insulin resistance and type 2 diabetes. Prebiotic fibre supplementation has been shown to reduce body fat percentage and improve insulin sensitivity associated with obesity in rodents and humans[2,3,4]. The aim of this study is to investigate the effects of prebiotic fibre supplementation on macrophage infiltration in adipose tissue using an established model of diet-induced obesity in rats.

Methods

Twelve-week-old Sprague Dawley rats were randomized into 3 groups; a group fed a high-fat/high-sucrose diet (HFS, n=12), a group fed a balanced chow diet (Chow, n=12), and a group fed a high-fat/high-sucrose diet supplemented with prebiotic fibre extract (HFS+F, n=12) for 12 weeks. Retroperitoneal (RET) fat samples were harvested, fixed in NBF (Neutral Buffered Formalin), and processed in paraffin. 10um sections were cut and stained using hematoxylin and eosin. Alternate slides were fluorescently labelled for macrophages using CD68-specific antibodies and DAPI to visualize nuclei. A confocal microscope was used to image fluorescent profiles and macrophage density was quantified manually. Kruskal-Wallis with Bonferroni post hoc testing was performed to determine differences between groups ($p \leq 0.05$).

Results

We identified five stages that lead to the formation of crown-like structures in adipose tissue, distinctly recognizable in samples. The five stages are individual cells, linear profiles, partial crowns, full crowns, and round clusters. The quantification of fluorescent profiles trended towards increased macrophage levels in HFS diet rats as opposed to chow diet. Partial crown structures demonstrated a statistically significant increase between rats fed a HFS diet compared to rats fed a chow diet. Rats with supplemented prebiotic fibre appeared to show decreased macrophage infiltration compared to rats without fibre.

Conclusions

Our results would suggest that adipose tissue expansion causes an increase in pro-inflammatory factors which induce macrophage infiltration. Previous studies showed that prebiotic fibre supplementation superimposed on the HFS diet possibly enhances satiety, blocks fat absorption, and reduces proinflammatory cytokines. In summary, feeding rats a HFS diet increases macrophage infiltration into adipose tissue. Looking at other trends we hypothesize that with an increased duration of feeding, prebiotic fibre supplementation will show a decrease in macrophage infiltration, thus contributing to the maintenance of metabolic homeostasis and a decrease in low level inflammation of the host system.

References

[1]Bai et al., 2015. Obesity Reviews, 16(2), pp. 127–136.
[2]Parnell et al., 2009. Am J Clin Nutr, 89: 1751–1759.
[4]Rios et al., 2019. Scientific Reports, 9(1).

Figures

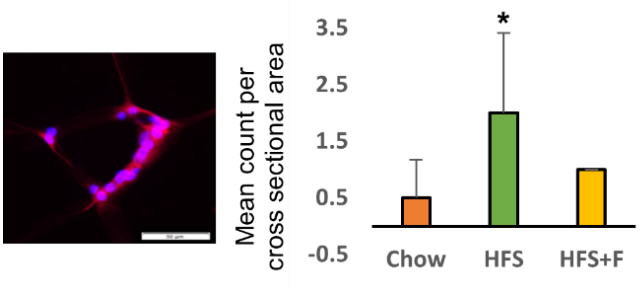


Figure 1: Graph showing average counts of partial crowns (imaged left) with standard deviation bars. *Significant difference compared to chow

Measuring Localized Trabecular Bone Loss Using HR-pQCT Images of Human Knees Following ACL Injury

Mateo Rueda Montes, Nathan J. Neeteson, Steven K. Boyd
McCaig Institute for Bone & Joint Health, University of Calgary, Calgary, AB

Introduction

High resolution peripheral quantitative computed tomography (HR-pQCT) is an imaging modality that provides precise *in vivo* measures of bone microarchitecture [1]. This allows for longitudinal quantification of changes in bone during injury recovery. HR-pQCT can also be used to detect localized areas of low bone density by detecting void spaces, which are regions within the trabecular compartment that are void of mineralized tissue [2].

Longitudinal analysis of void spaces could provide insight into trabecular remodeling following injury. For instance, a significant link between anterior cruciate ligament (ACL) injury and post-traumatic osteoarthritis (PTOA) is well established [3] and post-injury microarchitectural remodeling could be a contributing factor [4]. We hypothesize that ACL tears in knees will lead to a significant increase in the number and volume of void spaces in the injured knee while these measures will remain unchanged in the contralateral knee.

Methods

Bilateral knee scans were performed using HR-pQCT (XtremeCT II, Scanco Medical, 61 μm). Longitudinal data is obtained, and image registration is performed for both the injured and contralateral knee. To study void spaces, 10 ACL patients were examined at months 0 (baseline), 2, 4, 8, starting within 6 weeks of injury. A void space is defined as an empty space between trabeculae with a diameter that is 3 standard deviations above the mean separation of a healthy population (⌀ 0.74 mm) over a continuous volume (17 mm^3).

Void space number and volume are each computed separately in five sagittally divided compartments of the knee [5]. We use mixed effect models for each of the femur and tibia in each knee to observe longitudinal growth.

Results

Figure 1 shows individual longitudinal mixed effect models of void space number trends in the medial and lateral injured and contralateral femurs. Growth is observed only in the medial compartment of the injured femur. Similarly, only the subspinous region of the injured tibia had growth in both void space quantity and volume (not shown).

Conclusions

Mixed effects modelling indicates that evolution of void space number and volume are an outcome of post-injury bone remodeling. Further, the observed asymmetrical compartmental evolution suggests that injury mechanism could also play a role in where void spaces will develop.

Future studies will look at void space prevalence in late-stage osteoarthritis patients.

References

1. Manske, SL et al. (2015). Bone, 79(213-221)
2. Whittier, DE et al. (2021). Bone, 143(115785)
3. Wang, LJ et al. (2020). A. R. & T., 22(57)
4. Kroker, A et al. (2019) J. Orthop. Res., 37: 2325-2336.
5. Hunter, DJ et al. (2011) O. and C. 19(8): 990-1002

Figures

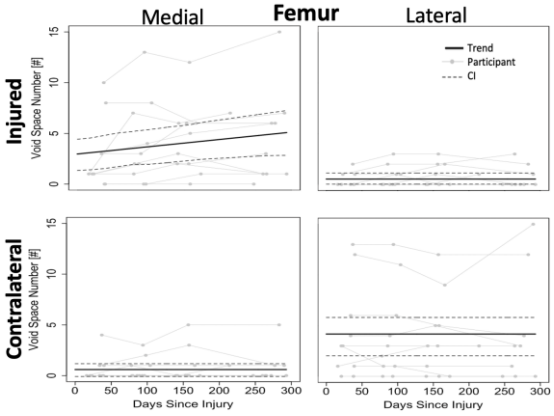


Figure 1: Void space number increases asymmetrically in the injured femur while seeing no change in contralateral knee.

Following the migraine cycle in children and youth using magnetic resonance spectroscopy

Lydia Cho[1,2,3], Tiffany K. Bell[1,2,3], Serena L. Orr[2,3,4], Ashley D. Harris[1,2,3]
[1]Department of Radiology, University of Calgary, [2]Hotchkiss Brain Institute, University of Calgary, [3]Alberta Children's Hospital Research Institute, University of Calgary, [4]Departments of Pediatrics, Community Health Sciences, and Clinical Neurosciences, Cumming School of Medicine, University of Calgary

Introduction

Migraine is a neurological disorder of cyclical nature with multiple phases (i.e., migraine cycle): prodrome/premonitory, aura, headache, postdrome, and interictal. An excitation-inhibition imbalance in the brain, such cortical hyperexcitability leading up to an attack, is suggested to contribute to migraine pathophysiology.(*1*) Previous data from our lab suggest that the neurochemicals responsible for excitation and inhibition (glutamate and γ-aminobutyric acid [GABA], respectively) may fluctuate throughout the migraine cycle.(*2*)

My project uses advanced magnetic resonance spectroscopy (MRS) to quantify glutamate and GABA across the migraine cycle in children and youth. I expect that as a migraine attack approaches, glutamate will increase and GABA will decrease. During and after an attack, I expect a 'reset' as glutamate will decrease and GABA will increase.

Methods

Individuals (8-18 years old) with migraine will be asked to come in for 4 MRI scans over 2 weeks. Standardized daily headache diaries will be completed during the study period.

Glutamate and Glx (glutamate + glutamine) will be quantified in the sensorimotor cortex (SM), thalamus (Thal), and occipital cortex (OCC) using conventional MRS acquisition methods. GABA will be quantified in the SM and Thal using macromolecule-suppressed GABA-edited MRS. This advanced technique removes the overlapping signal from macromolecule contamination to increase specificity of GABA measurements. Data will be analyzed using linear mixed effect models with sex, age, race, intervention type, and migraine cycle phase as factors.

Results

Preliminary results included 14 participants (9 female; 5 male). After quality assessment, scans were binned into different migraine cycle phases (interictal, prodrome, headache, and postdrome) as determined by daily headache diaries. In the SM, increased levels of Glx were seen in the prodrome, suggesting hyperexcitability, and decreased levels were measured during the headache and postdrome, in line with my hypotheses (Figure 1). GABA measurements were lowest in the prodrome and highest in the headache phase.

Conclusions

While preliminary, results suggest that there are fluctuations in neurochemicals across the migraine cycle in children and youth. This project's combination of a novel study design and use of state-of-the-art MRS methods will offer a unique view of migraine that can aid in identifying potential treatment targets focused on the neurobiology underlying the migraine cycle in children and youth.

References

1. G. Cosentino *et al.*, *Pain.* **155**, 1070–1078 (2014).
2. T. Bell *et al.*, *Pain.* **162**, 300–308 (2021).

Figures

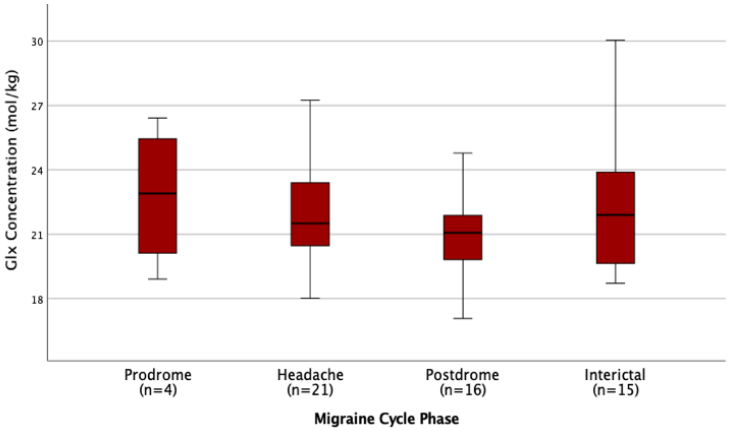


Figure 1. Glx concentrations (mol/kg) across the migraine cycle in the sensorimotor cortex.

Evaluating critical care patient muscle density and cross-sectional area loss using computed tomography internal calibration

Ainsley C.J. Smith[1,2,3], Michael T. Kuczynski[1,2,3], Brandon M. Hisey[2], Justin J. Tse[2,3], Kirsten N. Bott[2,3], Christopher Grant[2], Christopher J. Doig[2], Steven K. Boyd[1,2,3], Sarah L. Manske[1,2,3]
[1]Biomedical Engineering Graduate Program, University of Calgary; [2]Cumming School of Medicine, University of Calgary; [3]McCaig Institute for Bone and Joint Health, University of Calgary

Introduction

Muscle weakness commonly occurs in critical care patients and can lead to long-term physical impairment and loss of independence [1, 2]. Assessing muscle weakness in the intensive care unit (ICU) is typically time consuming and requires patient consciousness and cooperation. However, routinely acquired critical care computed tomography (CT) images can potentially be repurposed to assess muscle density and cross-sectional area (CSA), indicators of muscle weakness. Previously, we developed a CT internal calibration method that provides a reliable measure of muscle density [3]. The purpose of this project was to apply CT internal calibration to observe changes in muscle density and CSA over the course of critical illness.

Methods

We retrospectively acquired abdominal CT images of patients who were admitted to a Calgary ICU from 2016-2022. We used a semi-automatic approach to segment the psoas muscle and total muscle at the level of the third lumbar vertebra. We applied the internal calibration method, which involves selecting air and adipose regions of interest within the scan and using their material properties to estimate the effective scan energy and convert Hounsfield Units (HU) into muscle density (g/cm^3). Image analysis was conducted using ITK-SNAP (v3.8.0) and Python (3.8.8).

Results

We analyzed baseline and follow-up CT scans for 6 critical care patients. We observed a significant decrease in psoas muscle density and HU from baseline to follow-up ($p < 0.05$). Critical care patients lost a median 14.34% (IQR = 19.24%) of psoas muscle CSA, 0.53% (IQR = 1.04%) of psoas muscle density, and 11.04% (IQR = 27.25) of psoas muscle HU from baseline to follow-up. Critical care patients lost a median 17.10% (IQR = 9.60%) of total muscle CSA, 0.37% (IQR = 0.67%) of total muscle density, and 13.45% (IQR = 23.02) of total muscle HU from baseline to follow-up. Time between the baseline and follow-up was a median 13.50 (IQR = 18) days.

Conclusions

We applied a novel internal calibration muscle density analysis method to critical care CT scans. We found that critical care patients experienced a reduction in psoas muscle density and HU over the course of their ICU stay. Next steps include increasing our sample size and understanding factors that influence changes in muscle (e.g., presence of sepsis). This work will help improve our understanding of how muscles react to critical illness and potential long-term complications of critical illness.

References

[1] Appleton et al., 2014. *J Int Care S.*
[2] Vanhorebeek et al., 2020. *Int Care Med.*
[3] Smith et al., 2022. *bioRxiv (pre-print).*

Figures

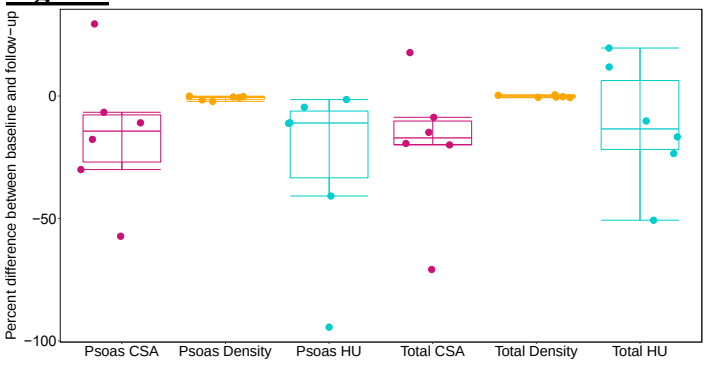


Fig. Boxplot showing psoas and total muscle density, HU, and CSA percent changes between critical care patient (n = 6) baseline and follow-up scans taken 2-59 days apart.

Replicating Patient-Specific Orthodontic Treatment on an In Vitro Orthodontic Simulator Mechanical Tester

Robyn de Wet [1], Arya Subramanian [1], Manuel O. Lagravere [2], Paul W. Major[2], Dan L. Romanyk [1, 2]
[1] Department of Mechanical Engineering, University of Alberta, Edmonton, Canada
[2] Department of Dentistry, University of Alberta, Edmonton, Canada

Introduction

Orthodontic braces are commonly used to treat tooth misalignments, but the link between the applied mechanical loads on the teeth and the measured tooth movement is not well-studied. An in vitro laboratory orthodontic simulator can be used to measure 3D forces and moments exerted on the teeth due to the bracket and wire combination, however, spatial constraints make patient-specific bracket data replication difficult. This work aims to develop a digital and additive manufacturing workflow to generate patient-specific misalignments on an orthodontic simulator for use in measuring force/moment changes throughout treatment.

Methods

3D printed jigs were used to replicate patient bracket data on an electro-mechanical in vitro Orthodontic Simulator (OSIM; Figure 1), developed at the University of Alberta [1]. First, digital patient dental models were taken with an iTero intraoral scanner. The models were aligned in the 3D Slicer software [2], and points were manually added on all bracket slots. The data were exported to an in-house developed Matlab script, which calculated custom jig dimensions for each tooth based on the selected bracket coordinates. Customized jigs were created in Solidworks, 3D printed in standard resin with the Formlabs Form 2 SLA printer and secured onto the OSIM. Orthodontic brackets were bonded to the jigs, as shown in Figure 1, and a FARO Arm was used measure the experimental bracket positions.

Results

Bracket coordinate measurements taken with the FARO Arm were plotted against patient bracket coordinates selected in 3D Slicer. Preliminary data has shown that the discrepancies between the FARO Arm and patient bracket coordinates is between 2.9mm to 5.5mm for the in-plane (buccolingual and mesiodistal) direction, and 0.02mm to 2mm in the out-of-plane (occlusal gingival) direction.

Discussion and Conclusions

Custom 3D printed jigs provide a promising tool to simulate patient-specific bracket positions on the OSIM. The current jigs can replicate bracket coordinates within an accuracy range of 2.9mm to 5.5mm for the in-plane direction, and 0.02mm to 2mm in the out-of-plane direction. Bracket thickness was not accounted for in the original code, and this is the likely cause for a large portion of the error. Based on the current iterative design process, it is estimated that results can be improved to 0.5mm of accuracy, by accounting for bracket thickness in the code.

References

[1] H. M. Badawi et al, "Three-dimensional orthodontic force measurements," *American Journal of Orthodontics and Dentofacial Orthopedics*, vol. 136, no. 4, pp. 518–528, 2009.

[2] A. Fedorov et al, "3D Slicer as an image computing platform for the Quantitative Imaging Network," *Magnetic Resonance Imaging*, vol. 30, no. 9, pp. 1323–1341, 2012.

Figures

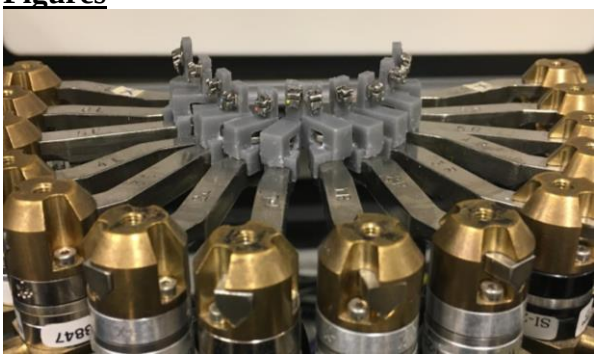


Figure 1: 3D-printed jigs (with bonded brackets) mounted on the OSIM

Tensile Properties of 3D Printed Alginate Tissue Scaffolds

Amanda Zimmerling[a,b,*], Maximilien Vincent[a], Christina Sunil[a], Jim Boire[a,c], Xiongbiao Chen[a,d]

a) Division of Biomedical Engineering, College of Engineering, University of Saskatchewan, 57 Campus Dr. Saskatoon, SK, Canada, S7N 5A9
b) Vaccine and Infections Disease Organization (VIDO), University of Saskatchewan, Saskatoon, SK, S7N 5E3, Canada
c) RMD Engineering Inc., #1 Cory Place East Cory Industrial Park, RM Corman Park, Saskatoon, SK, Canada, S7K 3J7
d) Department of Mechanical Engineering, College of Engineering, University of Saskatchewan, Saskatoon, SK, Canada

Introduction

Tissue engineering aims to develop tissue-like scaffolds for use in modelling or regenerative medicine applications. Soft hydrogel materials are often used due to their biocompatibility and compatibility with 3D printing technologies which allows for repetitive fabrication of complex structures [1]. Mechanical characterization of these printed scaffolds is important to ensure similar properties to the native tissue of interest; however, attaining tensile properties of 3D printed scaffolds composed of soft materials is challenging [2]. The aim of this study was to utilize a novel tensile tester specific for tensile testing of soft tissues and 3D printed hydrogel materials, to investigate the influence of material concentration, scaffold height, and scaffold design on 3D printed alginate scaffolds.

Methods

Sodium alginate solutions (2-5% w/v) underwent rheological characterization using a RVDV-X rheomoeter and a Herschel-Bulkley fluid flow model was fit to the data. A GeSiM Bioscaffolder 3.2 was then used to extrude the materials to determine their printability. Printing speeds and pressures were selected to attain similar strand dimensions between materials. Following the printability assessment, scaffolds were printed from each material concentration for tensile testing. The 4% alginate solution was then used for investigation of the influence of scaffold heights (1-5mm) and scaffold design (layer angles of 45°, 60°, and 90°). Tensile testing was carried out to failure at a rate of 50µm/s. The collected data was then converted to stress-strain curves and analyzed using SPSS 28 statistical analysis software.

Results

Rheological testing determined that higher concentrations of alginate demonstrated more viscoelastic behavior that more closely fit the flow model. Correspondingly, increased printing pressure was required for materials with higher alginate concentrations. Use of the novel apparatus in the tensile tests of 3D printed soft hydrogel scaffolds provided the opportunity to characterize these constructs once printed. It was found that both Young's modulus and ultimate tensile strength increase with increased concentration of alginate. Reduced heights of printed constructs led to a decrease in Young's modulus and increase in ultimate tensile strength, while a decrease in the angle between subsequent layers caused a decrease in both Young's modulus and ultimate tensile strength.

Conclusions

Tensile loading of 3D printed scaffolds composed of soft materials is difficult, bordering on impossible using existing technologies. This study demonstrated that it is feasible via a novel tensile tester and further determined the influence of material concentration, scaffold height, and scaffold design on the tensile properties of printed alginate scaffolds.

References

[1] X. Chen, Extrusion bioprinting of scaffolds for tissue engineering applications, Cham: Springer, 2018.

[2] T. Shameen, "Development of a Biaxial Testing System for Research of Soft Tissue Biomechanics using Laboratory Models," City University, New York, 2021.

Delamination Strength and Stiffness in the Annulus Fibrosus from Adult Spinal Deformity Patients

Manmeet S. Dhiman[1,6], Taylor J. Bader[2,6], David A. Hart[3,4,6], Ganesh Swamy[4,6], Neil A. Duncan[5,6]
[1]Department of Biomedical Engineering; [2]Department of Medical Sciences; [3]Faculty of Kinesiology; [4]Department of Surgery; [5]Department of Civil Engineering; [6]McCaig Institute for Bone and Joint Health, University of Calgary, Alberta, Canada

Introduction: The intervertebral discs (IVDs) in patients with adult spinal deformities, including degenerative spondylolisthesis (**dSpondy**), degenerative scoliosis (**dScoli**), and adolescent idiopathic scoliosis (**AIS**), often exhibit severely degenerated discs at the time of surgery. These conditions are accompanied by biomechanical and biochemical changes, can cause significant pain, and affect mobility [1]. Deficiency of estrogen plays a key role in the development of disc degeneration with higher rates in post-menopausal women than men and premenopausal women, yet a clear cause and treatment strategy remains elusive [2]. It is hypothesized that in post-menopausal women, degeneration of the disc leads to decreased delamination strength and stiffness. The objective of the present study was to measure the interlamellar mechanical properties of the annulus fibrosus (AF) in these deformity patients compared to those in non-deformity degenerated discs (**degen**).

Methods: Human AF tissue samples (n=6 men, n=9 women) were collected from spine surgeries with degenerative disc disease and deformities. Tissues were prepared freshly and were loaded in custom-built clamps to measure the delamination properties of the AF using a peel test as per Gregory et al. [3]. The tissue underwent 10 cycles of preconditioning with 0.05 mm cyclic displacement and 100% water vapor hydration, followed by a stress-relaxation for 2 minutes. The tissue was peeled at 0.5 mm/s until complete separation [3]. The force-displacement curve was analyzed using a custom Python script to calculate the peel stiffness and strength (adapted from [3]). Stiffness and strength values were compared between men and women using a one-tailed Mann-Whitney U test ($\alpha = 0.05$), and the samples were split into four groups: degen (n=6), dSpondy (n=4), dScoli (n=2), and AIS (n=3).

Results: Samples from men had a mean peel stiffness of 0.09 N/mm^2 ± 0.05 SD and a peel strength of 0.62 N/mm ± 0.32 SD whereas samples from women had a mean peel stiffness of 0.14 N/mm^2 ± 0.08 SD ($p = 0.16$) and a peel strength of 0.88 N/mm ± 0.24 SD ($p = 0.034$) (Figure 1).

Conclusions: These preliminary results indicate an increased delamination stiffness and strength in samples from women compared to men in these surgical patients. Increased sample numbers will be required to evaluate statistically significant differences in interlamellar stiffness and strength between the groups. Healthy control samples will also be required to determine if the delamination properties in the AF are different in these surgical patients.

References: [1] Gregory D, et al. The Spine J. (2014). 14(7):1265-71 [2] Wang Y, et al. Radiology. (2010). 257(2):318-20 [3] Gregory D, et al. Eur J Spine. (2012). 21:1716-23

Figures

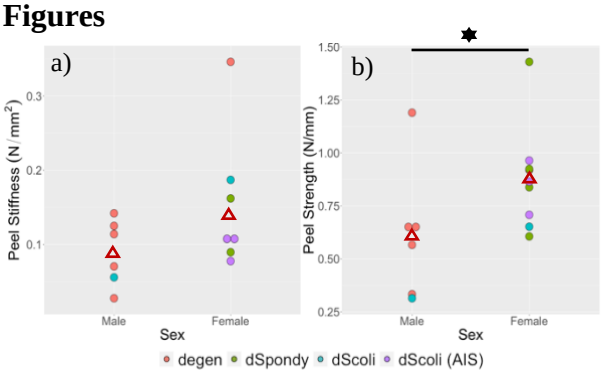


Figure 1: Comparison of the a) peel stiffness, and b) peel strength between male and female surgical patients. Red triangle represents the mean of the group. Patients with the four conditions were grouped together for sex differences. Black star shows statistical significance ($p < 0.05$).

Texture analysis of bovine meniscus T2* maps

Fernandez, EI[1], Cui, L[3], Emily McWalter, EJ[1,2]
[1]Biomedical and [2]Mechanical Engineering, University of Saskatchewan; [3]Siemens Healthineers

Introduction

The meniscus is a fibrocartilaginous knee tissue that is C-shaped in the axial plane and wedge-shaped in the sagittal and coronal planes. It is a highly organized tissue whose structure varies by plane. With magnetic resonance image (MRI) it is possible to assess gross meniscal damage and sub-clinical degeneration, via T2* relaxation time maps[1]. Most often T2* relaxation time data is averaged across regions of the tissue, which results in the loss of relative pixel information. With approaches such as texture analysis, it is possible to glean more information about the tissue's structure. Texture is the characteristic variation of pixel intensity in a region of an image[2] and several parameters have been described to classify texture[3]. The goal of this project was to determine if texture parameters of bovine menisci T2* relaxation time maps vary by plane.

Methods

A series of MRI scans were acquired in six bovine stifle joints using an in-house, flexible ultra-short echo time (FUSE) MRI sequence (3T, Siemens)[4]. The output images had an isotropic resolution of 1 mm allowing for reconstruction in all three imaging planes (axial, coronal, and sagittal). Meniscus masks were applied to the images. T2* relaxation time maps were produced using an in-house, mono-exponential fitting algorithm (MATLAB, MathWorks,).

The gray level co-occurrence matrix (GLCM), which describe the frequency of occurrence of different pixel pairs along specific directions[2], was calculated for each T2* map in four directions (0°, 45°, 90° and 135°), using a step length of one. Each matrix was quantized into eight gray levels and made symmetric. GLCM matrices that were composed only of zeros were discarded before the extraction of the texture parameters. Texture analysis was performed in a slice-by-slice manner on the three image planes of the meniscus T2* maps. Four GLCM parameters were extracted (contrast, correlation, energy, and homogeneity)[3]. After the extraction, parameters were averaged over the different offset directions. Differences in the GLCM parameters between planes were determined using a Kruskal-Wallis test with a post-hoc Dunn's.

Results

Significant differences were found for the correlation parameter ($\chi^2(2)=6.4$, $p=0.041$, mean rank score 11.75 axial, 11.75 coronal, 5 sagittal). The Dunn's test showed differences between the axial and coronal (p=0.028) and axial and sagittal (p=0.028) planes (Fig. 1). For the number of samples tested, no other differences were found.

Conclusions

Differences were observed by plane for correlation. Correlation measures the intensity of association of a pixel and its neighbour over the whole image. This may suggest that correlation reflects tissue structural features. Future work will examine the GLCM directions separately as well as additional GLCM parameters.

References

1) Williams et al, Osteoarthr Cart 2012; 2) Davies ER. Computer vision principles. 2018; 3) Haralick et al: IEEE Tran Sys, Man, and Cybern 1973; 4) Cui L. U of S Thesis, 2021

Figure

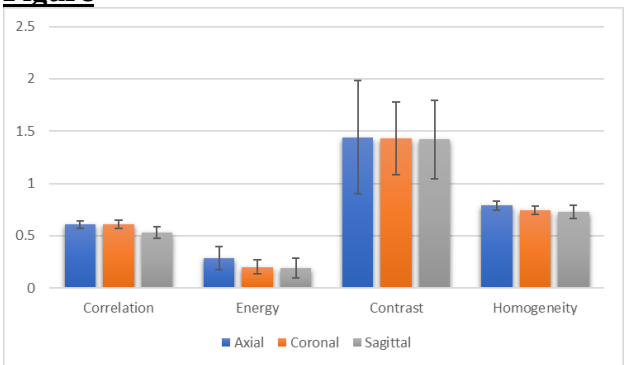


Figure 1: Average GLCM parameters.

Modeling a Robotic Hand in a Virtual Reality Environment

Alexander D. Nichols[1*], Patrick M. Pilarski[2], Jacqueline S. Hebert[2,3], Ahmed W. Shehata[2,3]
[1]Department of Mechanical Engineering, Faculty of Engineering, University of Alberta
[2]Division of Physical Medicine and Rehabilitation, Department of Medicine, University of Alberta
[3]Department of Biomedical Engineering, Faculty of Engineering, University of Alberta

Introduction

Individuals with upper-limb amputations face challenges with learning how to use their prostheses. With current developments, artificial limbs can be controlled using muscle contractions in the residual limb; however, this technology requires training and practice to be effectively integrated into daily use [1]. Virtual Reality Environments (VRE) are capable of making users feel immersed in their surroundings and allows them to interact with objects using virtual prostheses [2]. A VRE provides a method of remotely training persons to use their electromechanical prosthetic devices in a monitored and safe environment. However, a VRE must have realistic physics interactions with objects for the participant to have an optimized experience and to remain engaged. The aim of this project was to implement a novel prosthetic hand developed by the Bionic Limbs for Improved Natural Control (BLINC) lab into their current VRE.

Methods

We evaluated the current prosthetic computer aided design models (SolidWorks, 2021) and modified them to ensure their functionality in the VRE. In Unity, the physics interactions (e.g. colliders, rigid bodies, torque limits, and combined inertias) between the prosthetic hand and different virtual objects such as a milk carton, vegetables, and books, were implemented to increase the accuracy and realism of the tasks using an iterative process (Fig. 1). To control the virtual prosthesis, muscle signals were collected using surface electrodes and then mapped through a pattern recognition algorithm to the velocity of joint motors in the virtual prosthetic arm.

Results

A stable version of the BLINC lab's VRE was developed with the new prosthetic hand implemented into all of the virtual scenes. The virtual prosthetic hand properly interacted with game objects and users were able to complete all tasks in the VRE. Finally, we tested this environment with clinicians and occupational therapists to obtain their feedback about the design of the environment, the quality of the implemented interactions, and the difficulty levels of the tasks. Their feedback was incorporated in the environment and a new version of the VRE was developed.

Conclusions

A prosthetic hand was modeled, adapted, and imported into a VRE to further develop a virtual training system for myoelectric prosthesis users. This training tool will help healthcare professionals to better provide personalized rehabilitation for patients with limb loss. Training on this intermediate platform prior to prosthetic fitting may allow users to gain an understanding of myoelectric control that may then translated to a wearable system for better performance with any prosthetic hand of their choice. The next step is to use this VRE in a full study involving participants with upper limb deficiencies and implement other commercially available prosthetic hands into the VRE.

References

[1] E.A. Biddiss and T.T. Chau,"Upper limb prosthesis use and abandonment: A survey of the last 25 years," Prosthet. Orthot. Int., vol. 31, no.3, pp. 236–257, 2007.
[2] M.Hauschild, R.Davoodi, and G.E.Loeb,"A virtual reality environment for designing and fitting neural prosthetic limbs," IEEE Trans. Neural Syst. Rehabil. Eng., vol. 15, no. 1, pp. 9–15, Mar. 2007.

Figures

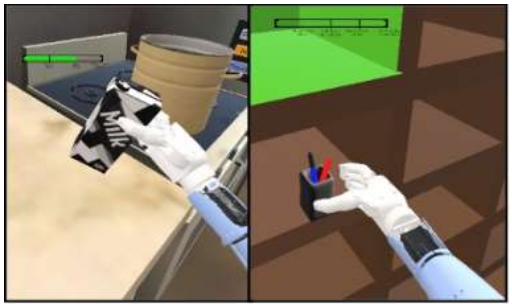


Figure 1. Images of the prosthetic hand in the VRE.

Intraspinal Microstimulation Implants Based on Microcoils

Soroush Mirkiani[1,4], Don Wilson[2,4], Neil Tyreman[2,4], Carly L O'Sullivan[1,4], Richard Fox[3,4], Vivian K Mushahwar[2,4]

[1] Neuroscience and Mental health Institute, University of Alberta, Edmonton, AB, Canada
[2] Department of Medicine, University of Alberta, Edmonton, AB, Canada
[3] Division of Neurosurgery, Department of Surgery, University of Alberta, Edmonton, AB, Canada
[4] Sensory Motor Adaptive Rehabilitation Technology (SMART) Network, University of Alberta, Edmonton, AB, Canada

Introduction

Intraspinal microstimulation (ISMS) is a neuromodulation technique that targets the lumbar spinal cord containing control centers for locomotion[1]. ISMS implants were successfully used in cats and were able to restore standing and walking after spinal cord injury[2]. However, there are challenges in translating the ISMS implants to humans. This is mainly due to the higher range of motion (ROM) in the spinal cord, that could potentially lead to electrode dislodgement and failure of the implant[3]. Coiled cables have been previously used for stabilization of neural implants and reducing the applied force to the neural tissue[4]. In this study, we describe fabrication of ISMS implants for pigs using microcoils. We characterized the mechanical properties of the developed device and tested its functionality in domestic pigs.

Methods

Microwires (50µm, Pt-Ir, 80%-20% insulated with polyimide) were used for fabrication of electrodes. The tips of the microwires were de-insulated with laser pulses (248 nm) and sharpened. Microcoils (OD: 160µm, L:6mm) were fabricated from 25µm microwires, coated with poly-dimethyl siloxane (PDMS), and connected to the microelectrodes by laser welding (1070nm). Sixteen microelectrodes were fabricated with this method. Mechanical properties of the coiled microwires and coiled cable were assessed by uniaxial tension tests.

The implants were tested in 3 domestic pigs. Briefly, a laminectomy was performed at the L3-L5/L6 vertebral levels and dura mater was opened. Eight microelectrodes were then implanted in each side of the spinal cord based on the observed motor responses evoked through microstimulation. Biphasic, current pulse trains (1s, 40Hz, 200µs pulse width) with amplitudes of 50µA-300µA were delivered to the spinal cord. The kinematics and isometric joint forces of the evoked responses were recorded.

Results

Microcoils were stretched up to 30% beyond their initial length with an average force of 19.4±0.46 mN (mean±SD). Angle changes in the left and right knee joints evoked by ISMS with 200µA pulse trains were 17.7±1˚, and 18.1±1˚, respectively, leading to full extension. The maximal forces evoked by ISMS at 300µA were 12.21± 0.91N, and 7.4± 0.71N for knee extension and hip flexion, respectively.

Conclusion

The lumbosacral spinal cord undergoes ~11% of length change, moving from a hyperextended to hyperflexed position[3], and the minimum dislodgment force for implanted electrodes in the pig spinal cord is 24.5 mN[3]. The mechanical properties of microcoils can potentially prevent the dislodgment of microelectrodes. The measured joint forces showed a gradual increase with increasing current amplitudes, implying a near-physiological recruitment order of motor neurons[1]. The results show the functionality of the developed ISMS device and its potential for future long-term use in humans.

Reference

1-Holinski, et al. 2016. "Intraspinal Microstimulation Produces Over-Ground Walking in Cats." J. Neural Eng 13 (5): 56016.

2-Saigal, et al. 2004. "Intraspinal Microstimulation Generates Functional Movements after Spinal Cord Injury." IEEE Trans 12(4): 430–40.

3-Toossi, et al. 2017. "Mechanically Stable Intraspinal Microstimulation for Human Translation." Ann of Biomed Eng 45(3):681–94.

4-Sun, et al. 2021. "High-Stability Polyimide-Based Electrodes to Interface Vagus Nerve." BioRxiv.

Multi-axis robotic 3D bioprinting using the FRESH method

Joonhwan (Jeff) Shin, Dr. Jihyun Lee, and Dr. Keekyoung Kim
Mechanical and Manufacturing Engineering, University of Calgary

Introduction

3D bioprinting is an additive manufacturing process to construct 3D structures which mimic the behaviours of natural living systems using biocompatible materials. Currently, however, 3D bioprinting is mostly incapable of printing functional solid organs because of the inability of the bioprinted constructs to support vascularization *in vivo* [1]. In order to overcome this challenge, this study proposes to develop a robotic 3D bioprinting platform that is a 6-axis robotic bioprinter integrated with a freeform reversible embedding of suspended hydrogels (FRESH) extrusion printing system. The FRESH printing is an extrusion-based bioprinting approach that enables suspended 3D structure printing to increase shape fidelity. Robotic 3D bioprinting is a new trend in this field to increase flexibility in the direction of printing [1]. This is the first study that uses a robotic arm to 3D bioprint using the FRESH method, which allowed the end-effector to be kept perpendicular to the surface during printing to reduce the staircase effect and for strength optimization.

Methods

The robotic bioprinter for a FRESH extrusion printing system was developed using a 6-degrees-of-freedom robotic arm (UR5e) as shown in Figure 1. A pneumatic extrusion system was used to extrude the bioink. The nozzle is attached to the robotic arm via a custom-built 3D-printed nozzle mount and connected to the pneumatic extrusion system via a tube. The Script file for the desired print was obtained via PowerMill to create a multi-axis additive toolpath. Then, the Script file was re-engineered to integrate the pneumatic extrusion system. Initial tests were run using alginate-gelatin hydrogel as the bioink and gelatin slurry as the supporting bath. After printing $CaCl_2$ solution is used to crosslink the bioink and extract the printed parts. Mechanical and biological tests are conducted post-print to evaluate the platforms performance.

Results

Pilot tests have been conducted using our robotic 3D bioprinting platform and alginate-gelatin hydrogel bioink. Surface coating strategies can be used to bioprint for hand burn wound reconstruction as shown in Figure 2(a). The biomaterials were deposited in a layer-by-layer fashion utilizing PowerMill's multi-axis abilities. The resulting structure is shown in Figure 2(b).

Conclusions

The results demonstrate that bioprinting using the FRESH method paired with multi-axis printing enables complex scaffolds to be bioprinted while the staircase effect is minimized to improve surface quality. The proposed robotic 3D bioprinting platform will be further improved by leveraging artificial intelligence and computer vision to improve the accuracy and robustness of 3D bioprinting.

References

[1] S. Derakhshanfar *et al.*, *Bioactive Materials*, vol. 3, no. 2, pp. 144-156, 2018.

Figures

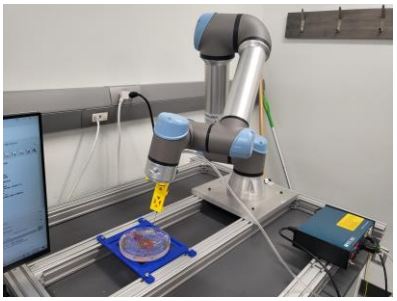
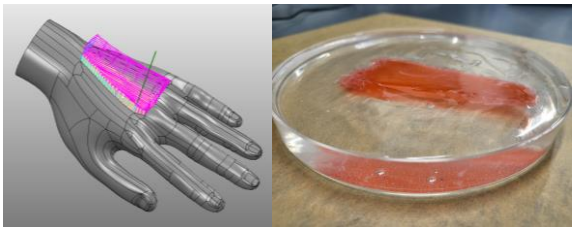


Figure 1: The robotic bioprinter



(a) (b)

Figure 2: (a) Surface coating strategy for hand burn wound reconstruction. (b) Resulting structure in a clear glycerol bath

The effect of a 3-week delayed prebiotic fibre intervention on muscle integrity in rat vastus lateralis in a diet-induced obesity model

Hannah Smith[1-3], Elaine Nguyen[2], Nada Abu Gazaleh[1-3], Ruth-Anne Seerattan[2], and Walter Herzog[1-3]
[1]Department of Biomedical Engineering, University of Calgary; [2]Faculty of Kinesiology, Human Performance Lab, University of Calgary; [3]McCaig Institute for Bone and Joint Health, University of Calgary

Introduction

Obesity and associated metabolic syndrome are risk factors in the development of sarcopenia, or muscle wasting. As muscle mass is a key indicator of long-term health [1], it is important to understand the relationship between diet and muscle integrity. In previous work, we demonstrated that a high fat/high sucrose (HFS) diet induces obesity and low level systemic and local joint, bone, and muscle inflammation in male Sprague-Dawley rats [2,3]. This has led to an increase in fat infiltration and fibrosis in the vastus lateralis (VL) muscle [2]. Fibrosis is the deposition of excess collagen and is a feature of abnormal muscle repair [5]. A link has been speculated to exist between intramuscular fat and fibrosis; intramuscular lipid content in skeletal muscles induces local inflammation which signals the muscle repair process, leading to increased fibrosis and compromised structural integrity [3].

To counter the damage associated with obesity, previous studies have successfully introduced prebiotic fibre diet interventions coinciding with the start of a HFS diet [4]. These studies have shown that fibre induces a change in gut microbiota that decreases gut permeability to bacterial lipopolysaccharides, or endotoxins, thus decreasing inflammation [5]. However, the effects of delayed dietary fibre interventions on the VL muscle of rats exposed to a HFS diet have yet to be explored.

The objective of this study was to determine whether a 3-week delayed prebiotic fibre intervention alleviates or modifies fat accumulation in the VL muscle of Sprague-Dawley rats exposed to a HFS diet. We hypothesize that a critical timeline exists for the fibre intervention to affect skeletal muscle fat infiltration, and the group receiving HFS with the delayed fibre intervention will have similar fat infiltration as the control group.

Methods

Thirty-five, male Sprague Dawley rats at twelve weeks of age, were randomized into three experimental groups: 1) animals fed a chow diet ($n=12$); 2) animals fed a HFS diet ($n=12$); and 3) animals fed a HFS diet with a prebiotic fibre intervention at 15 weeks old ($n=11$). Interventions were maintained for nine weeks. Rats were sacrificed and the VL muscles harvested at 24 weeks of age. The VL muscles were then analyzed for fat content using the histological stain Oil Red O and then quantified using ImageJ.

Results

Fat content into VL differed across all groups ($p < 0.05$). Rats in the HFS group had the highest percentage of fat content ($2.7\% \pm 1.5$), followed by the group fed the HFS plus prebiotic fibre diet supplement ($1.2\% \pm 0.9$). The chow-fed control group had the lowest fat content ($0.3\% \pm 0.3$).

Conclusions

Based on these results we conclude that a 3-week delayed prebiotic fibre diet intervention is still within the critical timeline where it has a protective effect on the VL muscle of Sprague Dawley rats. This confirms our hypothesis, as both the control and the fibre intervention group had significantly less fat infiltration than the HFS group. This finding provides important information about the timeline for implementation of a diet intervention to alleviate and prevent muscle degeneration in animals exposed to an obesity inducing diet. These results may also inform human clinical trials and suggest prebiotic fibre supplementation as a treatment modality that may prevent muscle degeneration in patients with obesity and metabolic syndrome.

References

[1] Srikanthan & Karlamangla, 2014. *AM. J. Med.* 127.
[2] Collins et al., 2016. *Sci. Rep*. 6.
[3] Collins et al., 2016. *J. Orthop. Res*. 34(12).
[4] D'Souza et al., 2015. *Physiol. Rep*. 3(8).
[5] Rios et al., 2019. *Sci. Rep*. 9(1).

Articular Cartilage T_2 Relaxation Time Decreases in Regions of Loaded Contact in Cadaver Knees

[1]Bzowey NM, [2]Black MS, [1]Cui L, [1]Thorson CS, [1]Martel MM, [1]McWalter EJ
[1]Department of Mechanical Engineering, University of Saskatchewan, Saskatoon, SK, Canada
[2]Department of Radiology, Stanford University, Stanford, CA, United States

Introduction

Articular cartilage degeneration is important in knee osteoarthritis (OA) progression[1]. T_2 relaxation time is a quantitative MRI (qMRI) metric that increases with OA[2] and is associated with collagen organization and water content[3,4], both of which contribute to the load-carrying characteristics of the tissue. Most qMRI studies acquire data in the unloaded knee, but it has been shown that T_2 relaxation times decrease when the knee is loaded[5]. Whether this is a global or local phenomenon has not been ascertained. Therefore, the aim of this work was to identify focal changes in T_2 relaxation times inside and outside of tibiofemoral contact in loaded cadaver knee whole, superficial and deep layers of articular cartilage.

Methods

Six cadaver knees (70.3±9.3 years; no history of injury/surgery; no full-thickness cartilage defects) were scanned using a modified quantitative double-echo in steady-state (qDESS) sequence at 3T[6] (Magentom Skyra, Siemens, Germany). Images were first acquired unloaded and then the knees were axially loaded in displacement control to approximately 800N using a custom, MRI-safe loading apparatus. There was a 110-minute delay between load application and image acquisition to account for cartilage stress relaxation. Femoral and tibial cartilage and the region of tibiofemoral contact were manually segmented (Analyze 14.0, AnalyzeDirect, USA) and T_2 relaxation time maps were generated[7]. Projection maps of the femoral and tibial cartilage were created, and the unloaded projection maps were subtracted from the loaded maps to create difference maps. The loaded tibiofemoral contact area was projected onto the difference maps, and clusters of increased (positive) and decreased (negative) T_2 relaxation time were identified inside and outside of the contact area[8,9]. A cluster was defined as groups of contiguous pixels for which 1) T_2 relaxation time was greater than 10ms for femoral cartilage and 5ms for tibial cartilage, and 2) area was greater than 1% of the total projection map area[10]. The percentage of the area inside and outside of the contact boundary occupied by positive (%CL+) or negative (%CL-) clusters was calculated. A Wilcoxon Matched Pair test was used to identify differences in %CL+ and %CL- inside and outside of the contact region (SPSS, IBM, USA). Superficial and deep layers of cartilage were separated based on the mid-point of cartilage thickness and the same methodology as the whole cartilage thickness was applied.

Results

Negative clusters, indicating a decrease in T_2 relaxation time with load, appeared predominantly inside of the femoral and tibial cartilage contact areas. The median percentage of loaded femoral and tibial cartilage contact area covered in negative clusters was 39% (Range: 23-52%, $p = 0.028$) and 56% (Range: 27-90%, $p = 0.028$), respectively. The superficial layer had significantly more negative clusters within the tibial and femoral contact region compared to the deep layer ($p = 0.028$).

Conclusions

Both positive and negative focal changes in T_2 relaxation time are present in loaded cartilage, and majority of negative focal changes were observed within the tibial and femoral cartilage contact area. Greater negative focal changes within the tibial and femoral cartilage contact area were observed in the superficial layer of cartilage.

References

1. Lee *Biol and Med* 2016; 2. Dunn *Radiology* 2004; 3. Raya *ISMRM* 2017; 4. Nieminen *MRM* 2001; 5. Subbaraj, *JOR* 2012; 6. Starosweicki *MRM* 2012; 7. Sveinsson *MRI* 2017; 8. Monu *OA&C* 2016; 9. Black *Stanford Thesis* 2019; 10. Thomas *Cartilage* 2021

Effect of high and low epidural spinal cord stimulation and intraspinal microstimulation on cFos positive neuron distribution

Carly L. O'Sullivan[1,2], James R. Krauth[3,4,5], Neil Tyreman[1,6], Wilbur A. O'Steen[3,4,5], Soroush Mirkiani[1,2], Maxwell Boakye[3,4], Dena R. Howland[3,4,5], Vivian K. Mushahwar[1,2,6]

[1]Neuroscience & Mental Health Institute, University of Alberta, Edmonton, AB, Canada

[2]Sensory Motor Adaptive Rehabilitation Technology (SMART) Network, University of Alberta, Edmonton, AB, Canada

[3]Kentucky Spinal Cord Injury Research Center, University of Louisville, Louisville, Kentucky, USA

[4]Department of Neurological Surgery, University of Louisville, Louisville, Kentucky, USA

[5]Robley Rex VA Medical Center, Louisville, Kentucky, USA

[6]Division of Physical Medicine and Rehabilitation, Department of Medicine, University of Alberta, Edmonton, AB, Canada

Introduction

Spinal cord injury has devastating effects on an individual's motor function, including locomotion, which significantly impacts quality of life. Two methods of spinal cord stimulation show promise at overcoming loss of locomotion, epidural spinal cord stimulation (ESCS) and intraspinal microstimulation (ISMS). ESCS involves placing an array of electrodes on the dura mater of the spinal cord (1), and ISMS involves inserting ultrafine microwires directly into the ventral horn (2). Both methods work by directly or indirectly stimulating the locomotor networks to facilitate walking (2, 3). The goal of this project is to identify the sites of action of ESCS and ISMS in the spinal cord by determining the distribution of neurons activated by each stimulation modality.

Methods

5 neurologically intact female domestic pigs were used in this study and were divided into 5 treatment groups: low amplitude ESCS, high amplitude ESCS, low amplitude ISMS, high amplitude ISMS, and naïve sham. In the treatment conditions, a laminectomy was performed to expose the lumbosacral enlargement and the stimulation array was implanted. Stimulation duration in the treatment groups was 5 hours and was set to just above motor threshold in the low amplitude groups, and to levels that produced clinically meaningful large movements in the high amplitude groups. In the naïve sham the animal was anesthetized for 5 hours with no surgical intervention. Following surgery, the animals were euthanized and perfused with a fixative solution. The spinal cords were removed for immunohistochemical analysis to assess the distribution of neurons activated. This was determined by using an antibody against cFos, a marker of neuronal activity (4), and an antibody against NeuN, a marker of neurons (5).

Results

Quantitative analysis is currently underway to determine the distribution of activated neurons. Early results show an increase in cFos in the dorsal and intermediate regions of the grey matter in ESCS and in the ventral and intermediate regions of the grey matter in ISMS.

Conclusions

To the best of our knowledge this is the first time that the distribution of neurons has been examined and compared following ESCS and ISMS. These data will provide the normative distribution of activated neurons for ESCS and ISMS for future research involving spinal cord injury.

References

[1]Shealy et al., 1967. Electrical Inhibition of Pain by Stimulation of the Dorsal Columns: Preliminary Clinical Report

[2]Mushahwar and Horch, 1997. Proposed specifications for a lumbar spinal cord electrode array for control of lower extremities in paraplegia.

[3]Harkema, et al., 2011. Effect of epidural stimulation of the lumbosacral spinal cord on voluntary movement, standing, and assisted stepping after motor complete paraplegia: a case study.

[4]Bullit, 1990. Expression of C-fos-Like Protein as a Marker for Neuronal Activity Following Noxious Stimulation in the Rat

[5]Mullen et al., 1992. NeuN, a neuronal specific nuclear protein in vertebrates.

Ex-Vivo Heart Perfusion Flow Meter

Natasha Kabarchuk, Guilherme M. Bessa, David S. Nobes
Department of Mechanical Engineering, University of Alberta, Edmonton, Canada

Introduction

Ex-vivo heart perfusion (EVHP) is a system that can replace conventional cold storage for donor heart preservation. It perfuses the heart with warm and oxygenated blood, keeping the heart beating outside the body. This method extends the preservation period that a heart can remain out of a body, expands the heart donor pool, and allows for testing the metabolic and mechanical function of the heart. A flow meter has been developed to record and assess inflow and outflow rates of the heart to allow mechanical performance testing. It is important that the flow meter design gives accurate and repeatable measurements of pulsatile flow and be disposable due to the biological hazards from contact with blood.

Methods

An orifice plate flow meter was the chosen design as it is easily manufacturable and allows for measurement of bidirectional unsteady flow [1]. There were several chosen designs that were manufactured and tested. The flow meters were 3D printed (Form 3, Formlabs Inc.) as one component as shown in Fig 1(a) to reduce sealing issues. As the accuracy of an obstruction flow meter is highly dependent on the geometry, the designs were post machined on a 5-axis milling machine (Pocket NC V2-50 CHK, Pocket NC) to produce the geometry with a high tolerance shown in Fig 1(b).

Once the designs were manufactured, they were tested in a flow loop to evaluate their accuracy. For initial testing the flow meters were fed a steady flow of water from a peristaltic pump and a DAQ recorded the results from the pressure transducers connected to the flow meters. This was converted into volumetric flow rate using a modified version of Bernoulli's unsteady equation:

$$A\frac{dq_v(t)}{dt} + B|q_v(t)|q_v(t) = \frac{\Delta P(t)}{\rho} \quad (1)$$

where A and B are parameters based on the geometry [2]. This was compared to a ground truth flow rate to determine the flow meters discharge coefficient.

Results

The flow rate derived from the pressure data collected across the orifice plate was plotted with the ground truth volume flow rate. The results show that the flow rate obtained from Bernoulli's unsteady equation is linearly related to the actual volumetric flow rate. The collection of data is still ongoing for the different flow meter designs.

Once testing with the peristaltic pump is complete the flow meters will be tested using a left ventricular assist device to more closely mimic the pulsatile flow conditions of the heart. The working fluid will also be changed to a non-Newtonian fluid to view the effects on the results of the flow meters.

Conclusions

This study will concentrate on determining the most effective flow meter design for the EVHP system through the experimental analysis discussed previously. The presentation will discuss design choices, experimental setup, and review results that have been collected up to the date of the conference.

References

[1] Plamondon et al., CSME Congress (2022)
[2] Beaulieu et al., Flow Measurement and Instrumentation 22 (2011)

Figures

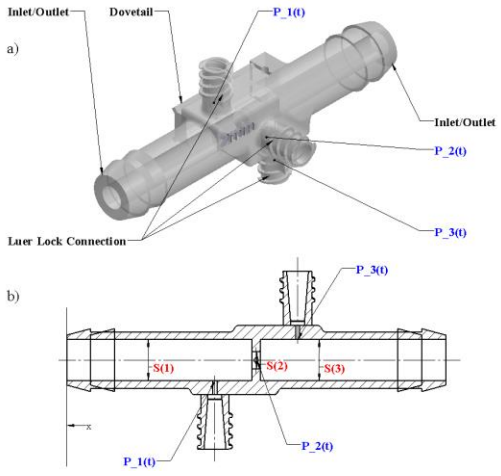


Figure 1: Example design of EVHP flow meter (a) and the cross sectional geometry (b).

Measuring Dental Implant Stability with the Advanced System for Implant Stability Testing (ASIST)

Chester Jar[1], Andrew Archibald[1,2], Monica Gibson[2], Lindsey Westover[1]
[1]Department of Mechanical Engineering, University of Alberta, Edmonton, Canada
[2]Faculty of Medicine and Dentistry, University of Alberta, Edmonton, Canada

Introduction

Dental implant failure results in surgical complications, and mainly occurs during the early stages of healing due to insufficient integration of the implant in bone [1]. Many devices, such as the Osstell®, use resonant frequency analysis to estimate stability. However, a stability threshold has not been defined, as resonance frequencies are related to external factors such as abutment mass and geometry. The Advanced System for Implant Stability Testing (ASIST) [2] is a measurement device developed at the University of Alberta. The ASIST mechanically strikes the system and records the acceleration response during impact. An approximate analytical vibration model of the system is used to fit the response and estimate the bone-implant interface stiffness, reported as the ASIST Stability Coefficient (ASC). This study presents a preliminary evaluation of the ASIST to measure dental implant stability.

Methods

In-vitro models were created using two Straumann bone-level implants (3.3 mm, 4.1 mm diameter), each with two corresponding abutments. Three densities of polyurethane foam (20, 30, 40 pcf; Sawbones) were used as a bone substitute. Implants were installed with or without adhesive to simulate implants that have been integrated or newly placed, respectively. ASC values were compared between bonded and non-bonded implants, substrate density, implant type, as well as Osstell® ISQ measurements. Consistency of ASC values was evaluated by testing different abutments for implant systems with adhesive, as bonding fixes the interfacial properties. A significance level of 0.05 was used for all comparisons.

Results

Shown in Figure 1, the most significant difference in ASC values was found between bonding condition followed by density, while implant type was not significant. No significant difference was found between ASC measurements of the same replicate with different healing abutments despite distinct acceleration responses (Figure 2), showing that interface properties can be isolated from the rest of the system. ISQ values differed significantly with implant type and appears to plateau despite changes in ASC values in upper stability regions (Figure 3). This implies that the ASIST is capable of detecting and isolating changes in the properties of the interface and surrounding material over a wider range than the Osstell®.

Conclusions

The ASIST was shown to be more sensitive to changes in stability over a greater range than the Osstell®. ASC values were able to differentiate implant stability in terms of bonding condition and substrate density, making the ASIST a viable candidate for dental implant stability measurement.

References

[1] Staedt et al. (2020). Int J Implant Dent 6(1):81.
[2] Westover et al. (2016). J Biomech 49:3651-3659.

Figures

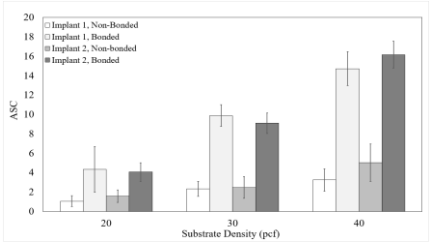


Figure 1: Comparison of ASC results between bonding condition and density.

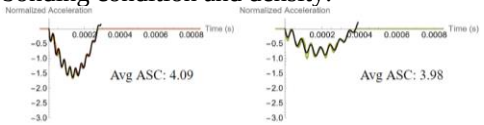


Figure 2: Acceleration response and ASC obtained with different abutments on the same implant system.

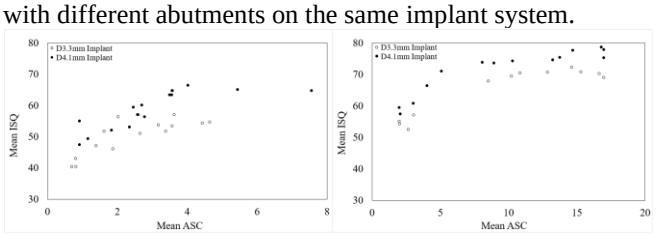


Figure 3: ISQ vs. ASC for non-bonded (left) and bonded (right) implants.

Using Machine Learning to Discover Genetic Effects on Brain Aging in the UK Biobank

Emily Munro,[1-5] Karen Ardila,[2-7] Aashka Mohite,[2-5] Charlotte Curtis,[3,8] Amanda V Tyndall,[9] M. Ethan MacDonald[2-5]
Departments of [1]Chemical Engineering, [2]Biomedical Engineering [3]Electrical & Software Engineering, & [4]Radiology, [5]Hotchkiss Brain Institute, University of Calgary, Canada
[6]Department of Electronic and Automation, Biomedical Engineering, Universidad Autónoma de Manizales, Manizales, Colombia; [7]MITACS Globalink Internship Program,
[8]Department of Mathematics & Computing, Mount Royal University, Calgary, Canada
[9]Department of Medical Genetics, University of Calgary, Canada

Introduction

The influence of genetic predisposition on changes in brain morphology during aging remains largely unknown. Determining relationships between genetics and brain aging could help find candidate genes that influence accelerated brain aging and neurodegenerative disease. Past research has used genome-wide association studies (GWAS) to identify candidate single nucleotide polymorphisms (SNPs); however, these studies are limited in total power by the cohort sizes (<20,000 subjects) and only test for linear associations between brain regions of interest (ROIs) and SNPs [1]. Our work will use the largest available dataset and machine learning models to explore genetic effects on brain aging.

Methods

We obtained genetic and T1-weighted structural MRI data from the UK Biobank for 40,403 subjects aged 44 to 82 years. Brain age gap estimation (BrainAGE) was done by inputting measurements from a single ROI to a machine learning based age prediction model. Predicting brain age and subtracting chronological age gives the brain age gap, which can be used as a biomarker of brain aging. Three ROIs were used to obtain BrainAGE: Total brain volume, ventricular cerebrospinal fluid (CSF) volume, and total hippocampal volume. BrainAGE found using each ROI is then compared with genetics in a GWAS performed using PLINKv1.9 [2].

Results

The GWAS identified several significant SNPs for each ROI. Total brain volume had all SNP associations in a gene locus on chromosome 17 that has been previously associated to brain aging (Figure 1); with the lead SNP being NM_001256299.3(CRHR1):c.-492-27737C>G. Ventricle CSF volume had two significant SNPs, one of which was NM_014840.3(NUAK1): c.579+837A>T (chromosome 12), a novel finding in a gene known to play a role in cell senescence [3] (Figure 2). Finally, total hippocampal volume had all significant SNPs on chromosome 19 in the APOC1 and TOMM40 gene regions (Figure 3), with the lead SNP being NM_001645.3(APOC1):c.*459A>G.

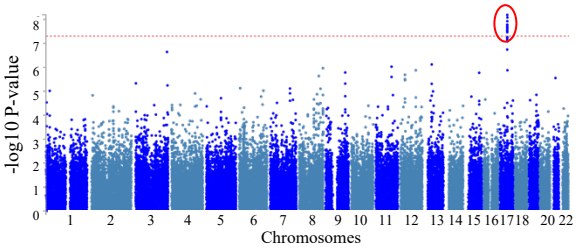


Figure 1: *Manhattan plot of significant SNPs for brain aging using total brain volume. All SNPs are on chromosome 17 with the lead SNP on the CRHR1 gene.*

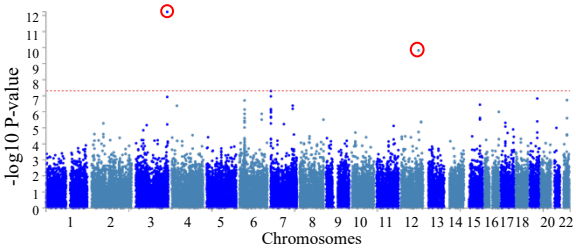


Figure 2: *Manhattan plot of significant SNPs for brain aging using ventricular CSF volume. The left SNP is in the GMNC gene region while the right is on the NUAK1 gene.*

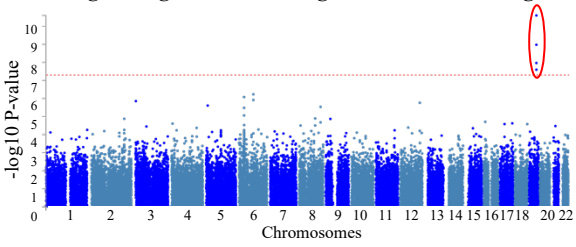


Figure 3: *Manhattan plot of significant SNPs for brain aging using total hippocampal volume. All SNPs are on chromosome 19, with the lead SNP on the APOC1 gene.*

Conclusions

The model identified many SNPs affecting morphological changes for each ROI during brain aging. By using a machine learning model, complex relationships between genetics and brain aging may be discovered and allow precision medicine approaches to treat brain aging and neurodegeneration.

References

[1] E. Uffelmann, *et al.*, "Genome-wide association studies," Nature Reviews Methods Primers, vol. 1, no. 1, Aug. 2021.
[2] A. T. Marees, *et al.*, "A tutorial on conducting genome-wide association studies: Quality Control and statistical analysis," International Journal of Methods in Psychiatric Research, vol. 27, no. 2, Feb. 2018.
[3] X. Hou *et al.*, "A new role of NUAK1: directly phosphorylating p53 and regulating cell proliferation," Nature Oncogene, no. 30, Feb. 2011.

Investigating the Role of HIF-1α Signaling in Pneumococcal Pneumonia Using a Vascularized 3D Lung-On-A-Chip Model

Hellen Kang[1], Nicole Rosin[2], Sarthak Sinha[2], Jeff Biernaskie[2], Mark R. Gillrie[1,3]
[1]Department of Microbiology, Immunology and Infectious Diseases, University of Calgary; [2]Department of Veterinary Medicine, University of Calgary; [3]Schulich School of Engineering, University of Calgary

Introduction

Pneumococcal pneumonia is a lung infection caused by *Streptococcus pneumoniae* (SP). SP adheres to alveolar epithelial cells to induce inflammation, and can enter the bloodstream via vascular endothelial cells to cause invasive pneumococcal diseases such as meningitis. Hypoxia-inducible factor 1-alpha (HIF-1α) is a subunit of the transcription factor HIF-1 that canonically regulates cellular responses to hypoxia. HIF-1α has been implicated in immune responses to several infectious diseases, but the effects of hypoxia- and inflammation-driven HIF-1α signaling during SP infection are unclear. There are major limitations in SP research because current 2D cell culture and small animal models do not account for complex organ microenvironments or species-specific immune pathways, respectively. To address this, we created a vascularized 3D lung-on-a-chip (LoC) model to better characterize HIF-1α signaling during infection.

Methods

LoC devices were created by casting PDMS into 3D printed molds. To create an air-liquid interface (ALI), H441 human lung epithelial cells were seeded into the central airway space after endothelial cells (HUVEC) and fibroblasts (nhLF) were seeded in a 3D matrix surrounding the airway (**Fig. 1**). LoC devices were treated with SP for 4 hours +/- HIF-1α inhibition by BAY 87-2243. Whole human blood with fluorescently labeled immune cells ($CD15^+$ neutrophils and $CCR2^+$ pro-inflammatory monocytes) or fluorescent tracers (dextrans) were perfused in LoC to study the impact of HIF-1α signaling on inflammatory cell recruitment and vascular-epithelial barrier function, respectively. LoC devices were imaged using a Leica SP8 confocal scanning microscopy.

Results

Luminex cytokine arrays and single cell RNA sequencing of LoC treated with SP for 4 hours demonstrated early HIF-1α target gene activation. SP infection increased $CD15^+$ neutrophil recruitment to tissue and airway compartments compared to the control, and this recruitment was reduced following HIF-1α inhibition by BAY 87-2243. No significant changes in $CCR2^+$ pro-inflammatory monocyte recruitment were observed. Initial results from LoC perfused with fluorescent tracers demonstrated reduced vascular-epithelial barrier function during SP infection.

Conclusions

These preliminary findings suggest that HIF-1α-dependent inflammation is involved in early cellular responses to SP infection by partially mediating immune cell recruitment from microvessels to tissue and airway compartments. Results highlight the 3D LoC model as an effective pre-clinical human model that can identify key inflammatory and cell-cell interactions in pneumococcal pneumonia. Future experiments will aim to identify how HIF-1α mediates immune cell recruitment and characterize downstream transcriptional targets during SP infection.

Figures

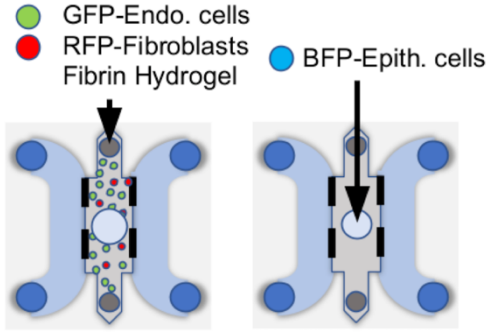


Figure 1. LoC device. Endothelial cells and fibroblasts are seeded in a fibrin hydrogel. Once blood vessels have formed, alveolar epithelial cells are seeded in the airway space, forming the ALI. All cells are fluorescently labeled for imaging.

Challenges of Respiratory Signals Measurement in fMRI Studies

Abdoljalil Addeh, Fernando Vega, M. Ethan MacDonald
Departments of Biomedical Engineering, Electrical & Software Engineering, and Radiology, Hotchkiss Brain Institute, University of Calgary, Canada

Introduction

In many functional magnetic resonance imaging (fMRI) studies the physiological signals (respiratory and cardiac) are often unavailable or don't have acceptable quality, due to issues with subject compliance. Therefore, it is not possible to remove the effect of physiological variation from fMRI data. In the case of respiratory signals, technical problems such as improper attachment of the belt to the transducer, and improper fitting the belt around subject's abdomen can corrupt the data. In this study the quality of recorded respiratory signals in Human Connectome Project in Development (HCP-D), HCP in Aging (HCP-A), and HCP young adult (HCP-YA) [1] is investigated.

Method

We evaluated respiratory signal of 614 subject in HCP-D (HCD0001305 to HCD2996590), 624 subjects in HCP-YA (115017 to 350330), and 550 subjects in HCP-A (HCA6002236 to HCA9007968). Figure 1 shows three respiratory belt traces from HCP-D dataset as an example. The first plot in this figure shows a partially corrupted belt trace, the second plot illustrates a belt trace with high spurious spike artifacts which cannot be removed by signal processing algorithms, and the third plot shows a belt trace with removable spike artifacts. We classified the belt traces into three main groups: group 1) failed recording, group 2) unremovable spikes, group 3) without or removable spikes.

Results

Table 1 compares the amount of scans in each group. Figure 2 shows the number of corrections in the third group to remove the spikes shown by color dots.

Table 1. Amount of data in each group

HCP	Age range	No. subjects/scans	Group 1 (%)	Group 2 (%)	Group 3 (%)
D	[5, 21]	614/2451	3.3	**84.3**	12.4
YA	[22, 35]	624/2359	2	46.3	**51.7**
A	[36, 100]	550/2187	**4.3**	77.4	18.3

Conclusions

Model-based techniques for removing respiratory effect from fMRI data often perform very well – however, they require the collection of external signals, which can be technically difficult, particularly in pediatric and aged populations, and prone to noise in an MR environment. Considering the difficulties and cost of respiratory signal recording during fMRI scans, and shortcoming of data-driven approaches, it could be highly beneficial to have a tool to extract respiratory signal variation waveform directly from fMRI data without the need for peripheral recording devices.

References

1. Harms, M.P., et al., *Extending the Human Connectome Project across ages.* NeuroImage, 2018. **183**: p. 972-984.

Figures

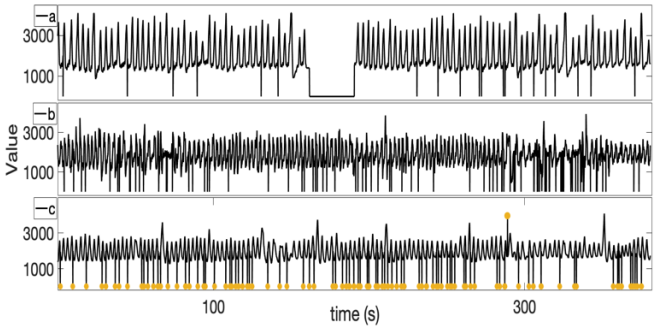


Figure 1. *Examples of respiratory signals in HCP-D, a) signal not-recorded partially, b) signal with large number of spikes, c) signal with removable spikes shown by color dots*

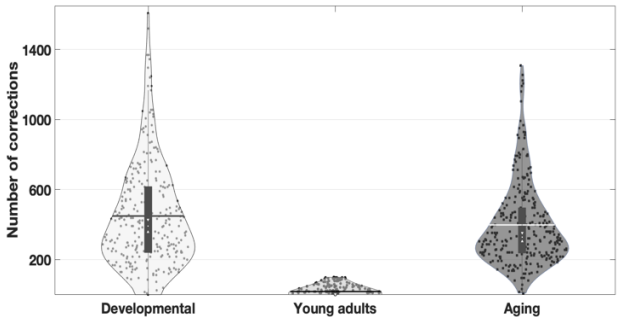


Figure 2. *Number of spike artifact corrections in the third group to have a usable respiratory signal*

Examination of Bone Turnover Biomarkers in Ovariectomized Cynomolgus Monkeys Associated with Antiresorptive Treatment

Alana Stahl[1, 2], Alexandra Olsen[1, 3], Andrew Sawatsky[1, 2], W. Brent Edwards[1, 2, 3], Roman Krawetz[1, 3, 4]

[1]McCaig Institute for Bone and Joint Health, [2]Faculty of Kinesiology, [3]Department of Biomedical Engineering, [4]Department of Cell Biology and Anatomy, Cumming School of Medicine, University of Calgary.

Introduction

Osteoporosis is a metabolic bone disease characterized by escalated bone turnover. Antiresorptive treatments available include denosumab (DMAb) and alendronate (ALN), which inhibit the function/survival of osteoclasts and the action of osteoclasts, respectively (Cummings, 2009). The purpose of this study was to obtain a stronger understanding of the effects ALN and DMAb have on osteoblasts, osteoclasts, mesenchymal stem cells (MSCs), and hematopoietic stem cells (HSCs) via histochemical bone turnover markers: osteonectin, osteopontin, TRAP, PRRX1, and CD34.

Methods

Adult cynomolgus monkeys (n=30) were ovariectomized and divided into groups: Vehicle (VEH;12 months), VEH (6 months) then DMAb (6 months) (VEH-DMAb), ALN (12 months), ALN (6 months) then DMAb (6 months) (ALN-DMAb), and DMAb (12 months). The humeri were fixed in NBF, decalcified in EDTA, then paraffin embedded. Sections were stained with bone turnover markers and identified with fluorescent imaging. Images were quantified using TissueQuest, detecting cells that were stained by the selected marker. The number of cells/mm^2 was displayed for analysis and comparison.

Results

Staining of histological markers was detected within animals from all groups in cortical bone (Fig. 1). Cell count varied amongst marker and group.

Discussion

DMAb slowed bone turnover most effectively in all groups, decreasing osteoblast, osteoclast, MSC, and HSC count drastically in cortical bone. PRRX1 and osteopontin demonstrated a higher cell count in the ALN group than the VEH-DMAb group. In other words, DMAb treatment for 6 months had a larger impact on osteoblasts and MSCs than ALN did for 12 months, suggesting DMAb strongly suppresses osteoblasts and their progenitors, due to the coupled action of bone resorption and formation. Otherwise, mainly similar trends were identified in the bone marrow cavity. Because these bone turnover markers have not previously been studied within the humeri of cynomolgus monkeys, these findings have important implications for the efficacy of osteoporotic therapies on bone turnover, expanding knowledge of how these treatments specifically target cells involved in bone turnover: osteoblasts, osteoclasts, MSCs, and HSCs.

References

1. Cummings SR, et al. Denosumab for prevention of fractures in postmenopausal women with osteoporosis. N Engl J Med. 2009; 361:756– 76

Figures

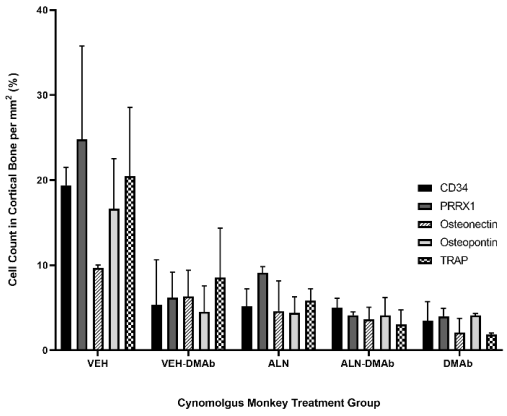


Fig. 1. Mean and SD of cortical bone cell count per mm^2 (%) of various histological markers within each treatment group. Cell count via osteonectin, TRAP, and CD34 staining is highest in VEH (12 months), followed by VEH-DMAb, ALN, ALN-DMAb, and lastly DMAb. Other than a slightly higher cell count in the ALN group than the VEH-DMAb group, sections stained with PRRX1 or osteopontin followed a similar trend compared to the other histological markers.

Opportunistic 3D Modelling of Clinical CT for the Development of a Subject Specific Assessment of Fracture Risk

Alexander W. Iwasyk[1,2], Gouri Deshpande[1,3], Frank Saville[4], Peter Salat[1,2], Steven K. Boyd[1,2]
[1] McCaig Institute for Bone and Joint Health, University of Calgary, 3280 Hospital Drive NW, Calgary, Alberta, T2N 4Z6, Canada.
[2] Department of Radiology, Cumming School of Medicine, University of Calgary, Calgary, Alberta, Canada.
[3] Department of Electrical and Computer Engineering, Schulich School of Engineering, University of Calgary, Calgary, Alberta, Canada
[4] Amelue Technologies Inc

Introduction

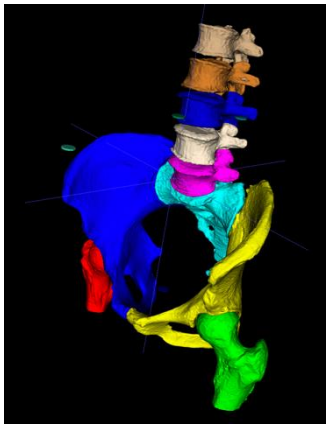
Osteoporosis is a debilitating disease which often goes undiagnosed until fracture or serious injury occurs.. Screening for osteoporosis plays a critical function in guiding nutrition management, physical activity, and physician assessments and drug treatment. Across Canada, millions of clinical computed tomography (CT) scans are carried out annually, where at-risk skeletal regions for osteoporotic fractures, specifically the spine and hip, are imaged. While the use of CT for the sole purpose of osteoporosis diagnosis is impractical due to cost and radiation risks, pre-existing data sets acquired for other medical reasons can be utilized opportunistically. Our goal is to develop and demonstrate the feasibility of a tool that provides a cost and time effective patient-specific assessment of fracture risk.

Methods

Image datasets were acquired from Alberta Health Services and included at-risk regions for osteoporotic fracture including the proximal femur to the lumbar spine. Using a viewing and segmentation application called ITK-Snap, an initial seeding of 10 bones of interest was manually performed with unique identifiers in the three anatomical planes. A graph-cuts algorithm was applied to the seeded frame, producing a fully segmented 3D model. The model is corrected for over/under-segmentation errors encountered after automated landmarking by the algorithm, where the model is reviewed and approved by the radiologist (PS). Using this process, a control cohort of approximately 100 modeled CT scans is being developed for the training of convolutional neural networks (CNN). Ongoing testing includes a UNet (nnU-Net) and a 35-layer ResNet model.

Results

54 out of 100 CT scans have been successfully segmented into 3D models for the ground-truth cohort (Figure). The time necessary to complete the manual segmentation, application of the graph cuts algorithm, and final corrections for a single clinical CT scan is approximately 72 to 94 hours. Completed models were used to train the CNNs. ResNet resulted in Dice scores >0.97 and requiring <90 seconds for inference.



Discussion

The construction of a ground-truth CT cohort is a significant undertaking and provides a valuable basis to train CNNs. Both the 35 layer ResNet and the nnU-Net showed promise in automatically segmenting 10 bones from clinical CT scans. These CT data will be the basis for measuring volumetric bone mineral density and applying simulated loading using finite element modeling. We have acquired a dataset of 4000 clinical CT scans to demonstrate our fully automated pipeline for opportunistic screening. Ultimately, our approach may lead to a reduction in fracture risk for Canadians.

Quantifying and visualizing regional bone changes in the knee following an ACL tear

Alida C Morrison, Steven K Boyd
McCaig Institute for Bone and Joint Health, Cumming School of Medicine, University of Calgary

Introduction

Bone mineral density decreases in the knee joint in the acute phase after anterior cruciate ligament (ACL) injuries[1]. Previous research on bone density variation after ACL injuries used imaging modalities of dual-energy X-ray absorptiometry (DXA) and high resolution peripheral quantitative computed tomography (HR-pQCT) to investigate differences in subregions of the distal femur and proximal tibia[1,2]. Analysis of localized effects based on pre-selected regions of a scan is limited in spatial scope and may leave out other areas of a bone scan that reveal important change[3]. The purpose of this study is to develop a method to quantify and visualize regional bone changes over the whole scanned joint following an ACL tear.

Methods

Data from 10 participants (2 male, 8 female) from the ongoing retrospective observational SALTACII study will be used for analysis. Participants are included if they had one annual follow-up visit completed by August of 2022 and had not undergone reconstructive surgery. They were between 32 and 55 years of age upon study enrolment, with 7 participants having complete ACL tears and 3 participants having partial tears as confirmed by magnetic resonance imaging. In addition to the ACL tear, there is a mix of soft tissue and ligament injuries in the cohort as diagnosed by a radiologist. Participants had no history of traumatic knee injury on either side prior to the ACL tear. Image data will consist of HR-pQCT and dual energy computed tomography (DECT) scans of the participants' knees. Radiology reports of baseline magnetic resonance images will provide further details on each injury.

Image processing will include a mix of image processing language and Python with SimpleITK. Baseline and follow-up scans will be registered for both HR-pQCT and QCT images. The baseline greyscale image will be subtracted from the follow-up image to identify overall changes in bone density over one year. The process will be repeated at a range of image resolutions to determine the optimal resolution for identifying image differences. The differences will be visualized separately for the tibia and femur. Finally, the visual map of differences will be inspected to determine regions of significant change throughout the femur and tibia scans, and the changes will be quantified based on greyscale voxel values.

Results

Results from the longitudinal analysis of DECT and HR-pQCT images will be compared to determine whether high resolution images reveal more information on bone density changes than clinical images. Furthermore, the results will help investigate the regional effect of a recent ACL tear on bone density in the distal femur and proximal tibia. Factors such as the mechanism of injury, type of injury, age and sex will be evaluated for their relationship to the magnitude and location of bone density variation.

Conclusions

A method to quantify and visualize longitudinal bone changes in the knee following an ACL tear can be applied to study data in our lab to further understand the impact of ACL tears on bone density.

References

1. Kroker, A. et al. J Orthop Res. 2019;37(11):2325-2336.
2. Bayar, A. et al. The Knee. 2008;15(5):373-377.
3. Kurth, F. et al. Brain Mapping. 2015:345-349

Bone fatigue properties across different dimensional scales following bisphosphonate treatment in ovariohysterectomized rabbits

Ana Gloria Angulo[1 2 3], Ifaz Haider[2 3], Andrew Sawatsky[2 3], Douglas Morck[4], David Hart[3], Prism Schneider[3], W. Brent Edwards[1 2 3]

[1]Department of Biomedical Engineering, [2]Human Performance Laboratory,[3]McCaig Institute for Bone and Joint Health, and [4]Faculty of Veterinary Sciences, University of Calgary

Introduction

Antiresorptive medication, including bisphosphonates, is the current front-line therapy to treat osteoporosis. Nonetheless, there is growing concern over the association of long-term bisphosphonate therapy with rare adverse events such as atypical femoral fracture (AFF), a type of insufficiency fracture of the femoral shaft [1]. The most prevalent hypothesis for AFF is that supressed bone remodeling from antiresorptive agents impairs fatigue resistance and toughness through alterations to collagen and mineral quality and/or microdamage accumulation [2]. However, bisphosphonate therapy is also associated with improved density and structure at the whole-bone level [3]. Therefore, the purpose of this study was to quantify the influence of bisphosphonate therapy on the fatigue properties of whole-bone and bone tissue in an ovariohysterectomized rabbit model.

Methods

Eleven ovariohysterectomized adult female New Zealand White rabbits were treated with 0.15 mg/kg alendronate (ALN; n=6) or 1 mL/kg vehicle saline (VEH; n=5) via subcutaneous injection, 3 days per week for 6 months. After treatment, lower limbs were harvested and imaged to assess bone mineral density (BMD) using quantitative computed tomography (QCT; 120 kVp, 150 mA, 0.26 x 0.26 x 0.625 voxel size). The left femur and tibia were cyclically loaded in uniaxial compression (peak load 1260 N) at 2 Hz to determine fatigue life at the whole-bone level. Beam samples (1.3 x 0.9 x 16 mm) were prepared from the cortical shaft of the right femur and cyclically loaded (peak load 110 MPa) in phosphate-buffered saline at 37 °C using a 4-point-bending configuration to determine fatigue life at the material level. Fatigue life for all specimens was quantified as the number of loading cycles until failure, which was indicated by a complete fracture or a runout of 500,000 cycles. Apparent, dry and ash density were assessed from beam samples using an established protocol. Differences between treatment groups were analyzed using an independent sample t test or its nonparametric equivalent, a Mann Whitney U test.

Results

QCT measurements indicated that ALN treatment was associated with greater BMD at both the whole femur ($p=0.044$) and tibia ($p=0.041$). No difference in apparent ($p=0.879$), dry ($p=0.891$) or ash ($p=0.480$) density was observed at the material level. Likewise, differences in fatigue life for whole-bone ($p=0.14$) and bone tissue ($p=0.817$) were not statistically significant between treatment groups.

Conclusions

Despite 6-months of ALN treatment being associated with greater BMD at the whole-bone level, this did not translate to longer fatigue-life measurements. We assume this was because ALN preferentially targeted high-turnover regions of trabecular bone that did not play an important mechanical role in this loading mode. Importantly, we did not observe any detrimental effects to fatigue life across these different dimensional scales. Therefore, the findings from this study were unable to support the wide-held hypothesis that impaired fatigue resistance associated with antiresorptive medication is responsible for AFF.

References

[1] Shane et al. 2014. JBMR, 29(1), 1-23.
[2] Ettinger et al. 2013. Bone, 55(2), 495–500.
[3] Boivin et al. 2000. Bone, 27(5), 687-694.

Development of a Discrete Element Model to Evaluate Contact Stress in the Equine Metacarpophalangeal Joint

Andrew Koshyk[1], Holly D Sparks[1], W Michael Scott[1], Donald D Anderson[2], W Brent Edwards[1]
1. University of Calgary, Calgary, Alberta, Canada. 2. University of Iowa, Iowa City, IA, USA

Introduction

Fatigue fracture of the metacarpophalangeal (MCP) joint is one of the most common injuries in racehorses. While several factors contribute to the development of these injuries, the magnitude of the stress that the tissue experiences plays a critical role. The purpose of this study was to establish a computational workflow for the estimation of contact stress distributions at the MCP joint using discrete element analysis (DEA).

Methods

Distal forelimbs were harvested from four mature male and female horses euthanized for reasons unrelated to this research, then imaged using computed tomography. Scans were obtained using a GE Revolution GSI (GE Healthcare, Waukesha, WI) with image acquisition settings of 120 kVp and 180 mA (voxel size 0.488 x 0.488 x 0.625 mm). Bone geometries were segmented in Mimics (Materialise, Leuven, Belgium) and exported as stereolithography files for DEA in Matlab (Mathworks, MA, USA).

DEA was used to estimate contact stress between the third metacarpal (MC3) and proximal phalanx (P1) and between the MC3 and sesamoids at 11 instances throughout the stance phase of gait. An animal-specific, non-uniform cartilage geometry was assumed and applied loads accounted for contributions from tendons, ligaments, and ground reaction forces for a 500 kg horse trotting at a speed of 1.4 m/s. From ground contact to midstance, the applied loads ranged from 4000 N to 19000 N and the joint underwent 24° of extension[1,2]. A series of sensitivity analyses were conducted to investigate the influence of cartilage thickness, cartilage stiffness, and loading magnitude on the resulting contact stress distribution.

Results

Peak stress between the MC3 and P1 ranged from 40 MPa at ground contact to 96 MPa at midstance, while peak stress between the MC3 and sesamoids ranged from 52 MPa at ground contact to 161 MPa at midstance. Peak stress varied by 50 MPa (SD = 22 MPa) between horses, but these peaks were always located on the palmar aspect of the MC3 near the parasagittal groove. A 10% increase in cartilage stiffness or loading magnitude resulted in a 5% increase in peak stress, while a 10% increase in cartilage thickness resulted in a 5% decrease in peak stress.

Conclusions

The location of peak stress from DEA was consistent with typical fracture locations in racehorses[3], and peak stress magnitude compared reasonably well with previously reported finite element models[4]. Although cartilage stiffness and thickness assumptions influenced DEA predicted outcomes, changes to peak stress magnitudes were only moderately sensitive to these assumptions. DEA is an efficient method to estimate contact stress distributions in the equine MCP joint and may provide unique insight into the development of fatigue fracture.

References

1. Harrison et al. (2010). J. Exp. Biology., 213, 3998-4009.
2. Clayton et al. (2007). Vet. Comp. Orthop. Traumatol., 20, 86-91.
3. Riggs. (1999). Equine vet. J., 31 (2) 116-120.
4. Harrison et al. (2014). J. Biomech., 47(1), 65-73

Figures

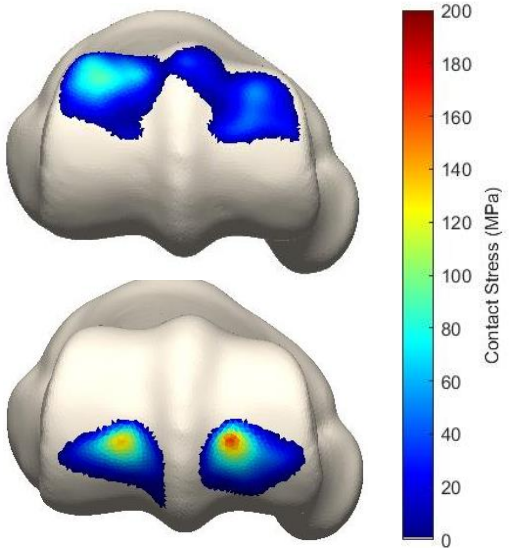


Figure 1: MC3 contact stress distribution at midstance when in contact with the P1 (top) and sesamoids (bottom).

Introducing Unsupervised ML Technique to Children's Brain MR Imaging

Anik Das[1], Mariana Pinheiro Bento[1,2,3]

[1] Department of Biomedical Engineering, University of Calgary\ [2]Alberta Children's Hospital Research Institute; [3]Hotchkiss Brain Institute

Introduction

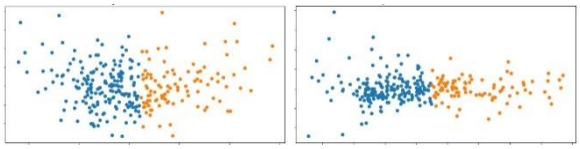
Magnetic Resonance Imaging (MRI) is an essential clinical assessment to support diagnosis and treatment [1]. Machine learning has an extensive application in the medical sector, especially in brain MR image processing, analyzing and treatment evaluation. However, most of the developments have been done for adult individuals over the age of 18. So, there is a challenge to introduce ML to child brains. Our goal is to develop an unsupervised machine learning model to study children's brain, a choice to bypass the deficiency of annotated child brain scans and overcome other challenges like data variability as children's brains are constantly changing/developing, and data quality due to patient motion during data acquisition.

Methods

This research and experiments are preliminary and ongoing. We aim to study structural T1-weighted MR images of 126 children, aging varying between age of 1.95 and 8.04, using a publicly available dataset [https://osf.io/y9jcv]. We also had access to subjects demographics. We performed data pre-processing, handle missing data, used freesurfer for brain volumetry [1] and tissue classification (generate white matter, gray matter, and CSF) using software named Statistical Parametric Mapping (SPM) and FSL with STAPLE to combine them. Then, we implemented both K-Means and Agglomerative Hierarchical clustering methods by considering brain matters masks and freesurfer measurements. PCA [2] can be used with allow visualization of a multi-dimensional dataset.

Results

Our preliminary result after completing preprocessing and implemented the clustering techniques shown in Figure 1. Models were able to secure low variance in multiple datasets by predicting almost similar output. Next step will be to correlate brain parameters with other demographics, and speech characteristics of children based on their age group.



(a) (b)

Figure 1: Result of clustering for brain tissue masks (a) and freesurfer volumetry dataset (b) is shown above. X and Y axes indicate PCA primary and PCA secondary axes respectively.

Conclusions

We developed an unsupervised technique to study children's brain using MR imaging. While these experiments and results are preliminary, our goal for future work is to introduce domain adaptation technique to overcome the drawback of data variability, allowing the translation and usage of models developed using adults data for children's data.

References

[1] OSF. (2019, April 2). Calgary Preschool MRI dataset. OSF. Retrieved February 14, 2022.

[2] Bruno, M. A. (2019). Artificial Intelligence and machine learning in Radiology. Error and Uncertainty in Diagnostic Radiology, 199–226.

What factors drive bone phenotyping – does resolution play a significant role?

A.R. Bugbird[1], D.E. Whittier[2], S.K. Boyd[1]
[1]McCaig Institute for Bone and Joint Health, University of Calgary, [2] Institute of Biomechanics, ETH Zurich

Introduction

Osteoporosis is an age-related degenerative disease, characterized by increased bone fragility and susceptibility to fracture [1]. Osteoporosis commonly remains undiagnosed until a fragility fracture takes place [2], therefore, improved fracture prediction is paramount.

Bone strength can be expressed as a combination of density and structural parameters [3]. It is hypothesized that categorizing the population into groups of similar combinations of parameters, known as phenotypes, will aid in identifying individuals with heightened fracture risk and develop a greater understanding of the etiology of fragility fractures. The purpose of this study is to: (1) understand which morphological parameters influence bone phenotypes, and (2) understanding the effect of image resolution on identifying morphological features.

Methods

The cohort used for this study consisted of participants (n=1,236) recruited as part of a population-based study [4]. All participants underwent scanning using HR-pQCT (XtremeCTII, Scanco Medical, Switzerland; 61 µm). The manufacturer's standard patient evaluation protocol was followed to obtain density and morphological parameters. The data was normalized prior to model training.

Participants were grouped into three clusters using a fuzzy c-means (FCM) clustering algorithm. The number of clusters was determined by a previously trained model based on 82 µm data, and identified as 'Healthy', 'Low Volume', and 'Low Density' [5].

To understand how parameters influence the determined phenotypes, partial correlations between individual parameters and cluster membership coefficients was performed.

Results

In both resolution models, the *healthy* bone phenotype consistently had positive partial correlations with cortical microarchitectural parameters, cross-sectional areas, and failure load. The *low-density* phenotype was characterized by negative partial correlations with bone mineral density (BMD), cortical microarchitectural parameters and failure load. The *low volume* had negative partial correlations with cross-sectional areas, and failure load but positive BMD.

The main differences observed between the models (**Fig 1**) were for total BMD, trabecular number, trabecular homogeneity, cortical thickness, and cortical area. These differences are likely a result of improved measurement accuracy obtained at a higher resolution (61 µm).

Conclusions

The correlation between the variables and phenotypes is fairly consist between the models, indicating the bone phenotyping is largely independent of resolution. To improve on this model, parameters such as trabecular thickness and trabecular separation, that can only be captured accurately at the higher resolution (61 µm), could be included to understand whether further morphological features become evident with increasing resolution.

References

[1] Gallagher et al., Am J Med, **90**(90):646-50,1994.
[2] Fonseca et al., Sports medicine,**44**(1):37-53,2014.
[3] Hansen et al.,Calcif Tissue Int,**89**(4):335-346,2011.
[4] Whittier et al., JBMR, **35**(11): 2151-2158, 2020.
[5] Whittier et al., JBMR, **37**(3): 428-439, 2020.

Figures

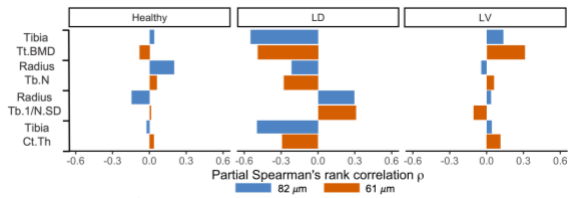


Figure 1: Plot of the Spearman's partial correlation between individual parameters and cluster membership for 82 µm [5] and 61 µm resolution.

Using Robotics to Automate the Fabrication of Cannulae

Anthony Thomas Demong[1], Josh Feddema[1], Colin Dalton[1,2]
[1]Department of Biomedical Engineering, Schulich School of Engineering, University of Calgary
[2]Department of Electrical and Software Engineering, Schulich School of Engineering, University of Calgary

Introduction

The development and fabrication of invasive medical devices often requires a high level of accuracy and precision that cannot be performed manually. This is especially true for cannulae: biocompatible, flexible tubes designed to deliver blood directly into – or out of – a critically-ill patient. Irregularities in the surface or geometry of these cannulae could disturb or inhibit blood flow, with potential life-threatening consequences for the patient.

Cannula fabrication involves a process called dip-coating, where a metallic shaft, or mandrel, is repeatedly dipped into a liquid polymer bath and cured using an oven. Subsequent dips add new layers of polymer, increasing cannula thickness. When an ideal thickness is achieved, the polymer coating is then cooled and removed from the mandrel to create a hollow, cylindrical cannula.

Previous research noted that manual dip-coating results in highly variable section measurements. To reduce this variability, a robot has been designed to provide superior control during the dip-coating procedure.

Methods

The robot, seen in Figure 1, was designed using CAD software. It will be controlled over Wi-Fi using a Raspberry Pi microcontroller, allowing for more consistent – but adjustable – mandrel dips into the liquid polymer bath.

Results

Once assembled, the geometric accuracy and precision of the machine-dipped cannulae will be compared to the hand-dipped precursors, as well as existing commercial cannulae.

Discussion

As medical technology advances and becomes more complex, so does the technology required to design and produce it. This robot will provide insight into the design of a more capable, mass-production cannulae dip-coating system.

Figures

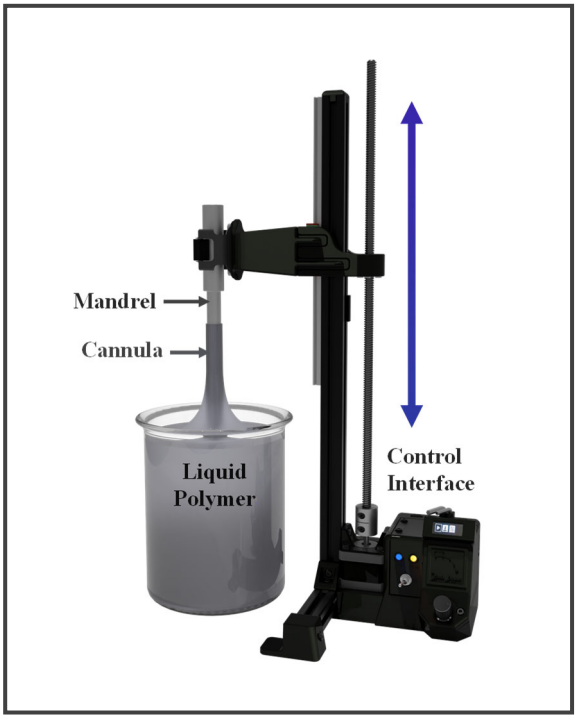


Figure 1: A render of the dip-coating robot withdrawing a mandrel from a polymer bath.

Measuring sarcomere dynamics following fluorescent labelling of α-actinin and myomesin structural proteins

Armaan Sekhon, Dhairya Desai, Timothy Leonard, and Walter Herzog
Human Performance Laboratory, Faculty of Kinesiology, University of Calgary

Introduction

Myofibrils are subcellular organelles made of sarcomeres and are responsible for contraction in muscles. Characterizing the interaction between constitutive proteins actin, myosin, and titin may rationalize contractile mechanisms. Towards such, labelling of titin with fluorescent antibodies may reveal segmental elongation of specific domains while subverting shortcomings including inconsistent intensity and asymmetricity of striations (A-band, I-band) inherent to bright field or phase contrast microscopy methods[1]. Considering antibody labelling has been associated with impairments of sarcomere dynamics and force production[2,3,4], we investigated the effect of labelling structural epitopes on α-actinin (Z-disc) and myomesin (M-line) to determine how parameters including solution concentrations or contractile conditions might induce impairments to passive force and sarcomere lengths (SLs).

Methods

Myofibrils were harvested and purified from psoas muscle of New Zealand White rabbits. Labelled samples were incubated in rigor with anti-α-actinin (A7811, Sigma-Aldrich) and anti-myomesin (mMaC myomesin B4, DSHB) primary antibodies, and IgG (H+L) AlexaFluor488 (A32723, Fisher Scientific) secondary antibodies. Samples were flushed with relaxing solution, restrained in needle-nanolever systems and observed on an Olympus IX83 (Olympus) microscope under 100x magnification. Optical resolution was 65 nm/pixel. Myofibrils (labelled, n>6, 150 sarcomeres; controls n=7, 141 sarcomeres) were stretched passively from sarcomere length (SL) ranges of 2.5-2.6 μm (relaxed position; RP) to 3.1-3.25 μm (stretched position; SP). Datasets were analyzed natively on CellSens software (Olympus).

Results

Investigating passive stress in myofibrils at stretched positions, mean values of 66 ± 22 and 60 ± 23 nN/μm^2 were obtained in control and labelled myofibrils (Figure 1). No statistical significance was identified, indicating antibodies did not constrain dynamics in limited passive stretch conditions. Standard deviation of individual SLs decreased from 0.15 to 0.09 μm (39% decline) and 0.17 to 0.13 μm (24% decline) in RP1 and SP1. Decrease in non-uniformity was pronounced at shorter SLs, indicating antibodies may have stiffened lattice structures to induce subtle contraction. SL measurement precision was improved in fluorescent trials compared to phase-contrast controls by an average of 21% per sarcomere.

Conclusions

Antibodies had minimal influence at longer lengths but became increasingly constraining at shorter lengths in sarcomeres. Such results inform methods while labelling titin domains during more invasive experiments to identify how titin participates in sarcomere dynamics.

References

[1]Schmidt et al., 2021. *J. Biomechanics.* 126: 110628.
[2]Telley et al., 2006. *Biophysical J.* 90(2): 514-530.
[3]Shimamoto et al., 2008. *PNAS.* 106(29): 11954-11959.
[4]DuVall et al., 2017. *J. Exp. Bio.* 220(23), 4418-4425.

Figure

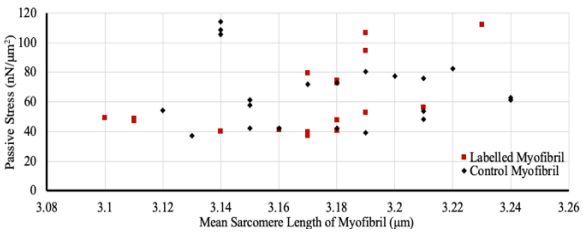


Figure 1: Passive stress of control and labelled myofibrils in stretched positions.

Abstract: Alberta BME Symposium

The effect of a 3-week delayed prebiotic fiber intervention on fat infiltration in vastus lateralis muscles of female Sprague-Dawley rats

Authors: Arman Murani (University of Calgary, Department of Biological Sciences), Hannah Smith (University of Calgary; Department of Biomedical Engineering), Ruth-Anne Seerattan (University of Calgary, Faculty of Kinesiology), Walter Herzog (University of Calgary, Faculty of Kinesiology)

Rationale: Obesity and metabolic syndrome are risk factors in the development of sarcopenia or muscle wasting. As muscle mass is a key indicator of long-term health, it is important to understand the relationship between obesity and muscle integrity. It has been shown that a high fat/high sucrose (HFS) diet induces obesity and low level systemic and local joint, bone, and muscle inflammation in male Sprague-Dawley rats. These metabolic changes caused by obesity also lead to an increase in fat infiltration in muscle which compromises its structural and functional properties.

In contrast, fibre-based diets have been shown to counteract obesity and obesity related musculoskeletal degeneration. Studies have shown that a diet rich in fibre induces a change in the gut microbiota that decreases systemic and local inflammation. This pre-clinical model of obesity-induced musculoskeletal degeneration has only been investigated using male Sprague-Dawley rats. Female Sprague-Dawley rats have less metabolic disturbances when exposed to an HFS diet, and thus, may be better protected from musculoskeletal degeneration than their male counterparts.

Objectives: The objectives of this study are i) to determine the effect of the HFS diet on muscle integrity in female Sprague-Dawley rats; and ii) to investigate if muscle degeneration can be prevented using a diet rich in fibre on top of the HFS diet. We hypothesize that the fiber intervention prevents fat infiltration in the vastus lateralis (VL) muscle in female Sprague-Dawley rats.

Methodology: 36 female Sprague-Dawley rats at 12-weeks of age were randomized into three experimental groups: (i) a control group fed a standard rat diet, (ii) an experimental group fed a HFS diet, and (iii) an experimental group fed a HFS diet with a prebiotic fibre supplement at fifteen weeks old. VL muscles were harvested following a 12-week HFS diet intervention period. The primary outcome measure was intramuscular fat infiltration in the VL. Mid-belly slices of 10 μm thickness were harvested using a cryostat. Serial sections were adhered to slides. Alternate slides were stained with Oil Red O for fat content. Stained sections were imaged and quantified using Image J. The percentage fat will be determined from the stained sections. Statistical analysis will be done using the Kruskal-Wallis H test.

Results: Fat infiltration into the VL differed across all groups where the HFS group had the highest amount of fat infiltration (1.64 ± 0.47) and the chow fed group having the least (0.59 ± 0.27). There was no statistically significant difference between the fibre intervention group (1.13 ± 1.12) and the other 2 groups. There was, however, a significant difference between the chow fed group and the HFS group ($p<0.05$).

Conclusion: The results show that a fibre diet supplement has a protective effect on the fat infiltration in the VL thus proving the hypothesis, however, it is not statistically significant and hence the effect of prebiotic fibre on the prevention of intramuscular fat infiltration remains to be seen.

The role of the subtalar and ankle joints to maintain stability while walking on uneven surfaces

Banin M. Al-Shimari[1,2], Jayishni Maharaj[3], Michael J. Asmussen[2]
[1]University of Calgary, [2]Mount Royal University, [3]Griffith University

Introduction

Walking can pose a challenge to stability in the medial and lateral direction (i.e., to the inside or outside of your foot), which is exacerbated on uneven surfaces. Humans adopt several strategies to correct this instability. During the stance phase of walking, the subtalar and ankle joint displacements are counteracted by forces produced by muscles and passive tissues, causing energy absorption which is returned later in the stance phase to contribute to toe-off[1,2]. Examples of such muscles that control the functions of these joints include the tibialis anterior and tibialis posterior[1,2]. Their specific role in maintaining mediolateral stability during walking is currently unresolved[1,2]. Therefore, the purpose of this study is to determine the compensatory strategies utilized by the subtalar and ankle joints under mediolateral perturbations while walking.

Methods

11 participants walked at 1.8 m/s on an instrumented treadmill. 3D motion capture was used to measure the segment motion of the pelvis, thigh, shank, calcaneus, midfoot, forefoot, and toes. Mediolateral perturbations were induced using lateral and medial ridges on 3D printed custom-made footwear, promoting, and limiting pronation, respectively. In addition, changes in muscle fascicle length of the tibialis posterior, tibialis anterior and peroneus brevis were examined through muscle ultrasonography.

Results

At the subtalar joint, a greater supination internal moment was produced in the lateral ridge condition to counteract the pronation perturbation induced by footwear ($p<0.05$). More positive power was produced at the subtalar joint in the lateral ridge condition ($p<0.05$), corresponding to a reduction in positive power at the ankle joint ($p<0.05$), suggesting a redistribution of power production across the two joints. Additionally, from a kinematics standpoint, greater dorsiflexion in the medial ridge condition ($p<0.05$) indicates that the subtalar and ankle joints work together in response to the perturbations induced during walking Future muscle-level analysis will uncover how muscles are able to control the functional role of these joints.

Conclusions

To conclude, the subtalar and ankle joints effectively compensate for perturbations in the mediolateral direction during walking. These effects were most prominent in the lateral ridge condition as a greater supination moment and positive work were produced to counteract excessive pronation that could create an instability while walking. The function of the ankle and subtalar joints suggests that these work in unison whereby less motion at one joint is compensated by an increase in motion at the other joint, resulting in a redistribution of joint work while walking on an uneven surface.

References

1. Maharaj, J. N., Cresswell, A. G., & Lichtwark, G. A. (2016). The mechanical function of the tibialis posterior muscle and its tendon during locomotion. *Journal of Biomechanics*, *49*(14), 3238–3243. https://doi.org/10.1016/j.jbiomech.2016.08.006
2. Maharaj, J. N., Cresswell, A. G., & Lichtwark, G. A. (2019). Tibialis anterior tendinous tissue plays a key role in energy absorption during human walking. *Journal of Experimental Biology*. https://doi.org/10.1242/jeb.191247

The expansion of human skin-derived Schwann cells in stirred suspension bioreactors to improve cellular production for clinically relevant quantities of cells.

*Edward Melnyk[1,2], **Brett Abraham[1,3]**, Tak Ho Chu[4,5], Rajiv Midha[4,5], Jeff Biernaskie[6], Michael Kallos[1,2]*
[1]Pharmaceutical Production Research Facility, University of Calgary, Calgary, AB, Canada
[2]McCaig Institute for Bone and Joint Health, University of Calgary, Calgary, AB, Canada
[3]Department of Biomedical Engineering, University of Calgary, Calgary, AB, Canada
[4]Hotchkiss Brain Institute, University of Calgary, Calgary, AB, Canada
[5]Department of Clinical Neurosciences, University of Calgary, Calgary, AB, Canada
[6]Faculty of Veterinary Medicine, University of Calgary, Calgary, AB, Canada

Introduction

Over 300,000 people suffer from peripheral nerve injury (PNI) in North America every year. Nerve grafts are the standard surgical treatment for PNIs with gap but often result in low recovery and donor site morbidities. Currently, Schwann cells (SCs) offer a promising cell therapy alternative for the repair of PNIs. However, the isolation of traditional nerve-derived SCs is invasive and large quantities of SCs are required for clinical application. Recently, a novel method has been developed to extract and purify human skin-derived SCs (hSk-SCs) as an alternative to nerve-derived SCs[1]. However, the large-scale production of SCs remains a challenge, and standard static expansion methods are unable to efficiently generate clinical numbers of cells. Stirred-suspension bioreactors address this by providing a scalable platform for the robust generation of therapeutic cells. Therefore, in this work, the expansion of hSk-SCs was transitioned into suspension bioreactors to assess scalability and overall cell production compared to static monolayer culture.

Methods

When grown in suspension, small microcarrier beads (MCs) must be added to provide a surface for cellular attachment. Twelve commercially available microcarriers were screened for compatibility with hSk-SCs. Screening was performed in non-adherent well plates, with confocal fluorescent microscopy and cell viability assays used to determine cellular attachment and viability. The top three MCs were then tested in suspension bioreactors, and cell counts were performed to determine cellular fold-increase. Post-expansion immunohistochemistry (IHC) was used to determine maintenance of characteristic SC phenotype. Finally, a factorial design of experiments was carried out to improve cellular fold-increase by modulating three key bioprocess variables: cell seeding density, bioreactor microcarrier density, and the presence of conditioned medium.

Results

Of the 12 tested MCs, Cytodex1 and Cytodex3 were found to provide the greatest fold-increase over a 7-day culture, and ultimately Cytodex3 yielded the highest harvested cell number. IHC staining of post-bioreactor hSk-SCs, showed hSk-SCs retain expression of characteristic SC markers p75 and SOX10. The results of the factorial experiment showed the best treatment combination resulted in a 9-fold increase in hSk-SCs, a value 3 times greater than what is typically achieved in static culture. Further, the suspension process required 3.5 times fewer starting cells than static culture.

Conclusions

In this work hSk-SCs were successfully cultured in suspension bioreactors. By screening for various bioprocess parameters, a 3-fold improvement in cell expansion was achieved over static culture while also decreasing the amount of starting material by 3.5 times. Given these values, two 100mL bioreactors would theoretically yield over 100 million and could be seeded from the cells isolated from a 10cm^2 skin sample.

Figures

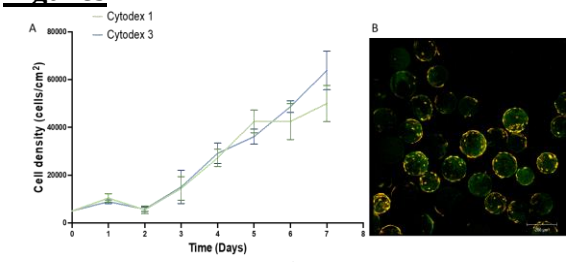


Figure 1: A) growth kinetics of hSk-SCs on Cytodex MCs. B) expression of P75 (green) and SOX10 (orange) of hSk-SCs on Cytodex3 MCs

Referencess

[1] Chu, T.-H., Baral, K., Labit, E., Rosin, N., Sinha, S., Umansky, D., Alzahrani, S., Rancourt, D., Biernaskie, J., & Midha, R. (2022). Comparison of human skin- and nerve-derived Schwann cells reveals many similarities and subtle genomic and functional differences. *Glia*, 1– 26. https://doi.org/10.1002/glia.24242

Using deep learning to augment osteoporosis screening

Bryn Matheson[1], Gouri Deshpande[1,3], Peter Salat[1,2], Steven K. Boyd[1,2]
[1] McCaig Institute for Bone and Joint Health, University of Calgary, Alberta, Canada.
[2] Department of Radiology, Cumming School of Medicine, University of Calgary, Calgary, Alberta, Canada.
[3] Department of Electrical and Computer Engineering, Schulich School of Engineering, University of Calgary, Calgary, Alberta, Canada

Introduction

Osteoporosis, characterized by low bone mass, microarchitectural deterioration of bone tissue and decreased bone strength, is underdiagnosed and undertreated.[1] The current assessments for osteoporotic fracture risk include using dual X-ray absorptiometry scanning (DXA) to calculate bone mineral density (BMD). This method has many constraints, mainly because DXA screening rates are low and usually only occur following a fracture.[2] However, millions of clinical computed tomography (CT) scans, which include relevant osteoporotic fracture sites, are performed each year, giving rise to the opportunity to use these scans to screen for osteoporosis. Our long-term goal is to create a software product utilizing previously acquired clinical CT scans for subject-specific fracture risk screening. Within this larger project, the first step was to train deep learning (DL) algorithm to perform the segmentation process. Therefore, the purpose of the current study was to develop a DL method to automatically segment bones of interest from previously acquired clinical CT images.

Methods

A total of 4,000 clinical CT exams including the relevant osteoporotic screening sites (the proximal femur and the lumbar spine), were obtained from Alberta Health Services. These scans follow the standard CT imaging protocol for the kidneys, urinary tract and bladder (CT KUB). The CT KUB protocol consists of 120 kVp, 1.25 slice thickness, -0.8 slice interval and a standard-type reconstruction kernel. From this data set, 50 scans were manually segmented. This process consisted of seeding osteoporotic bones of interest with the application ITK-Snap, applying a graph-cuts algorithm and then manually correcting the graph-cuts algorithm segmentation errors. A subset of this manually segmented data was then used to train a data set for the automated segmentation process by using several possible DL methods. We used 10-fold cross-validation, which helped us train and test our DL model.[3] Dice and Jaccard scores were used to evaluate our model fit.

Results

Comparisons between our DL models paired with our fixed data will identify the best fit model. A dice score higher than 88% (> 0.88) suggests good agreement between the predicted and manual segmentation methods. Jaccard scores will assess the similarity between different models. Ultimately, results will compare several DL models and determine if they are an adequate fit or whether other avenues should be explored.

Conclusions

A DL algorithm that automatically segments non-quantitative clinical CT scans is the first step to developing a software product for a subject-specific screening of osteoporosis and fracture risk. Implementing such a process in clinical practice will reduce healthcare costs and prevent unnecessary radiation exposure that accompanies additional DXA screening. Furthermore, early identification may prevent subsequent fractures and maintain the quality of life in aging individuals.

References

1. Coughlan T, et al. Clin Med (Lond). 2014; 14(2):187-91
2. O'Malley CD, et al. J Clin Densitom. 2011; 14:100–107.
3. Jung Y, et al. J Nonparametr Stat. 2015; 27(2):167-179.

Ultrasound imaging of the periodontium

Carlos Alberto Figueredo[1], Lawrence H. Le[2], Kim Cuong Nguyen[2,3], Thanh-Giang La[2], Edmond H. M. Lou[4], Neelambar R. Kaipatur[1], Hollis Lai[1], Monica P. Gibson[1], Carlos Flores-Mir[1], Paul W. Major[1*]/ Fabiana T. Almeida[1*]
[1] School of Dentistry, Faculty of Medicine and Dentistry, University of Alberta. Edmonton, AB, Canada.
[2] Department of Radiology and Diagnostic Imaging, University of Alberta, Edmonton, AB, Canada T6G 2E1.
[3] Department of Biomedical Engineering, University of Alberta, Edmonton, AB, Canada T6G 2V2.
[4] Department of Electrical and Computer Engineering, University of Alberta, Edmonton, AB, Canada T6G 1H9.

Introduction

The periodontium is a complex structure responsible for supporting teeth. It is composed of alveolar bone, cementum, periodontal ligament, and gingival tissues. Assessment of the alveolar bone and gingival tissues is vital in periodontitis cases and during orthodontic tooth movement [1, 2].

Currently, imaging methods that assess the alveolar bone have limitations including superimposition of anatomical structures and cumulative radiation doses. [3]

Ultrasound (US) is a free of radiation and noninvasive imaging method commonly used in medicine. The US use in dentistry has been investigated for decades, and recent studies have successfully demonstrated its potential use to assess the periodontium in dental patients [4, 5]. Therefore, the objective of this study was to determine the intra- and inter-rater reliability of measurements between periodontium landmarks in US images.

Methods

Sixty-four patients participated in this study. US scanning was conducted with a 20MHz intraoral transducer. A total of 752 and 180 images were included in the intra-rater and inter-rater reliabilities, respectively.

Landmark measurements in the periodontium included the distance between alveolar bone crest and cementoenamel junction (ABC-CEJ), gingival thickness (GT), and alveolar bone thickness (ABT) (Figure 1). Measurements were conducted by 3 raters and inter correlation coefficients (ICC) were calculated.

Results

The ICC scores for intra-rater reliability were excellent for ABC-CEJ, GT, and good for ABT. The ICC scores for inter-rater reliability was excellent for GT, and good for ABC-CEJ and ABT.

Conclusions

This study showed high reliability of US in periodontium assessment. There might be a potential to use US as a complementing tool to assess periodontium. Further research to investigate ultrasound accuracy is needed as a next step.

References

[1] Evangelista K, Vasconcelos KDF, Bumann A, et al. (2010) Dehiscence and fenestration in patients with class I and class II division 1 malocclusion assessed with cone-beam computed tomography. Am J Orthod Dentofacial Orthop. 138:133

[2] Walter C, Schmidt JC, Dula K, et al. (2016) Cone beam computed tomography (CBCT) for diagnosis and treatment planning in periodontology: A systematic review. Quintessence Int. 47:25–37.

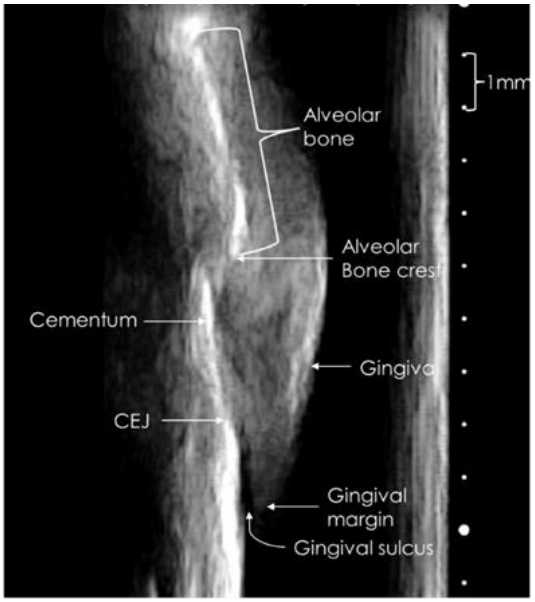
[3] Shah N, Bansal N, and Logani A. (2014) Recent advances in imaging technologies in dentistry. World J. Radiol. 6:794–807.

[4] Sun M, Liu X, Xia T, et al. (2021) Non-invasive evaluation of labial gingival and alveolar crest thickness in the maxillary anterior teeth region by 15-MHz B-mode ultrasonography. BMC Oral Health 21:10.

[5] Nguyen KCT, Le LH, Kaipatur NR, et al. (2016) High-Resolution Ultrasonic Imaging of Dento-Periodontal Tissues Using a Multi-Element Phased Array System. Ann Biomed Eng 44:2874–2886.

Figures

Figure 1. US image of the periodontium of tooth #11 with labelled landmarks.



Microneedle Array Load Factors

Catherine Betancourt Lee[1], Kazim Haider[1], Thomas Lijnse[1], Colin Dalton[1,2]
Department of Biomedical Engineering, University of Calgary [1] Department of Electrical and Software Engineering, University of Calgary[2]

Introduction

Hypodermic needles can cause significant pain as well as needle phobia. Microneedles (tiny projections with heights of 100 - 1000 µm and diameters of 5-300 µm) can serve as an alternative. Microneedle arrays can result in less pain due to distribution of insertion force over a larger area. [1].

An important principle to help increase microneedle penetration without breakage is balancing the insertion force with the buckling force. Buckling occurs if the insertion force outweighs the critical load factor (CLF), which is a ratio between the buckling load and the applied load.

This is also dependent on the number of microneedles per array (density), alongside variation between each individual design.

Methods

Microneedle simulations were conducted with a 10N axial applied force to understand CLF variation with varying microneedle dimensions and designs[2].

The models were categorized as:

1) Single microneedle robust (200 µm diameter)
2) Single microneedle slender, sharp tip (100 µm diameter)
3) Single microneedle blunt tip (60 µm diameter)
4) Microneedle Array (2x2) robust
5) Microneedle Array (3x3) robust

The linear buckling analysis returned a CLF, then was analyzed using a 3D volume deformation and a single needle force analysis per array.

Results

The CLFs were 0.60771 for the 200 µm diameter, 0.1634 for the 100 µm diameter and 0.0699 for the 60 µm diameter. The array of 4 and 9 were respectively 3.4635 and 7.9437, modelled with the robust microneedle design, returning an individual per needle value of 0.87.

Conclusions

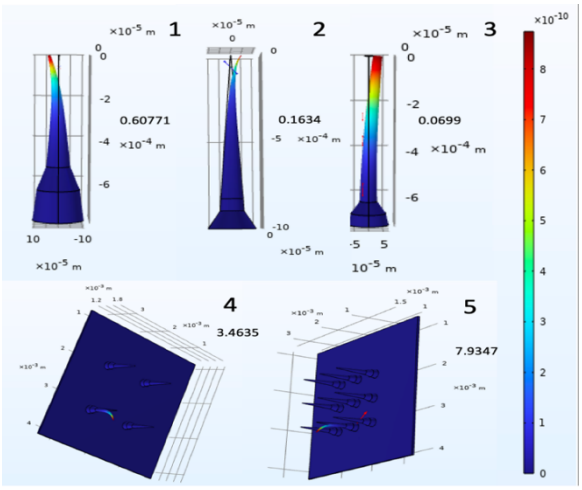
The 200 µm diameter microneedle was the most mechanically robust, having the greatest CLF in both unit and array. The increase between increase of arrays was proportional and experimentally feasible.

Mechanically robust designs increase the probability of insertion without fracture and provide resistance to heavier loads. Comparison to experimental microneedles were also conducted to create a simulation-experiment model for future tests.

References

[1] R. F. Donnelly, et al., Microneedle Manufacturing and Testing (2018).
[2][Van Gerwen DJ, et al., A survey of experimental data (2012).

Figures



Figure/Table: 3D Volume Deformation Simulations of Respective Microneedles. CLF is identified next to each outcome.

Developing Smart-Traps to Observe Physiological Stress Responses in Wild-Caught Rodents

Chetan Gupta[1,3], Erin Casper[2,3], Mathieu Pruvot[2,3], Karthikeya Murari[1]
[1]Department of Biomedical Engineering, University of Calgary, Calgary, AB
[2]Faculty of Veterinary Medicine, University of Calgary, Calgary, AB
[3]Pruvot Lab. University of Calgary, Calgary, AB

Introduction

Stress responses within wild animals can be quite damaging to their overall health with implications such as reduced fertility, decreased immune function and death. An animal's 'coping capacity' or, its ability to cope with these stressors is defined as its resilience. Currently however, there is very little research into how to assess or measure this resilience. This study aims remedy this by manufacturing an acute stressor, with a trapping event, to induce a dynamic stress response that can be monitored, within wild-caught deer mice.

Methods

To monitor the stress response, corticosterone is defined as the dynamic indicator of resilience (DIOR) and measured in the mouse's blood post stressor, immediately and over time until baseline is recovered. Corticosterone levels only remain elevated for 2 minutes leaving a short period of time for travel, handling and sampling of the mouse. The trap model (Figure 1) has been modified with a phototransistor and wireless chip to send a signal to the stationed team once the doors close/trap is triggered, reserving enough time for data collection. Using photoplethysmography (PPG) systems outfitted along the outer mesh of the cage, additional information about the behavioral and physiological responses immediately post capture can be collected.

Results

At this stage, prototyping is in progress with the sensor setup, including the phototransistor and wireless chip, being attached to the trap for pilot field testing. PPG systems are in research phase with out-of-lab testing needing to be completed before integration.

Discussion

This research shows technological improvements upon a widely used yet heavily out-of-date trapping model. The applications of this are broad within the field of veterinary research including wild animals.

Figures



Figure 1: XS Sized Unmodified Havahart Trap: The trap model used and modified upon to conduct this research

The Effect of Hold Time on Mechanical Properties of Myofibrils Stretched Passively due to Immunoglobulin Domain Unfolding and Refolding

Chris Tiessen, Tim Leonard, Walter Herzog
Human Performance Lab, University of Calgary

Introduction

Passive force can be generated in muscle by stretching in a relaxed condition. In an intact muscle, passive force is attributed to connective tissue and to the spring-like protein titin running lengthwise along sarcomeres. However, if individual myofibrils are isolated and stretched passively, force can be attributed solely to the protein titin. [1] This allows testing for the mechanical properties of titin. Mechanically, the protein titin behaves as a non-linear biological spring, with two main regions: the PEVK region, and the immunoglobulin (IG) domain region. [2]

The PEVK region is considered to be approximately elastic; the IG domain region contains domains that can unfold and refold depending on force conditions. [2] Under passive tension, myofibrils show stress relaxation, particularly at longer lengths ($\gtrsim 3.6\ \mu m$ / sarcomere) where the IG domains begin to unfold, lengthening the myofibril. [3] During the shortening phase, IG domains have the ability to refold, and the PEVK region shortens like a spring; [3] this process recovers some energy from the myofibril depending on the degree of stress relaxation.

Purpose

To investigate the effect of hold time on IG domain unfolding and refolding in myofibrils, to elucidate IG domain and PEVK stress contributions during stretch / shortening, and to quantify hysteresis in myofibrils relative to hold time.

Methods

Myofibrils were isolated from the psoas muscle of female New Zealand White Rabbits. Passive force testing was conducted in paired tests (n = 7) using a piezoelectric motor. Myofibrils were stretched over a period of two seconds, and then released over a period of two seconds in the first test; myofibrils were stretched over a period of two seconds, held for four seconds, and released over two seconds in the second test. Stress was calculated for both tests and then used to determine the corresponding hysteresis. Relative contributions of the PEVK and IG domain regions of titin are currently under analysis using a worm-like chain model.

Results

No significant difference was found between normalized hysteresis observed in the paired tests ($P = 0.22$ using a Wilcoxon matched-pairs signed-ranks test). Analysis of contributions of the PEVK and IG domains remains in progress.

Discussion and Conclusion

The lack of significance in hysteresis between the two experimental conditions can likely be explained by the rate of stress relaxation in myofibrils. It seems the majority of stress relaxation happens quickly both during stretch, and just after the target length is achieved. Even though stress relaxation in a myofibril continues for a longer period of time in the hold protocol, this effect is likely small relative to the initial stress relaxation present in both tests. It is also possible that this small difference is not detectable due to sample size (n=7) and the force resolution of the system.

References

[1] Trombitas et al., *Journal of Cell Biology.,* 1998.

[2] Linke et al., *Biophysics and Computational Biology*., 1998.

[3] Freund & Linke., *J Appl Physiol.,* 2019.

Physical activity monitor validation study in youth and young adults

Christina J. Alexander[1,2,3], Leigh Gabel[1,2,3,4]
[1]Biomedical Engineering Graduate Program, University of Calgary
[2]Faculty of Kinesiology, University of Calgary
[3]McCaig Institute for Bone and Joint Health, University of Calgary
[4]Alberta Children's Hospital Research Institute, University of Calgary

Introduction

Accelerometers are commonly used to examine relationships between free-living physical activity and health outcomes, including bone health. Older ActiGraph accelerometer models collected data in a proprietary measure called counts, whereas newer models measure raw accelerations. Understanding whether data are comparable between models is necessary to determine if old accelerometer data can be compared with new accelerometer data.

This study aims to compare physical activity measures between older (GT1M) and newer (GT9X) ActiGraph accelerometers. We chose the GT1M because there is a large UBC[1] physical activity dataset that used these accelerometers to analyze the relationship between physical activity and bone health and the GT9X is the newest ActiGraph accelerometer.

Methods

In this study, healthy individuals (N = 4) between the ages of 7-22 participated in 9 different physical activities: walking, brisk walking, jogging, sprinting, jumping jacks, side-to-side shuffling, vertical jumping, climbing stairs, and cleaning up pylons. Participants wore a GT1M (older) and GT9X (newer) ActiGraph accelerometer on their right hip. The GT1M was initialized to record data in 15 second epochs and the GT9X recorded raw acceleration data that were converted to 15-second epochs in post processing.

GT1M and GT9X data were compared using linear regressions and Bland-Altman plots. Bland-Altman plots were created for combined participant data and each individual activity. Bland-Altman plots gave a visual of agreement between devices (bias in error between the data [GT1M – GT9X]).

Results

GT1M measurements lagged GT9X by 1-2 epochs (15-30 seconds) and were subsequently corrected. GT1M and GT9X data were strongly correlated (R^2 = 0.91). Agreement between GT1M and GT9X counts using Bland-Altman plots showed no systemic or directional bias (mean bias = 3.8 counts). Bland-Altman plots for the individual activities showed greater error and poorer agreement for sprinting and jumping jacks than the other activities.

Conclusions

Counts recorded by GT1M and GT9X ActiGraph accelerometers are strongly correlated with minimal bias. The data compared in this study were epoched count data. However, as the GT9X records raw acceleration data, future work will determine how GT1M count data compares with GT9X acceleration data.

References

[1] Gabel *et al* (2015) Bone architecture and strength in the growing skeleton: the role of sedentary time.

Figures

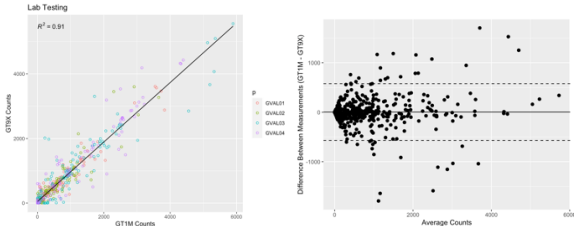


Figure 1: Linear regression (each color representing a different participant) with R^2 = 0.91 (LEFT) and Bland-Altman plot with mean bias = 3.75 (RIGHT) for physical activity count data measured by the GT1M and GT9X ActiGraph accelerometers.

Using Artificial Intelligence to Predict Tumour Recurrence Based on PET-CT Images

C. Keen[1], J. Pyne[2], A. Hareendranathan[1], P. Sivarajah[2], J. Jaremko[1], B. Kelly[1], D. O'Connel[2]
[1]Department of Radiology and Diagnostic Imaging, University of Alberta
[2]Department of Surgery, University of Alberta

Introduction

Head and neck cancer (HNC) represents the 6th most common type of primary malignancy, and often requires a combination of surgical and adjuvant treatments. Additionally, PET-CT imaging is often used to evaluate disease and treatment progress. In recent years, artificial intelligence (AI) has gained popularity in machine assisted medicine and has been successful in tasks such as image classification and predicting treatment outcomes[1].

In this work, we investigate the application of a neural network model for identifying recurrent disease in HNC patients, based on pre and post treatment PET-CT images.

Methods

Pre and post treatment image sets for 60 adult head and neck cancer patients (30 with tumour recurrence and 30 without) were collected and anonymized. Corresponding PET and CT images were processed before being merged as a single 3D image. Images were then evenly split into two balanced datasets: a 45 image training set and a 15 image validation set.

Neural networks consisting of a combination of convolutional layers, recurrent cells, and fully connected layers were trained on a NVIDIA V100 GPU using a binary cross-entropy loss function. Model accuracy was quantified using receive operating characteristic (ROC) curve metrics.

Results

The model which performed best during training and testing consisted of four convolutional layers and two levels of pooling prior to a single layer 3D convolutional LSTM, followed by a fully connected classification layer (Fig).

This model achieved a curve area (AUC) of 0.73, a Youden's index of 0.80, a sensitivity of 0.71, and a specificity of 0.88. Based on Youden's index, a classification accuracy of 80% was derived. A confusion matrix of model performance on the 15 image validation set was generated, and revealed that the model consistently identified cases of non-recurrence, but was also slightly prone to false negative classifications.

Conclusions

This work demonstrates the feasibility of using AI models to identify HNC recurrence based on PET-CT images. Given the small sizes of the training and validation sets, it is possible that the above results were limited by overfitting and low sample size. Continuing work will expand the two datasets as well as implement other factors such as tumour staging and pathological details into the final classification layer.

References

[1] Enshaei A, Robson CN, Edmondson RJ. Artificial Intelligence Systems as Prognostic and Predictive Tools in Ovarian Cancer. *Ann Surg Oncol.*

Figures

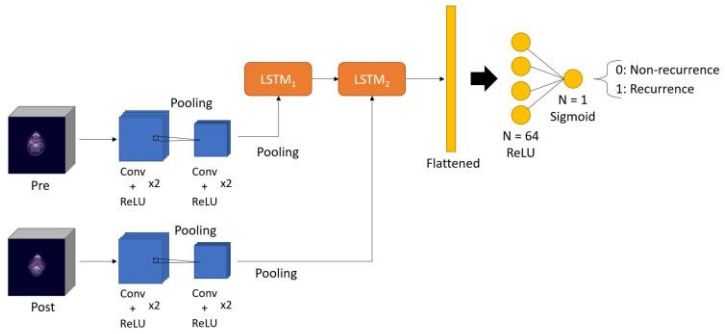


Fig. Architecture of the most successful recurrence classification neural network.

Evaluating glial cell response to functional microelectrode implants in vitro

Christopher Tsui [1,2,4,5], David Roszko [3,4,5], Soroush Mirkiani [3,4,5], Anna DeCorby [2,4,5], Matthew Birtle [2,4,5], Matthew Churchward [2,4,5], Vivian Mushahwar [3,4,5], Kathryn Todd [1,2,4,5]

[1] Department of Biomedical Engineering, [2] Neurochemical Research Unit (Department of Psychiatry), [3] Division of Physical Medicine & Rehabilitation (Department of Medicine), [4] Neuroscience and Mental Health Institute (NMHI), [5] Sensory Motor Adaptive Rehabilitation Technology (SMART) Network, University of Alberta

Introduction

The goal of this project is to develop a systematic approach to evaluating cell reactivity to implanted neural interface devices. Insertion of functional microwire implants designed to interface with nervous tissue elicits an inflammatory response that includes gliosis, cell death, and glial scar formation that can exacerbate injury and prevent healthy recovery of affected tissue [1]. Central to the inflammatory response are glia - whose functions include surveillance and defense of the central nervous system.

Methods

Microwires: Platinum-iridium microwires (75 μm diameter) were deinsulated at the tip with a laser and beveled to 45°. Custom polydimethylsiloxane (PDMS) ports were designed and cured to secure the microwires to the surface of 12-well cell culture plates.

Cell Culture: Mixed glial cell cultures were generated from Day 2 transgenic C57BL/6J CX3CR1$^{+/eGFP}$ mice expressing green fluorescent protein (GFP) in microglia.

Electrical Stimulation: Paradigm (0.1-1.5 mA, biphasic symmetric, 25 Hz, 200 μs pulse duration, 4 hour daily interval) is based off what is used for intraspinal microstimulation (ISMS), and is adapted from previous *in vivo* work [2]. Cell cultures were stimulated for various timecourses (4 hours, 3 days, 7 days) prior to fixation.

Results

Image data assessing mouse glial response to embedded 75 μm diameter platinum-iridium electrodes suggest localized responses at the electrode-culture interface, and support published *in vivo* results [2].

Over the prescribed timecourses, microglia and astrocytes were observed to have gradually accumulated around the implanted microwires (absent of stimulation) which suggests an attempt by the cells to encapsulate the implant. Time-series live cell imaging revealed the gradual occurrence of microglial cell death around the vicinity (~150 μm) of electrodes over a single 4 hour stimulation course, with higher stimulation currents leading to greater reductions in GFP signal. Following experiments, wires were examined with a scanning electron microscope which revealed profound degradation of the deinsulated tip for wires that received high stimulation.

Conclusions

A mixed glial cell culture system was used to deliver electrical stimulation through an embedded microwire implant. This study evaluated the feasibility of adapting ISMS experiments to an *in vitro* context; stimulation amplitudes that were up to 10 times higher than what is normally used *in vivo* were used to establish preliminary techniques and proof-of-principle. Cell death occurred as a result of stimulation, but over several days cells also began to repopulate the space generated around the electrode from stimulation. Future experiments will aim to modify stimulation paradigm parameters (current, pulse duration, waveform shape, etc.) and compare their effects on glial cells.

References

[1] A.F. Jeffery, M.A. Churchward, V.K. Mushahwar, K.G. Todd, A.L. Elias, Hyaluronic acid-based 3D culture model for in vitro testing of electrode biocompatibility, Biomacromolecules. 15 (2014) 2157–2165. https://doi.org/10.1021/bm500318d.

[2] J.A. Bamford, K.G. Todd, V.K. Mushahwar, The effects of intraspinal microstimulation on spinal cord tissue in the rat, Biomaterials. 31 (2010) 5552–5563. https://doi.org/10.1016/j.biomaterials.2010.03.051.

Preliminary Compression Testing of Aramid-Epoxy Braided composites for use in Prosthetics

Daniel P. Gye, Ahmed S. Ead, Jason P. Carey
Department of Mechanical Engineering, University of Alberta

Introduction

Prosthetic limbs have been used extensively throughout human history. The transtibial prosthetic leg is designed to replace the lower leg below the knee of a user, and includes a cylindrical shaft called a pylon [1] which serves as a weight bearing component in the prosthesis. It is usually manufactured from stainless steel, titanium alloy, and aluminum alloy. The strength of these materials must withstand forces which can be as high as nine times the bodyweight of an individual [2]. It is hypothesized that the pylon can be replicated by a tubular braided composite (TBC) which are highly customizable composite materials made of high strength interlaced fibers impregnated with a matrix resin. Its performance depends on fibers and resin properties, unit cell structure and braid angle of the braided composite.

Methods

Samples were manufactured with Twaron® para-aramid fiber, and different internal diameters and braid angles. Five 1-inch-long samples were made for each variant, resulting in thirty total. Manufacturing followed a braiding process from previous work [5]. Testing was conducted in an MTS Series 312.21 machine equipped with flat platens, and digital image correlation (DIC) was completed with two mounted stereo cameras, as seen in figure 1. Samples were compressed at a rate 0.050 inch/min according to ASTM D695-15, and images were collected every two seconds. Collected images were analyzed in an image processing software, which provided strain data. Stress was determined from the load data.

Results

Results indicate that the 45-degree braid angle produced the highest ultimate compressive strength (UCS) for both diameter variants, while the 35-degree braid angle performed the worst. The highest observed UCS was large diameter 45-degree braid had an UCS of 26.45 MPa, while the lowest UCS came from the 35-degree large braid which was 7.58 MPa. All of the above values were smaller than that of aluminum, stainless steel, and titanium.

Conclusions

When tested, the results indicate that the 45-degree angle, which provided an even balance between fiber direction and a closed mesh, led to TBCs that exhibited the best overall performance in compression.

References

[1] R. LeMoyne, “Passive Transtibial Prosthesis and Associated Prosthetic Components,” in *Advances for Prosthetic Technology*, 2016. doi: 10.1007/978-4-431-55816-3_5.

[2] S. Sasimontonkul, B. K. Bay, and M. J. Pavol, “Bone contact forces on the distal tibia during the stance phase of running,” *Journal of Biomechanics*, vol. 40, no. 15, 2007, doi: 10.1016/j.jbiomech.2007.05.024.

[3] B. K. O. Cheung and J. P. Carey, “Improving two-dimensional braided composite tensile properties by including low angle yarn twist: Production, experimental verification, and modeling,” *Journal of Engineered Fibers and Fabrics*, vol. 15, 2020, doi: 10.1177/1558925020946449.

[4] E. A. Lepp and J. P. Carey, “An examination of initial structural degradation in tubular braided composites through region-by-region strain analysis,” *Journal of Engineered Fibers and Fabrics*, vol. 15, 2020, doi: 10.1177/1558925020978325.

[5] G. W. Melenka and J. P. Carey, “Experimental analysis of diamond and regular tubular braided composites using three-dimensional digital image correlation,” *Journal of Composite Materials*, vol. 51, no. 28, 2017, doi: 10.1177/0021998317695418.

[6] AZoM, “Stainless Steel - Grade 316 (UNS S31600),” *AZO Materials*, vol. 316, 2001.

[7] AZoM, “Titanium Alloys - Ti6Al4V Grade 5,” *AZO Materials*. 2002.

[8] AZOM, “Aluminium Specifications , Properties , Classifications and Classes,” *Azom Material*, 2005.

Validating *in-vivo* HR-pQCT bone remodelling measurements in knee osteoarthritis

Daphne A. Kaketsis[1,2,3], Jason Werle[2,4], Nicholas Desy[4], Richard Ng[2,4], Emma O. Billington[1,2,3], Peter Salat[2,3], Sarah L. Manske[1,2,3]

[1]Biomedical Engineering Graduate Program; [2]McCaig Institute for Bone and Joint Health; [3]Department of Radiology, Cumming School of Medicine; [4]Department of Surgery, Cumming School of Medicine

Introduction:

Osteoarthritis (OA) is a whole-joint disease that involves multiple tissue pathologies, including abnormal metabolism in subchondral bone [1]. Abnormal subchondral bone remodelling has been considered to have an important role in OA pathogenesis, and some propose that it could offer a target for OA treatment [2]. Clinically, measures of bone remodelling have been performed on iliac crest bone biopsies [3] which are invasive and do not capture local changes. Recently, high resolution peripheral quantitative computed tomography (HR-pQCT) has been utilized in several different ways to analyse bone dynamics [4][5], such as abnormal bone metabolism, or remodelling, in the subchondral bone. However, these measures lack validation.

Total knee arthroplasty (TKA) patients offer a unique opportunity to acquire bone samples needed for validation, as during surgery a portion of the proximal tibia is removed. The objective of this study is to validate HR-pQCT as a non-invasive method to measure bone remodelling *in-vivo* in humans.

Methods:

We recruited 4 participants with end-stage knee OA awaiting TKA. Baseline and 4-month follow-up HR-pQCT scans of the proximal tibia were acquired prior to TKA. A scan-rescan protocol was implemented at one study visit for reproducibility measures. Longitudinal image registration was conducted to align baseline and follow-up scans [6]. Bone remodelling analysis was then conducted following similar principles as a previously established method [8]. Each image was filtered to reduce noise and then segmented to produce a binary image of bone using a threshold. Three thresholds (250, 320 and 337 HU) were tested. These segmentations were then added together voxel-by-voxel to identify voxels 1) only present in the baseline image (presumed resorption), 2) voxels only present in the follow-up image (presumed formation), and 3) the overlapping area in both images where there was no presumed change. This analysis was also conducted on the scan-rescan images to determine whether changes measured over time were larger than the noise in the scans.

Results and Discussion:

Preliminary results show that bone changes detected between baseline and follow-up scans are of a larger magnitude overall than changes detected from a same day rescan. Figure 1 illustrates that increasing the threshold decreases the percentage of voxels changed between images, although the difference between scan-rescan and baseline-follow-up remained relatively constant regardless of the threshold. Although motion was not observed, noise and registration accuracy likely contribute to the error observed.

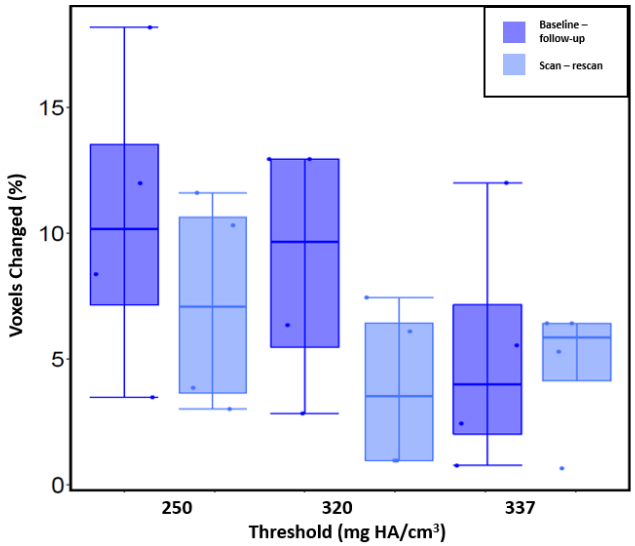


Figure 1: Preliminary sensitivity analysis of segmentation thresholds.

Future work will include a larger sample size, refining the threshold and the registration process to ensure changes captured are true remodelling in the bone. Additionally in order to validate these measurements, they must be compared with dynamic histomorphometry measures that will be conducted on bone samples obtained from surgery.

Significance:

This study has the potential to advance the way bone remodelling is measured, and it has significant implications in the field of orthopaedics, as it would aid in assessment of joint health without the need for an invasive biopsy.

References:

[1] Loeser et al., 2012. *Arthritis & Rheumatism*, 64
[2] Lajeunesse, 2004. *Osteoarthritis and Cartilage*, 12
[3] Armas et al., 2012. *Bone*, 50
[4] Brunet et al., 2020. *BMC Medical Imaging*, 20
[5] Christenet al., 2018. *PLoS ONE*, 13:
[6] S. C. Brunet *et al.*, 2021. *Scand. J. Rheumatol.*, 50
[7] S. C. Brunet *et al.*, 2020. *BMC Med. Imaging*, 20

Directional cues in context affect perceptions and kinematics for manual materials handling

Dean Stewart, Kayla Walker, Conor Tosh, Jon Doan
Engineering & Human Performance Lab, University of Lethbridge, Lethbridge AB Canada

Introduction

Work-related musculoskeletal injuries continue to be a problem, and many workplaces struggle to feasibly control musculoskeletal demands [1]. Part of that difficulty may stem from the measures used to characterize lifting, as many of these don't translate well to instructions and observations of safe lifting training [2]. This research aimed to examine perceived affordance and kinematics during a manual materials handling (MMH) task embedded with implicit directional cues. We predicted participants would perceive a smaller lateral reaching distance (MMH closer to initial position) when chevron cues point toward the individual. In addition, we predicted that current and intuitive kinematics used in sports performance would reflect the same differences and might provide better foundation for lifting training.

Methods

30 healthy young adults (21.8 +/- 1.3 years, 171.5 +/- 12.8 cm, 17 F) participated in the study, with participants randomly assigned to one of three visual cue groups (LEFT, NONE, RIGHT). The cues were positioned before participants arrived and they were not aware that other visual cue walls existed, and no mention of the cues was made during the experiment. The handling surface (conveyor belt) was adjusted to 51% of the participant's height. The researcher read a set occupational script then rotated the conveyor (and load) away from and towards the participant until they set their maximum safe reaching distance (affordance threshold; (AT). Participants then completed multiple MMH trials at their AT, along with common relative and absolute distances. Trials were motion captured (Motus 9, VICON International) with 11 markers placed along bony landmarks of the spine and upper and lower extremities. MMH kinematics including peak X-factor [3] and Crunch Factor [4] were calculated for each trial, averaged within participant, and compared between groups using ANOVA.

Results

Figure 1 shows group mean values (+SEM) for height normalized perceived affordance threshold for LEFT, NONE, and RIGHT cued groups in blue and group mean peak X-factor value for the same groups on the secondary y axis in grey. Participants tended to perceive a larger safe reaching distance when the visual cue is pointing up the conveyor and away from the subject. These increased affordances were coupled with a significantly increased peak X-factor during MMH tasks at AT [$F(2,27)=4.74$, $p=.017$].

Conclusions

Sport kinematic measures are reflective of MMH differences, and might provide more intuitive instructions for safe lifting training at work.

References

[1] Griffith, L. E. et al. 2012. *American Journal of Public Health*, *102*(2); 309–318.

[2] Doss, R et al. 2018. *IISE Transactions on Occupational Ergonomics and Human Factors*, *6*: 116–127.

[3] Joyce, C., 2017. *Journal of Sports Sciences, 35*(20), 2035-2041.

[4] Portus, M et al. 2017. Journal of Science and Medicine in Sport 20S e86

Figures

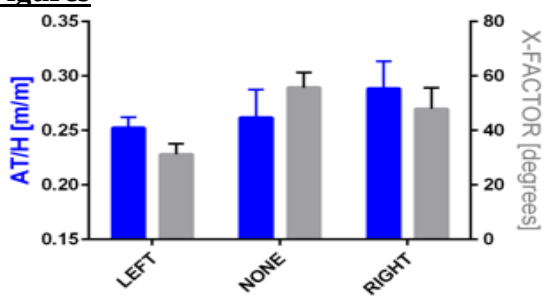


Figure 1. ***Perceptions and behavioural kinematics for an experimental MMH task.***

Investigating sarcomere length non-uniformity and repeatability in immunofluorescent labelled skeletal rabbit psoas muscles

Dhairya Desai, Armaan Sekhon, Tim Leonard, and Walter Herzog
Human Performance Lab, Faculty of Kinesiology, University of Calgary

Introduction

Measuring sarcomere lengths (SLs) in skeletal muscle fibers and myofibrils has traditionally been accomplished using bright-field and phase contrast (PC) microscopy. This can produce inaccuracy and unrepeatability in results[1]. Promising and reliable epitope labelling can be done on sarcomeric structural proteins α-actinin (Z-disk) and myomesin (M-line)[2]. However, antibody labelling has been associated with reductions in myofibril function and active force production[3], and the impact of antibody labelling on sarcomere dynamics remains inconclusive. The purpose of this study was to design and evaluate antibody labelling protocols primarily by determining measurement precision, and explore the impact on dynamic sarcomere characteristics such as the development of SL non-uniformity theory (SLNT) in passive and actively stretched myofibrils.

Methods

Myofibrils from the psoas muscle of New Zealand White rabbits were extracted. Labelled samples were incubated with anti-α-actinin, anti-myomesin primary antibodies, and polyclonal IgG (H+L) AlexaFluor488 secondary antibodies, then observed under an Olympus IX83 microscope using PC and FITC-filtered microscopy. Myofibrils (Labelled, n=7 and Control, n=7) were attached to force-measuring cantilevers and stretched.

Passive: Myofibrils were stretched passively from a mean SL length of 2.5-2.6 µm (relaxed position; RP "#") to 3.1-3.2 µm (stretched position; SP "#").

Active: Myofibrils were activated isometrically at RP using a calcium drip solution.

Force and SLs were recorded throughout experiments.

Precision of sarcomere length (SL) measurements was assessed by calculating the standard deviation (SD) of repeated measurement (n=3) of SLs in RPs and SPs.

Results

Pearson correlation coefficient calculations between SLs in labelled (n=150) and control (n=141) myofibrils yielded values of 0.48 (labelled), 0.80 (control) for RP1-RP3, and 0.71 (labelled), 0.76 (control) for SP1-SP3 after repeated passive stretches, indicating greater clustering of SLs at shorter lengths (decreased SL non-uniformities). Reliability yielded decreased standard deviation in labelled SL measurements at all positions compared to control SL measurements (RP1 – 0.015 µm, RP3 – 0.017 µm, SP1 – 0.012 µm, and SP3 – 0.018 µm), indicating greater precision in SLNT measurements. Results from calcium-activated experiments are to be collected.

Conclusions

Results suggest that introduction of antibodies impaired dynamic sarcomere characteristics at shorter lengths following passive stretches, causing a decrease in normal SL non-uniformity. This method, however, did increase precision and repeatability in SL measurements, indicated by decreased SD between repeated measurements in labelled samples. Future investigation of antibody concentration-dependent experiments is warranted to elucidate molecular details, and potentially mitigate observed functionality impairments.

References

[1] Schmidt et al., 2021. *Journal of Biomechanics*. 126: 110628.
[2] Telley et al., 2006. *Biophysical J.*, 90(2), 514-530.
[3] DuVall et al., 2017. *Journal of Experimental Biology*, 220(23), 4418-4425.

The influence of culturing conditions on the proteome of human induced pluripotent stem cells

Tiffany Dang[1,2], Emilie J. Gysel[1,2], Daniel Young[3,4], Breanna S. Borys[1],
Donavan Stagg[1], Sanchit Chopra[1], Joshua Day[1], Antoine Dufour[3,4,5], Michael S. Kallos[1,2]
1 Pharmaceutical Production Research Facility (PPRF), Schulich School of Engineering, University of Calgary
2 Department of Biomedical Engineering, Schulich School of Engineering, University of Calgary
3 Department of Physiology and Pharmacology, University of Calgary, Calgary, Alberta, Canada
4 McCaig Institute for Bone and Joint Health, University of Calgary, Calgary, Alberta, Canada
5 Department of Biochemistry and Molecular Biology, University of Calgary, Calgary, Alberta, Canada

Introduction

Human induced pluripotent stem cells (hiPSCs) offer a large spectrum of regenerative medicine opportunities due to their differentiation capabilities, reduced ethical concerns, and ability for autologous treatment. To manufacture hiPSCs in clinically relevant quantities, bioreactors are typically used due to their improved scalability, opportunity for process monitoring and control, and homogenous culture environment. However, the effects of hydrodynamic forces on hiPSC grown as aggregates in dynamic culture can be understood using -omics tools. By identifying what factors influence key signaling pathways, we gain insight into interactions between the culture environment and the networks that influence health, phenotype, and product quality.

Methods

In this study, hiPSCs were cultured under different culturing conditions. This included (1) two-dimensional mono layer culture, (2) two-dimensional suspended aggregate culture, and (3) three-dimensional suspended aggregate culture in Vertical Wheel bioreactors®. Growth kinetics were monitored for six days under different combinations of these conditions. Experiments were run with an N=4 number of replicates. Further, samples were collected for metabolomic and proteomic analysis.

Results

Preliminary findings have shown that there exists a difference in growth kinetics when comparing the different culturing conditions. This was further emphasized by the day sixfold expansion. Preliminary proteomic analysis also revealed that Rho GTPase signaling pathways were up regulated in three-dimensional bioreactor culture when compared to two-dimensional static mono layer culture. However, further analysis using the new sample size will improve resolution of these proteomic findings and give insight into changes in metabolic profiles.

Conclusions

The use of omics-based strategy such as proteomics and metabolomics can provide further insight on the effects of the culturing environment and the resulting quality of hiPSCs. The preliminary results of this study show that there does exist differences between culture conditions. However, further analysis coupled with metabolomics will provide more wholistic understanding of the effects of growth conditions and hydrodynamic forces on hiPSC quality.

Figures

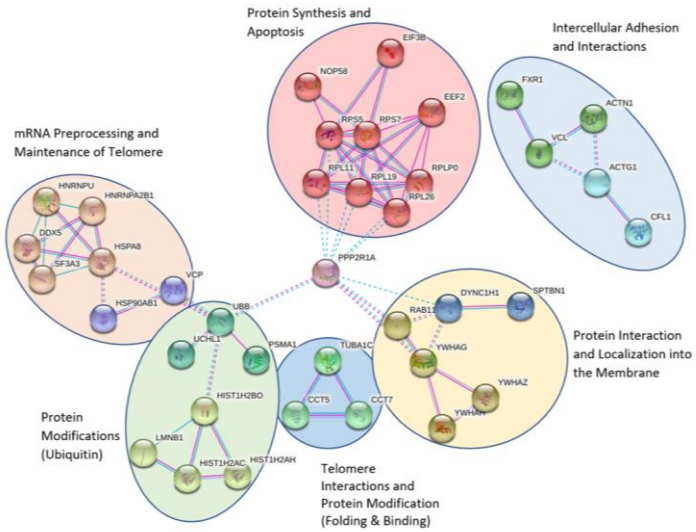


Figure 1. String DB analysis of proteomics data comparing static monolayer versus three-dimensional suspended aggregate in VW bioreactors. Colored areas are different groupings of proteins.

Using wearable fitness trackers to predict intrapersonal activity and sleep outcomes with supervised machine learning

Emily Dittmer, Sayeh Bayat
Healthy City Lab, Biomedical Engineering Department, University of Calgary

Introduction

Advancements in wearable fitness tracking technology enable increasingly accessible health monitoring methods [1]. Machine learning (ML) uses historical data inputs to predict relationships and patterns [2]. Changes in one's lifestyle (e.g., the COVID-19 pandemic) can be analyzed with these tools to identify a need for change to support healthy living. This study aims to determine the predictability of one's activity and sleep outcomes using ML techniques.

Methods

~2.4 years of data was collected from a Fitbit Versa Smartwatch of a 60+ aged participant registered in the University of Calgary Wearable Technology Citizen Science database. March 12th, 2020, when COVID-19 pandemic restrictions were first implemented in Alberta, was chosen as the intervention between classes (before vs during pandemic). Samples (days) were randomly split into 75% training, and 25% testing. Standardized Activity (ACT) inputs (steps, floors, calories, basal-metabolic rate, light, fair, and very active minutes, and sedentary minutes) and Sleep (SP) inputs (duration, deep, light, rem, and time awake) were processed using ML models (logistic regression, support vector machine, and k-nearest neighbor) [2] programmed in Python after removing nonsignificant colinear variables.

Results

The logistic regression model performed best for ACT values, with an area under the receiver operating characteristic curve (AUC-ROC) of 0.92 and f1 score of 0.94. For SP, k-nearest neighbor performed best with an AUC-ROC of 0.58 and f1 score of 0.85.

Conclusions

The findings suggest wearable fitness trackers provide a meaningful tool for analyzing a lifestyle intervention's impact on activity and sleep patterns. A significant change was detected in ACT values of the individual before and after the life event, represented by a higher separability between classes. Sleep values, however, indicated low separability meaning a less significant change occured. This study provides a basis for future studies to utilize commercial smartwatches for determination of a life event's impact on the individual.

References

1. John Dian et al. *IEEE Access*. 8: 69200-69211, 2020.
2. Nasteski, Vladimir. *Horizons*. 4:51-62, 2017.

Figures

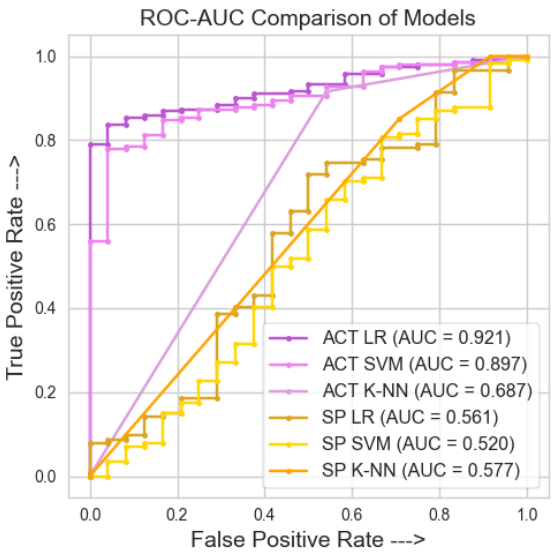


Figure 1: The final area under the receiver operating curve (AUC-ROC) score across logistic regression (LR), support vector machine (SVM), and k-nearest neighbor (KNN) models.

RED-S Risk and Bone Mineral Density Changes in Long Track Speed Skaters

Emily M. Smith[1], Paige M. Wyatt[2], Kelly Drager[2], Erik M. Groves[2], Steven K. Boyd[1], Lauren A. Burt[1]
[1] McCaig Institute for Bone and Joint Health, Cumming School of Medicine, University of Calgary, Calgary, Canada
[2] Canadian Sport Institute Calgary, Calgary, Canada

Introduction

Relative Energy Deficiency in Sports (RED-S) refers to impaired physiological functioning largely as a result of low energy availability (LEA). Health consequences of RED-S include decrements in bone quality, menstrual function, endocrine and metabolic health, among other concerns [(1)]. Depending on the sport, LEA signs and symptoms are present in ~2–60% of athletes [(2)]. Exploring bone mineral density (BMD) with respect to LEA has been previously investigated in long distance runners [(3)]. The purpose of this study was to identify long track speed skaters (LTSS) at risk of RED-S and report changes in BMD over 12 months.

Methods

National team LTSS attended the Bone Imaging Laboratory at the University of Calgary for two sessions, 12 months apart. To identify RED-S risk four variables were explored: low body mass index (BMI) <18.5 kg/m^2 [(4)], previous stress fracture via self-report, low BMD (Z-score <-1.0) [(4)] and for females, low energy availability in females questionnaire (LEAF-Q) identified by a score of ≥8 [(5)]. Identification of any above-mentioned variable resulted in RED-S risk classification.

BMD was assessed using DXA scans of the lumbar spine (LS), hip (femoral neck, total hip) and total body (GE Lunar iDXA). Z-scores were used to compare athletes' BMD with age-, sex- and weight-matched normative data. Athletes with a Z-score <-1 were flagged as having low BMD [(4)]. To compare changes in BMD over time, Wilcoxon Signed-Rank tests were performed using (SPSS).

Results

Twelve LTSS (female: 83%, mean age: 24 years) were recruited. At baseline, four individuals were identified as being at-risk for RED-S (33%, all female). No athletes were identified as having low BMI, previous stress fractures, or low BMD. However, 40% of females were identified at-risk based on LEAF-Q. Overall, LS BMD increased 2.1% over time (p=0.028, all athletes combined). Athletes identified as not at-risk for RED-S at baseline demonstrated an increase in LS BMD (2.3%, p=0.017). While there were no significant changes in BMD for individuals at-risk of RED-S, losses of up to 4% were observed.

Conclusions

This study was able to identify athletes at-risk of RED-S and observe changes in BMD over 12 months. However, a significant limitation is our small sample size. As additional longitudinal data is collected, it is possible significant declines in BMD will be observed in athletes identified as at-risk for RED-S. Within the context of all athletes, irrespective of sport, we hypothesise change in BMD might be a better identifier, than low BMD, for RED-S risk.

References

1. Mountjoy M, et al. BJSM. 2014;48(7):491–7.
2. Gibbs JC, et al. MSSE. 2013;45(5):985–96.
3. Heikura I, et al. IJSNEM. 2018; 28:403-411.
4. Mountjoy M, et al. BJSM. 2015;49(21):1354.
5. Melin A, et al. BJSM 2014;48(7):540–5.

Kinematic Comparison of Cervical Vertebrae Following Total Disc Arthroplasty

Emily Bangsboll[1,3], Tomasz Bugajski[3], Amina Saleh[1], Ganesh Swamy[2,3], Janet Ronsky[1,2,3]
[1]Biomedical Engineering Department, Schulich School of Engineering; [2]Department of Surgery, Cumming School of Medicine; [3]McCaig Institute for Bone and Joint Health, University of Calgary, Alberta, Canada

Introduction

Intervertebral disc (IVD) degeneration of the cervical spine is characterized by joint decay, pain, and other neurological symptoms. The condition commonly impacts the aging population and severe cases may require surgical intervention, such as joint fusion [1]. A limitation of this approach is the potential change in cervical spine kinematics, resulting in altered mechanical load transfer and the development of adjacent segment disease [2]. Cervical total disc arthroplasty (cTDA) is an alternate intervention which may better retain native kinematics [3]. A prior study validated a method to characterize kinematics of the cervical spine using high-speed biplanar video-radiography (HSBV) [4]. However, the ability to distinguish kinematic differences with cTDA is still unknown. The purpose of this pilot study was to use the developed methodology to accurately calculate pre- and post-cTDA cervical spine kinematics using HSBV.

Methods

For one male cadaver, radiostereometric analysis (RSA) beads were implanted into the C4 and C5 vertebrae, followed by a computed tomography (CT) scan of the same vertebrae. The cadaver was then mounted onto a pulley system within the calibrated HSBV system to simulate a flexion/extension (FE) head movement. A single trial of head FE was recorded using HSBV imaging (60 Hz). Afterwards, the cadaver underwent a cTDA, having the IVD between C4 and C5 replaced with a prosthetic (M6-C®, Orthofix, USA). Another CT scan and HSBV collection was repeated for this condition. CT images were segmented in Amira (VSG, Germany) to create 3D models of C4 and C5, which were used to obtain anatomical coordinate systems for each vertebra.

Using a custom MATLAB program (R2021b, USA), the centroids of the RSA beads for the C4 and C5 vertebrae were tracked at every frame of the HSBV images, allowing for the calculation of FE angles for C4 and C5 with respect to their anatomical coordinate systems. To compare pre- and post-cTDA kinematics, the root mean square error (RMSE) of the FE angles between each condition were calculated from 0-15 deg of vertebral flexion (normalized to 0-100% time). An inspection of the FE angle not normalized to time was also performed, with slopes calculated to compare flexion rates.

Results

The RMSEs for C4 and C5 were 3.05 and 1.42 degrees, respectively. The FE angle, when not normalized to time, revealed that both C4 and C5 exhibited greater rates of FE in their native state than post-cTDA, indicated by the larger slope (Fig. 1).

Conclusions

Larger kinematic differences were observed in C4 than C5, noted by the RMSE. This may originate from the difference in flexion rate for pre- and post-cTDA, as changes in the rate of FE were also greater for C4 than C5 (Fig. 1). Additionally, the increased error attributed to the C4 kinematics may indicate that the prosthetic impacts the superior vertebrae to a greater extent. These findings support the use of the HSBV methodology for future studies, which will be conducted to further investigate 3D in-vivo cervical spine kinematics for pre- and post-cTDA.

References

[1] Teraguchi et al., 2014, Osteo. & Cart. 22(1):104–10.
[2] Alhashash et al., 2018. Spine 43 (9): 605–9.
[3] Boselie et al., 2012, Cochrane Syst. (9):CD009173.
[4] Figueroa, 2020, “In Vivo Cerv. Spine Kin.” (thesis).

Figures

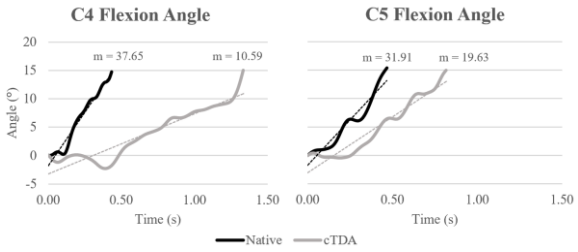


Figure 1. FE angles and corresponding slopes (m) for C4 and C5 under native and cTDA conditions.

Effect of Hydrodynamic Properties on Mesenchymal Stromal Cell Expansion on Microcarriers

Erin L. Roberts[1,2,3], Thomas G. Koch[4], Michael S. Kallos[1,2]
[1]Pharmaceutical Production Research Facility, [2]Department of Biomedical Engineering, [3]Biomedical Engineering Graduate Program, University of Calgary, 2500 University Dr. NW, Calgary, AB, T2N 1N4
[4]Department of Biomedical Sciences, Ontario Veterinary College, University of Guelph, Gordon St., Guelph, ON

Introduction

Mesenchymal Stromal Cells (MSCs) are currently being investigated for the treatment of a wide range of ailments and diseases due to their immunomodulating properties. However, conventional static expansion methods using T-flasks are insufficient in generating the large number of cells required for treatment. Stirred suspension bioreactors using microcarriers as an attachment surface have the potential to generate large numbers of cells with reduced time, labour, space and monetary requirements. Conventional bioreactors use a horizontal blade (HB) impeller, however recently a newer bioreactor geometry has emerged, called the Vertical Wheel (VW) Bioreactor, that uses a rotating wheel combining radial and axial flow components to provide a uniform distribution of hydrodynamic forces. Hydrodynamic forces can have a significant effect on the expansion process, therefore this study investigated the effect of agitation rate and bioreactor geometry on the expansion of MSCs.

Methods

Equine cord blood mesenchymal stem cells (eCB-MSCs) were expanded in static T-flasks and passaged into either 100mL horizontal blade bioreactors or 100mL vertical wheel bioreactors, containing collagen coated microcarriers at a density of 5.4cm^2/mL. Four different agitation rates of 20rpm, 40rpm, 60rpm, or 80rpm were investigated for each bioreactor geometry. After 5 days, the cells were harvested from the bioreactors using TrypLE and an agitation rate of 100rpm.

Results

After 5 days of expansion, there was no statistically significant difference in cell expansion between the HB and VW bioreactors at any agitation rate. There was also no statistically significant difference in cell expansion between the different agitation rates within the HB condition. Within the VW bioreactor condition, the 80rpm VW bioreactor had significantly lower cell expansion than the 20rpm and 40rpm condition. There was no significant difference between harvesting efficiency between the HB and VW bioreactors. Images of all conditions on Day 5 can be seen in Figure 1.

Conclusions

In this study investigating the effect of hydrodynamic forces on the expansion of eCB-MSCs, it was found that eCB-MSCs could be expanded within a wide range of agitation rates and with two different bioreactor geometries without a significant effect on cell expansion and harvesting. However cell functionality and characterization need to be studied to investigate if hydrodynamic forces have an effect on these parameters.

Figures

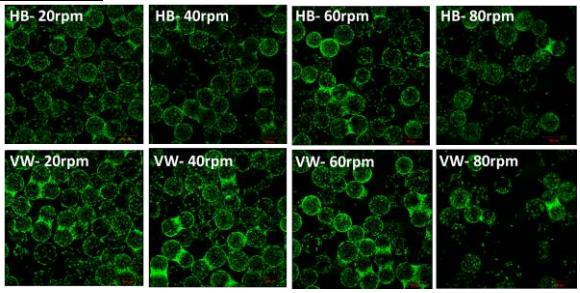


Figure 1: eCB-MSCs on collagen coated microcarriers in either VW or HB bioreactors at the 4 different agitation rates. Nuclei is stained in green.

Session-Based Recommender Systems and Hyper Parameter Optimization for Machine Learning of Administrative Data

Faezehsadat (Fuzzy) Shahidi[1], M. Ethan MacDonald,[1,2] Geoffrey Messier[1]
[1]*Electrical and Software Engineering Department, University of Calgary, Calgary, Alberta, Canada.*
[2]*Biomedical Engineering Department, University of Calgary, Calgary, Alberta, Canada.*

Introduction: People are suffering from mental illness all around the world and Canada is not an exception. People who are experiencing homelessness are more likely to suffer from mental illness [1] and they are more likely to be involved in police and criminal justice interactions [2]. Timely access to mental health services is a key to addressing mental health issues. Thus, finding optimal mental health interventions before police interactions is a great help to the people and government systems. Studies showed that among machine learning techniques, recommender systems (RSs), especially, session-based recommenders (SBRs) [3] improved decision-making in healthcare [4] . Recommender methods are based on short-term interaction and can predict based on the most recent behavior of the individuals.

Methods: An administrative database was utilized, built by linking several main Alberta Health datasets including, practitioner claims, Discharge Abstract Database (DAD), emergency department visits and day procedures, and pharmaceutical information network (PIN) dispense. The study cohort included individuals living in Calgary and diagnosed with mental illness. The adverse outcomes in our study were homelessness and police interaction.

In the pre-processing phase, the events that happened in a window size of thirty days were put together as a session. One individual may have more than one session. We used the weighted random sampling method to balance the homelessness, and police interaction classes.

In our architecture, a session-based recommender system (SBRs) was developed. This model consists of several parts. First, an Embedding layer was applied to assign a numeric vector to each event and also to calculate the semantic similarity. Second, a two-layer neural network was applied to receive the output of embedding layer and estimate the homelessness or police interaction classes.

The developed model was trained and tested (with a split rate of 90-10) on the balanced and pre-processed administrative data for individuals with mental illness. During the training, the weights with the least loss function were chosen to decrease the errors for the unseen data. Accuracy was used to assess the performance.

Results: The least test loss score received in epoch 10 was 0.05. The best test and train accuracy scores were 95% and 92% respectively. The predicted values gained by our model for the test data set were shown in Figure 1.

Conclusion: Session-based recommenders are emerging in the field of healthcare. These models gave higher weight to the recent time-series data so that the recent activities are given more attention once estimating the outcomes. In this study, we used a session-based recommender system to estimate the next outcome using administrative data. We used the test loss score to choose the best weights while training the model.

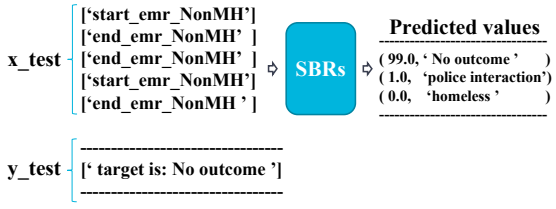


Figure1: Predicted values received by the trained model with the least loss function error for test dataset.

References:

[1] Thomas, et al., Cham: Springer Int. Pub., 2019.
[2] Roy, et al., Psych. Services, 2014.
[3] S. Wang, et al., ACM Comput. Surv., 2022.
[4] K. Haas., et al., AMIA, 2019.

A comparative study between a Newtonian and non-Newtonian droplet impact in a liquid pool

Guilherme M. Bessa[1], Jake Hadfield[1], Sutendra Gopinath[2], Darren H. Freed[2], David S. Nobes[1]
1-Department of Mechanical Engineering, University of Alberta, Edmonton, AB, Canada
2-Department of Surgery, Physiology & Biomedical Engineering, University of Alberta, Edmonton, AB, Canada

Introduction

Ex-vivo heart perfusion systems (EVHP) preserve the natural beat of a human donor's heart outside the body while it is transported to the recipient. A present concern in this system is blood drip that may result in damage to the blood cells, known as hemolysis. To address this hypothesis, the present work aims to investigate the stress distributions over the entire time domain of drop impact into a liquid pool. As extensional flow causes deformation of a fluid particle, it is assumed that this can lead to disruption of the red blood cell membrane. For such, an experimental setup was designed to allow flow measurements below the liquid surface with Particle Image Velocimetry (PIV). Particularly, as blood is a shear-thinning fluid, a blood-like non-Newtonian solution must be used in order to account for the non-linear rheological effects on the flow domain.

Method

An experimental setup was designed to enable optical access of the flow field below the drop impact point on a liquid surface. An acrylic tank was used to hold the liquid pool seeded with tracer particles. A blood-like non-Newtonian solution is prepared with water-glycerol 40 wt/wt% and 200ppm of Xanthan gum. The droplet impinged the liquid surface by using a syringe with different sized needles to generate droplets of approximately 2.5, 4.0 and 5.5 mm. A syringe pump drives the syringe for dispensing drops in a controlled manner. The impingement height was varied by using a vertical traverse system. A high-speed camera (Phantom v611, Vision Research, Inc., USA) was used to capture the drop impact velocity and the flow field below the liquid surface. The experiment was performed using a continuous-wavelength DPSS laser (LRS-0532 Series, LaserGlow Technologies) to illuminate the region of interest.

Results

The impact of the non-Newtonian droplet was evaluated in comparison with that of a Newtonian droplet made with water-glycerol 40% w/w under similar initial conditions. Preliminary results reveals that depending on the dynamic conditions, a downward moving vortex ring is formed in the process by viscous diffusion in the early- or in the late-impact regimes–after an upwards jet rebounds, as shown in the Fig. 1. The criteria for the generation of the vortex, which requires a balance between inertia, capillary, and viscous forces, have been quantified in terms of the Weber (We) and Ohnesorge (Oh) numbers. It has been observed in the literature [1] that there is a critical threshold for both dimensionless numbers below which a vortex ring is formed .

Conclusions

The occurrence of vortices in the flow domain are characterized quantitatively using the We and Oh numbers. The present study will focus on measuring the spatiotemporal features of the shear-stress distributions from early- to late-impact regimes to evaluate whether the fluid stresses arising from the drop impact reach levels that can translate into red blood cell membrane failure. The presentation will discuss the experimental setup and review preliminary results.

References

[1] Behera et al., Phys. Fluids 31, 082108 (2019).

Figures

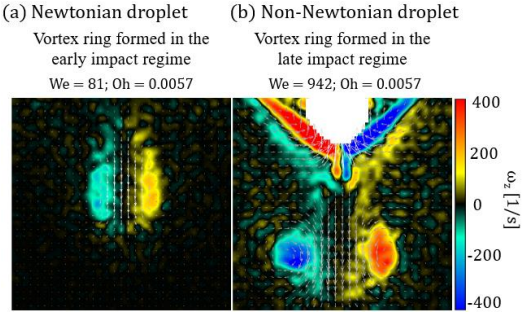


Figure 1: Vorticity fields underneath the liquid surface for the Newtonian droplet (a), and the non-Newtoninan droplet (b).

Deep Learning Model for Frequency and Phase Correction of MR Spectroscopy MEGA-PRESS Data

Hanna Bugler[1-4] BEng, Rodrigo Pommot Berto[1-4] BEng, Roberto Souza[1,3,5] PhD, Ashley Harris[2-4] PhD
[1]Biomedical Engineering Department, University of Calgary, [2]Department of Radiology,
[3]Hotchkiss Brain Institute, [4]Alberta Children's Hospital Research Institute, University of Calgary, [5]Electrical and Software Engineering Department, University of Calgary

Introduction

Magnetic resonance spectroscopy is the only non-invasive method to measure metabolite concentrations in vivo. MEGA-PRESS, an edited MRS technique, is used to remove the contribution of overlapping metabolites of non-interest by subtracting two subspectra. Due to the limited signal-to-noise ratio (SNR) achievable with this technique, accuracy of post-processing steps is vital to retaining the integrity of the original signal.

Of these steps, frequency and phase correction (FPC) is required to improve the misalignment of subspectra caused primarily by scanner instabilities and participant motion [1]. Commonly used techniques, such as spectral registration [1], have been proposed to correct phase and frequency drifts. In recent literature [2][3], deep learning models have been proposed to improve the results of existing methods.

Tapper et al. created a fully connected deep learning network which made FPC predictions sequentially [2]. Ma et al. expanded on Tapper et al.'s model adding convolutional layers for improved performance [3]. The model described in this work seeks to improve on existing methods by using multiple transients from a single scan to make FPC predictions, using both the real and imaginary values of spectral points throughout the model and to combine FPC into a single network.

Methods

Two hundred and fifty base transients were simulated using FID-A [4] to create 250 scans of 320 transients by adding random amplitude noise, discrete and linear frequency and phase shifts using in-house python scripts. Three datasets with varying SNR ranges and fixed frequency and phase offsets were created from this data for training and validation of the model.

A single deep learning network was created for FPC predictions (Figure 1). The network takes in all transients of a single scan which results in an output array with the predicted frequency and phase shifts.

The model will be compared to the deep learning models of Tapper et al. [2], Ma et al. [3], and to more traditional spectral registration (SR) [5] using 24 in vivo datasets with similar parameters from Big GABA [6] and previously collected data in the Harris Lab.

Results and Conclusions

I expect the expansion of the models of Tapper et al. and Ma et al. to improve both frequency and phase prediction accuracy as compared to traditional SR. This work improves FPC predictions by utilizing the complex values of all transients of a single scan and incorporating frequency and phase predictions into a single network.

References

[1] Near et al., 2014, *Magn. Reson. Med*.
[2] Tapper et al., 2020, *Magn. Reson. Med*.
[3] Ma et al., 2021, *Magn. Reson. Med*.
[4] Simpson et al., 2017, *Magn. Reson. Med*.
[5] Near et al., 2015, *Magn. Reson. Med*.
[6] Mikkelsen et al., 2017, *Neuroimage*

Figures

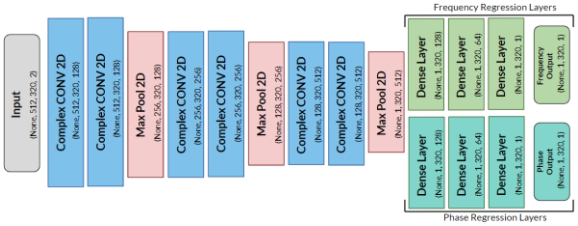


Figure 1. Frequency and Phase Correction Network. A scan of 320 transients (grey) passes through three sets of two complex 2D convolution layers (blue) and a 2D max pooling layer (red). The network then branches into frequency (light green) and phase (dark green) dense layers which will predict FPC values.

Validating a markerless motion capture system for sit to stand testing

Hannah MacDuff, BSc Kinesiology, Kaelan Findlay, BSc Kinesiology, Amber Wardrop, Kiitan Okesanya, Sumaya Soufi, Emily Armstrong, BSc, & Martin Ferguson-Pell, PhD, C.Phys. FRSA

Introduction

The sit-to-stand test is utilized as a predictor of falls and declines in acts of daily living. This test measures lower limb and core strength, endurance, and balance (Segura-Ortí & Martínez-Olmos, 2011). It is difficult to accurately assess the desired parameters by observation alone; therefore, the aim of this study is to further investigate the validity of Kinetisense, a markerless motion capture technology. Currently, the gold standard for measuring biomechanical motion is marker-based systems. While accurate, these systems are expensive, stationary, and difficult for practitioners to use. The alternative of markerless motion capture systems would provide practitioners with a low-cost and portable alternative to evaluate patients across the province remotely.

Methods

A convenience sample of 29 healthy participants was used. The study protocol involved a 5 second pause to assess standing sway, followed by 5 repetitions of sit-to-stand from a chair. Participants were recorded simultaneously using the marker-based Optitrack Motive system and the markerless Kinetisense program for direct comparison.

Results

Initial results indicate that Kinetisense follows Optitrack very closely for the H response, but there may be some inconsistencies when recording forward/backward motion. The H response (essentially frequency of motion) is an important measure, as the time taken to complete a sit to stand cycle can be indicative of a risk of falls, with slower motion indicating a higher risk.

Conclusions

Initial results suggest that Kinetisense is an acceptable tool for use when recording sit to stand and analyzing for falling risk.

References

Segura-Ortí, E. & Martínez-Olmos, F. J. (2011). Test-retest reliability and minimal detectable change scores for sit-to-stand-to-sit tests, the six-minute walk test, the one-leg heel-rise test, and handgrip strength in people undergoing hemodialysis. *Physical Therapy*, *91*(8), 1244–1252. DOI: 10.2522/ptj.20100141

Effect of Protein Supplementation on the Isolation of Exosomes Derived from Human Cancer Cells

Heather Booth[1,2], Sara Hassanpour-Tamrin[1,2], Arindom Sen[1]
1. Pharmaceutical Production Research Facility, Department of Chemical and Petroleum Engineering, Schulich School of Engineering, University of Calgary, Calgary, AB, Canada
2. Department of Biomedical Engineering, University of Calgary, Calgary, AB, Canada

Introduction

Lung cancer is one of the most prevalent types of cancer; however, early diagnosis is uncommon due to a lack of early-stage biomarkers [1]. Exosomes (EXs), which are spherical extracellular vesicles (EVs) secreted by cells, have been proposed as a very early biomarker for cancer [1]. It has been observed that cancerous samples contain more EXs than healthy controls [2]; however, this opportunity has not been fully explored for diagnostic applications. Therefore, EXs from lung cancer and normal cell lines will be compared to potentially enable early-stage diagnosis. To conduct this comparison, EXs must be successfully isolated.

To date, ultracentrifugation (UC) is the most commonly used approach to isolate EXs [3]. However, the low recovery associated with UC remains a primary limitation of this isolation approach. It has been noted that proteins such as albumin may interact with EVs and provide stability in circulation [4]. Therefore, the objective of this study was to investigate whether adding proteins could improve the recovery of lung cancer EXs using UC.

Methods

Human adenocarcinomic alveolar basal epithelial cells (A549 cells) were cultured in Dulbecco's Modified Eagle's Medium supplemented with 10% fetal bovine serum (FBS). Prior to use, the medium was centrifuged at 105,000 *g* for 18.5 hours to remove EXs that typically exist in FBS. Cells were grown in this medium (control group) or the medium supplemented with 25% more protein (test group). Cells were passaged on day 3 and the conditioned medium from the cell culture was collected from each group. EXs were isolated from each conditioned medium using multi-stage differential UC: 300 *g*, 2000 *g*, 10,000 *g*, and 105,000 *g*.

Results

It was observed that supplementing the cell culture medium with proteins produced a visible pellet (test group), whereas the lack of added protein did not (control group). The preliminary results suggest that UC recovered more EXs when the amount of protein within the medium was increased, supporting the addition of proteins to improve EX recovery using UC.

Conclusions

While preliminary results indicate that proteins assist in the production of a visible pellet and improve EX isolation efficiency, additional testing will be conducted to further verify the presence and quantity of EXs. If verified, this approach to EX isolation could overcome a bottleneck currently preventing the analysis of lung cancer EXs. Furthermore, this could allow EXs from lung cancer and normal cell lines to be compared to assist in the development of EX-based diagnostics.

References

[1] K. Xu, C. Zhang, T. Du, A. N. A. Gabriel, X. Wang, X. Li, L. Sun, N. Wang, X. Jiang and Y. Zhang, "Progress of exosomes in the diagnosis and treatment of lung cancer," Biomedicine & Pharmacotherapy, vol. 134, p. 111111, 2021. DOI: 10.1016/j.biopha.2020.111111.

[2] P. Munson and A. Shukla, "Exosomes: Potential in Cancer Diagnosis and Therapy," Medicines, vol. 2, no. 4, pp. 310-327, 2015. DOI: 10.3390/medicines2040310.

[3] B. P. Munson and A. Shukla, "Introduction to Exosomes and Cancer," in Diagnostic and Therapeutic Applications of Exosomes in Cancer, Elsevier Inc., 2018, pp. 1-10. DOI: 10.1016/B978-0-12-812774-2.00001-8.

[4] E. I. Buzas, E. A. Toth, B. W. Sodar and K. E. Szabo-Taylor, "Molecular interactions at the surface of extracellular vesicles," Seminars in Immunopathology, vol. 40, pp. 453-464, 2018. DOI: 10.1007/s00281-018-0682-0.

Serum Metabolite Predictors of Preterm Birth in Primigravida

Ian Han[1,2], Katarina Laketic[1,2], Donna M. Slater[1,3], Chunlong Mu[1,3], Suzanne C. Tough[1,4], Jane Shearer[1,2,3]*.
[1]Alberta Children's Hospital Research Institute; [2]Biomedical Engineering Graduate Program; [3]Department of Biochemistry and Molecular Biology; [4]Department of Pediatrics and Community Health Sciences. Cumming School of Medicine, University of Calgary, Calgary, AB. CANADA

Introduction

Preterm birth is defined as any birth before 37 weeks of completed gestation and impacts approximately 8% of all newborns while posing adverse health risks to both mothers and infants. Common risk factors for preterm birth include past pregnancy history and certain lifestyle habits such as smoking or the occurrence of obesity. Objectives of the present study were to assess the predictive value of serum metabolomics analysis for preterm birth in first time mothers (primigravida's).

Methods

Maternal serum was collected at 28-32wk gestation (3rd trimester) from primigravida's (18+ years) with a singleton pregnancy from the All Our Families Cohort (AB, Canada). Serum from 24 preterm and 47 term births were analyzed by untargeted metabolomic analysis by liquid chromatography/mass spectrometry using reverse phase chromatographic separation with positive ionization (QTOF 6550i, Agilent). Pattern recognition algorithms were used to identify and isolate significant metabolites based on their observed mass to charge ratios. Multivariate modeling (OPLS-DA, VIP) was conducted using SIMCA (v17).

Results

Several metabolite differences between term birth and preterm birth primigravida's were identified. Network analysis highlighted compounds involved in several metabolic pathways and to be strongly associated with preterm birth. Lysine and arginine pathways were altered with pre-term birth (VIP>1). In addition, women who delivered preterm had significantly elevated levels of various oxidized phospholipids. Among the at term participants, women receiving induced delivery had greater phospholipid levels than those who underwent spontaneous delivery. On the other hand, induced delivery showed lower serum tyramine levels, suggesting an alteration in tyrosine metabolism. For primigravida's experiencing preterm birth, there were significant metabolite differences between spontaneous preterm and medically indicated preterm delivery. Higher abundance of histidine, monoglycerides and diglycerides were observed in serum of medically indicated preterm mothers. They were also associated with increased levels of free nucleobases in serum which likely corresponds to the higher metabolic activity of preterm infants.

Conclusions

Several metabolic pathways were altered in primigravida's encountering preterm birth. While additional investigation is necessary to validate these findings, maternal metabolites in the third trimester may be promising biomarkers for identifying women at risk of preterm birth, and LC/MS provides a powerful tool to screen for these compounds. Such analysis may serve as an additional evaluation tool for physicians to administer timely prevention, monitoring, and intervention to avoid harmful consequences to both mother and child.

Figure

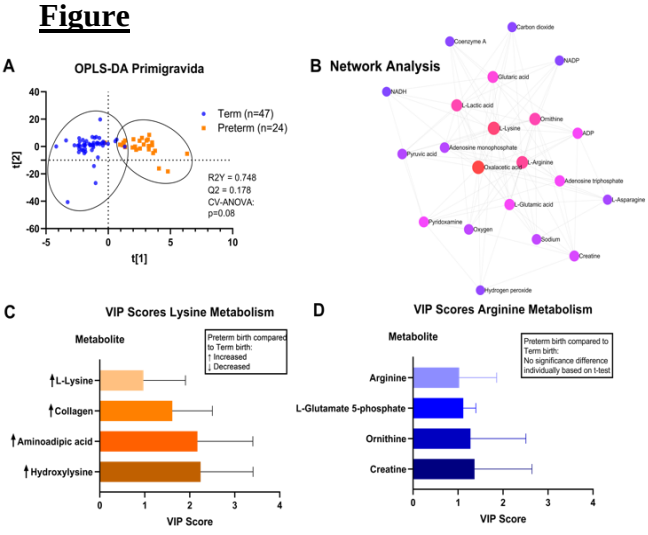


Figure 1. Preterm (<37wk) vs Term (≥37wk). (A) OPLS-DA plot of term (n=47) and preterm birth (n=24) in primigravida. **(B)** Network analysis by MetaboAnalyst 5.0 of significant compounds. **(C)** Variable Importance in Projection (VIP) values modelled from OPLS-DA plot for compounds in the lysine metabolic pathway. **(D)** Variable Importance in Projection values modelled from OPLS-DA plot for compounds in the arginine metabolic pathway.

Validation of knee joint space width and quadriceps angle using EOS imaging

Isabella Vandergaag, Steven Boyd
McCaig Institute for Bone & Joint Health, University of Calgary, Calgary, AB

Introduction

The anterior cruciate ligament (ACL) is one of the most frequently injured ligaments among young, athletic individuals[1]. While several studies have identified injury mechanism components (neuromuscular imbalances) and potential hormone related influences, key bone and joint geometry factors are not well understood. Previous research has shown that anatomical factors, such as joint space width (JSW) and quadriceps angle (Q-angle), are associated with both ACL tear incidence and reoccurring injury[2, 3].

There is limited investigation with these anatomical factors, particularly because they require multiple images. However, there is potential to investigate both measures using EOS (EOS Imaging, Paris, France). EOS is a novel low dose bi-planar X-ray scanner that is ideally suited to measure lower limb geometry. Its software interface holds potential to measure JSW and Q-angle (SterEOS)[4], but this has not been implemented. By measuring both parameters at the same time, it eliminates the need for two separate scanners and improves efficiency. We are interested in these anatomical factors because they may contribute to pain movements that link geometric factors to ACL recovery outcomes.

Methods

This project recruits 30 people for reproducibility and repeatability measurements of Q-angle and JSW. Our novel protocol will scan each individual twice in a standing position with bi-planar X-ray (EOS) and twice with traditional gold standard X-ray, resulting in a total of four scans per participant. Gold-standard reference measurements of Q-angle will be conducted with a goniometer following each EOS scan. Statistical analysis will compare the Q-angle and JSW to their gold-standard references to establish accuracy and reproducibility (RStudio).

The Q-angle is defined as a measurement from two lines: (1) the anterior superior iliac spine to the midpoint of the patella, and (2) the midpoint of the patella to the tibial tubercle. JSW will be assessed at three sites each of the medial and lateral compartments of the femur (inner, middle, outer; units mm).

Expected Results

Results from the repeated measures of EOS, goniometer, and X-ray will be compared to determine whether JSW and Q-angle can be accessed accurately using EOS. These results will help establish a baseline that specific geometric factors (Q-angle and JSW) can be measured under a single imaging modality. This data will contribute to a larger investigation that geometric factors contribute to long term quality of life (QoL) prediction. Specifically, we aim to understand whether patients with key geometric factors at baseline lead to reduced QoL during the recovery phase of an ACL tear.

Conclusions

Overall, this method to quantify JSW and Q-angle will be utilized to establish accurate geometric measurements under a single imaging modality and will further our understanding of these anatomical risk factors following an ACL tear.

References

1. Hughes G, Watkins J. A. Sports Medicine 2006;36(5): 411-28.
2. Jones MH, Spindler KP, Fleming BC, et al. Osteoarthritis and Cartilage 2015;23(4): 581-88.
3. Herrington L, Nester C. Clinical Biomechanics 2004;19(10): 1070-73.
4. Kalifa G, Charpak Y, Maccia C, et al. Pediatric radiology 1998;28(7): 557-61.

Fluorometric Aptasensor; evaluation of stability and comparison to standard ELISA assay

J. Carlos Kuri, Varun Vij, Raymond J. Turner, and Orly Yadid-Pecht
Department of Electrical & Software Engineering and Biological Sciences in University of Calgary

Introduction

Celiac disease (CD) is an immune system disorder triggered by ingesting gluten [1]. Hence gathered attention and addressed using an antibody-based biosensor for gluten quantitation, Enzyme-linked immunosorbent assay (ELISA).

Nevertheless, ELISA was quickly considered synonymous of expensive, time consuming and complex [2]. On the other hand, DNA aptamers have shown competitive potential due to their selectivity, sensitivity, temperature stability, pH stability, simplicity and rapid testing advantages over ELISA [3].

In this study, a fluorometric Aptasensor long-term stability is shown and its accuracy contrasted to ELISA assay.

Methods

The system is heavily based on the fluorescence resonance energy transfer (FRET) phenomenon, which allows the fluorophore attached to a DNA aptamer (gli4) to be quenched by reduced-graphene oxide. Once the aptamer binds to the analyte (33-mer peptide), the fluorophore is freed from the quencher and allowed fluorescence.

The more binds the aptamer does to its analyte, the more fluorescence within the assay. The fluorescence intensity is gathered by a photoreceptor and contrasted to a set of premade gluten concentrations for interpolated measurements.

Results

The experiments took place every 2 to 3 days for 8 weeks each run, giving a total of 4 runs. And only the first set of results from each run was contrasted to ELISA.

836 tests were studied, averaged and graphed to find the accuracy of the method. The accuracy in this study is defined as correctly classifying gluten-free (GF) labeled products as GF, and not classifying regular products as GF. GF products are only those which contain no more than 20 ppm (parts per million, or mg/kg) of gluten.

In the first set of results of each run, the studied method accuracy is 100% on GF products and 96.30% on regular products. Within the first 4 weeks the accuracy is stable around 90%, and quickly decreases to around 72% henceforth. ELISA accuracy from the first set of results underperforms at 86%.

Conclusions

The aptamer-based biosensor has shown competitive advantage over ELISA in the first set of results of each run; yet, at long-term study, the biosensor is unstable. Hence, further additives and improvements ought to be studied and implemented before influencing the global healthcare.

References

[1] A. Fasano and C. Catassi, “Celiac disease,” *N. Engl. J. Med.*, vol. 367, no. 25, pp. 2419–2426, 2012, doi: 10.1056/NEJMcp1113994.

[2] Y. Zhang, B. S. Lai, and M. Juhas, “Recent advances in aptamer discovery and applications,” *Molecules*, vol. 24, no. 5. 2019, doi: 10.3390/molecules24050941.

[3] M. Xhaferaj *et al.*, “Recent progress in analytical method development to ensure the safety of gluten-free foods for celiac disease patients,” *J. Cereal Sci.*, vol. 96, p. 103114, 2020, doi: 10.1016/j.jcs.2020.103114.

Geometric Correction of Fluoroscopic Imaging Systems by Self-Calibrating Bundle Adjustment

Jackson Cooper [1], Jacky Chow MD, MBA, PhD [2], Derek Lichti PhD [1]
[1] Department of Geomatics Engineering, University of Calgary, Calgary, Canada, [2] Department of Radiology, Cumming School of Medicine, University of Calgary

Introduction

Fluoroscopy is a non-invasive imaging technique that provides a video sequence of x-ray images. It has found everyday use in various medical and biomechanical applications, including endovascular treatment for acute stroke, image-guided joint injections, and assessment of joint kinematics. In addition to the valuable captured images, quantitative geometric properties can be extracted from the data. This geometric information can be invaluable in the automation of certain radiology studies, such as the quantitative measurement of diaphragm paralysis (Chow, 2022), resulting in improved inter-observer reliability in diagnosis. The value of this information is dependent on the metric integrity of the imagery, which is strongly influenced by various systematic image distortions inherent to fluoroscopic imaging systems. The accuracy can be improved by performing geometric calibration of the fluoroscopic imaging system to estimate the distortion parameters and then performing software-based geometric correction of captured imagery. This has been successfully demonstrated for dual-fluoroscopy imaging systems (Lichti, 2015). In this work, the application of the self-calibrating bundle adjustment is used to calibrate a single fluoroscopic system, and correct imagery used for the analysis of diaphragm paralysis.

Methods

This work was accomplished through the application of a controlled experiment. A highly redundant (~4000 degrees-of-freedom) and geometrically strong network of 22 images of a purpose-built target field was collected with a Philips Easy Diagnost R/F System. The target field comprised 121 pre-surveyed tantalum beads embedded on 25.4 mm x 25.4 mm acrylic. Some 1998 image points were observed. A free-network, self-calibrating bundle adjustment based on the augmented collinearity equations was performed.

Results

The modelling process resulted in the estimation of 19 distortion coefficients. Addition of these terms resulted in 83.7% improvement in terms of precision (model fit): from 1.74 pix to 0.28 pix after calibration. When projected into 3-dimensional space for metric measurements, this improved the spatial distance accuracy from 0.37 mm to 0.08 mm.

Conclusions

The successful application of the self-calibrating bundle adjustment and resulting improvement in precision paves a way forward for new applications and improved quantitative measurement for single-plane fluoroscopy.

Acknowledgements

Support from NSERC. Thanks to Gregor Kuntze for use of the target field.

References

Chow, J., & Hatem, M. (2022). Quantitative analysis of diaphragm motion during fluoroscopic sniff test to assist in diagnosis of hemidiaphragm paralysis. *Radiology Case Reports*, *17*(5), 1750–1754.

Lichti, D. D., Sharma, G. B., Kuntze, G., Mund, B., Beveridge, J. E., & Ronsky, J. L. (2015). Rigorous geometric self-calibrating bundle adjustment for a dual fluoroscopic imaging system. *IEEE Transactions on Medical Imaging*, *34*(2), 589–598.

Tibial acceleration is not a valid surrogate measure for predicting musculoskeletal loads

Jean Tu[1,2,3], Olivia L Bruce[1,2,3,4], W. Brent Edwards[1,2,3,4]
1. Human Performance Laboratory, Faculty of Kinesiology, University of Calgary
2. Wearable Technology Research and Collaboration Training Program, University of Calgary
3. McCaig Institute for Bone and Joint Health, University of Calgary
4. Department of Biomedical Engineering, Schulich School of Engineering, University of Calgary

Introduction

Tibial acceleration is often used as a surrogate measure to predict musculoskeletal loads[1]. However, the relationship between tibial acceleration and joint contact force has not been validated in previous studies. Stride length manipulation has been shown to influence both musculoskeletal loads[2] and tibial acceleration[3]; therefore, a correlation between these two variables may exist. The aim of this study was to evaluate the relationship between tibial acceleration and ankle joint load in response to stride length manipulation during level-ground running.

Methods

To date, nine physically active participants ran ten trials in each of five stride length conditions: preferred, ±5%, and ±10% of preferred stride length at preferred speed Motion capture, force platform, and tibial acceleration data were collected. Ankle joint contact forces were calculated using an inverse-dynamics-based static optimization routine. Pearson correlations were evaluated between peak resultant tibial acceleration and peak resultant ankle joint contact force for each participant. Mean peak resultant ankle contact force and peak resultant tibial acceleration were calculated for each condition, and Friedman tests were used to evaluate differences between conditions.

Results

Peak ankle contact force was reduced with shorter stride lengths ($p = 0.004$); however, tibial accelerations remained unaffected. Overall, there was no evidence of a relationship between peak resultant ankle contact force and peak resultant tibial acceleration ($r^2 < 0.126$, Figure 1).

Conclusions

These preliminary results provide no evidence of a correlation between ankle contact force and tibial acceleration during level-ground running when stride length is manipulated. Presently, we are analyzing more participants to better evaluate this relationship. Our results suggest that gait retraining studies should avoid the use of tibial acceleration as a surrogate for musculoskeletal loading. Although this has discouraging implications for the use of single variable surrogates for internal joint loads, there is still possibility of using a multi-sensor approach to predict joint loads using wearable technology[4].

References

[1]Matijevich et al. (2019) PloS ONE, 14(1)
[2]Bowerstock et al. (2017). J Sport Sci, 35(20)
[3]Kliethermes et al. (2021). BJ Sports Med, 55
[4]Matijevich et al. (2020). Human Movement Sci, 74

Funding from We-TRAC CREATE training program

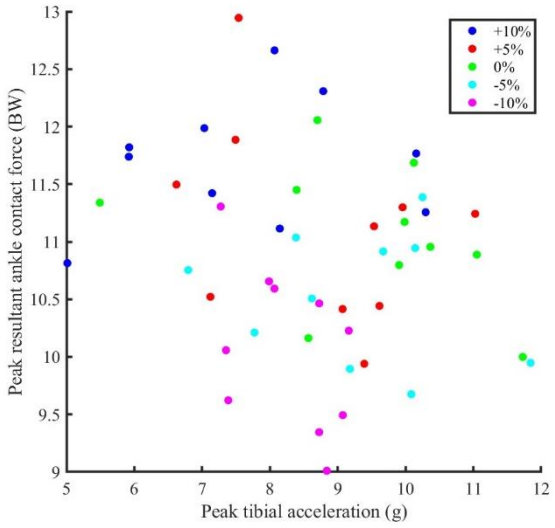


Figure 1: A representative participant illustrating the lack of a correlation between tibial acceleration and ankle contact force.

Determining Strategies to Produce a Low-Cost Media for Human Induced Pluripotent Stem Cell Expansion in Vertical-Wheel® Bioreactors

Jenna S. Holloway[1,2], Tiffany Dang[1,2], Brett Abraham[1,2], Breanna S. Borys[1,3], Hannah Worden[3], Emilie J. Gysel[1,2], Sunghoon Jung[3], Michael S. Kallos[1,2]
[1]Pharmaceutical Production Research Facility, University of Calgary, Calgary, AB, Canada
[2]Department of Biomedical Engineering, University of Calgary, Calgary, AB, Canada
[3]PBS Biotech Inc., Camarillo, CA, USA

Introduction

Cell and gene therapies are emerging as the fourth pillar in healthcare. In this field, human induced pluripotent stem cells (hiPSCs) are of primary interest due to their proliferation and differentiation capacity. Vertical-Wheel® (VW) bioreactors are the preferred method of achieving clinically relevant hiPSC densities. However, the large-scale production of hiPSCs is constrained by the cost of media, the liquid containing nutrients for cells. This study demonstrates the ability of a cost-effective media, called homebrew media (HBM), in conjunction with in-house growth factors for the expansion of hiPSCs in VW bioreactors.

Methods

HBM performance was tested in static and VW bioreactor culture and compared against a commercially available media, called mTeSR, using the hiPSC line TC1133. Subsequently, two growth factors present in HBM, TGFβ and bFGF, were generated in-house and compared against commercial forms in static and bioreactor culture. Following, HBM with in-house growth factors was tested in the seed train preceding bioreactor culture to evaluate its effect on upstream operations. Growth kinetics, aggregate morphology, and staining for key pluripotent markers were used as comparison metrics.

Results

HBM sustained hiPSC growth in static and bioreactor culture while maintaining normal cell and aggregate morphology. HBM with in-house growth factors also maintained cell growth in static and bioreactor culture (Figure 1). However, HBM with in-house growth factors did not support cell proliferation after passaging in the static seed train. Aggregate staining of key pluripotent markers showed that pluripotency was maintained in HBM, but a weak signal existed.

Conclusions

This research demonstrates that HBM in conjunction with in-house recombinant growth factors is a viable option for the growth of hiPSCs. This medium formulation has the potential to overcome the identified cost-related bottlenecks of hiPSC expansion.

Figure

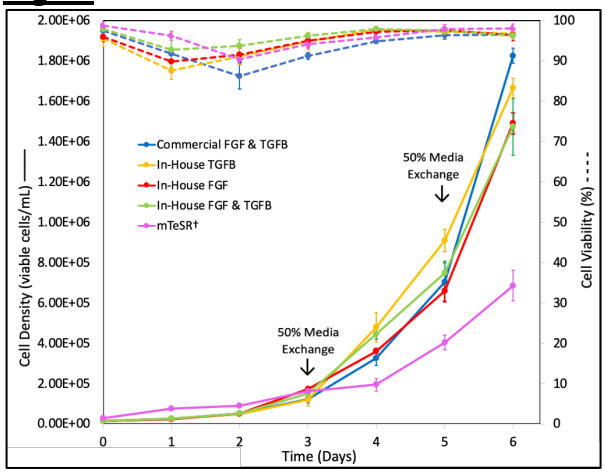


Figure 1. Growth kinetics (solid lines) and viability (dashed lines) in VW bioreactors comparing both in-house and commercial growth factors in HBM against commercial media. A 50% media exchange was performed on days three and five. †Was not performed in parallel with the other conditions.

Proteoglycan 4's impact on the intervertebral discs

Jessica May Corpuz[1,2], Kristian Corpuz[1], Samantha Heschl[1,2], Roman J. Krawetz[2,3]
[1]Department of Biomedical Engineering, Schulich School of Engineering, University of Calgary; [2]McCaig Institute for Bone and Joint Health, University of Calgary; [3]Deparment of Cell Biology and Anatomy, Cumming School of Medicine, University of Calgary

Introduction

Lower back pain is one of the most common musculoskeletal disorders. Several diverse factors have been implicated in the onset and severity of lower back pain, with many of these pathways converging around the degeneration of the intervertebral discs (IVDs). Despite their functional importance in the spine, the IVDs are one of the earliest tissues to undergo degeneration in the body and our understanding of the mechanisms involved in this degenerative process are lacking.

Based on our lab's previous research, we hypothesize that Proteoglycan 4 (*Prg4*) plays an important role in the maintenance of the IVDs. *Prg4* is essential for bio-lubrication in articular joints and is enriched in tissues that undergo in vivo loading. *Prg4* also regulates tissue homeostasis, as mice lacking *Prg4* (*Prg4*$^{-/-}$) show premature tissue degeneration. Due to these findings, there is strong rationale to investigate if *Prg4* is essential for the maintenance of the IVDs and if the loss of *Prg4* results in spontaneous IVD degeneration. Therefore, the purpose of this project is to investigate this relationship between *Prg4* and IVD degeneration to provide the field with a better understanding of the mechanism(s) of IVD degeneration.

Methods

Lumbar regions of *Prg4*$^{-/-}$ and C57Bl/6 mice (n=5 for each strain/timepoint) were collected at 5, 12, 24, and 36 weeks of age. The L1-L3 motion segments (vertebrae-disc-vertebrae) from each animal were collected, fixed, and decalcified for histological analysis. Safranin-O/Fast Green was used to determine gross morphological changes and immunofluorescence was used to examine changes in cell populations and signaling molecules.

Results

The IVDs from *Prg4*$^{-/-}$ mice show clear morphological differences relative to age matched control IVDs (Figure 1). At increasing timepoints, the *Prg4*$^{-/-}$ IVDs show a reduction of height with infiltration of the central nucleus pulposus into the surrounding annulus fibrosus. Decreased proteoglycan staining with concurrent calcification of the endplates is also seen within the *Prg4*$^{-/-}$ IVDs.

Conclusions

Based on these preliminary results, it is evident that *Prg4* plays a vital role in the maintenance of IVDs. Biomechanical testing and proteomics will provide further insight into Prg4's role and effect on IVD functionality and microenvironment. Altogether, this project will provide us with a better understanding of the mechanisms behind IVD degeneration. By elucidating the role of *Prg4* within IVDs, it will uncover additional downstream targets that can be further explored and possibly exploited to inhibit IVD degeneration.

Figures

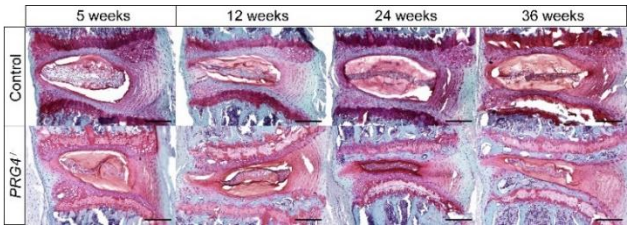


Figure 1. Saf-O/Fast Green staining of lumbar intervertebral discs of control and Prg4$^{-/-}$ *mice at various timepoints. While control discs maintain a central nucleus pulposus and clear boundaries between the different structures, KO discs showcase a reduction in height and infiltration of the nucleus pulposus into the anulus fibrosus. Scale bar of 200μm*

Simulation Analysis for the Development of ECMO Cannula

Joshua Feddema[1], Anthony Thomas Demong[1], Colin Dalton[1,2]
[1]Department of Biomedical Engineering, Schulich School of Engineering, University of Calgary
[2]Department of Electrical and Software Engineering, Schulich School of Engineering, University of Calgary

Introduction

Extracorporeal Membrane Oxygenation (ECMO) systems provide life support when the body cannot deliver sufficient oxygen supply despite mechanical ventilation. ECMO devices drain blood from the venous system, pass this blood through a semipermeable membrane for oxygenation and then return the blood to the body. This process can significantly reduce the stresses placed on the lungs and heart, prolonging life, and increasing the chance of recovery.

A key component of ECMO systems are the cannulae (tubes) which interface between a patient's circulatory system and the device. These cannulae must be precisely manufactured for optimal blood handling, remain kink free, and be blood compatible.

Methods

Manufacturing of these medical devices is performed through precision dip-coating of liquid polymer onto a mandrel (rod). This research covers curing times quantification, initial dip-coat testing, and preliminary simulations. Modeling of the dip coating process was performed with COMSOL Multiphysics to understand the complex three phase fluid dynamic interaction of withdrawing a rod from an entraining fluid. Parallel simulations investigate heat transfer phenomenal during hot dipping. Dip coating experiments are performed to validate simulation results and establish the manufacturing process.

Acknowledgments

I would like to acknowledge Ecmius Biomedical and NSERC for their joint support.

Results

This project aims to span multiple technology readiness levels (TRL) moving from initial prototypes to industrial scale manufacturing of regulatory approved cannulae. Current research has quantified the materials characteristics and the dynamic behaviour of the dip coating process. Initial simulations seen in Figure 1 provide a framework for more comprehensive models and must be experimentally validated.

Figures

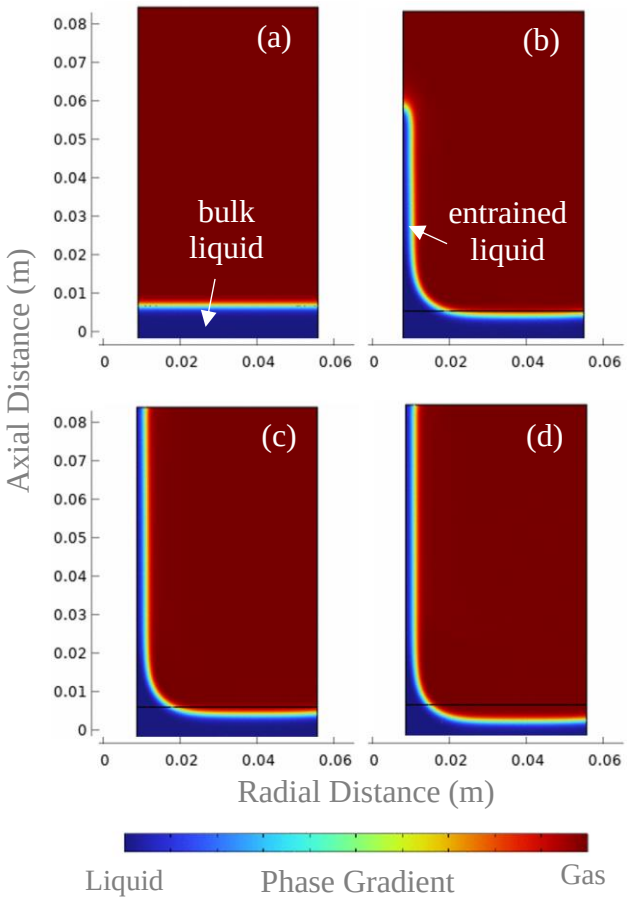


Figure 1: Phase field COMSOL simulation showing liquid polymer entrainment on rod (left boundary) moving at 7.5 cm/s (a) t = 0 s, (b) t = 1 s. (c) t = 2 s, (d) t = 5 s. Note difference in bulk fluid level over time and consistent film thickness (blue line).

Effects of forearm crutch length on latissimus dorsi activity during swing-through gait

Joshua Ellis[1], Gregor Kuntze, PhD[2], Janet L. Ronsky, PhD[1], Ranita H. K. Manocha, MD, MSc[3]
[1]Department of Mechanical and Manufacturing Engineering, University of Calgary; [2]Faculty of Kinesiology, University of Calgary; [3]Division of Physical Medicine & Rehabilitation, University of Calgary

Introduction

Forearm crutches (FCs) are often used by individuals with lower limb impairments [1,2]. Using FCs results in repetitive and substantial upper limb loading. Previous research suggests that latissimus dorsi is an essential muscle for FC-assisted swing-through gait [1,2,3], during which, it is thought to propel forward and bear weight through shoulder adduction and extension. These prolonged demands can lead to pain or discomfort in the upper body. There has been little research into upper limb muscle activity during FC-assisted gait, but some suggests that pain can be amplified by improper crutch length [1]. As such, we aimed to assess latissimus dorsi activity during swing-through gait and evaluate the effects of altered crutch length on the intensity of that activity.

Methods

Fifteen healthy adult males (mean±SD age 24.5±5.8 years, BMI 24.9±2.4 kgm^{-2}) with no crutch training were fitted to 3 sets of FCs: a standard fit based on clinical guidelines, a pair 5 cm longer, and a pair 5 cm shorter. Bipolar surface electromyography (EMG) electrodes were placed over left latissimus dorsi (seniam.org). Participants performed 15 trials of swing-through gait with each crutch condition in a randomized order. EMG data were processed using a wavelet analysis approach in MATLAB. Wilcoxon signed-rank tests were performed in SPSS ($\alpha<0.05$) to evaluate muscle power from 0-25% and 25-50% of the gait cycle as well as peak muscle intensity from 0-50% of the gait cycle.

Results

The latissimus dorsi was active in crutch stance phase with its greatest activity occurring from mid-stance to terminal stance (25-50% of the gait cycle). Activity fully diminishes as crutch swing phase begins. There was no effect of altered crutch length on latissimus dorsi activity at any part of the gait cycle.

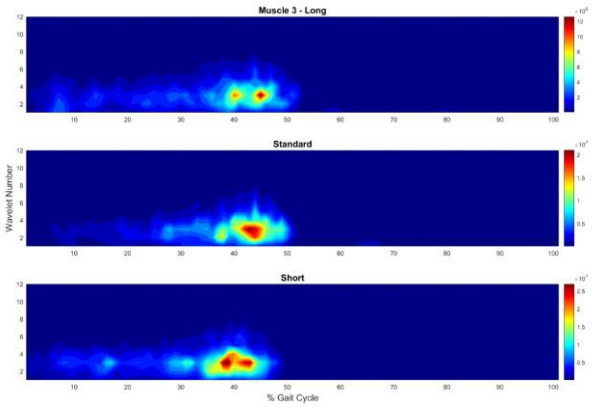
Conclusions

The latissimus dorsi likely functions during crutch stance phase to extend the shoulder and bear weight. The increase in activity at mid-stance indicates that it contracts after the arm extends past the coronal midline. Neither short nor long crutches affected the activation intensity of latissimus dorsi. The peak intensity between the crutch conditions was not affected. These lack of changes in intensity further corroborate the functions of latissimus dorsi during swing-through gait. Shoulder extension from 25-50% of the gait cycle does not oppose gravity and thus, more easily propels the body forward for any crutch length. The body weight is also supported consistently between crutch conditions as the center of mass descends in height. Understanding the activation patterns and likely functions of latissimus dorsi can help healthcare professionals better prescribe walking aids as well as treat discomfort caused by forearm crutches.

References

1. Manocha et al, 2020. *PM&R.*
2. Crosbie, 1993. *Clinical Rehabilitation*. 7: 229-238.
3. Butler, 1984. *Prosthetics and Orthotics International.* 8: 33-38.

Figures



Average latissimus dorsi activity (n=1)

Blood Metallomic Signatures Associated with Pregnancy Smoking Exposure

Katarina Laketic[1,2], Sophie Lalonde-Bester[1], Donna Slater[1], Suzanne C. Tough[1], Kimberly Smyth[1], Hans J. Vogel[3], Chunlong Mu[1], & Jane Shearer[1,2*]. [1]Alberta Children's Hospital Research Institute, Cumming School of Medicine, University of Calgary, Calgary, AB T2N 4N1, Canada. [2]Biomedical Engineering Graduate Program, University of Calgary, Calgary, AB, Canada. [3]Department of Biological Sciences, Faculty of Science, University of Calgary, Calgary, AB T2N 1N4, Canada.

Introduction

Despite warnings, some women continue to smoke during pregnancy. Identifying circulating ions related to cigarette exposure may provide insights into the deleterious impacts that exposure may have on both the mother and offspring.

Methods

The primary aim of the study was to determine whether ions from both prior to pregnancy and pregnancy smokers were distinguishable from pregnant non-smokers. Secondary analysis compared heavy (smoking ≥7 cigarettes/week) and light (smoking <7 cigarettes/week) smokers. Lastly, heavy pre-pregnancy smokers and heavy pregnancy smokers were compared to assess whether distinct ion profiles were apparent. An untargeted metabolomics approach was employed and serum samples from 148 pregnant women were evaluated. Maternal serum samples were collected at 28-32 weeks of gestation from the All Our Families (Alberta, Canada) cohort and assessed using Inductively Coupled Plasma-Mass Spectrometry (ICP-MS). For analysis, smokers were paired with age-matched pregnant non-smokers (1:2) to examine ions associated with smoking-related factors. Multivariate analysis (PCA, OPLS-DA, and VIP) were used in conjunction with univariate volcano plots and t-tests. Descriptive statistics were used to describe maternal health and birth outcomes.

Results

Education (p=<0.001) and gestational weight (p=<0.01) were significantly altered between smokers and non-smokers. There was a trend for lower incomes among smokers (p=0.06) and although not statistically significant, birthweights of infants born to smokers were 78 grams less than the birthweights of infants born to non-smokers. Amongst smokers and non-smokers, 9 discriminant ions were identified with VIP scores greater than 1 (CV-ANOVA=4.37e-6) and 13 discriminant ions were identified from the volcano model, with some overlap with the VIP results. Of note, serum iodine was significantly reduced in smokers and isotopes of calcium were significantly increased (Fig 1. A-D). Amongst heavy and light smokers, serum titanium was found to be significantly greater in heavy smokers (Fig 1. E-H). Amongst heavy pre-pregnancy smokers and heavy pregnancy smokers, serum magnesium was significantly reduced while chromium was significantly increased in heavy pregnancy smokers (1. I-L).

Conclusions

Overall, significant metallomic signature differences were found across all three levels of comparison. Although results do warrant further validation, significant biomarkers may provide future insights into smoking's effects on maternal and birth-related outcomes.

Figures

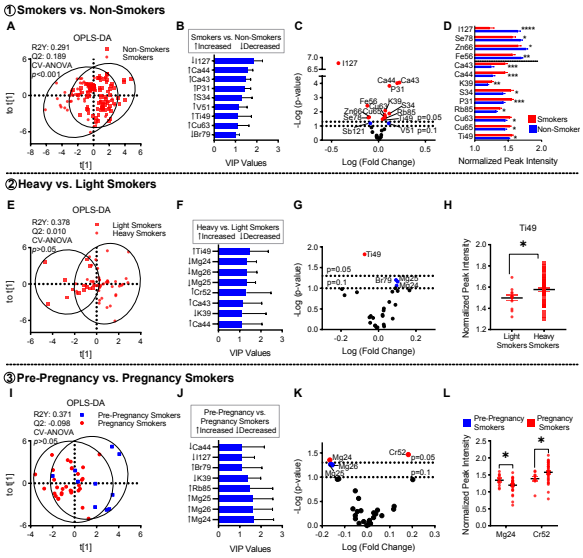


Figure 1. Pre-pregnancy and pregnancy smoking leads to altered metallomic profiles. The first row depicts smokers vs. non-smokers, the second row depicts heavy vs. light smokers, and the third row depicts heavy pre-pregnancy vs. heavy pregnancy smokers.

The Use of Electromyography as a Novel Assessment Tool in Multiple Sclerosis

Le K[1], Orton SM[1], Jarvis SE[1], Asmussen MJ[1,2]
[1]Department of Biology, Mount Royal University [2]Faculty of Kinesiology, University of Calgary

Introduction

The foundation of clinical and research work in neurological diseases such as multiple sclerosis (MS) is highly dependent on accurate measurements of disability as it allows clinicians to effectively track recovery and disease progression. Recently, research in the fields of rehabilitation and diagnostics have tried to present the postural biomechanics of MS foot and ankle control and gait patterns. As new treatments and therapies are developed, the need for accessible and reliable tools to measure disease progression becomes increasingly important. The gold standard in strength testing is usually isokinetic dynamometry. Although this method is reliable, the machine is expensive, time consuming to use, and requires clinician attendance, making it impractical for routine and widespread use. More recently, a new device was developed to measure tibialis anterior (TA) force (Asmussen et al., 2020). This new device has been proven to be easy to use, reliable, and effective. Furthermore, muscle activity collected by electromyography (EMG) can provide an estimate of muscle strength and can be used to develop new techniques for tracking disease progression and effectiveness of treatment changes. Therefore, the purpose of this study is to determine whether combining these muscle testing data with EMG and new data processing techniques could improve how persons with MS (PwMS) track their disease progression.

Methods

The data for this project was collected in a local neurology clinic for a previous study by Asmussen et al. (2020) and was recorded from 20 PwMS (13 females and 7 males; age 50.8 ± 9.3 years; expanded disability status scale (EDSS) score of 3.8 ± 1.5 (mean ± SD)). Participants performed maximum dorsiflexion voluntary contractions while EMG was recorded from the TA. Data analysis and data processing was completed with a custom code written in the MATLAB program that altered the bandpass filter of the EMG signal. Specifically, the low pass filter was set to 500 Hz and the high pass filter was systematically altered from 10Hz to 450 Hz in 10 Hz increments to determine how it affected the relationship between EMG signal from the TA and dorsiflexion force.

Results

The values used to evaluate the effects of the different band pass filters were the correlation coefficient and the root mean square (RMS) difference. As the frequency of the high pass filter increased, the correlation coefficient between force and EMG increase while the RMS difference decreased (see Figure 1).

Conclusions

High pass filtering indicates and improvement in the relationship between dorsiflexion force of the TA and EMG in PwMS. These findings suggest that the filtering techniques proposed in this study can be used with muscle function tests and other technologies to help PwMS track their disease routinely and remotely.

References

Asmussen MJ et al., (2020). Multiple Sclerosis and Related Disorders, 40, 101940.

Figures

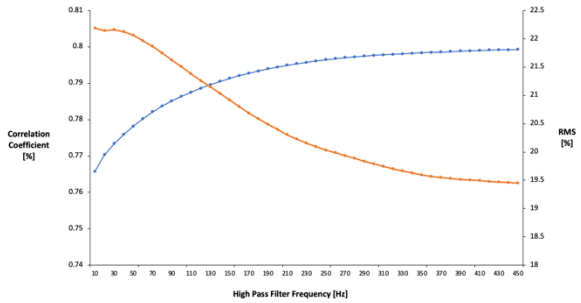


Figure 1. Correlation coefficient (blue) and RMS (orange) of EMG and force from increases in the high pass filter frequency from 10 Hz to 450 Hz. As the frequency of the high pass filter increases, the relationship between muscle EMG and muscle force estimate of the TA improves.

Development of a Remote Health and Activity Monitoring Assessment Tool with Ultra-Wide-Band Tracking

Linna Qian, Dr. Andrew Chan, Dr. Adriana Rios-Rincon, Dr. Geoff Gregson, Dr. Michael Lipsett
Glenrose Rehabilitation Research, Innovation and Technology, University of Alberta

Introduction

With a growing older adult (65+) population, demand for long-term care is projected to increase at a yearly rate of 2.7% [1]. Implementing indoor positioning allows functional mobility and activities of daily living (ADLs) to be monitored in patients with cognitive disabilities or frailty to promote a safer homecare environment [2]. This project's objective is to determine whether ultra-wide-band (UWB) positioning is sufficiently accurate to localize a user in-home (purported 10-20cm accuracy) to label ADLs.

Methods

The accuracy of the UWB system was evaluated in two assessments. First, A UWB tracker was placed at 32 points in a motion capture space and accuracy of the tracker was compared to motion capture (mo-cap) as a gold standard. (Fig. 1) Second, the UWB tracker was placed at 17 points of interest in a mock condo and error was calculated relative to positions that were manually measured positions using a laser measure (Fig 2). For each point, three randomized, static measurements were collected. The effect of anchor height and line-of-sight were also evaluated.

Results

UWB localization had an average absolute error of 6.12 ± 6.17 cm in x-direction and 5.11 ± 6.93 cm in the y-direction compared to the motion capture standard. In the condo, UWB had an average absolute error of 4.20 ± 27.5 cm in x-direction and 9.59 ± 19.0 cm in the y-direction compared to the laser measured standard. Reduced anchor height (<0.5m from the floor) and metallic line-of-sight barriers reduced accuracy by 2cm and 1.2cm respectively.

Conclusions

Despite UWB tracking precision being reduced in the smart condo, likely due to walls and obstructions, it remains adequate for furniture-scale positioning. Anchor placement and metallic barriers do not significantly affect position accuracy. Future work must be completed to evaluate the system dynamically, identify transfers and ADLs and assess gait.

References

[1] "Meeting the Demand for Long-Term Care in Canada.' [Online]. Available: www.cma.ca/sites/default/files/2018-11/9228_Meeting%20the%20Demand%20for%20Long-Term%20Care%20Beds_RPT.pdf.

[2] L. Brims and K. Oliver, "Effectiveness of assistive technology in improving the safety of people with dementia: a systematic review and meta-analysis," *Aging & Mental Health*, vol. 23, no. 8, pp. 942–951, Apr. 2018.

Figures

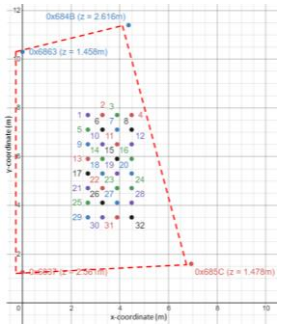


Figure 1. UWB setup in the mo-cap test space.



Figure 2. UWB setup in smart condo

Decision Support Using Accelerometry and Machine Learning

Mackenzie Wallich
Biometric Technologies Laboratory, Schulich School of Engineering, University of Calgary

Introduction

Accelerometry has been extensively studied as an objective means of measuring upper limb function in patient's post-stroke. With the recent advancements in machine learning, novel investigations have included the use of long-term accelerometry data collection and machine learning algorithms to detect upper limb weakness quickly and accurately. The objective of this research is to determine whether the accelerometry-derived measurements frequently used in more long-term rehabilitation studies can also be used to monitor and rapidly detect sudden changes in upper limb motor function in more recently hospitalized stroke patients

Methods

In this study, a literature review was conducted to explore clinical and accelerometry-derived measurements in relation to visual characterizations of upper limb motor function post-stroke. The literature showed that the accelerometry measurements and visualizations that provided the most valuable information about a patient's state within the first few months post-stroke appeared to be hours of paretic and non-paretic limb use, use ratio, median paretic limb acceleration, and paretic limb acceleration variability. Other seemingly effective measurements were the magnitude ratio and bilateral magnitude.

Potentially useful visualizations were explored using an open-source dataset [1] and replicating the preprocessing steps with Python's matplotlib module.

Six binary classification models were created by training on variable data window times of paretic upper limb accelerometer feature data. The models were assessed on their abilities to classify new input data into two classes: severe or moderately severe motor function.

Results

Four preliminary visualizations were proposed to provide health professionals with information that characterizes a patient's duration, intensity, symmetry, and variability of upper limb activity.

The classification models yielded Area Under the Curve (AUC) scores that ranged from 0.72 to 0.82 for 15-minute data windows to 0.77 to 0.94 for 120-minute data windows. The closer the AUC score is to 1, the better the model is at distinguishing between classes.

Conclusions

These results served as a preliminary assessment and a basis on which to further investigate the efficacy of using accelerometry and machine learning to alert healthcare professionals to rapid changes in motor function in the days immediately following a stroke.

References

[1] C. Lang et al. "Upper Limb Performance in Daily Life Approaches Plateau Around Three to Six Weeks Post-Stroke." *Neurorehabilitation and Neural Repair*, vol. 35, no. 10, 2021, pp. 903–14

Figures

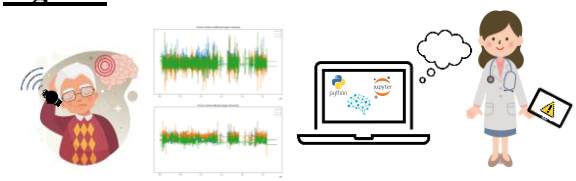


Figure 1. 1) The raw accelerometer data is collected by wireless accelerometers worn on the wrists. 2) Differences in the accelerations between the two arms can be visualized. 3) The data is processed using Python and Machine Learning. 4) The healthcare professional is alerted if abnormalities are detected.

I would like to thank my supervisor Dr. Svetlana Yanushkevich and the Program for Undergraduate Research Experience for supporting my research this summer.

Investigating the Use of PCU as a Talus Bone Implant Coating

Maha Ead[1], Tao Liu[1], Isaiah Wong[1], Nadr Jomha[2], Kajsa Duke[1], and Lindsey Westover[1]
[1]Department of Mechanical Engineering and [2]Department of Surgery, University of Alberta, Canada

Introduction

The talus bone in the human ankle joint has a limited blood supply, making it vulnerable to osteonecrosis when injured or fractured which can lead to severe ankle pain [1]. Talar replacement is a surgical procedure where the talus bone is replaced with an artificial prosthesis which can preserve ankle functionality and reduce pain [2]. Metal-based implants are commonly used as they demonstrate good biocompatibility. However, they may lead to joint degeneration due to excessive wear [3].

To represent a better physiological joint environment, researchers have utilized polycarbonate-urethane (PCU) as an artificial material that can function as cartilage in the knee and hip joints and have reported good outcomes [4,5]. Utilizing PCU in the ankle joint has not yet been investigated and therefore, the current study aims to explore this. Coating talus implants with a layer of PCU to act as cartilage can potentially reduce the likelihood of wear in the ankle joint. The first phase of this project involves designing an interface for the PCU to attach to the implant.

Methods

A lattice structural interface with two different designs and two cell sizes was modelled using nTopology® software. These four lattice models were metal 3D printed in the shape of disks with a 4 mm solid stainless steel layer and a 2 mm lattice stainless steel layer (Figure 1). Since injection molding will be used to add the PCU layer, a custom mold was designed to hold the lattice disks and inject PCU (Bionate® II 80A – DSM Biomedical, Pennsylvania, USA) on top such that it creates a 2 mm layer of solid PCU (Figure 1). The hypothesis is that the high pressure will force the PCU to flow through the lattice and act as a bonding layer between the disk (implant) and the layer of solid PCU used as a cartilage substitute. In order to quantifiably compare the four lattice disks as bonding interfaces for the PCU layer, the volume of PCU that flowed through the lattices will be determined by scanning the disks with a 3D X-ray microscope. The 3D models produced will then be exported to an image processing software (ORS Dragonfly®) where the volume of voids and PCU can be extracted.

Results

The adherence of PCU to the samples was manually inspected by attempting to detach the PCU layer and it appeared to be strongly bonded to the metal. Preliminary scans were performed on a sample plastic lattice disk coated with PCU. Results indicated that the 2 mm lattice layer embedded with PCU consisted of: 26% plastic lattice, 28% voids, and 46% PCU.

Conclusions

A smaller volume of voids in the lattice layer is more desirable as the solid PCU layer will more likely adhere to the implant. The next stage of the project will involve wear testing the PCU against articular cartilage. Shear tests will also be conducted to mechanically quantify the strength of the lattice designs as bonding layers for PCU.

References

[1] Delanois, R E et al., *J Bone Jt Surg*, 80:529–36, 1998.
[2] Taniguchi, A et al., *J Bone Jt Surg - Am Vol*, 97:1348–1353, 2015.
[3] Hussein, M A et al., *Materials*vol. 82749–2768, 2015.
[4] Alley, R et al., *Orthop J Sport Med*, 8:2020.
[5] Lazic, S et al., *HIP Int*, 30:303–308, 2020.

Figures

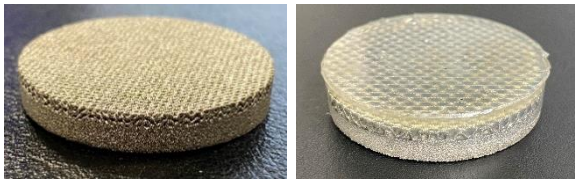


Figure 1: Diamond shaped lattice disk before and after coating.

The impact of data normalization and plane view in deep learning methods for classifying disease subtypes in multiple sclerosis using brain magnetic resonance imaging scans

Mahshid Soleymani[a], Mariana Pinheiro Bento[a], Yunyan Zhang[b]
[a]Department of Biomedical Engineering, University of Calgary, AB, Canada; [d]Department of Radiology and Clinical Neurosciences, University of Calgary, Calgary, AB, Canada

Introduction

Multiple sclerosis (MS) is a chronic inflammatory demyelinating and neurodegenerative disease of the central nervous system (CNS) that affects 115,000 Canadians. Most people start with a relapsing-remitting course (RRMS). However, without appropriate treatment, more than 50% of RRMS patients worsen to a secondary progressive phenotype (SPMS)[1]. Despite the number of disease-modifying therapies available for RRMS, there is no effective treatment for SPMS. Therefore, developing methods that classify disease states for early treatment of high-risk RRMS patients is critical[2]. Artificial intelligence technologies have shown the strong potential in this regard, especially with an optimized preprocessing pipeline. Our aim was to develop a 2D convolutional neural network (CNN)[3] model to distinguish RRMS and SPMS using brain magnetic resonance imaging (MRI) scans.

Methods

The dataset contains brain MRI from 19 MS patients (10 RRMS, and 9 SPMS). Each scan included T1-weighted, T2-weighted, and fluid-attenuated inversion recovery (FLAIR) images. A VGG19[4] CNN model was used through transfer learning with pre-trained weights initialized. The tests started with axial images to find the best model hyperparameters. Afterwards, we tested other common plane views (sagittal and coronal) and their combinations. We also investigated different data normalization methods, including min-max, z-score and both, in our preprocessing pipeline to understand their influence on the results.

Results

Best results were acquired when using the z-score method to normalize the data and using sagittal and coronal views. The best performance achieved an average 81% accuracy in validation (fig.1). The associated hyperparameters were batch size = 30, dense unit = 256, dropout t = 0.2, learning rate = 0.001, and number of trainable layers = 1, 30 epochs.

Conclusions

In contrast to the current intensively used min-max normalization method, our study showed that z-score normalization enabled the best classification results using the VGG19 model. Further, most of the studies in this field using 2D CNN rely on the axial view of MRI scans. Our study is unique by taking advantage of the other views, sagittal and coronal, which are almost always advantageous in improving the CNN performance in the current experiments.

References

[1] Gross, H. J. and Watson, C., "Characteristics, burden of illness, and physical functioning of patients with relapsing-remitting and secondary progressive multiple sclerosis: a cross-sectional US survey," Neuropsychiatr. Dis. Treat. **13**, 1349–1357 (2017).

[2] Dobson, R. and Giovannoni, G., "Multiple sclerosis – a review," Eur. J. Neurol. **26**(1), 27–40 (2019).

[3] O'Shea, K. and Nash, R., "An Introduction to Convolutional Neural Networks," ArXiv151108458 Cs (2015).

[4] Simonyan, K. and Zisserman, A., "Very Deep Convolutional Networks for Large-Scale Image Recognition," ArXiv14091556 Cs (2015).

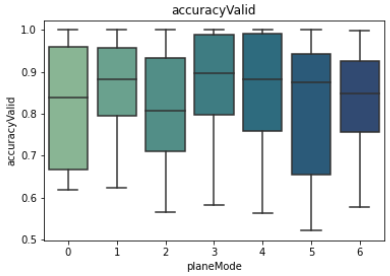


Figure 1- VGG19 validation accuracy with z-score normalized input had the best performance among the three normalization methods. Plane modes 0-2 each contain an individual plane view, 3-5 contain pairs of plane views and 6 contains all three plane views.

Investigation of axial rigidity of Kevlar® tubular braided composites for cardiovascular catheter application

Mairi Boucher Hoglin, Ahmed Samir Ead, Jason P. Carey
University of Alberta

Introduction

Cardiovascular catheterization is a common medical procedure used to diagnose and treat several conditions. Catheterization, however, is tedious and involves multiple steps, making it uncomfortable for patients and more complex for clinicians. One potential way to reduce the number of steps in the catheterization process is to replace the current catheter-guidewire system with a Tubular Braided Composite (TBC). TBCs are composite materials that are manufactured by interlacing fiber yarns around a mandrel through a technique called braiding to create a tubular preform, which is then impregnated with a polymeric matrix. One benefit of braiding is the easy tailorability of their mechanical properties through modification of the braid angle. Braid angle is defined as the angle between the longitudinal axis of the TBC and the orientation of its fibers. If a TBC is manufactured with sufficient axial rigidity (EA) to navigate blood vessels, it could replace the typical catheter-guidewire system, greatly simplifying the cardiovascular catheterization process.

Methods

In this study, TBC catheters were manufactured at three different braid angles (15°, 20°, and 30°) using Kevlar® 49 fibers. They were then cured using two different resins: NR-906 polyurethane or Epon 826 Epoxy. Figure 1 shows a sample Kevlar®-polyurethane TBC manufactured for this study. Sample lengths, diameters, and braid angles were measured and recorded. Tensile testing was conducted on each sample following ASTM Standard D3039 to determine the elastic modulus (E) of each sample[1]. Using sample cross-sectional dimensions and E, EA was calculated.

Results

According to literature, if a catheter has an EA value of greater than or equal to 450N, it has the axial rigidity needed for the cardiovascular catheterization process [2]. Results from this study showed that Kevlar® polyurethane and Kevlar® epoxy TBCs between the braid angles of 15 and 30 degrees had an EA above 450N.

Conclusions

Due to the difficult cardiovascular catheterization process, there is a need to redesign catheters. Using the combinations of fiber and resins manufactured and tested in this work, it was concluded that the TBC catheters have the axial rigidity needed for cardiovascular catheter applications. This experimental data expands upon the existing analytical data obtained by Carey [2]. Future work includes investigating the flexural and torsional rigidities of these TBCs for the cardiovascular catheterization process. Ultimately, this study was a step towards introducing TBCs into the catheterization process, improving the procedure for both patients and clinicians.

References

[1] ASTM International, “Standard Test Method for Tensile Properties of Polymer Matrix Composite Materials,” D3039/D3039M-17, Dec. 11, 2017 doi: 10.1520/D3039_D3039M-17.

[2] J. Carey, A. Fahim, and M. Munro, “Design of braided composite cardiovascular catheters based on required axial, flexural, and torsional rigidities,” *Journal of Biomedical Materials Research - Part B Applied Biomaterials*, vol. 70, no. 1, pp. 73–81, Jul. 2004, doi: 10.1002/JBM.B.30017.

Figures



Figure 1 - Sample manufactured TBC

A Machine Learning Study on Rural-Urban Differences Among Older Drivers

Maria Law, Sayeh Bayat
Departments of Geomatics and Biomedical Engineering, Schulich School of Engineering, University of Calgary

Introduction

Rural-urban differences in driving have been previously examined, but without focus on individuals' naturalistic driving behaviours [1-3]. The purpose of this project was to investigate how well machine learning (ML) models can discriminate between rural and urban drivers based on their driving data. This would provide insight into whether inclusion of urban/rural residency in driving-based ML models, such as one predicting presence of pre-Alzheimer's disease [4], may improve their accuracy and interpretability.

Methods

Naturalistic driving data was obtained by in-vehicle data loggers for a cohort of older adults (n_{rural} = 8, n_{urban} = 239) and consolidated into a summary dataset with 38 driving features. The data was also used to determine home location and corresponding rural-urban encoding (based on five classification systems) for each participant.

Four ML models (standard balanced random forest and SMOTE-enhanced logistic regression, XGBoost, and random forest) were built from four driving predictors, using SMOTE oversampling or balanced class-weights to combat class imbalance.

Results

Important driving behaviours include: total days in study, distance travelled, weekday to weekend ratio, and minimum speed.

Model metrics are reported in the table. All models had area under the curve (roc_auc) scores above 0.90, with the best model (SMOTE-logistic regression) achieving an roc_auc score of 0.96.

Conclusions

The findings indicate that, as expected, location of residence may be important to consider when using driving behaviours as an ML predictor.

One limitation of this study is potential overfitting of models, since feature selection and hyperparameter tuning used the entire dataset. Future work should include more data and adjust for confounding factors.

References

[1] Q. Wu, G. Zhang, X. Zhu, X. C. Liu, and R. Tarefder, "Analysis of driver injury severity in single-vehicle crashes on rural and urban roadways," Accident Analysis & Prevention, vol. 94, pp. 35–45, Sep. 2016.
[2] R. Payyanadan, J. Lee, and L. Grepo, "Challenges for Older Drivers in Urban, Suburban, and Rural Settings," Geriatrics, vol. 3, no. 2, p. 14, Jun. 2018.
[3] L. F. Beck, J. Downs, M. R. Stevens, and E. K. Sauber-Schatz, "Rural and Urban Differences in Passenger-Vehicle– Occupant Deaths and Seat Belt Use Among Adults — United States, 2014," MMWR. Surveillance Summaries, vol. 66, no. 17, pp. 1–13, Sep. 2017.
[4] S. Bayat et al., "GPS driving: A digital biomarker for preclinical Alzheimer disease," Alzheimer's Research & Therapy, vol. 13, no. 1, p. 115, Jun. 2021.

Figures

Table: Cross-validated test scores (mean and standard deviation) for each model

	SMOTE-logistic regression		SMOTE-XGBoost		SMOTE-random forest		Standard balanced random forest	
	Mean	***SD***	***Mean***	***SD***	***Mean***	***SD***	***Mean***	***SD***
Accuracy	0.922764	0.267509	0.947154	0.224181	0.943089	0.232144	0.955285	0.207100
Roc_auc	0.962677	0.034926	0.902835	0.190239	0.909223	0.115818	0.932334	0.099282
Precision	0.275655	0.134428	0.296667	0.190536	0.295833	0.226973	0.329167	0.265561
Recall	0.800000	0.299122	0.525000	0.343166	0.425000	0.335410	0.400000	0.307794
Balanced accuracy*	0.861801	0.14475	0.742782	0.171482	0.696561	0.170777	0.688270	0.307794

***mean of recall for each class

in vivo changes in articular cartilage and meniscus UTE-T2* with load in osteoarthritis

Masoomikhanghah, M[1], Cui, L[3], McWalter, EJ[1,2]

[1]Division of Biomedical Engineering and [2]Department of Mechanical Engineering, University of Saskatchewan; [3]Siemens Healthineers

Introduction

Articular cartilage and meniscus are two important tissues in the knee joint that provide a load-bearing function. In joint diseases such as osteoarthritis (OA), the extracellular matrix degrades, compromising the tissues' response to load[1]. Quantitative magnetic resonance imaging (qMRI) metrics such as T2* relaxation time can detect early tissue changes with OA and load[2,3]. However, the deep layer of cartilage and meniscus have limited to no signal on conventional MRI images due to their short T2 relaxation times, making qMRI challenging. Our group has developed a flexible ultrashort time to echo (FUSE) sequence[4] which allows T2* mapping of these tissues. The aim of this study is to assess changes in T2* relaxation time of knee cartilage and meniscus in response to *in vivo* loading in OA.

Methods

The dominant knee of healthy participants (n=15) and the affected knee of OA patients (n=15) will be scanned at 3T (Siemens Healthcare) in loaded and unloaded conditions. A custom-made, MRI-compatible device will be used to apply a load to the knee joint. A series of conventional MR images will be acquired in an unloaded condition to determine the MRI Osteoarthritis Knee Score (MOAKS) score[5]. Unloaded and loaded images will be acquired with FUSE for T2* relaxation time mapping (echo times between 0.6 to 40 ms). The FUSE scan parameters will be optimized through a pilot study by calculating signal to noise ratio (SNR), contrast to noise ratio (CNR), and T2* of cartilage and meniscus. For data analysis, tibial and femoral cartilage and meniscus will be segmented manually using packaged software (Analyze 14.O, Analyze Direct Inc, Overland Park, KS, USA). T2* relaxation time maps will be created using a mono-exponential fit. T2* relaxation time data will be used to calculate various outcome measures, namely regional averages, focal regions of change (clusters) in cartilage, and depth-dependent measures. For the regional analysis, average T2* will be calculated in tibial and femoral cartilage (medial, lateral, inside and outside loaded contact area), medial and lateral meniscus (body, posterior and anterior horns). Focal changes in cartilage T2* will be evaluated using a cluster approach. Briefly, projection maps will be created for both the unloaded and loaded cartilage; the unloaded and loaded projection maps will be registered; difference maps will be generated by subtracting the loaded map from unload map; clusters of increased and decreased T2* will be identified according to established size and intensity thresholds[6,7]. A Wilcoxon signed-rank test will be used to assess differences between groups. Spearman's rho correlation coefficients will be used to assess correlation between MOAKS score and T2*.

Results

Currently, we are developing methodology and will begin data collection soon.

Conclusions

We expect T2* relaxation time will be higher in individuals with OA but decrease in loaded regions in both groups. We also expect that the cluster approach will provide additional information about location and patterns of water redistribution in degenerated cartilage with load, as compared to conventional regional approaches which may not detect focal changes.

References

1 Fukubayashi, T. *et al. Acta Orthopaedica Scandinavica* 51, 871–879 (1980). **2** Williams, A. *et al. Osteoarthritis and Cartilage* 20, 486–494 (2012). **3** Nishii, T. *et al. Journal of Magnetic Resonance Imaging* 28, 175–180 (2008). **4** Lumeng Cui. (University of Saskatchewan, 2022). **5** Hunter, D. J. *et al. Osteoarthritis and Cartilage* 19, 990–1002 (2011). **6** Sofko, K. *et al.* (ISMRM, 2022). **7** Black, M. S. (Stanford University, 2019)

Fluid shear stress and involution: Implications for postpartum breast cancer

Maya Stibbards-Lyle[1], Kristina Rinker[2,3]
[1]Biomedical Engineering Graduate Program, University of Calgary [2] Department of Biomedical Engineering, University of Calgary [3]Arnie Charbonneau Cancer Institute, University of Calgary

Introduction

Patients under 50 account for 18% of all cases of breast cancer, the most diagnosed cancer[1]. Furthermore, new mothers that develop breast cancer are at a doubled risk of metastatic, deadly cancer, as compared to other young women with breast cancer[2]. Recent research has suggested that these poor outcomes may be due to involution, a remodeling process that occurs after nursing ends to return the breast to a pre-pregnancy state[3]. Once the flow of milk stops, a series of events occurs to breakdown structures involved in lactation and carry away debris. Our group has shown that fluid shear stress (FSS) affects cellular processes involved in tissue remodeling and cancer progression including epithelial-to-mesenchymal transition[4]. How shear stress is involved in modulating involution and breast cancer development is not understood.

We hypothesize that FSS is a key regulator of involution and plays an important role in the breast cancer progression in new mothers. Key activities involved in involution – such as inflammation, tissue remodeling, and lymphangiogenesis – have independently been linked to FSS. Specifically, these processes engage in bidirectional regulation with FSS, and can enter dysregulated feedback loops[5,6]. Cell culture models of lactation and involution will be developed and used in combination with molecular database mining and bioinformatics to identify mechanisms involved in FSS modulation of involution. This may allow for identification of important biomarkers for detection and treatment of breast cancer in young women.

Methods

Mice transcriptomics data from Bach et al. (2017) and Kunnen et al. (2018) were compared to identify common targets between involution and shear stress conditions, respectively. Genes with >2-fold ($p<0.01$) changes between the control and experimental conditions for each study were identified and ranked. A protocol using a parallel plate flow chamber, as previously described[7], was developed to mimic the fluid mechanics during lactation and involution. MDA-MB-231 breast cancer cells were exposed to 20h of 1 Pa pulsatile, lactational flow, followed by a brief period of very low flow (0.01 Pa) mimicking weaning, followed by 3 hours of moderate (0.5 Pa) non-pulsatile flow mimicking interstitial flow present during remodeling. At each timepoint, the health of the cells was evaluated by phase contrast microscopy, then supernatant and cells were collected for molecular analysis. The levels of markers of interest at each time point were evaluated using western blot according to the manufacturer's protocol.

Results

Of the ~1500 genes in each dataset, 267 genes were present in both FSS and involution conditions. Relevant markers observed to be upregulated in both involution and under FSS include LCN2, CLDN4, and SPP1. Other targets were identified, including several targets from the matrix metalloproteinase family (MMPs) and drivers of lymphangiogenesis, which are involved in tissue remodeling and are upregulated when exposed to shear stress. While testing the developmental protocol, we identified the minimum flow rate required to deliver nutrients and maintain healthy cells, while still approximating the low-flow conditions when an infant begins weaning and milk flow ceases.

Conclusions

Early investigation suggests that involution and fluid shear stress share many pathways, and that this novel experimental protocol will help clarify the role that these processes play in breast cancer in new mothers.

References

[1] Ademuyiwa et al. (2016) *Breast Cancer* **[2]** Goddard et al. (2019) *JAMA Netw. Open.* **[3]** Borges et al. (2020) *Cancer Res.* **[4]** Fuh et al. (2021) *Breast Cancer Res.* **[5]** Vaahtomeri et al. (2017) *Genes Dev.* **[5]** Zakkar et al. (2016) *Curr Vasc Pharmacol.* **[6]** **S**hepherd et al. (2011) *Am J Physiol Heart Circ Physiol.*

Analyzing Gait Adaptations to Surgically Induced Fractures in Young and Old Mice

Neashan Mathavan[1], Cael McLennan[1], Dilara Yilmaz[1], Gisela Kuhn[1], Esther Wehrle[1]*, Ralph Müller[1]*

[1] Institute for Biomechanics, ETH Zurich, Zurich, Switzerland. * *Equal contribution*

Introduction

Gait parameters and associated functional outcomes are influenced by age-related declines in motor function.[1] Understanding how age affects gait patterns following physical trauma is not well understood. Our aim is to explore the relationship between age and relevant gait parameters following surgically induced femoral osteotomy in PolgA mice - a mouse model of premature aging.[2]

Methods

Pre- and post-surgical gait data was collected using the CatWalk XT system (Noldus, Wageningen, The Netherlands) for 11 young (12 weeks) and 15 old (35 weeks) female PolgA mice at two time points: pre-surgery and 1-week post-surgery (license: ZH229/19). Individual runs were included based on speed ($\leq$ 50 cm/s) and number of steps ($n \geq 10$). Manual correction of footprint bounding boxes was necessary to ensure accurate results.[3] Excluding non-compliant runs, a total of 112 young mice runs and 147 old mice runs were processed. The following parameters were evaluated: Run Speed, Stand, Duty Cycle, Stride Length, and Swing Speed. In addition, post-surgical parameters were normalized to their baseline counterparts to observe relative changes.

Results

Body weight was significantly different between young (19.6 ± 1.13g) and old (22.8 ± 1.29g) mice. Average running speeds in pre-surgical mice were significantly higher for young mice (31.5 ± 3.75 cm/s) compared to old (23.7 ± 1.95 cm/s). This observation was also present post-surgically. Stand duration in the fractured right hind limb (RH) was significantly higher in old mice (Pre: 0.158 ± 0.0179ms; Post: 0.145 ± 0.0657s) than young mice (Pre: 0.133 ± 0.0118s; Post: 0.0762 ± 0.0292s). Post-surgically, stand duration only decreased significantly in young mice (Fig. 1A). Swing speed in RH was significantly lower post-surgically in both age groups (Fig. 1C). Moreover, swing speed was significantly lower in old mice compared to young mice at both time-points (Fig. 1C). Duty cycle in RH was significantly lower post-surgically in both age groups (Fig. 1E). Significant differences of $p \approx 0.03$ and non-significant differences were observed within the normalized values (Fig. 1BDFH).

Discussion and Conclusions

Consistent with a decline in motor function, old PolgA mice were found to run slower with longer stand duration and slower swing speed both pre- and post-surgically, with greater variability post-surgery. Comparing normalized data, it becomes apparent that gait adaptations post-fracture are remarkably consistent across young and old mice. Despite a loss of muscle control with age, these mice appear to retain their ability to adapt to physical trauma.

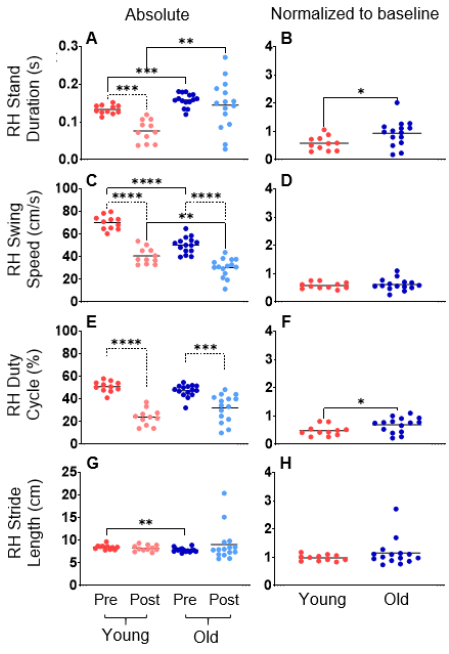


Fig 1. Average and relative mouse gait parameters. Statistics: Based on tests for normal distribution, Young vs. Old comparisons were performed using two-tailed t-test or Mann–Whitney U-test. Pre- vs. Post-surgery comparisons using paired t-test or Wilcoxon matched-pairs signed rank test.

References

[1] Broom et al. Front. Aging Neurosci. 2021.
[2] Mathavan et al. J. Bone Miner. Res. 2021.
[3] Chen et al. Journal of Neurosci. Methods 2017.

Sex estimation by linear classification of statistical shape models (hemipelvis and talus)

Mehrdad Palizi[1], Lindsey Westover[2], and Samer Adeeb[1]
[1] Department of Civil and Environmental Engineering, University of Alberta, Edmonton, Alberta, Canada
[2] Department of Mechanical Engineering, University of Alberta, Edmonton, Alberta, Canada

Introduction

Statistical shape models (SSMs) are powerful tools to parameterize and analyze the complex geometry of anatomical shapes. SSMs have successfully quantified the geometrical variations on bone structures and soft tissues [1]. However, the morphological studies on sexual dimorphism of anatomical shapes are mainly limited to discrete measurements of landmarks and not the entire geometry, e.g. see [2] for the pelvis. The current study aimed to investigate the potential of SSMs to classify anatomical shapes based on sex for the hemipelvis and the talus.

Methods

The study used the segmented computed tomography image data sets for the pelvis (20 male and 20 female left-right hipbones, overall 80 hemipelves) and the talus (41 female and 55 male samples). The original triangle meshes are refined by screened Poisson surface reconstruction and Taubin smoothing [3]. To find correspondence, 5,000 points are sampled from each refined mesh. The point sets are coarsely aligned with respect to translation, rotation, and scaling [3]. A normalized sample is considered as the *template*; using coherent point drift method [3], the template is deformed to capture the sample shapes, called *deformed templates*. The rigid transformation between the deformed templates is discarded by generalized Procrustes analysis [3]. Principal component analysis (PCA) is employed on the spatial coordinates of the deformed templates to build SSMs [4].

Four SSMs are built based on the morphology (hemipelvis or talus) and considering/ignoring the actual scale of samples (form/form-size). Each SSM constitutes an average configuration and a set of deformation modes called principal components (PCs, ordered based on modal contribution). The PC weights are computed for each sample. Using a one-dimensional classification criterion, the individual PCs with minimum male/female misclassification are detected and visualized for each morphology. Fisher linear discriminant analysis [4] is employed on the space of PC weights (called *feature space*) to find male/female splitting direction. The dimension of the feature space is determined by the number of included PCs. Lastly, the capability of the SSM-based classifiers to predict new samples' sex, called *sex-estimation ability*, is evaluated by a series of leave-one-out experiments. The left-right hemipelves of individual samples are removed simultaneously.

Results

Our results show that (i) the PCs with minimum misclassification for the hemipelvis and the talus are, respectively, the second form PC and the first form-size PC (3 misclassifications for 80 hemipelves and 13 for 96 tali, Fig. 1a-b); (ii) the feature space of the first 10 PCs is sufficient for the hemipelvic SSMs to split the male/female data sets by Fisher discriminant, while the majority of the PCs must be included for the talus models (81/85 for the talus form/form-size out of 95 PCs); (iii) based on the leave-one-out tests, the highest sex-prediction ability belongs to the hemipelvic form SSM with only 2.5% misclassified samples for the cumulative modal variance of 85% and the misclassification percent is higher for the talus SSMs (Fig. 1c).

Conclusions

The pelvis is a highly dimorphic region of the human body [2]. The current study developed a linear SSM-based male/female classifier and demonstrated that the developed classifier has a higher sex-estimation ability for a hemipelvic data set, compared with a data set of the talus.

References

[1] Sarkalkan, N., et al. (2014). Statistical shape and appearance models of bones. *Bone*, *60*, 129-140.
[2] Bruzek, J. (2002). A method for visual determination of sex, using the human hip bone. *American Journal of Physical Anthropology*, *117*(2), 157-168.
[3] Laga, H., et al. (2018). *3D Shape analysis: fundamentals, theory, and applications*. John Wiley & Sons.
[4] Bishop, C. M., & Nasrabadi, N. M. (2006). *Pattern recognition and machine learning* (Vol. 4, No. 4, p. 738). New York: springer.

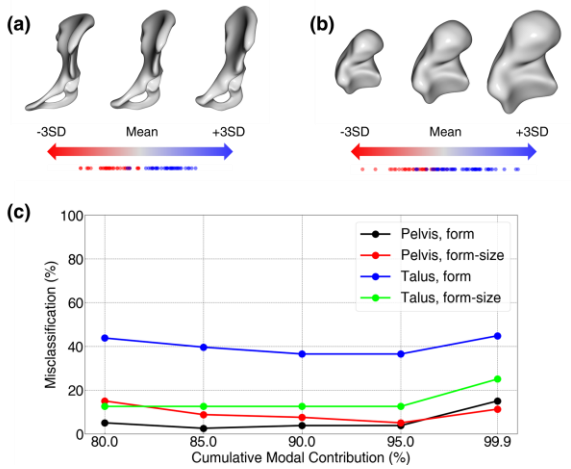


Figure 1. PC visualization and male/female weight distribution (female, red & male, blue) for the second PC of the hemipelvic form SSM **(a)** and the first PC of the talus form-size SSM **(b)**. Sex-estimation ability of the SSMs **(c)**.

A biomechanical comparison of two modern suture techniques for arthroscopic rotator cuff repair: Suture Bridge versus Modern Ripstop

Michael Thatcher BSc.[1], James D. Johnston PhD P.Eng.[2], Jeremy Reed MD FRCSC[1]
[1] College of Medicine, University of Saskatchewan, Saskatoon, SK, Canada
[2] Mechanical Engineering Department, University of Saskatchewan, Saskatoon, SK, Canada

Introduction

The coalescence of the 4-rotator cuff tendons of the human shoulder serve to provide motive power to the arm and are an important contributor to the stability of the glenohumeral joint. Injury to the rotator cuff results in pain, weakness, decreased function and, most importantly, quality of life. Surgical treatment for a torn rotator cuff is becoming the standard of care, as they are known to progress in size and eventually lead to irreversible loss of function of the associated muscles in the form of fatty atrophy.

The integrity of the employed rotator cuff repair (RCR) is paramount. Repair failure can be near catastrophic, and a stronger repair allows the clinician to permit their patient earlier range of motion and rehabilitation, which in turn limits stiffness and pain. There is uncertainty, however, regarding the optimal suture pattern used during arthroscopic RCR of the human shoulder.[3,4] The most prominent mode of RCR failure in recent years is breakdown at the suture-tendon interface.[5] The suture pattern used by the surgeon may mitigate the risk of suture-tendon interface failure.

One method is the "Suture Bridge", a commonly accepted double-row, 4 anchor, suture pattern.[6] A more recent technique, referred to as the "Modern Ripstop", is a double-row, 4 anchor Mason-Allen stitch pattern through cuff tendon combined with a suture-bridge.

The objective of this research is to compare the mechanical strength of these different suture patterns.

Methods

Specimens: 18 swine shoulders (right and left shoulders from 9 specimens, humerus included) from local supplier.

Mechanical Testing: Shoulders will be dissected and mounted into a custom fixture in a material testing system (MTS Bionix). The infraspinatus tendon will be removed from its insertion on the humerus and resected back to an area of full thickness tendon to simulate tendon preparation during RCR. Half of the shoulders will be treated with the "Suture Bridge" technique while the contralateral shoulder will be treated with the "Modern Ripstop" approach. Elongation to failure will be performed at 3mm/s. Ultimate tensile failure load will be defined for each specimen.

Statistics: Paired t-tests will be used to compare failure loads with the different suture patterns.

Results

This work is currently ongoing. Mechanical testing fixtures are being constructed. Remaining research pertains to mechanical testing.

Anticipated Conclusions

We anticipate that the Modern Ripstop technique applied to infraspinatus tendons will allow the construct to withstand higher loads to failure compared to the current Suture Bridge technique. Ultimately, this research will improve knowledge of rotator cuff repair, and in turn, clinical care.

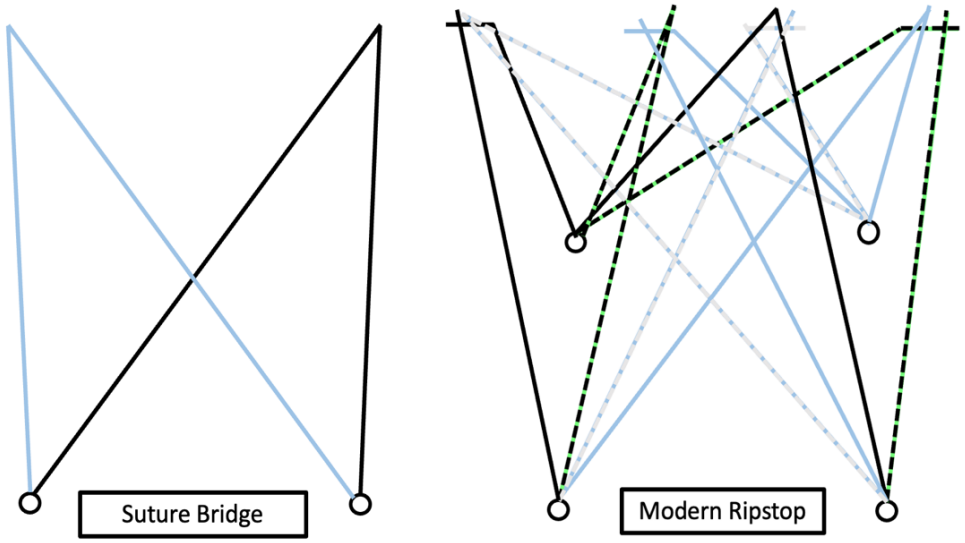


Figure 1 Comparison of suture patterns for rotator cuff repair.

References

1. Baker et al., 2003
2. Yamamoto et al., 2017
3. Thangarajah et al., 2021
4. Parada et al., 2015
5. Cummins et al., 2003
6. Jost et al., 2012

Development of a Brain Controlled Robot for Paralympic Sport

M. Kerr McNutt[1], D. Comaduran Marquez[1], I. Robu[1], E. Zewdie[1], E. Kinney-Lang[1], A. Kirton[1]
BCI4Kids Calgary, Department of Pediatrics, Cumming School of Medicine, University of Calgary

Introduction

Boccia is a Paralympic sport that has enabled athletes with mobility limitations to participate with a ramp and an assistant that adjusts the ramp following the athlete's instructions[1]. However, individuals who are unable to communicate with the assistant cannot participate. The project objective is to design a novel Boccia ramp capable of being controlled by a brain-computer interface (BCI). BCIs measure and translate brain signals into actions on a computer or electronic system, like the proposed ramp. BCI has never been used in sport before; implementing the proposed ramp will allow individuals with complex physical needs to access sports for the first time.

Methods

The novel BCI-enabled ramp was designed based on relevant properties identified in commercially available Boccia ramps. Insights on design were provided by expert Boccia coordinators with the final ramp design modified to accommodate motors. A digital model of the design was created using Fusion 360 (Fig. 1A). Stepper motors and linear actuators were picked to provide the required precision of movement and speed for real-time Boccia play. To build the prototype, custom parts were fabricated out of metal, wood, and PLA with a 3D printer (Fig. 1B). Materials were chosen to account for unique shape and strength requirements. An Arduino microcontroller receives commands from a graphical user interface built in Unity Game Engine. The BCI control mechanism is integrated with the interface through custom software packages. [2]

Results

A full-sized prototype of the mechanical design has been constructed. This prototype is capable of the expected motions and the components are structurally sound. Software wise, a connection between Unity and the Arduino Mega has been established and the linear actuators can be controlled through the connection. Additionally, the basic setup of the user interface has been developed. Visual based BCI paradigms are under investigation for use in the system, with speed of selection vs. accuracy as the key components we are looking to evaluate.

Conclusions

The next step is integrating all aspects of the prototype together and ensuring the systems function as a collective. From there future work includes testing the novel ramp with typically developing adults followed by testing it with children with complex physical disabilities. Everyone deserves the opportunity to play sports, this project could allow individuals with severe disabilities access to sports for the first time.

References

[1] "Boccia Canada." https://bocciacanada.ca/en/boccia/
[2] BCI4Kids, "BCIEssentials." Jun. 13, 2022. https://github.com/kirtonBCIlab/bci-essentials-unity

Figures



Figure 1A: Fusion 360 digital ramp design
Figure 1B: Constructed ramp prototype

Evaluating CNN with a cross-validation approach to classify adolescent idiopathic scoliosis (AIS) severity

Mostafa Hassan[1], Nada Mohamed[1], Qipei Mei[2], and Lindsey Westover[1]
[1] Department of Mechanical Engineering, University of Alberta, Edmonton, AB T6G 2G8, Canada
[2] Department of Civil and Environmental Engineering, University of Alberta, Edmonton, AB T6G 2E1, Canada

Introduction

AIS is a prevalent type of scoliosis, affecting 80% of structural scoliosis patients[1]. X-ray exposure during scoliosis management increases the risk of cancer later in life. Thus, our group has developed a markerless surface topography (ST) technique to quantify AIS and reduce the risk of x-ray radiation[2]. To get spine information from trunk ST, our group utilizes state-of-the-art artificial intelligence (AI) techniques on the ST scans, specifically, Convolutional neural networks (CNNs). CNNs have been used for the past five years to measure cobb angle on a 2-d x-ray radiograph; however, this is the first application to scoliosis-related ST scans. We use CNN to classify the severity of AIS (mild/moderate/severe) based on ST scans. One major challenge is the limited availability of data, which makes the CNN classification accuracy relatively low. Thus, we use the K-fold cross-validation technique to select the best training set out of the dataset for optimum performance.

Methods

521 ST scans on AIS patients (age 10-18 years) from clinics in Edmonton and Brazil were collected after excluding those with missing data for the classification model. Cobb angle was measured from an x-ray for these patients. Classification is based on the one with the max cobb angle for a particular patient visit. Moreover, Patients had not undergone surgical treatment. The CNN model consists of two convolutional layers, each followed by a max-pooling layer, and a dropout layer was added to avoid overfitting. Three classes are utilized to predict scoliosis severity as follows: Mild ($10 < \text{Cobb angle} < 25$), Moderate ($25 < \text{Cobb angle} < 40$), Severe ($40 < \text{Cobb angle}$). The collected data were processed into deviation maps between the original and reflected torso[2] and then converted to a two-channel pseudo image as an input to the CNN. Using Stratified K-Folds cross-validation, the dataset was split into ten folds, and then each of these was used as a validation set at once. Furthermore, the best-performing model was selected.

Results

The selected model achieves a training accuracy of 76.92%, and network performance in precision, specificity, and sensitivity are shown in Table 1. As we can see, the network has 100 % precision and specificity in predicting mild scoliosis. Moreover, it is 100% sensitive to the severe class.

Table 1: CNN Classification Results

		Actual			Precision
		Mild	Moderate	Severe	
Predicted	Mild	17	0	0	100 %
	Moderate	7	14	0	67 %
	Severe	3	2	9	64 %
Sensitivity		63 %	88 %	100 %	
Specificity		100%	81 %	88 %	

Conclusions

An ST-based CNN with a cross-validation approach shows promising results in predicting AIS severity. We suggest that the implantation of this approach may allow clinicians to reduce the reliance on x-rays for scoliosis monitoring.

References

1. Choudhry MN, Ahmad Z, Verma R. *Open Orthop J*. 2016;10(1):143-154. doi:10.2174/1874325001610010143
2. Komeili A, Westover LM, Parent EC, Moreau M, El-Rich M, Adeeb S. *Spine J*. 2014;14(6):973-983.e2. doi:10.1016/j.spinee.2013.09.032

High-Flow and Low-Flow Oxygen Delivery by Nasal Cannula Evaluated in Neonatal and Adult Airway Replicas

Mozhgan Sabz[1], Michelle Noga[2], Warren H. Finlay[1], Hossein Rouhani[1], Andrew R. Martin*[1]
*Correspondence: andrew.martin@ualberta.ca
[1]Department of Mechanical Engineering, University of Alberta, Edmonton, Alberta, Canada.
[2]Department of Radiology and Diagnostic Imaging, University of Alberta, Edmonton, Alberta, Canada

Introduction

The nasal cannula is for the most part a safe and effective means of administering low-flow and high-flow oxygen to patients regardless of their age. However, oxygen administration via nasal cannula results in considerable variation in the delivered fraction of inhaled oxygen (FiO_2) and can thus pose health risks associated with inadequate or excessive oxygenation (Blakeman, 2013). This study aimed to find a formulation for predicting FiO_2 based on oxygen flow and patient breathing parameters over a wide parameter range and for different age groups.

Methods

Realistic nasal airway replicas derived from medical scans of adults (Chen et al.,2017) and of children less than 3 months of age (Tavernini et al.,2018) were used to measure FiO_2 delivered through nasal cannulas during low-flow and high-flow oxygen delivery. A lung simulator was used to control tidal breathing through nasal airway replicas. A previously derived flow-weighted equation that assumes ideal mixing of administered oxygen with entrained room air was evaluated for its ability to predict measured FiO_2 values (Katz et al.,2019). To test this equation, a variety of nasal cannula flow rates, respiratory rates, inhalation: exhalation ratios and tidal volumes were used with the aim of creating different breathing patterns for both age categories.

FiO_2 measurements were plotted against Q_{NC}/Q_i, where Q_{NC} (L/min) represents nasal cannula flow rate, and Q_i (L/min) represents average inhaled air flow rate, which is equal to tidal volume divided by inhalation time.

Results

For both age categories, the flow-weighted calculation derived from previous studies (Katz et al., 2019), overpredicted measured FiO_2 values above 60%, corresponding to a Q_{NC}/Q_i ratio of approximately 0.5. When measured FiO_2 was plotted against Q_{NC}/Q_i, the data sets for low-flow and high-flow oxygen delivery in the two age categories overlapped (**Figure 1**). A new predictive correlation for FiO_2 that encompasses both low-flow and high-flow oxygen regimes was obtained, which provides accurate prediction of measured FiO_2 values for both age categories and for wide-ranging nasal cannula flow rates, from 0.5 to 60 L/min.

Conclusions

A new correlation was proposed to provide improved prediction of FiO_2 as a function of breathing pattern and the oxygen flow rate provided via nasal cannula.

References

Blakeman TC. **Respir. Care** 2013. **58**(10):1679-1693
Chen JZ, et al., **Int J Chron Obstruct Pulmon Dis** 2017; **12**:2559.
Tavernini S., et al., **Aerosol Sci Technol**, 2018.**52**(4): p. 407-419.
Katz I., et al., **Respir. Res**., 2019. **20**(1): p. 1-1

Figures

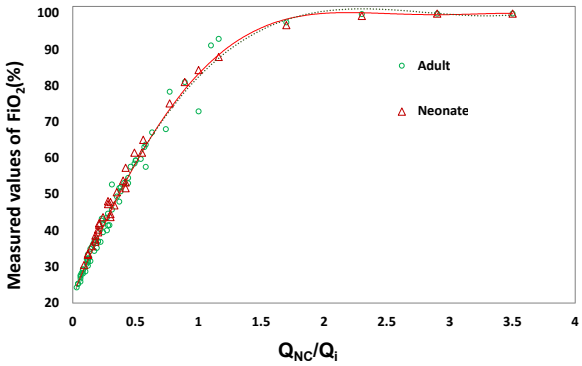


Figure 1. Measured values of FiO_2(%) vs. Q_{NC}/Q_i. The points illustrate all measured values for neonatal and adult' replicas.

Experimental Directivity Detection with Individual Biaxial Ultrasound Transducers

Nathan Meulenbroek[1], Sagid Delgado[1], Laura Curiel[1], Adam C. Waspe[2,3], Samuel Pichardo[1]
[1]University of Calgary, Calgary, Canada [2]Hospital for Sick Children, Toronto, Canada [3]University of Toronto, Toronto, Canada

Introduction

Biaxial ultrasound transducers are an emerging technology in the field of ultrasound imaging, with simulations demonstrating that biaxial transducers can passively estimate the direction of arrival of incident sound waves. This research seeks to establish directivity as an independent parameter detected experimentally by biaxial transducers. This demonstration will enable the integration of biaxial transducers with medical, geophysical, and industrial passive ultrasound imaging systems.

Methods

Three cuboid (3.84 mm x 3.84 mm x 5.92 mm) biaxial piezoceramics with two pairs of orthogonal electrodes (one pair applied laterally and one pair applied in the polling direction) were manufactured and characterized. Each transducer was placed in a water tank where an independent hemispherical source was attached to a moveable arm and operated at 250 kHz. Terminal voltages were recorded for eighty-one source positions in a plane parallel to the transducer's front face and at a depth of approximately 9 cm. Collection was repeated three times per transducer to ensure reproducibility. Two derived metrics were then calculated using both the forward and lateral terminal voltages: the phase difference and amplitude ratio. A Mann-Whitney U test was used to test for statistical significance.

Results

Biaxial transducers demonstrate a statistically significant ability to estimate the direction of arrival of incident sound waves. The phase difference and amplitude ratio complement each other to provide repeatable estimates over a range of 48 degrees (from -24 degrees to +24 degrees). These relationships are independent of any time-of-flight information. These results justify the integration of biaxial transducers with a variety of medical, geophysical, and industrial passive ultrasound imaging techniques to improve image fidelity and spatial localization of acoustic events.

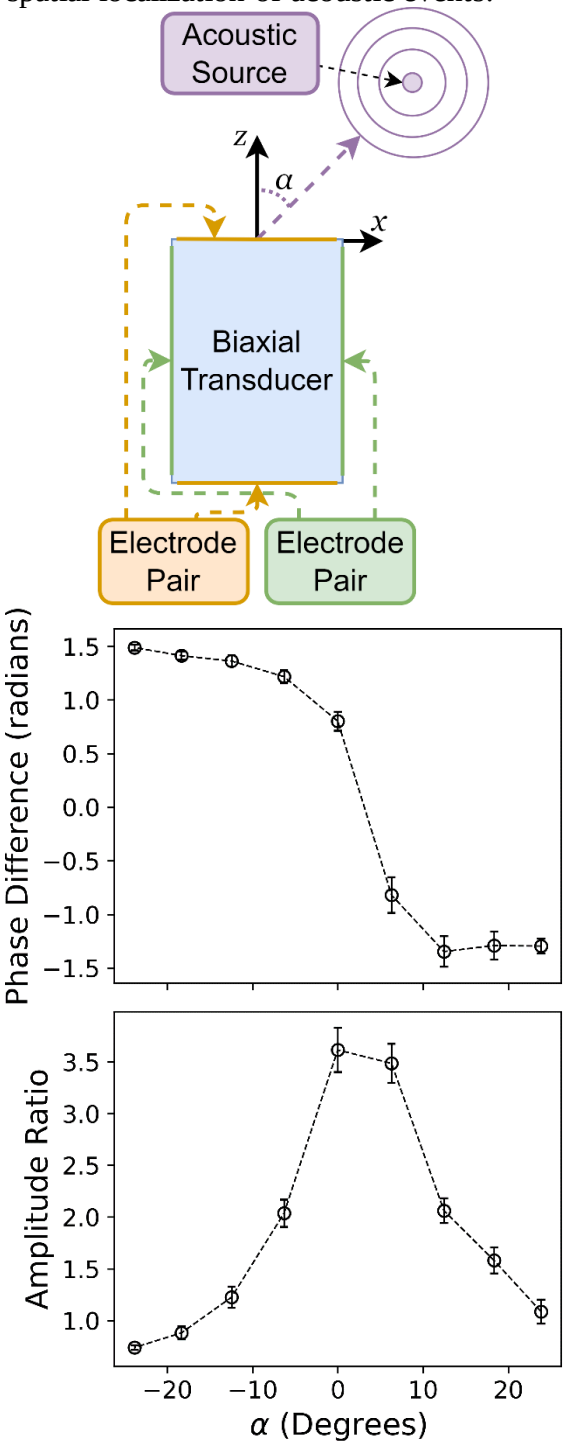


Figure 1 : Depiction of a biaxial transducer with two electrode pairs, as well as average phase difference and amplitude ratio curves.

Developing methodology to monitor tendon strain within the equine forelimb

Olivia Kenny, Kent Paulson, Sammy Patwary, Mohammad Janghorban, Richa Pandey, Nigel Shrive, John EA Bertram, Holly Sparks
University of Calgary

Introduction

Within thoroughbred equine forelimbs, 75-93% of injuries involve the superficial digital flexor tendon (SDFT) [1]. Due to the complexity of both the passive and active components of the musculoskeletal system in equine biomechanics, it has yet to be determined how muscle activation (or fatigue) can modify the strain experienced within the tendons of the forelimb. While cadaveric testing and computer modeling can shed some light on this understanding, in vivo measurements remain a requirement to validate their utility.

Here, we develop and validate a novel microelectrical mechanical system (MEMS) combined with polymeric, capacitive strain gauges for future *in vivo* use in horses [2]. We hypothesize this novel strain sensor will be reliable and repeatable compared to the current standards of strain measurements *ex vivo* and situated for *in vivo* trials.

Methods

Novel MEMS strain gauges were created by masking conductive carbon ink between layers of flexible and elastic substrate. Sensor accuracy will be confirmed on non-biological elastic materials before an application to viscoelastic biological tissues. An *ex vivo* in situ equine forelimb model and isolated tendon model have been developed to explore the measurement techniques. The limb can be loaded to forces experienced naturally during a trot and the isolated tendon can be stretched to previously reported strain levels. The sensors will be sutured atop 1) the accessory ligament of the SDFT, 2) SDFT, 3) DDFT (deep digital flexor tendon), and 4) accessory ligament of the DDFT as shown in Figure 1. The new sensor will be validated against existing literature values from *ex vivo* experiments as well as *in vivo* trials using liquid strain gauges and ultrasound based systems to assess repeatability and reliability in elastic materials.

Expected Results

We expect the novel strain sensor to provide accurate and reliable results relative to the existing strain measurement techniques and reported literature values. Such measurements will provide insight on the load distribution within the components surrounding the fetlock. The information will also be used to determine how the loads applied to the equine forelimb increased the strain experienced within the SDFT, DDFT and supporting ligament systems.

Conclusions

Validation of the novel strain sensor will allow for future use and in-depth research to be conducted *in-vivo*. For the equine species, knowing how and why strain is experienced in the SDFT can then be applied to the prediction, prevention and treatment of equine SDFT injuries.

References

[1] Thorpe, Clegg, and Birch, "A review of tendon injury: Why is the equine superficial digital flexor tendon most at risk?," *Equine Veterinary Journal*, vol. 42, no. 2, pp. 174–180, Feb. 2010.

[2] Zens *et al.*, "A New Approach to Determine Ligament Strain Using Polydimethylsiloxane Strain Gauges: Exemplary Measurements of the Anterolateral Ligament," *Journal of Biomechanical Engineering*, vol. 136, no. 12, p. 124504, Dec. 2014.

Figures

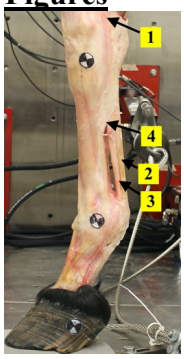


Figure 1 - Cadaveric model for novel strain sensor validation and locations of sensor placement

Using Deep Learning and Interpretable AI to Predict Outcomes in Medical Data

Annaa Osman Jakpa, Musa Taib, Brian Nguyen, Ethan MacDonald, Geoffrey Messier
Department of Electrical and Software Engineering, University of Calgary

Introduction: Administrative medical data is generated at every encounter with the health care centers [1]. By using machine learning (ML) models, prediction of adverse outcomes can be made to avert critical or life-threatening situations. Models are used in the medical field to help experts make the best decisions possible. Therefore, it is very important for predictive models to be interpretable and transparent. This paper seeks to compare the performance of an interpretable model (decision tree) and black box models (neural networks) in predicting adverse outcomes in patients up to a year after their last recorded interaction with the healthcare system.

Methods: A synthetic health care dataset created from Major League Baseball (MLB) data was used for the findings in this abstract. The entries total 452,995 from 1993 to 2011 and contains 915 unique individuals. The synthetic dataset's features were created by mapping MLB data's features to frequently occurring health care events. The target feature that each model predicted was adverse outcomes. Adverse outcomes in medical settings are life threatening and early identification is necessary for support.

Figure 1 represents a decision tree to perform binary classification on a dataset with four features (f1, f2, f3 and f4). To arrive at a decision (A or B), the tree asks sequential questions about the features associated with the examples. Examples are classified by following the path from the root to leaf. Combining simple questions about the data understandably makes decision trees interpretable and transparent.

In this study, two neural networks were used (ANN and RNN). ANNs are universal approximators because of their versatile pattern recognition abilities. As a result, the ANN serves as a great baseline for the comparison of outcomes to other models. The RNN, on the other hand, features a memory cell, which makes it a great model for time series data (medical records are mostly time series data).

Results: The ANN had the best performance out of all three models with precision of 0.68 and recall of 0.92, this was followed by the RNN with precision of 0.60 and recall of 0.85. The decision tree recorded a precision of 0.62 and a recall of 0.65.

The rules produced by the decision tree made it clear that the number of days a patient stays in the hospital was a major factor in determining if they will have an adverse outcome, while no such information could be deduced from the neural networks.

Discussion: Although utilizing the tree model rather than the deep learning model has a 27% reduction in performance in recall, it offers a much more straightforward and interpretative model and is anticipated to gain more acceptance in clinical practice. It should be noted, interpretable AI, and deep learning models both have benefits and limitations.

Future Work: While the results discussed in the abstract are all using the synthetic dataset, the future work will be done with the MIMIC-III dataset. MIMIC-III is a large administrative health database released by MIT in 2016[2], consisting of 46,520 patients admitted to a medical center between 2001 and 2012.

References:

1. Cadarette, S. M., & Wong, L. (2015). An Introduction to Health Care Administrative Data. The Canadian journal of hospital pharmacy, 68(3), 232–237. https://doi.org/10.4212/cjhp.v68i3.1457.
2. Johnson, A., Pollard, T., & Mark, R. (2016). MIMIC-III Clinical Database (version 1.4). PhysioNet. https://doi.org/10.13026/C2XW26.

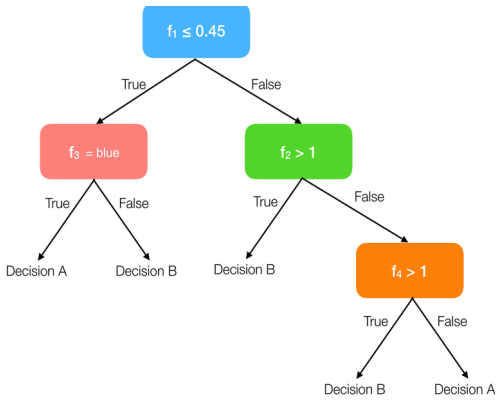


Figure 1: A Simple Decision Tree

Designing fully-automated smart vertical farming systems with the assistance of sensors as a solution to socio-economic problems

[1]Payal Wadodkar, [1]Vedant Parekh, and [2]Zahra Abbasi
[1] Department of Mechanical and Manufacturing Engineering, University of Calgary, Calgary, Canada
[2]Department of Electrical and Software Engineering, University of Calgary, Calgary, Canada

Introduction

The primary challenge to vertical farming is the absence of means to ensure quality of the vegetation developed. The optimal way to implement this, while eliminating errors due to changes in environment and human intervention is by integrating sensors that would entirely automate the process. Microwave sensors has shown a great potential to be used for real-time noncontact monitoring application due to their simple fabrication process, inexpensive structures, and easy system integration. The literature confirms the capability of pH sensing and moisture level monitoring using microwave sensor which provides the preliminary data for the applicability of theses sensors for plant health monitoring.
The objective of our project was to develop a smart vertical farming system that is affordable, easy to use and adaptable. With urban areas growing rapidly to keep up with population growth, traditional farms can no longer keep up with demand. Therefore, cities must become hubs for growing food whenever possible.

Methods

The first part of our project involved designing planters. Planters consist of two parts, a small reservoir for storing water and nutrient gel solution and a pot for containing the plant. On the side of the reservoir is a small circular tube for injecting the nutrient gel into the plant. The reservoir also has multiple draining holes which will be covered by biodegradable filters to prevent nutrient build up. Plants are contained in funnel-shaped pots with holes at the tapered end, which allow roots to grow out. The system will be monitored by humidity sensors, pH, antenna-based height sensors, photoresistors and water level sensors. These will cumulatively gather data on plant health, which will be displayed on the screen. The system works best when the plants are stacked up on shelves in a large room. The goal for this system is to be fully automated. This reduces the need for large watering, filtering, and lighting systems that are used in urban farms. By making this system affordable and easy to use, we break socio-economic barriers and help all members of our community have access to fresh, healthy food while tackling a global consumption issue.

Results

The design for the pH, humidity and distant sensor is performed using microwave structures. Apparatus is currently in its pilot phase. Certified results will be shared later.

Conclusions

The apparatus is being tested with the ideal conditions for plant growth and the sensors are being tested to ensure adequate readings and deployment of the required functions.

References

Z. Abbasi, H. Niazi, M. Abdolrazzaghi, W. Chen and M. Daneshmand, "Monitoring pH Level Using High-Resolution Microwave Sensor for Mitigation of Stress Corrosion Cracking in Steel Pipelines," in IEEE Sensors Journal, vol. 20, no. 13, pp. 7033-7043, 1 July1, 2020, doi: 10.1109/JSEN.2020.2978086.

Z. Abbasi, M. Baghelani and M. Daneshmand, "Zero Power Consumption Chipless Distant Microwave Moisture Sensor for Smart Home Applications," 2019 IEEE SENSORS, 2019, pp. 1-4, doi: 10.1109/SENSORS43011.2019.8956753

M. Dedecker, "'leaf and stem thickness will tell you the stress level of your plant,'" Hortidaily, 21-Jan-2020. [Online]. Available: https://www.hortidaily.com/article/9180875/leaf-and-stem-thickness-will-tell-you-the-stress-level-of-your-plant/. [Accessed: 09-Sep-2022]

Real-time Smart Switching in Home-based Lower-limb Exoskeletons

Pouria Faridi, Javad K. Mehr, Don Wilson, Frank Gauthier, Mahdi Tavakoli, Patrick M. Pilarski, and Vivian K. Mushahwar
Sensory Motor Adaptive Rehabilitation Technology (SMART) Network, University of Alberta, Edmonton, Canada

Introduction

The traditional method for choosing a walking mode while walking with an exoskeleton is to cycle through a fixed list of available modes using a switch button. This is tedious for users and increases the chances of errors [1]. Therefore, the goal of this study was to develop an intelligent method, capable of predicting users' intention for selecting a walking mode, by leveraging the common walking patterns of each user in home-based environments.

Methods

The Exo-H3 (Technaid S.L., Madrid, Spain) exoskeleton was used along with a walker that had a custom-made switch button and three GARMIN LiDAR sensors on its three sides to detect objects. The positional information of a user (from a Vicon motion capture system) and signals from the LiDAR sensors were passed through a reinforcement learning algorithm, known as general value functions (GVFs) [2], in real-time, to predict the future user selections of each walking mode. Five walking modes for left, right, slow, normal and fast speed (Figure 1), were then ranked in the switching list in descending order based on their GVF prediction magnitude. Figure 1 shows the experimental scenario, simulating a home-based environment. There were four colored paths for moving from the "bedroom" to the "office" and vice versa. The user arbitrarily switched between different paths during 3 sets of experiments.

Results

For a given user-selected path, we defined the error as "the number of switching actions minus 1" at each switching instance. Comparing the average errors for each path using the machine-learned list and the best possible fixed switching list showed a significant decrease in average errors for the adaptive strategy at each set (p-value < 0.05). The first experimental set had an average error of 3.4±5.3 vs 7.5±3.4, while the 2nd set showed 0.5±0.7 vs 8.4±3.6 and the 3rd set showed 0.25±0.4 vs 8±3.5 errors for the adaptive and traditional (fixed switching) strategies, respectively. Using the adaptive strategy, the user was able to reach the desired modes by hitting a switch button just once, in 81.25% of the switching instances.

Conclusions

Real-time application of GVFs for predicting exoskeleton users' intention was verified in this study for the first time. In total, a 48.5% reduction in the required number of switches for the machine-learned strategy was achieved.

References

[1] R. Baud, *et al*., "Review of control strategies for lower-limb exoskeletons to assist gait," *J. NeuroEngineering Rehabil.*, vol. 18, no. 1, p. 119, Dec. 2021.

[2] P. M. Pilarski *et al*., "Dynamic switching and real-time machine learning for improved human control of assistive biomedical robots," in *2012 4th IEEE RAS & EMBS, BioRob*, Rome, Italy, Jun. 2012, pp. 296–302.

Figures

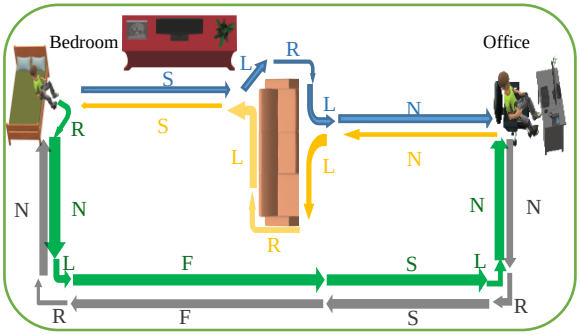


Figure 1. Experimental scenario in a home environment. The five available modes are shown as: walking speeds (slow (S), normal (N), fast (F)) and turning left/right (L/R). Switching errors at each path (blue (B), orange (O), green (G), black (K)) were averaged for each set. The order of the traversed paths at each set were as follows: Set 1 (B, O, B, O, B, O, G, K, G, K, G, K); Set 2 (B, K, G, O, G, K, B, O); Set 3 (B, K, G, O, G, K, B, K).

Cerebral blood flow and magnetic susceptibility are reduced in the bacterial lipopolysaccharide (LPS) mouse model of inflammation

Racheal Steele[1], Qandeel Shafqat[1], Ying Wu[1], Hongfu Sun[2], Jeff F Dunn[1]
[1]Hotchkiss Brain Institute, Cumming School of Medicine, University of Calgary, [2]School of Information Technology and Electrical Engineering, University of Queensland, Australia

Introduction

Inflammation is a key component of several neurological diseases[1]. It has also been associated with reduced cerebral blood flow (CBF) and cognitive deficits[1,2]. Brain hypoxia (a condition of low tissue oxygenation) has been reported in people with multiple sclerosis, an autoimmune neurological disease[2]. The cause of hypoxia in MS is unclear. We propose that inflammation might stimulate hypoxia[3]. A better understanding of hypoxia and inflammation and non-invasive methods to detect and monitor the extent of hypoxia are needed. We studied the effect of systemic inflammation induced by bacterial lipopolysaccharide (LPS) using 9.4T animal MRI measures of CBF and magnetic susceptibility.

Methods

C57BL/6 mice were randomly divided into saline injection (n=20) and LPS (2 mg/kg) injection (n=23) groups. Injections were given once a day for three days in both groups. 3 hours following the last injection (on day 3), we conducted MRI. QSM maps were generated using a 3D multi-gradient echo sequence (TR = 100ms, echo spacing = 4 ms) in a subgroup of mice (LPS n =7; saline n=10). An arterial spin labeling sequence (TR= 3000 ms, TE = 2.7ms) was used for CBF. T1 imaging was acquired using RARE-VTR. Magnetic susceptibility and CBF were measured in the cortex, bilateral hippocampi, and bilateral thalami.

Results

Susceptibility was significantly reduced in the LPS group in the cortex ($p<0.05$,), left hippocampus ($p<0.01$), and right hippocampus ($p<0.05$) as compared to the saline group (Fig 1A). We also found a significant reduction in CBF in the cortex, left hippocampus, and right hippocampus in the LPS group as compared to the saline group (Fig 1B).

Conclusions

We showed that systemic inflammation causes significant reductions in CBF and magnetic susceptibility. If reductions in CBF during inflammation are severe, and/or long-lasting, they could promote the development of brain hypoxia. Decreased susceptibility in the LPS group was opposite to what we expected, as the presence of hypoxia should increase susceptibility. Overall, we demonstrated that systemic inflammation causes significant changes in the brain, and ASL-MRI and QSM mapping are sensitive to such changes.

References

1.Perry V. Acta Neuropathol. 2010; 120: 277-86.
2.Davies et al. Ann Neurol 2013; 74; 815-25.
3.Yang R and Dunn JF. 2019; 25: 1715-8.

Figures

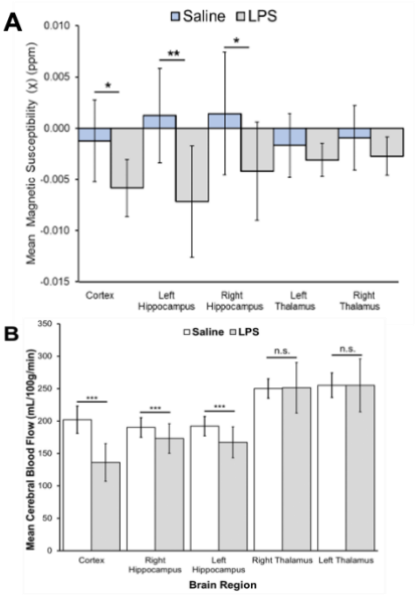


Fig. 1 A) Magnetic Susceptibility (mean±SD) and B) cerebral blood flow (mean±SD) measured in the 5 regions of interest of saline and LPS group

Multiphase Computed Tomography Perfusion Maps Predict Penumbra Volume in Patients with Acute Ischemic Stroke

Raneem Sheronick[1,2], Connor McDougall[1], Philip Barber[1,2,3]
[1] University of Calgary, [2] Hotchkiss Brain Institute, [3] Calgary Stroke Program

Introduction

Multiphase computed tomography angiography (mCTA) can be used to identify critically hypoperfused brain tissue in acute ischemic stroke patients comparable to CT perfusion (CTP). While CTP is the current standard in acute stroke imaging, mCTA is a low cost, less invasive alternative that is more widely accessible. We present a logistic regression-based method for predicting ischemic penumbra volume from mCTA perfusion maps.

Methods

295 acute stroke patients were imaged with three-phase mCTA and CTP. The mCTA scan of each patient was split into five vascular regions: anterior cerebral artery (ACA); middle cerebral artery (MCA); posterior cerebral artery (PCA); basal ganglia (BG); and cerebellum (CB). Feature maps were generated in each vascular region for every patient to measure various flow parameters. Feature maps were then used to train a logistic regression model to predict ischemic penumbra volume in each patient [1, 2]. Time to maximum (Tmax) maps were produced from CTP and thresholded at 9.9s to define an ischemic penumbra reference standard [3]. Receiver operating characteristic (ROC) curve analysis was then used to evaluate the predictive ability of the logistic regression model in identifying hypoperfusion in each vascular territory.

Results

For each vascular territory, the ROC analysis generated an Area-Under-Curve (AUC) of 0.77 (ACA), 0.85 (MCA), 0.74 (PCA), 0.85 (BG), 0.79 (CB).

Conclusions

mCTA derived feature maps can accurately predict ischemic penumbra volume in acute stroke patients. Identification of penumbra plays a critical role in acute stroke treatment planning. mCTA-based perfusion maps can be clinically useful for guiding interventional therapies in an acute stroke setting.

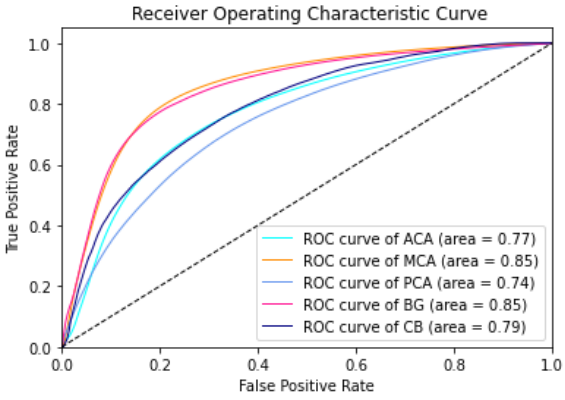
References

1) d'Esterre, C., McDougall, C., & Barber, P. (2022). *U.S. Patent Application No. 17/426,624*.

2) McDougall, C. C., Chan, L., Sachan, S., Guo, J., Sah, R. G., Menon, B. K., ... & Barber, P. A. (2020). Dynamic CTA-derived perfusion maps predict final infarct volume: the simple perfusion reconstruction algorithm. *American Journal of Neuroradiology*, *41*(11), 2034-2040.

3) Qiu, W., Kuang, H., Lee, T. Y., Boers, A. M., Brown, S., Muir, K., ... & HERMES collaborators. (2019). Confirmatory study of time-dependent computed tomographic perfusion thresholds for use in acute ischemic stroke. *Stroke*, *50*(11), 3269-3273.

Figures



Investigating the common driving routes and destinations among older adults

Reihaneh Derafshi, Sayeh Bayat
University of Calgary, Schulich School of Engineering

Introduction

Investigating older adults' driving behaviors and habits can result in a more senior-friendly urban environment and can contribute to addressing possible current shortages[1]. In this study, we are investigating behaviors considering driving-habits formation in elderly people. More specifically, we aim to see if our target population is biassed to use a particular path for their common destination, how frequently this path is used, and if the proportion of times this path is used depends on the degree of commonness of the destination.

Methods

We have gathered a dataset including driving GPS data of 246 participants over the age of 65 who live in St. Louis, Missouri, United States.[2]. The GPS collector begins working the moment the car turns on and records the car's longitude and latitude every 30 seconds. Common destinations of each participant, the number of paths they used for them, and the repetition of all mentioned are computed using hashing and clustering algorithms. In the next step, we did a preliminary statistical analysis on the first 10th most common destinations of all participants, including plotting the distributions and calculating the confidence intervals.

Results

Our preliminary results suggest that the number of distinct paths used for a destination decreases with the degree of commonness of the destination. Also, there is a most common path for each destination used by older adults, and the commonness of this path is independent of the commonness of the destination. Furthermore, the usage of this path among other used paths in 95% of the time is in the range of (62,73)%.

Conclusions

Our findings suggest that The behaviors of seniors in choosing a certain path for their most common destination and other less common destinations are not significantly different.

References

[1] Vlahodimitrakou Z, Charlton JL, Langford J, et al. Development and evaluation of a driving observation schedule (DOS) to study everyday driving performance of older drivers. Accid Anal Prev.2013;61:253-260.doi:10.1016/j.aap.2013.03.027
[2]Bayat, S., Babulal, G.M., Schindler, S.E. et al. GPS driving: a digital biomarker for preclinical Alzheimer disease. Alz Res Therapy 13, 115 (2021). https://doi.org/10.1186/s13195-021-00852-1

Figures

nth most common trip	Average times the trip is taken	average length of trip(min)	average number of paths used	Variance % used the most common path	Average % used the most common path	confidence interval, alpha = 0.95
0	209.47	11.14	14.54	785.88	69.85	(66.32, 73.38)
1	169.17	11.01	13.64	715.26	69.86	(66.5, 73.23)
2	111.49	11.02	10.52	690.4	67.99	(64.68, 71.29)
3	95.93	10.86	9.58	685.42	70.9	(67.6, 74.19)
4	76.92	11.84	9.28	766.81	65.82	(62.32, 69.31)
5	66.79	11.28	8.35	734.23	68.27	(64.85, 71.68)
6	58.27	12.23	7.64	702.61	67.02	(63.68, 70.36)
7	52.74	11.37	7.51	705.49	70.33	(66.98, 73.68)
8	47.29	13.68	8.3	801.79	66.43	(62.86, 70.0)
9	43.19	12.4	7.47	752.83	65.52	(62.06, 68.98)

Figure 1: Result of statistical analysis

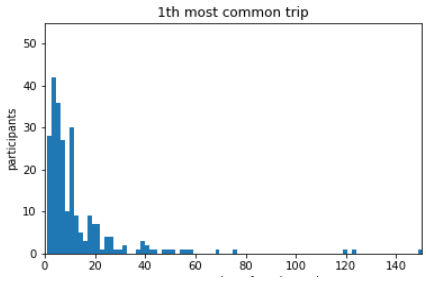


Figure 2: Population distribution regarding the number of paths used

A Novel Combination of Neural Networks and Statistical Shape Modelling for Automatic Knee Joint Geometry Construction from MRI

Reza Kakavand[1*], Mehrdad Palizi[2], Olivia L. Bruce[1], Samer Adeeb[2], W. Brent Edwards[1] and Amin Komeili[1*]
[1]Schulich School of Engineering, Department of Biomedical Engineering, University of Calgary
[2]Faculty of Engineering, Civil and Environmental Engineering Dept, University of Alberta
email: * reza.kakavand@ucalgary.ca

Introduction

Specific sports and occupations involving intense physical activity or prolonged loading of the knee are highly associated with OA[1,2]. The precise prediction of OA is therefore useful for developing preventative treatments. One efficient method for such prediction is the finite element (FE) method. FE models are used to estimate the internal pressure at contact surfaces and deformation of cartilage due to external forces. Constructing accurate bone geometry is a major initial step for developing patient-specific FE models of the knee joint. Magnetic resonance (MR) images are frequently used to manually segment knee geometry. However, manual segmentation is time-consuming. An automatic segmentation approach, that is as accurate as the manual one, would significantly facilitate knee joint biomechanics analysis. Here, we propose an automatic method, where a 2D U-Net convolutional neural network (CNN) and a statistical shape model (SSM) are combined to extract the distal femur and proximal tibia from MR images of the Osteoarthritis Initiative (OAI) database (https://nda.nih.gov/oai/). The validity of the predictions was verified by evaluating the maximum principal stress between the manual and automatic segmentations.

Methods

First, the femur and tibia were segmented using a 2D U-Net CNN[3]. The outcome was fed into a SSM to improve the accuracy of segmentation. The SSM was fitted to the femoral condyles and tibial plateaus predicted from the CNN. A limited-memory *Broyden-Fletcher-Goldfarb-Shanno (L-BFGS)* algorithm was used for the fitting process[4], where the vector of weights for principal components, translation, rotation and scaling were the unknowns.

256 MR images (61.87±9.33 years; 29.27±4.52 BMI [kg/m^2]; 0.36×0.36×0.7 image resolution [mm]) from the OAI database whose masks are publicly available[3] were used for training. Articular cartilage was added to the bones. A compressive force was applied to the femur for 6 s, while the tibia was held fixed. The maximum principal stress in the cartilage between the two segmentation methods was compared.

Results

The Dice similarity index for femur and tibia were 93% and 91%, respectively. The time history of the maximum principal stress from the two FE models developed using either manual or automatic segmentation is illustrated in Figure 1.Although, the location of the contact area slightly differs in the two models, the stress intensity and distribution are very close.

Increasing image resolution for CNN training could considerably increase the model accuracy, but also the computational time. Low quality image results in low quality surface construction. SSM was thus used to adjust and smooth this surface for higher quality while maintaining an acceptable accuracy and computational time.

Conclusions

The combination of CNN and SSM is a novel method for automatic segmentation and geometry development of patient-specific FE models of the knee joint. This method relies on both intensity (CNN) and coordinate (SSM) data of the region of interest, resulting in reliable stress distributions from FE analysis.

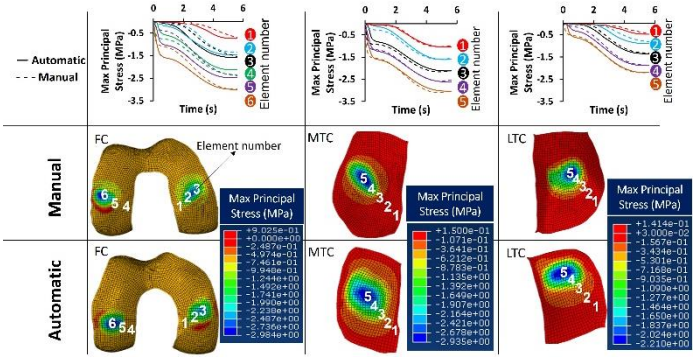


Figure 1. Time history comparison of maximum principal stress between automatic and manual segmentations.

References

1 Driban, J. B. *et al. J. Athl. Train.* 52, 497–506 (2017)
2 Andersen, S. *et al. Occup. Environ. Med.* 69, 325–330 (2012)
3 Ambellan, F. *et al. Med. Image Anal.* 52, 109–118 (2019)
4 Bruce, O. L. *et al. Comput. Methods Biomech. Biomed. Engin.* 1–12 (2021)

Blast Injury Prevention Device Finite Element Simulation

Robert Chauvet[1], Lindsey Westover[1], Simon Ouellet[2], Chris Dennison[3],
[1] Department of Mechanical Engineering, University of Alberta[2] Defense Research and Development Canada
[3] Department of Biomedical Engineering University of Victoria

Introduction

Traumatic Brain Injuries (TBI) are commonplace in society, and in military or physical activity environments these numbers are magnified. Physical surrogate models of the human head are commonly used to model cranial impacts and assess head injuries[1] The Blast Injury Prevention Device (BIPED) is a head form that contains a brain simulant, fluid layer, connective membranes, a skull, and a skin layer that can measure kinematics, pressures, and strains. [2] To help develop new iterations of head forms that better mimic the biological response of a head during impact, a finite element model can be used. This requires digitizing precise geometry, developing accurate material models and implementing realistic boundary conditions to the model. This study aims to create a digital model of the BIPED that can match experimental results in pressure and displacement under blunt impact scenarios.

Methods

The BIPED part geometries were taken from the manufacturing CAD models, and then they were meshed in Hypermesh before being assembled in ABAQUS. All parts were assigned material properties from manufacturer data. The brain material, Sylgard 527 was modelled with an Ogden hyperelastic and a Prony viscoelastic model as determined by experimental material testing. The CSF layer was modelled as a viscoelastic solid. All other parts were linear elastic. In order to test the model against experimental results, kinematics and force inputs from frontal impact tests were applied to the model. This was done for tests that measured the pressure in the brain at two sensor locations, as well as sperate tests that measured relative displacements of the brain compared to the skull.

Results

The pressure data from the simulation was in agreement with the experimental data collected, in both in the trend over time, and the magnitude. This held for both the force and kinematic inputs. A typical pressure response can be seen in Figure 1. Since this was a frontal impact, the maximum front sensor pressure (Coup location) and the minimum back sensor pressure (Contrecoup location) were compared to the experimental values. There was an average of 5.4 % error on the front sensor location and an error of 44.3% for the back sensor location.

The x and z displacements (sagittal plane) of five nodes relative to the skull were compared with experimental results. All five points agreed in terms of magnitude and trend relative to time.

Conclusions

This study demonstrates the success of developing a model that can work with either kinematic or force inputs, and discusses the differences between the results when comparing boundary conditions. This finite element model is an important step in designing the next iteration of the BIPED headform, as parametric studies can now be run. These tests could determine if sensor placement is in an ideal location in addition to other applications.

References

[1] A. Azar et Al *J. Biomech. Eng.*, vol. 142, no. 4, p. 041009, Apr. 2020,
[2] Li, Y et Al.., (May 18, 2021). ASME. *J Biomech Eng*. September 2021; 143(9): 091006.

Figures

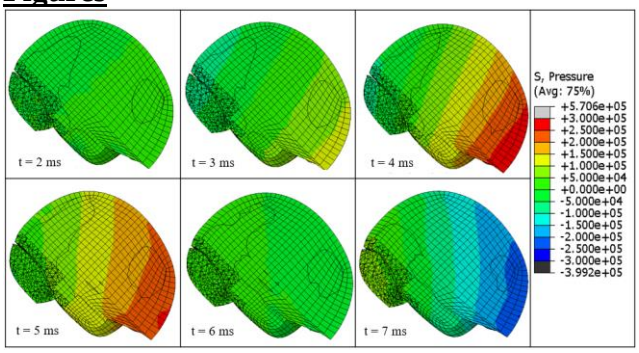


Figure 1. Pressure test results for the pendulum impacts.

Reducing GABA-edited Magnetic Resonance Spectroscopy Scan Times with Deep Learning

Rodrigo Berto[1-4] BEng, Ashley Harris[2-4] PhD, Roberto Souza[3,5] PhD
[1]Biomedical Engineering Department, University of Calgary, [2]Department of Radiology, Cumming School of Medicine, [3]Hotchkiss Brain Institute, [4]Alberta Children's Hospital Research Institute, University of Calgary, [5]Electrical and Software Engineering Department, University of Calgary

Introduction

Magnetic Resonance Spectroscopy (MRS) is a non-invasive imaging method that provides localized information on tissue chemical concentration. GABA-edited MRS involves subtracting two spectra to reveal the GABA signal, which is normally overlapped by other neurochemicals.

The subtraction of the spectra, however, decreases MRS signal quality [1], as most of the signal is eliminated in the subtraction process but noise is increased. This decreases the signal-to-noise ratio (SNR) and may lead to artifacts.

To improve the signal quality, many transients (i.e., measurements) are acquired and processed. This processing, called preprocessing, combines and denoises the transients [2], generating a single difference spectrum that is quantified for obtaining the neurochemical concentrations.

Acquiring many transients, however, results in long exam times, which decrease patient comfort and increase the chance of motion artifacts [1]. This work proposes to use Deep Learning (DL) models to develop a GABA-edited preprocessing pipeline that will obtain results equivalent to conventional pipelines while using less transients, resulting in faster exams.

Methods

GABA-edited MRS preprocessing pipelines with different configurations of DL models and conventional preprocessing steps will be developed. Those pipelines will be trained on simulated data, evaluated, and ranked to determine the optimal pipeline for accelerating exams.

Ground-truth spectra will be simulated with the FID-A toolbox [3], and noise will be added to them to generate noisy transients, which will be the input to the pipelines. The simulated data will be used to train the models in the pipelines, and the ground-truth spectra will be used as the target data. The pipelines will then be evaluated with simulated data and *in vivo* data from the big GABA dataset [4].

Results & Conclusions

Preliminary results using a simple U-NET model to combine difference transients into a single denoised difference spectrum showed promising results in terms of SNR and the shape of the spectrum. Figure 1 shows how the model was able to denoise the signal of an *in vivo* scan with only a quarter of the total transients, increasing SNR and decreasing spectral noise.

Based on similar studies that reduce scan times with DL [5], I expect to be able to obtain an acceleration rate of 4 while maintaining quantification results and SNR comparable to conventional preprocessing with the full number of transients.

References

[1] Mikkelsen, et al., 2018, *J. Neurosci. Methods*.
[2] Near, et al., 2021, *NMR in Biomedicine*.
[3] Simpson, et al., 2017, *Mag. Reson. in Med.*
[4] Mikkelsen, et al., 2017, *NeuroImage.*
[5] Souza, et al., 2019, 32nd *SIBGRAPI*

Figures

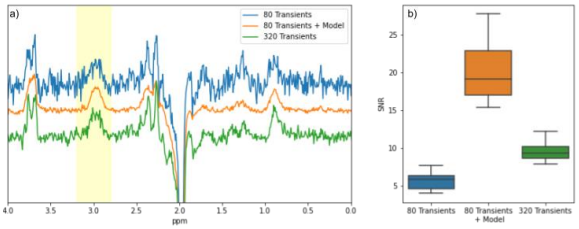


Figure 1. a) *In vivo* GABA-edited MRS spectrum for 3 configurations: (blue) conventional preprocessing using one quarter of the data (80 transients); (orange) DL model preprocessing using one quarter of the data (80 transients); (green) conventional preprocessing using all of the data (320 transients). Spectra are offset for better visualization. b) Peak SNR distributions for 36 scans from the Big GABA dataset, for the same 3 configurations.

The effect of Proteoglycan 4 on disc integrity and functionality

Samantha Heschl[1,2], Jessica May Corpuz[1,2], Roman J. Krawetz[1,2,3]
[1]Department of Biomedical Engineering, University of Calgary; [2]McCaig Institute for Bone and Joint Health, University of Calgary; [3]Cumming School of Medicine, University of Calgary

Introduction

Approximately 90% of individuals experience some degree of intervertebral disc (IVD) degeneration.[1] IVDs are essential for enabling movement and transmitting load throughout the spine, and their degeneration is often a major contributor to lower back pain. Despite its prevalence, the driving molecular mechanisms of IVD degeneration are not well understood. The bio-lubricant Proteoglycan 4 (*Prg4*) may play an important role in maintaining the IVD, as *Prg4* affects homeostasis in load-bearing tissues. Mice lacking *Prg4* (*Prg4*$^{-/-}$) experience premature tissue degeneration in their joints, yet IVD degeneration has not been thoroughly explored with this model. Thus, this study investigates how *Prg4* affects IVD biomechanical properties using a *Prg4*$^{-/-}$ mouse model.

Methods

Lumbar motion segments (vertebrae-disc-vertebrae) were harvested from *Prg4*$^{-/-}$ and C57 mice at 12 and 36 weeks of age. Micro-computed tomography (µCT) scans were performed to analyze vertebrae bone density. The motion segments then underwent biomechanical tests consisting of cyclic loading to 5% strain, stress relaxation, and ultimate failure. Histological analysis and Safranin-O staining was conducted on discs that herniated during ultimate failure testing to identify where the failure occurred.

Results

Trends in preliminary data suggest a lower instantaneous modulus and maximum stress in *Prg4*$^{-/-}$ discs during stress relaxation. Similarly, preliminary ultimate failure data suggests lower maximum stress and disc toughness in *Prg4*$^{-/-}$ samples. Paired t tests demonstrated significance between some groups (Figure 1).

Conclusions

Based on preliminary data, *Prg4*$^{-/-}$ IVDs demonstrated lower strength and toughness than controls during ultimate failure tests. The lower maximum stresses and instantaneous moduli measured from the *Prg4*$^{-/-}$ IVDs suggests decreased stiffness compared to the control discs. These suggested trends, supported by the significant differences found between some of the data sets, imply that *Prg4* does play a crucial role in maintaining IVD integrity and functionality.

References

[1] N. Kos, L. Gradisnik, and T. Velnar, "A brief review of the degenerative intervertebral disc disease," *Medical Archives*, vol. 73, no. 6, p. 421, 2019.

Figures

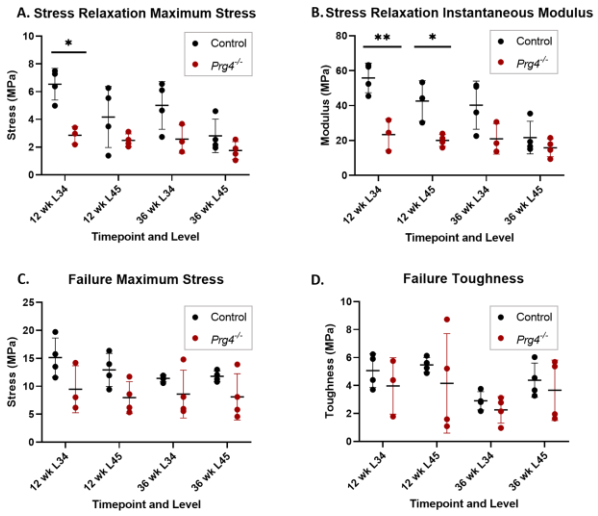


Figure 1: Stacked dot plots comparing *Prg4*$^{-/-}$ and control biomechanical results, consisting of: maximum stress from the stress relaxation test (A), instantaneous modulus (B), maximum stress from the failure test (C), and disc toughness (D). (* $p < 0.05$, ** $p < 0.01$)

Tissue effects on neurochemical quantification

Samantha Leech[1,2,3,4], Tiffany K. Bell[2,3,4], Sarah L. Manske[1,2], Paul G. Mullins[5], Ashley D. Harris[2,3,4]

[1]Deparment of Biomedical Engineering, Schulich School of Engineering, University of Calgary; [2]Department of Radiology, Cumming School of Medicine, University of Calgary; [3]Hotchkiss Brain Institute, Cumming School of Medicine, University of Calgary; [4]Alberta Children's Hospital Research Institute, University of Calgary; [5]School of Psychology, Bangor University, Bangor, Gwynedd, UK

Introduction

Single voxel spectroscopy (SVS) is a type of magnetic resonance imaging (MRI) used to measure neurochemical concentrations within a region (voxel) of interest. To accurately quantify neurochemical levels using SVS, it is important to account for tissue-specific neurochemical signal relaxation and concentration levels [1]. An equation that corrects for this tissue-specific neurochemical signal relaxation has been established [1], however, it requires an assumption of the relative concentrations of the neurochemical of interest in gray (GM) and white (WM) matter; cGM/cWM. This ratio is often ignored in quantification because a standard has not yet been established. Thus, this study aims to determine cGM/cWM for commonly measured neurochemicals, including creatine (Cr), N-acetyl aspartate (NAA), choline (Cho), myoinositol (mI), and glutamate (Glu) using SVS.

Methods

Data will be collected from 6 voxels (3 frontal voxels and 3 posterior voxels) with varying GM and WM contents in 30 healthy adults aged 18-40 years. SVS data will be collected using a short echo time (TE), to reduce signal loss due to relaxation, and a semi-LASER acquisition (localization by adiabatic selective refocusing), to reduce chemical shift displacement error (artifact). Scanning will be performed at 3T (GE 750W at the Alberta Children's Hospital) with a 32-channel head coil and TR/TE = 3 s/35 ms.

Voxels will be co-registered with a T1-weighted anatomical image and segmented to determine the GM and WM fractions within each voxel using the Gannet 3.2 toolbox [2] in MATLAB. Data will then be processed using FID-A [4] and LCModel [3] as well as tissue corrected for concentration quantification. The relationship between cGM and cWM will then be determined using a linear fit of the neurochemical concentrations to the voxel tissues fractions. Assuming data in 6 voxels can be obtained for each of the 30 participants, this study will generate 180 measures. In secondary analyses, the consistency of cWM/cGM ratios between the frontal and posterior voxels will be investigated.

Results

Based on observations from literature, I expect the concentrations of Cr, NAA, mI, and Glu to be greater in GM than WM and Cho to be lower in GM than WM.

Conclusions

The goal of this study is to improve the accuracy of SVS neurochemical quantification techniques for future research. Specifically, this project will determine the importance of accounting for differences in neurochemical concentrations between WM and GM, which is often overlooked, to enable more complete quantification.

References

1. Gasparovic C, et al, NMR Biomed. 2018; 31(6):1-9.
2. Harris AD et al, J Magn Reson Imaging. 2015; 42:1431-1440
3. Provencher S, NMR Biomed. 2001; 14(1): 260-264.
4. Simpson R et al, Magn Reson Med. 2017; 77(1): 23-33.

Sorting out the stay: predicting tendon strain in horses

Sammy Patwary, John Bertram, Holly Sparks, Olivia Kenny

Introduction

The forelimb of a horse has a complex system of support that uses a combination of passive and active components. The superficial and deep digital flexor muscles (SDF and DDF) and their tendons (SDFT and DDFT) are the two principle active supports of the fetlock – a main distal limb joint – but these are complimented by passive ligaments that run from each tendon to the limb skeleton. Despite the apparent redundancy in the support system, 75-93% of thoroughbred forelimbs injuries involve the SDFT. Ultimately, we would like to know why this tendon is so vulnerable.

Our underlying hypothesis is that the differences in muscle properties between SDF and DDF may lead to fatigue in the DDF causing overloading of the SDFT. Little is currently known regarding the loading distribution among this complex stay apparatus, particularly regarding the influence muscle activity has. The objective is to generate tools that can predict strain distribution throughout the stay apparatus under a variety of muscle activations.

Methods

A model was developed in MATLAB based on the anatomical organization of the distal equine limb. The model strain predictions were then compared to an ex vivo prep of the equine limb loading in a testing frame where muscle activity was replaced by independently controlled actuators. Markers were placed on tendons to track the strain ~~in~~ photometrically (Kinovea software).

Results

The model predicted SDFT max strains within 5% of the photometric results. Sensitivity testing highlighted a 200% change in output if all geometric inputs was altered by 15%.

Discussion

.

Early results are promising while improvements can be made to both the model and the empirical strain measurement techniques. Together the combination of a detailed predictive model confirmed by ex vivo measurements will provide substantial insight into the strain distribution of the equine forelimb.

Figures

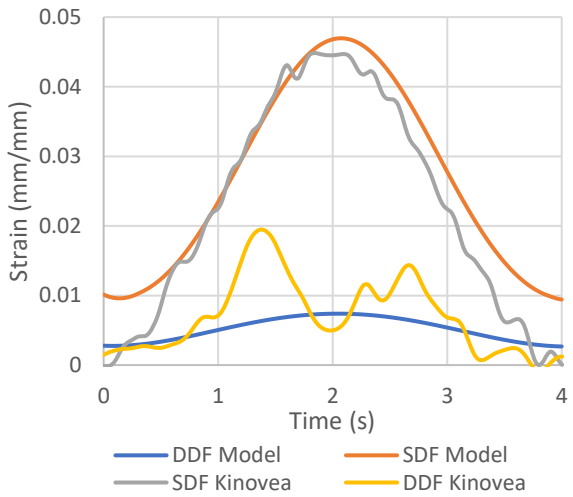


Figure 1: The Kinovea photometric strain data in comparison with the MATLAB model strain data.

Sensitivity-Enhanced Patch Antenna Sensor for Distant Hydration Monitoring Applications

Sarah Vestrum[1], Sorosh Abdollahi[2], Maryam Badv[2], and Zahra Abbasi[1]
[1] Department of Electrical and Software Engineering, University of Calgary, Calgary, Canada
[2] Department of Biomedical Engineering, University of Calgary, Calgary, Canada

Introduction

Monitoring the health of livestock is essential for the welfare of the animal. Hydration monitoring can aid in assessing the health of livestock as dehydration can be an indication of poor health and leave the animal susceptible to disease such as bovine respiratory disease [1].

Microwave circuits can be used for real-time, contactless sensing by observing the interactions of the electromagnetic field with the target sample [2]. By equipping a microwave sensor with an intermediate micro/meso- porous layer, like a dried hydrogel, a higher content of water can be absorbed on the sensor for hydration monitoring. The absorbed water then is transmitted and introduced to the surface of the sensor and sensed by the system.

Here, a patch antenna with an L-shaped slot has been developed and investigated for distant hydration monitoring. To increase the sensitivity of the antenna to the variation of dielectric properties of the sample under test placed at a distance, a sensing "tag" with a plus-shaped sensitive area has been introduced as the main sensing element. This tag provides higher sensitivity to the variation of dielectric properties when the sample is placed at a distance. The tag has been integrated with a hydrogel moisture absorber to highlight the impact of moisture variation.

Simulation and Design

The sensor was designed and simulated in Keysight's Advanced Design System (ADS). The substrate used for this design has a relative permittivity, ε_r, of 2.20 and 0.8 mm thickness. The dimensions of the patch were designed to provide a resonant frequency at 3.16 GHz. As the relative permittivity of the sample increases, the resonant frequency is expected to decrease. The sensing tag was designed to maximize the sensitivity of the sensor and to increase field interactions with the test material even as the distance to the patch antenna increases. In simulation, the presence of the sensing tag at a distance of 30 mm enables the system to demonstrate 15 MHz of frequency shift while the sample changes in permittivity (ε_r = 1 to ε_r = 10).

Experimental Results

The increased sensitivity of the sensor with the added sensing tag has been verified experimentally using a Vector Network Analyzer. The patch antenna and sensing tag are fabricated on Rogers RT/duroid 5880. A hydrogel is added to the surface of the sensing tag to absorb water and highlight the sensor's ability to monitor water content. With the sensing tag 20 mm away from the antenna, the sensor was able to detect changes in water content in 25 μL increments with a total frequency shift of 10 MHz when 150 μL was absorbed into the hydrogel.

Conclusions

The proposed sensing platform demonstrates the ability to be used for distant hydration monitoring of a sample, as small volumes of water absorbed by a hydrogel were able to be detected from a distance of 20mm. This non-invasive testing has potential for livestock hydration monitoring where animal welfare is essential.

References

[1] N. K. Van Engen and J. F. Coetzee, 'Effects of transportation on cattle health and production: a review', Anim. Health. Res. Rev., vol. 19, no. 2, pp. 142–154, Dec. 2018

[2] Abbasi, Zahra, et al. "High-Resolution Chipless Tag RF Sensor." IEEE Transactions on Microwave Theory and Techniques, vol. 68, no. 11, Nov. 2020, pp. 4855–64.

An Algorithm to Improve the Accuracy of Microwave Breast Imaging: Validation and Testing

S. Price[1], M. Owjimehr[1], J. Bourqui[1] and E. Fear[1]
[1] Department of Electrical and Software Engineering, University of Calgary, Calgary, AB, Canada

Introduction

Microwave imaging has been proposed as a modality for breast cancer treatment and disease monitoring as it has low exposure risks and can be performed at point of care [1]. These systems measure and map the permittivity of tissue, a dielectric property related to water content [2]. Due to the complexity of breast tissue, microwave signals can take multiple paths to travel from a transmitting to a receiving antenna during imaging (multipath propagation). These different paths can be caused by inclusions within the breast tissue (e.g., tumors) or areas with fatty and dense breast tissue. When multipath information is not incorporated into the signal processing algorithm of these systems, less accurate permittivity values may be evident in the final images. An algorithm developed to handle multipath propagation has not been tested with complex breast tissue models. This work aims to validate the algorithm by testing it with data from complex breast simulations and by applying it to data from breast cancer patients.

Methods

To test the algorithm, simulations of realistic breast models were created using an electromagnetic simulation software (SEMCAD, SPEAG, Switzerland). Breast models from [4] were used to develop simulations with realistic geometry and tissues properties. For validation, the results from the algorithm were compared to 2-dimensional projections of the simulation models. Improvements were identified via comparison to the images from the original algorithm. The patient data was taken from 15 women undergoing radiation treatment after breast conserving surgery who were scanned by a microwave transmission system [3] (study approved by HREBA.CC-17-0322). The images from the patient data were validated using treatment information extracted from the patients' mammograms.

Results

The results from the simulations indicate that the multipath algorithm located inclusions more accurately than the original algorithm in the complex breast tissue. Similar results were shown for the patient data where responses consistent with treatment became more obvious with multipath information.

Conclusions

By including multipath information, the microwave imaging system explored here more accurately located inclusions and responses to treatment in breast tissue. This is important for monitoring changes in the breast during cancer treatment, which has the potential to improve quality of life after treatment for these patients.

References

[1] M. N. Clemenshaw et al., "Current Approaches and Challenges in Monitoring Treatment Responses in Breast Cancer," *Journal of Cancer*, vol. 5, no. 1, pp. 58-68, Jan. 2014, doi: 10.7150/jca.7047.

[2] R. Pethig and D. Kell, "The passive electrical properties of biological systems: Their significance in physiology, biophysics and biotechnology," *Physics in Medicine and Biology*, vol. 32, no. 8, pp. 933–970, Feb. 1987, doi: 10.1088/0031-9155/32/8/001.

[3] J. Bourqui and E. C. Fear, "System for Bulk Dielectric Permittivity estimation of Breast tissues at microwave frequencies," *IEEE Transactions on Microwave Theory and Techniques*, vol. 64, no. 9, pp. 3001-3009, Sept. 2016, doi: 10.1109/TMTT.2016.2586486

[4] M. Omer and E. Fear, "Anthropomorphic breast model repository for research and development of microwave breast imaging technologies," *Scientific Data*, vol. 5, Nov., 2018Art. no. 180257, doi: 10.1038/sdata.2018.257.

Creating super-repellent bacterial nanocellulose membranes with tunable properties

*Sorosh Abdollahi[1], Emma Stephens[1], Milcah Angela Uy[1], Maryam Badv[1,2]**
[1]Department of Biomedical Engineering, Schulich School of Engineering, University of Calgary
[2]Libin Cardiovascular Institute, University of Calgary

Introduction

Bacterial nanocellulose (BNC) is a natural hydrogel that has recently gained interest in several biomedical applications. The non-toxicity, high porosity, and remarkable mechanical properties of BNC-based constructs, makes this biopolymer a great candidate for designing biomaterials [1]. In addition, due to the abundant hydroxyl groups present on the surface of BNC, surface modification and functionalization of BNC with different functional groups and biopolymers has been explored in numerous studies [2]. Despite the great potential of BNC for designing biointerfaces, this natural polymer lakes anticoagulant properties, therefore limiting its application in blood-contacting interfaces. In this study we report a new class of BNC biointerfaces that exhibit superior biocompatibility and repellency properties when compared to control BNC samples. Super-repellent BNC-based biomaterials were produced using chemical vapor deposition (CVD) of fluorosilane molecules, and infusion with a fluorine based lubricant. Further, the water repellency and hemocompatibility properties of modified lubricant-infused BNCs were tested and compared to non-treated BNC membranes.

Methods

BNC pellicles were produced by *Gluconacetobacter hansenii*, cultured in Hestrin-Schramm medium for three weeks. After collecting the pellicles and purifying them, they were frozen with liquid nitrogen and dried using lyophilization. BNC membranes were treated with trichloro perfluorooctyl silane (TPFS) using CVD. After the CVD step, samples were dipped into perfluoroperhydrophenanthrene (PFPP) lubricant, to create a lubricant-infused repellent barrier. The hydrophobicity of the treated and non-treated samples were investigated by measuring the water contact angle using a 5µl water droplet. Furthermore, to investigate the anticoagulant behavior of the lubricant-infused and untreated BNC samples, human plasma clotting assay was performed and the results were compared.

Results and discussion

In contrast to untreated BNC samples that immediately absorbed the water droplet, the lubricant-infused BNC samples showed water-repellency properties and a static contact angle higher than 115° was observed. Furthermore, modified BNC membranes had a significantly higher clotting time when compared with untreated samples (Figure 1, P <0.0001). In summary we report a simple surface modification method to significantly enhance the biocompatibility and repellency properties of BNC. The results confirm the successful treatment of super-hydrophilic BNC membranes with a super-repellent surface coating and creating BNC biointerfaces with superior anticoagulant properties that prevent non-specific adhesion.

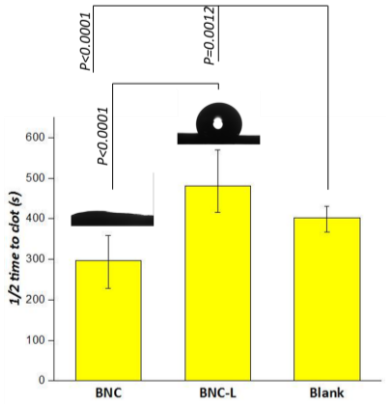


Fig 1. Human plasma clotting time in contact with BNC, lubricant-infused BNC, and blank plate

References

[1] Klemm, D. et al. Nanocellulose as a natural source for groundbreaking applications in materials science: Today's state. Mater. Today 21, 720–748 (2018).

[2] Gorgieva, S. Bacterial Cellulose as a Versatile Platform for Research and Development of Biomedical Materials. Processes 8, 624 (2020).

Stimulation-dependent quantification of trunk muscle responses to single-pulse epidural spinal stimulation

Sydney Schadan[1], Hossein Rouhani[1], Dimitry Sayenko[2], Albert H. Vette[1]
[1] Department of Mechanical Engineering, Faculty of Engineering, University of Alberta, Edmonton, AB, Canada.
[2] Department of Neurosurgery, Houston Methodist Research Institute, Houston, Texas, USA.

Introduction

Individuals with spinal cord injury (SCI) often suffer under impaired limb function and trunk control. Particularly the latter can result in the inability to remain upright posture during reaching and in secondary health complications such as compromised organ function [1]. Hence, it is not surprising that restoring trunk stability is ranked as a top priority among individuals with SCI. In this context, epidural spinal stimulation (ESS) delivers electrical current to the spinal cord to activate its networks. Through manipulation of ESS parameters (i.e., amplitude, frequency, pulse width) and of the stimulation location along the spine, ESS has been shown to improve lower limb function and trunk stability after SCI [2]. While past studies have investigated how ESS can improve functional outcomes of the trunk [1,2], the role of ESS parameters in the electrophysiological response of the trunk muscles is unknown. The objective of this study was to systematically investigate the effect of ESS electrode placement and single-pulse stimulation parameters on the muscle responses relevant to trunk stability.

Methods

10 adults undergoing electrode implantation for treatment of chronic lower back pain have been recruited to date. A 16- or 32-channel electrode array was implanted along the T4 to T8 vertebrae levels. We collected surface electromyography (EMG) from the external and internal obliques, rectus abdominis (bilaterally), and erector spinae muscles at the T6/T7 and L3 levels (unilaterally). Single-pulse ESS at 2 Hz and 500 µs pulse width was applied while two stimulation parameter domains were systematically manipulated: (1) electrode configuration (rostral-caudal, medial-lateral, anode-cathode variations); and (2) stimulation amplitude (1-10 mA). Collected EMG data were used to quantify relevant metrics, including amplitude, timing, and motor thresholds of evoked muscle responses. The metrics were then used to compare the effects of the stimulation parameters on trunk muscle responses.

Results

Variations in stimulation location along the rostral-caudal and medial-lateral axes affected the magnitudes, activation patterns, and motor thresholds of trunk muscle responses. Rostral vs. caudal stimulation produced varying magnitudes of responses, with 5 participants experiencing greater muscle responses from caudal stimulation (Fig. 1). Stimulation on the left vs. right side of the electrode array also affected the magnitudes of evoked muscle responses as all participants demonstrated preferential activation of ipsilateral muscles.

Conclusions

Trunk muscle activation via ESS is affected by stimulation amplitude and its location relative to the spine. Gained insights may guide ESS parameter selection for improving trunk stability after impairment.

Figure

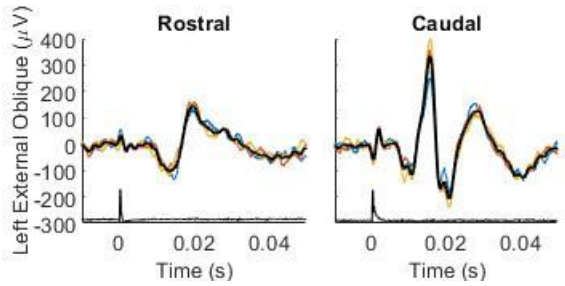


Fig. 1. Sample EMG data comparing evoked muscle responses of rostral and caudal ESS.

References

[1] M. Gill et al., Frontiers in Systems Neuroscience, vol. 14, Nov. 2020.
[2] C. Angeli et al., The New England Journal of Medicine, vol. 379, pp. 1244-1250, Sep. 2018.

Do Mechanical and Structural Differences in Degenerated Intervertebral Discs Result in Degenerative Scoliosis and Spondylolisthesis?

Taylor J. Bader, Manmeet Dhiman, David A. Hart, Neil Duncan, Paul Salo, Ganesh Swamy
University of Calgary, McCaig Institute, 3280 Hospital Dr NW, Calgary, Alberta, T2N4Z6

Introduction

Intervertebral disc degeneration (IVDD) is an age-related progressive structural failure of the disc[1]. Degenerated IVDs (degen) can result in back pain or radicular pain from impingement of nerve roots. Some patients develop malalignment of the spine, in the sagittal plane (degenerative spondylolisthesis (dSpondy)) or in the coronal plane (degenerative scoliosis (dScoli)). The incidence of both conditions is much higher in post-menopausal females[2,3].

While these conditions correlate to IVDD[4], why malalignment occurs in some cases and not others is poorly understood. We hypothesize that a reduction in shear stiffness of the AF may have a role in the development of the spinal deformities dSpondy and dScoli. The aim of the present study was to measure elastic shear properties between normal, degenerative, and deformity patient samples of the annulus fibrosus (AF).

Methods

Samples were collected from 30 patients undergoing anterior and lateral degen/dSpondy/dScoli surgeries, limited to L4-5 and L5-S1 discs (University of Calgary Ethics ID REB18-1308). Two identical 5mm^3 AF tissue cubes were prepared from each disc and shear loaded using custom made clamps. One cube was tested in radial shear, and the other in a circumferential direction, mimicking shear deformation observed in dSpondy and dScoli, respectively (Figure 1). Four strain intervals of 2.5% with 20-minutes of relaxation were employed, totalling 10% strain. Shear modulus was calculated using a line of best fit between each of the most stress-relaxed points of the four strain intervals.

Results

In the radial direction, there were no significant difference between groups (p=0.6) (Figure 2). In the circumferential direction, there was a trending decrease in dScoli sample shear stiffness when compared to degen (p=0.08) but also exhibited no overall significant difference between groups (p=0.3). Within the degen samples, AF from females had reduced shear stiffness as compared to male AF in both the radial (5±4 vs. 11±8, ($p<0.05$)) and circumferential (20±10 vs. 51±25 ($p<0.05$)) direction (Figure 3).

Conclusions

These results suggest that the degenerated AF in female patients is less stiff in shear than male patients. Ongoing expansion of the patient base and inclusion of data from normal control IVD samples will strengthen the current preliminary trending decrease seen between degen and deformity samples. Biochemical and histological assessments will additionally allow further investigation of structure-function relationships between dScoli / dSpondy IVDs and degen IVDs.

References

1. Adams,M.A. & Roughley,P.J. (2006).
2. Ghogawala, Z. *et al.* (2016).
3. Schwab, F. J. *et al.* (2013).
4. Castelein, R. M., (2020).

Figures

Figure 1

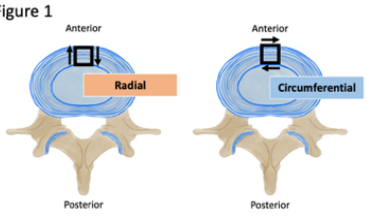


Figure 2

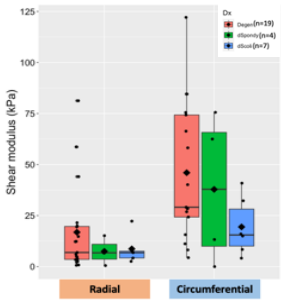
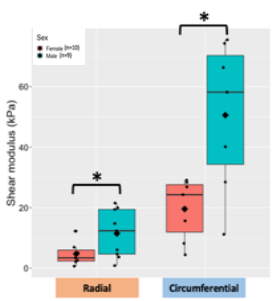


Figure 3



Development of a Finite Element Model to Examine the Response of the Advanced System for Implant Stability Testing (ASIST) in Dental Implants

Tod Vandenberg, Chester Jar, Lindsey Westover
University of Alberta, Department of Mechanical Engineering

Introduction

A dental implant can only be successful if the surface of the implant is effectively integrated into the bone. Many factors can affect the bone growth around the implant such as loading conditions, environmental conditions, and implant conditions [1]. To examine and measure the degree of osseo-integration between the implant and the bone, a new instrument has been developed: the Advanced System for Implant Stability Testing (ASIST) [1]. This device uses an impact rod to strike a dental implant and measure the vibration response. The response is then compared to a four degree of freedom mathematical model to find an estimate for the stiffness of the bone-implant interface. Development of a Finite Element (FE) model of the dental implant system under impact loading will allow for cross-validation of the ASIST modelling approach and enable simulation of a wide range of conditions that are difficult to replicate in a lab environment.

Methods

A simplified dental implant system (modelled after the Straumann bone-level implant and healing abutment) was created using SolidWorks. These parts were: a bone block, and interface layer, the implant/abutment, and the impact rod of the ASIST. The geometry was imported to ABAQUS, with material properties similar to the materials used when testing the ASIST on synthetic bone samples in previous experiments. Boundary conditions were applied, and the impact rod was given an initial velocity. The acceleration response of the impact rod as it struck the abutment was extracted and then compared with measured experimental data. A custom Mathematica code was used to determine its ASIST Stability Coefficient (ASC) which is a measure of the interface stiffness. The vibration frequencies were also extracted using Fast Fourier Transforms, as well as the R^2 value comparing the fit of the FE response to the experimental data. The ASC and frequencies were then compared between the model, and the lab experiment of the same properties and conditions.

Results

The data from the FEM gave an average R^2 value of 0.90 when compared to lab data. Each experimental data set's primary frequency was within 10% of the FE primary Frequency of 2301Hz and had a major frequency within 8% of the Secondary Frequency of 29.00kHz. The ASC value for the FE modelled implant was 14.4, while for similar implants tested, the ASC ranged from 13.6 to 16.7. An agreement between the FE response, and experimental data is shown in the attached Figure.

Conclusions

The evidence shows that the FEM response is closely aligned with the experimental data. Parameters of the model can now be tuned further to explain differences between similar experiments and predict behavior such as crestal bone loss or osseo-integration failure that cannot be created in a lab setting.

References

[1] Shriya Nimbalkar et al., *Materials Today: Proceedings*, vol. 43, pp. 970-976, 2021.

[2] e. Mostafa Mohamed et al., *Journal of Biomechanics*, vol. 124, p. 110570, 2021.

Figures

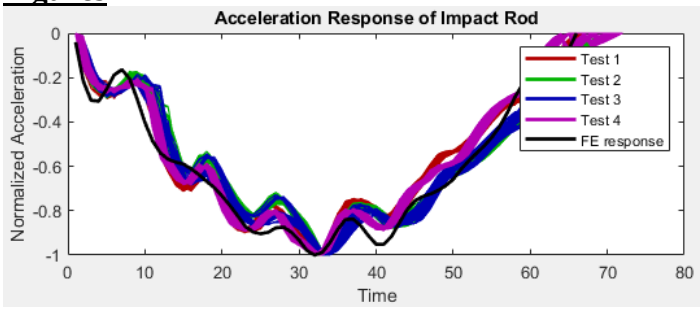


Figure 1: Comparison of FE and Experimental Acceleration Responses

Does Botox-Induced Paraspinal Muscle Weakness Result in Osteoarthritic Changes in Facet Joints?

Torri Heiser, Ruth Seerattan, Venus Joumaa, Andrew Sawatsky, Tim Leonard, Walter Herzog
Human Performance Lab, Faculty of Kinesiology, University of Calgary, Calgary, Alberta
McCaig Institute, University of Calgary, Calgary, Alberta

Introduction

Low back pain is a leading cause of disability [1]. Compromised facet joints (FJs), like in osteoarthritis, may contribute to this pain [2]. Paraspinal muscle (PS) weakness has been linked to FJ degeneration [3]. However, a cause-and-effect relationship between PS muscle weakness and compromised FJs has not been established. Injecting muscles with Botulinum toxin type-A (Botox) is a reliable way to induce muscle weakness, and this technique has been used previously to investigate the effect of quadriceps weakness on knee joint degeneration [4].

Our objective was to determine the possible cause-and-effect relationship between Botox-induced PS muscle weakness and osteoarthritic changes in the FJs in rabbits. We hypothesized that Botox-induced PS muscle weakness results in osteoarthritic changes in the FJs.

Methods

Twelve female New Zealand White rabbits were injected with Botox (3.5units/kg, experimental, n=6) or saline (control, n=6) into the PS muscles at L3-L4, L4-L5, and L5-L6. At week 24, the animals were sacrificed, and the L4-L5 and L5-L6 joints underwent decalcification, paraffin processing, and were cut and stained using Hematoxylin, Safranin O, and Fast Green. The slides were reviewed by two blinded observers and scored for osteoarthritic changes.

Results

The experimental Botox injected animals showed mild osteoarthritic changes compared to their control counterparts (Figure 1). A significant increase in the score of osteoarthritic changes was found at the L4-L5, but not the L5-L6 FJs of the experimental Botox group animals.

Discussion and Conclusions

These results suggest that PS muscle weakness may indeed be an independent risk factor for the development of FJ degeneration, possibly leading to FJ osteoarthritis and back pain. However, possible reasons for the absence of dramatic osteoarthritic changes in the FJs of Botox animals may be due to differences in load bearing of quadrupedal animals, like rabbits, when compared to humans. Additionally, Botox spreads after injection, therefore it is possible that the L4-L5 level was impacted more than L5-L6 as the animals were injected above, at, and below this level. Furthermore, altering the protocol to include multiple Botox injections, increasing the Botox dose, and evaluating the entire lumbar spine may provide more insight.

References

[1] Global Burden of Disease Study, 2010.
[2] Gellhorn et al., 2013.
[3] Kalichman et al., 2016.
[4] Youssef et al., 2009.

Figures

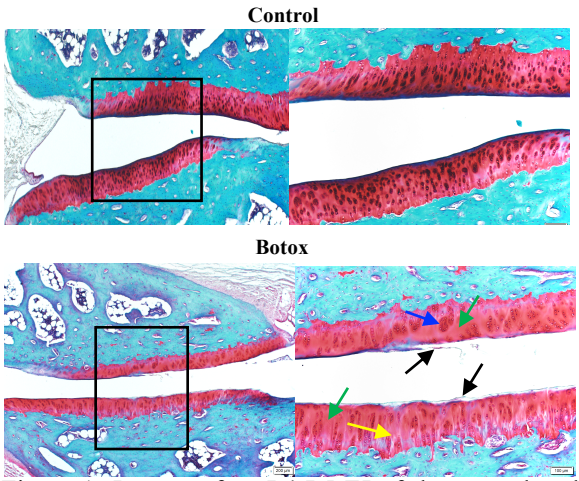


Figure 1. Images of an L4-L5 FJ of the control and Botox groups at x4 (Left) and x10 (Right) magnification. The Botox joint shows surface irregularities (black arrows), cell loss (green arrows), cell clustering (blue arrow), and matrix thinning (yellow arrow).

Effects of Cyclic Loading Interruption on Bovine Cortical Bone

Tudor Muresan, Ifaz Haider, W. Brent Edwards
Human Performance Lab and McCaig Institute for Bone and Joint Health, University of Calgary

Introduction

Stress fractures are a common injury among athletes. Their mechanisms are frequently studied *in vitro* by continuous cyclic loading of bone until failure[1]. However, *in vivo* bone is not continuously loaded, rather loading is interrupted during rest. The influence of load interruption on bone fatigue life remains unclear[1]. Thus, the purpose of this study was to quantify differences in fatigue life of bone loaded continuously vs. bone loaded with interruption.

Methods

30 samples of cortical bone were harvested from bovine tibiae and machined into 3 x 3 x 20 mm prismatic beams. Samples were split into two groups across three load levels (140, 150, and 160 MPa). Per level, groups were balanced such that apparent BMD differences were insignificant.

Samples were cyclically loaded in a 4-point bending configuration at 2 Hz until failure or runout (500,000 cycles). The control group was loaded without interruption, while the interrupted group received 2 hours of rest per hour of cyclic loading.

Results

Preliminary results from the 140 MPa level are discussed here. The mean (± SD) number of cycles to failure for the continuous and interrupted groups was 237,873 ± 211,957 and 220,180 ± 194,076, respectively (Figure 1). Survival analysis demonstrated this difference was not statistically significant (p=0.87).

Conclusions

Our preliminary results indicate no detectable difference between continuous and interrupted loading, suggesting passive strain recovery associated with load interruption does not influence fatigue life. However, this observation may be specific to load level and additional testing is ongoing.

References

1. Caler and Carter, 1989, J. Biomechanics

Figures

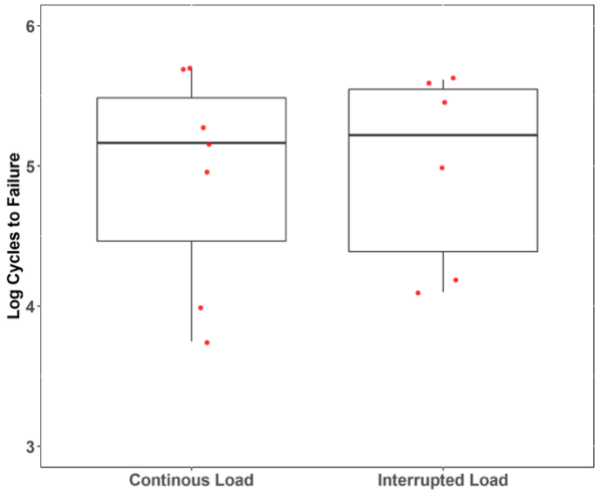


Figure 1: Fatigue testing results from 140 MPa load level. Differences between groups were not statistically significant (p=0.87)

Understanding Robotic Gait Trainers Usage Data for Children with Mobility Disorders

Santos TA[1], Diot CM[2], Friesen AH[3], Youngblood JL[3], Norman B[3], Condliffe EG[3,4]
[1]Schulich School of Engineering, [2]Alberta Children's Hospital, [3]Departments of Clinical Neuroscience and [4]Pediatrics Cumming School of Medicine
Alberta Children's Hospital Research Institute & Hotchkiss Brain Institute

Introduction

Training needs to be done frequently as well as long and intense enough for neurorehabilitation to be effective. Robotic gait trainers have been used in clinical settings with positive effects, but little is known of the usage in people's home communities. At home usage can address clinical limitations by allowing for more frequent sessions. We developed an approach to quickly process and present usage data that occurs during training to understand what occurs.

Methods

An observational study was performed involving participants who used a Trexo for six months. Trexo collects: the date, usage time, steps taken, and average cadence (steps/minute). Code was developed that sorts through the Trexo database, processes desired participants usage data, and generates summary usage information for each participant and the group.

Results

Over their first six months, 37 participants used a Trexo for median (25^{th}-75^{th} percentile) 63 (29 – 106) min/week, divided into 3 (1 – 4) sessions, taking 1267 (671 – 3192) steps/week, with an average cadence of 25 (12 – 35) steps/minute. At 6 months participants used the Trexo for fewer minutes and sessions/week but walked slightly faster while using it (Table 1).

Discussion

Although children are using the Trexo less after six months, they are achieving greater step counts that are otherwise unobtainable for the population and their training is becoming more efficient. This can be shown as there is no visible step decrease despite significant usage decrease. With the developed approach, clinicians and researchers can easily access usage data on an individual and group level to understand training times and intensities of training for children performing robot-assisted gait training in their home communities.

Figures

	Change in Usage median (25^{th} 75^{th} percentile)	p-value
Usage time (min/week)	-30 (-67 -1)	0.001
Times used (counts/week)	-2 (-3 -1)	<0.001
Steps (counts/week)	40 (-496 542)	0.83
Average cadence (steps/minute)	4 (-3 18)	0.032

Table 1: The change in usage at the 6-month compared with the first month's descriptive statistics and results of a Wilcoxon signed-rank test of difference for related samples (with a Bonferonni Correction ($\alpha = 0.0125$) are presented).

Investigating the effect of normobaric oxygen therapy in the experimental autoimmune encephalomyelitis (EAE) mouse model of MS

Uche J Ohaezukosi, Rania Muhammed, Qandeel Shafqat, Ying Wu, Jeff F Dunn
Hotchkiss Brain Institute, Cumming School of Medicine, University of Calgary

Introduction

Multiple sclerosis (MS) is a chronic neurological disease involving demyelination and inflammation. Recently, MS has been associated with significant reductions in cerebral blood flow (CBF) and brain hypoxia[1]. We propose that hypoxia can intensify inflammation in MS via activation of pro-inflammatory NF-κB[1]. This may hasten CNS damage and disease progression in MS[1]. It is important to understand the effects of hypoxia and possible treatments of it in the context of MS.

Previously, oxygen therapy was shown to slow the formation of demyelinating lesions in the spinal cord of an inflammation induced autoimmunity MS model known as the experimental autoimmune encephalomyelitis (EAE)[2]. Oxygen therapy might reduce brain hypoxia and inflammation, and ultimately improve symptomology in EAE. We investigated the effect of acute normobaric oxygen therapy on cerebral blood flow (CBF) and behavior in EAE mice using 9.4T in-vivo MRI.

Methods

C57BL/6 mice (n=18) underwent 9.4T MRI at baseline for CBF with arterial spin labeling (TE= 2.7, TR= 3). All mice were induced with EAE using myelin oligodendrocyte glycoprotein (MOG) in complete Freund's adjuvant and pertussis toxin (CFA-PTX). EAE mice were randomly split into a room air (n=11) or oxygen-treated group (n=7). Mice were assessed for symptoms using the 15-point clinical scoring scale. Oxygen treatment (100% normobaric) was started at the first sign of symptoms (~Day 12), for 6 hours/a day for 5 days. Following room air or oxygen-treatment, mice were imaged for assessment of CBF. Behavior was assessed using open field for changes in locomotion.

Results

At baseline (pre-EAE), there were no significant differences in CBF between the room air vs the oxygen-treated groups in the left hippocampus (188±14 mL/100g/min vs 188±13 mL/100g/min, respectively, $p>0.05$), right hippocampus (188±10 mL/100g/min vs 189±16 mL/100g/min, respectively, $p>0.05$), left cortex (223±5 mL/100g/min vs 228±19 mL/100g/min, respectively, $p>0.05$), or the right cortex (217±16 mL/100g/min vs 223±7 mL/100g/min, respectively, $p>0.05$). Using a paired t-test, we found that CBF in the room air EAE group was significantly reduced in the bilateral hippocampi and bilateral sides of the cortex at peak EAE as compared to pre-induction. In the oxygen treated EAE group, there were no significant differences in CBF after oxygen treatment at peak EAE as compared to pre-treatment CBF in the left and right hippocampus. However, there was a significant reduction in the CBF at peak EAE post oxygen treatment in the left and right cortex as compared to pre-treatment. The behavioral results are being analyzed. We expect an increase in locomotion post oxygen therapy.

Conclusions

We used CBF and behavior as markers of the magnitude of EAE (a model of MS). Given the range of variability of CBF, and that the hippocampal blood flow did not drop significantly in the oxygen treated animals, this study shows promise but is not definitive. Behavior data will follow.

References

1. Yang R and Dunn JF. Multiple sclerosis disease progression: Contributions from a hypoxia-inflammation cycle. Mult Scler. 2019; 25: 1715-8.
2. Davies et al. Neurological deficits caused by tissue hypoxia in neuroinflammatory disease. Ann Neurol. 2013; 74(6):815-25

Running with Varying Stiffness Across Different Shoes Affect Lower Limb Biomechanics

Nguyen V[1], Firminger CR[2], Cigoja, S [2], Fletcher JR[1], Clermont CA[1], Edwards WB[2], Nigg BM[2], Asmussen MJ[1]
[1]Department of Biology, Mount Royal University [2]Faculty of Kinesiology, University of Calgary

Introduction

Footwear longitudinal bending stiffness has been shown to affect a person's lower-limb biomechanics during running. However, the underlying mechanisms of why longitudinal bending stiffness affects lower limb biomechanics are not well understood. Additionally, there are a lack of studies focusing on the effects of footwear stiffness on a person's biomechanics during non-linear running, which may have different footwear requirements relative to linear running. The aim of this study was to investigate how running with varying stiffness across different shoes may affect lower limb biomechanics.

Methods

This study utilized previously collected data from Cigoja et al. (2019), where thirteen male, recreational runners ran on an instrumented treadmill at 3.5 m/s in four shoe conditions with modified stiffness from a carbon fibre insole: (1) control condition in both shoes, (2) stiff conditions in both shoes, (3) stiff condition in right shoe only and (4) stiff condition in left shoe only.

Results

Increased footwear longitudinal bending stiffness did not significantly decrease negative metatarsophalangeal (MTP) joint work or significantly increase positive MTP joint work (1,2). Furthermore, no significant differences between MTP joint angles (p=0.54) were found when running in varying stiffness conditions on each foot (3,4). However, there were significant differences between MTP joint moment ($p \leq 0.05$) and MTP joint work ($p \leq 0.05$) found when running in varying stiffness conditions on each foot (3,4).

Conclusions

Running with varying stiffness on each foot affects MTP joint biomechanics. Increased footwear stiffness resulted in an increase in negative MTP joint work. Furthermore, based from a kinematic standpoint, the MTP joint did not seem to be controlled independently when running with varying stiffness across different shoes. However, from a kinetic and energetics standpoint, the MTP joint seem to be controlled independently when running with varying stiffness across different shoes. A more thorough analysis of the hip, knee and ankle is currently being analyzed to understand how humans adapt to footwear with varying stiffness in each shoe.

References

Cigoja, S., Firminger, C. R., Asmussen, M. J., Fletcher, J. R., Edwards, W. B., Nigg, B. M. (2019). Does increased midsole bending stiffness of sport shoes redistribute lower limb joint work during running? *J Sci Med Sport*. 22:1272–7.

Figures

Right Foot MTP Joint Angle

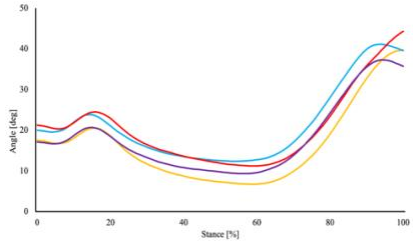


Figure 1. Right foot MTP joint angle across four footwear conditions: no (yellow), both (blue), left (red) and right (purple).

Right Foot MTP Joint Moment

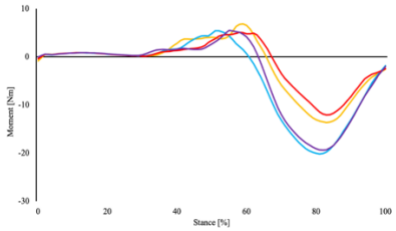


Figure 2. Right foot MTP joint moment across four footwear conditions: no (yellow), both (blue), left (red) and right (purple).

Right Foot MTP Joint Work

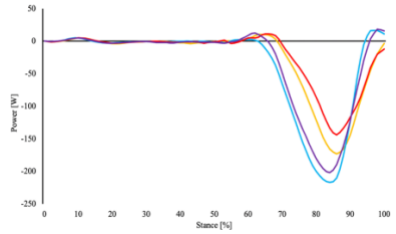


Figure 3. Right foot MTP joint work across four footwear conditions: no (yellow), both (blue), left (red) and right (purple).

A Dynamic Procedure to Detect Maximum Voluntary Contraction in Lower Back

Xun Wang[1], Karla Beltran Martinez[1], Ali Golabchi[2,3], Mahdi Tavakoli[4], Hossein Rouhani[1]

[1] Department of Mechanical Engineering, University of Alberta, Edmonton AB
[2] Department of Civil and Environmental Engineering, University of Alberta, Edmonton AB
[3] EWI Works Inc, Edmonton AB
[4] Department of Electrical and Computer Engineering, University of Alberta, Edmonton AB

Introduction

To evaluate muscle activities, a procedure is needed to normalize the raw electromyography (EMG) data from the sensor. The maximum voluntary contraction (MVC) test as a standard for normalization can be used to evaluate muscle activity and fatigue on an individualized basis [1]. However, the currently recommended MVC procedure for lower back muscles involves muscles that do not reach their maximum contraction level. Thus, the collected MVC data are lower than those collected in the actual task. Therefore, this study aims to propose a novel procedure for MVC data collection for lower back muscles and compare outcomes with those of traditional procedures.

Methods

We collected MVC data from 10 able-bodied participants (6 males, 4 females). EMG sensors (Trigno Avanti, Delsys, US) were placed on both right and left latissimus dorsi and thoracolumbar fascia. Four MVC procedures (trunk bending, leg bending, above combined and standing posture) were performed [2]. In addition, we proposed a fifth dynamic MVC procedure for lower back muscles, in which the participants were asked to lift a 45 lbs. weight with proper extra force against lifting only using the back muscles for 3 times as part of the MVC collection test. During this procedure, the elbow and knee joints were locked and the body motions were aimed to be smooth and slow. Then, the participants were asked to lift the weight freely without extra force to duplicate the actual physical test. We normalized the EMG data collected during this final test using the five earlier-mentioned MVC procedures. The max values of EMG data for the weight-lifting task after normalization with these MVC procedures were compared together.

Results

The actual lifting test results normalized by the proposed dynamic MVC procedure did not exceed 100%, unlike those normalized by the four traditional MVC procedures. Also, the dynamic MVC procedures normalization results always showed the lowest value among all five MVC procedures for all the participants (Fig. 1) and the results were tested by paired T-test with p-values less than 2.5%, which means the dynamic MVC value is much higher than other methods.

Conclusions

The traditional MVC procedures for the lower back muscles do not lead to higher contraction levels than those in the actual lifting tasks. Our proposed dynamic MVC procedure produced the highest contraction level and is recommended for EMG data normalization for the lifting tasks. Other dynamic MVC procedures should be proposed for other tasks.

References

[1] Butler, T R, Jason C G, "Exoskeletons Used as a PPE for Injury Prevention." Professional safety 64 (2019):32-37.

[2] Vera-Garcia F J, Moreside J M, McGill S M. "MVC techniques to normalize trunk muscle EMG in healthy women." Electromyogr Kinesiol. (2010):10-6.

Figures

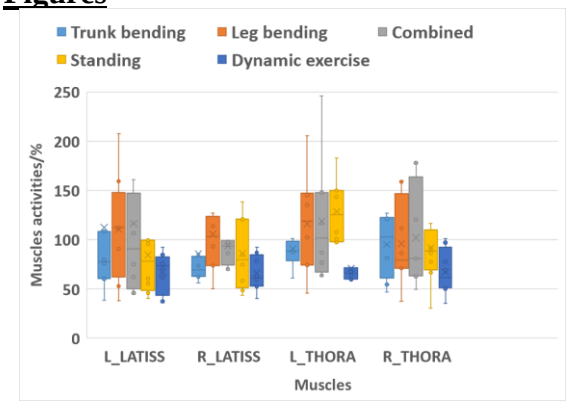


Fig. 1. Normalized results for simulated tasks by five MVC tests.

Development and Validation of a Depth-Dependent Transversely Isotropic Finite Element Model of Cartilage: Cross-Validation and Comparison with Fibril-Reinforced Poroelastic Approach

Zahra Khoz[1], Saija Kontulainen[2], J.D. Johnston[1]

1. Department of Mechanical Engineering, University of Saskatchewan, Saskatoon, Canada
2. College of Kinesiology, University of Saskatchewan, Saskatoon, Canada

Introduction: Osteoarthritis (OA) is a debilitating joint disease marked by cartilage degradation and changes to underlying subchondral bone. Approximately 10% of Canadians suffer from OA, 50% of which exhibit knee OA [1]. There is no known cure and the origins of the disease and joint pain are unclear.

Subject-specific finite element (FE) modeling has been used to investigate the origins of OA by evaluating the effects of altered subchondral bone geometry and mechanical properties on joint pain [2] as well as the effects of altered joint alignment, gait, impact loading, as well as fatigue loading on cartilage mechanical properties [3]. A recent study completed by our group found large differences in bone stress in individuals with high levels of joint pain [4]. However, the study was small (n=42) and further research with a larger-sample is needed. The applied FE model, which is continuum-based and well-suited for large-scale application, accurately modelled bone but used a simplified, unvalidated representation of cartilage. Specifically, cartilage was modelled as a uniform structure between articulating bones with a single elastic modulus, whereas cartilage is a complex structure with varying mechanical properties through-out the structure and different mechanical responses depending upon the loading type (e.g., static vs dynamic). There is a need to advance our FE model of cartilage to more accurately reflect cartilage mechanical behavior.

At present, poroelastic [5, 6] and fibril-reinforced FE approaches [7, 8], which characterize the dynamic, static, and time-dependent responses of materials, as well as contact mechanics, have been used to simulate the mechanical behavior of cartilage. These approaches, which are mesh-based, are often time-consuming to construct and the convergence time is long, making clinical application and large-scale investigations questionable. A less computationally expensive technique pertains to continuum-level FE models of cartilage, which can be integrated with our existing continuum-level FE model of bone. Here cartilage would be modelled using brick-elements with isotropic or transversely isotropic material properties which vary by depth from the cartilage surface [9]. These techniques though have not been validated for estimating cartilage mechanical behavior (e.g., stiffness, contact mechanics).

The overall objective of this research is to advance a continuum-level FE model of the knee to predict cartilage stiffness behavior.

Methods:

Specimens: Twenty fresh-frozen cadaveric knees (10M:10F), without any evidence of musculoskeletal disease or other injuries, will be acquired from an anatomical tissue bank.

Model Development: Distal femora and patellae will be dissected and imaged using high resolution peripheral CT. Mechanical indentation testing and needle testing (via a Mach 1) will be used to measure cartilage stiffness (instantaneous, equilibrium) and thickness across the articular surfaces. Cartilage thickness will be mapped to CT image data of femoral and patellar bone. Using an in-house solver (Matlab) [10,11], isotropic and transversely isotropic material properties of cartilage will be modelled with the depth-specific material properties [9].

Experimental Validation: Using the mechanical indentation results, combined with back-calculation, optimum material properties will be defined for the isotropic and transversely isotropic models of cartilage. Various material constants and E_1/E_3 ratios will be evaluated using a neural network and Nelder-Mead optimization [12]. Linear regression will be used to characterize model accuracy.

Comparison Study: Gold-standard fibril-reinforced poroelastic material models of cartilage [7,8] will be constructed and compared alongside the optimized isotropic and transversely isotropic models of cartilage.

Results to date: The research is currently in progress Testing devices have been prepared and methodologies are being developed.

References

[1] Health Canada, 2003 [2] Burnett, 2015 [3] Andriacchi, 2004 [4] Burnett, 2018 [5] Wilson, 2003 [6] Donahue, 2002 [7] Korhonen, 2003 [8] Li, 2000 [9] Federico, 2005 [10] Zaluski, 2020 [11] Franco, 2022 [12] Nazemi, 2017

Analysis of Human Musical Cognitive Preferences

Fariha Iffath, Marina L. Gavrilova
Department of Computer Science, University of Calgary, Calgary, AB T2N 1N4, Canada.

Introduction

Music has the potential of transmitting information to the brain that has substantial impacts on human cognition, emotional regulation, and aesthetic interactions. Over the last few decades, music has received unprecedented attention in the biomedical research [1]. Human aesthetic refers to a person's preference towards a particular subject material. Within this discipline, music aesthetics can be utilized to solve identification problems, as well as to analyze the stimulation of human brain, thoughts, feelings, and kinesthetic sense [2]. Our research demonstrates the efficacy of music aesthetics for person identification, which can be further extended for human cognitive analysis and biomedical research.

Method

The flow of the proposed system is divided into four stages: Data Pre-Processing, Feature Extraction, Feature Selection, and Classification. Initially, the raw mp3 data representing aesthetic music preferences is converted into mel-spectrograms. Next, a high-dimensional feature vector is extracted from the mel-spectrograms using a pre-trained CNN Residual Network (ResNet) architecture. A novel hybrid meta-heuristic feature selection algorithm based on Cuckoo Search and Whale Optimization (CSWOA) is proposed to generate a low-dimensional feature set. Finally, the selected subset of best features is fed into XGBoost classifier to establish an individual's identity.

Results:

From Table 1, it is observed that the proposed method obtained 99.54% and 99.79% rank 1 accuracy of person identification on a proprietary dataset FMA (Free Music Archive) and a publicly available dataset MPD (Million Playlists Dataset), respectively. The proposed method also outperformed the classical machine learning based state-of-the-art method [3].

Dataset	System	Accuracy
FMA	Classical ML [3]	95.74%
	Proposed Method	99.54%
MPD	Classical ML [3]	99.60%
	Proposed Method	99.79%

TABLE 1: Comparison of Rank 1 Accuracy with the State-of-the-Art Method.

Conclusion

As a rule-based sensory language, music aesthetic has recently emerged as a fascinating field of human cognitive analysis. This work proposed a deep-learning based framework for person identification from audio aesthetic. The system outperformed the existing state-of-the-art method in audio aesthetic research. The significant outcome of this study demonstrates that musical preference holds distinctive features that can be used in robotics and biomedical research.

References

1. Naser, D. S., & Saha, G. (2021). Influence of music liking on EEG based emotion recognition. *Biomedical Signal Processing and Control*, *64*, 102251.
2. Thaut, M. H. (2013). Biomedical research in music. In *Rhythm, music, and the brain* (pp. 61-84). Routledge.
3. Sieu, B., & Gavrilova, M. L. (2021). Person identification from audio aesthetic. *IEEE Access*, *9*, 102225-102235.

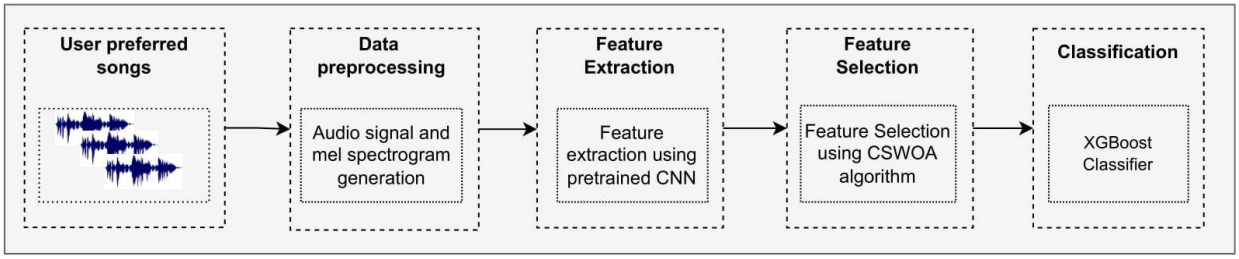


FIGURE 1: Overall flowchart of the proposed music aesthetics deep learning system.

IMAGING CHARACTERISTICS OF A WEIGHT-BEARING, CONE BEAM COMPUTED TOMOGRAPHY SYSTEM

Tadiwa H. Waungana[1,2,3*], Ying Zhu[2,3], Justin J. Tse[2,3] and Sarah L. Manske[1,2,3]
[1]Biomedical Engineering Graduate Program, University of Calgary, Alberta, Canada
[2]McCaig Institute for Bone and Joint Health, University of Calgary, Alberta, Canada
[3]Department of Radiology, Cumming School of Medicine, University of Calgary, Alberta, Canada
email: *tadiwa.waungana@ucalgary.ca

Introduction

Cone beam computed tomography (CBCT) has been used to facilitate weight-bearing computed tomography (WBCT), which allows cross-sectional imaging of the lower extremities whilst the patient is standing in a fixed-flexion position [1-2]. This allows WBCT to provide an improved representation of load-bearing joints compared to traditional supine CT [3]. Cone beam systems are known to present with characteristic cone beam artifacts towards the peripheries of the field of the view (FOV)[4], reducing the FOV in which accurate measurements can be made. To establish their efficacy as a quantitative imaging modality, CBCT systems need to be assessed using methods that have been developed for quantitative measures of CT performance. Quality assurance CT phantoms are used to measure key performance metrics such as the spatial resolution, linearity of x-ray attenuation and uniformity. The purpose of this study was to characterize the performance of a cone beam, WBCT scanner and to establish its efficacy in quantitative analysis of bone mineral density (BMD).

Methods

Three different CT phantoms were scanned using the HiRise CT imaging x-ray system (CurveBeam, Hatfield, PA) in the weight-bearing configuration (130 kVp, 6.5 mA). Individual image slices containing the relevant evaluation plates were extracted using 3DSlicer. The slant edge, geometrical accuracy and linearity evaluation plates were analysed using a semi-automated MATLAB code to quantitatively determine the spatial resolution, in-plane pixel spacing and linearity of x-ray attenuation respectively. Linearity was evaluated using vials of varying iodine concentration and the mean signal intensity measured at each vial. A BMD phantom consisting of uniform rods of varying hydroxyapatite (HA) concentrations was used to assess uniformity. The region along the height of the FOV that was unaffected by cone beam artifacts was determined using a Python-based code.

Results and Discussion

The measured spatial resolution (319µm) was larger than the nominal pixel size (300µm), indicating that some blurring will be present when observing an object that is the same size as the pixel size. The signal intensity varied linearly with increasing iodine concentration over the tested range ($R^2 = 0.98$). The measured in-plane pixel spacing (299µm) was smaller than the nominal pixel size, implying that errors may be present when estimating physical dimensions using the number of pixels traversed by an object in the image.

The useable height in the superior-inferior direction was estimated to be approximately 12.0 cm when looking at a central coronal slice. This indicates that approximately 62% of the total height of the FOV (40.1 cm diameter x 19.5 cm height) is absent of any cone beam artifacts and therefore useful for quantitative imaging. On average, the variation in measured BMD (mgHA/cm^3) along uniform BMD rods of 400 and 800 mgHA/cm^3 in the axial plane was 45 and 118 mgHA/cm^3 respectively. Corresponding variations in the coronal plane were 16 and 18 mgHA/cm^3 respectively. This was accompanied by a decrease in measured BMD in the superior-inferior direction of the coronal view.

Conclusion

These results demonstrate that the performance of the WBCT system, in isolation, is not adequate to conduct quantitative analysis of BMD. Corrective algorithms (e.g., improved calibration and beam hardening correction algorithms) may need to be developed to account for the signal intensity variations across the useable FOV.

References

1. N.A. Segal *et al.,* 2017. *J. Orth. Re.*
2. T.D. Turmezei *et al*., 2021. *Radiology*
3. E.K.J. Tuominen *et al*., 2013. *Am. J. Roent.*
4. J.F. Barret and N. Keat. 2004. *Radiographics*

The Link Between Oxygen Consumption Rate and In Vitro Chondrogenesis for Cartilage Tissue Engineering

Zhiyao Ma[1], Xiaoyi Lan[1], David X Li[2], Melanie Kunze[1], and Adetola B Adesida[1]

[1]Department of Surgery, Faculty of Medicine and Dentistry, University of Alberta
[2]Department of Civil and Environmental Engineering, Faculty of Engineering, University of Albert

Introduction: Cartilage has a limited capacity to self-heal due to a lack of blood supply and tissue engineering is a potential strategy for repairment. Two potential cell sources for engineering cartilage are nasal chondrocytes (NC) and bone marrow derived mesenchymal stromal cells (MSC) given their chondrogenic capacities. Both cell types exist under a low oxygen microenvironment. And low oxygen tension has been indicated to augment the chondrogenic capacity of BMSC. The coculture of NC and MSC was proposed as an alternative to pure cell culture due to their synergistic chondrogenic capacity. However, there is paucity of data on the role of oxygen tension or its consumption during chondrogenic coculture of NC and MSC. Understanding how oxygen tension and its consumption contributes to the synergistic interaction of NC and MSC may advance our understanding of the role of oxygen tension in *in vitro* chondrogenesis. In this study we investigated the relationship between oxygen consumption rate and chondrogenic capacity through gene expression, matrix deposition, and mechanical strength measurements of pellets composed of different ratios of NC and MSC.

Materials and methods: NC were isolated from human septal cartilage specimen via collagenase treatment and MSC was isolated via plastic adherence culture. Both cell types were expanded in culture until passage (P1) before cryo-banking. To construct a 3D pelleted culture model, the banked NC and MSC were thawed and expanded to passage 2, after which NC and MSC were mixed at various ratios (NC: MSC 1:1, 2:1, 3:1, 1:2, and 1:3) or kept as monoculture to form 0.5 million cells/pellet by centrifuge. The pellets were statically cultured for 4 weeks under normoxia (21% O_2) in chondrogenic media and the real-time oxygen consumption rate (OCR) during the entire period of culture was measured (every 15 min) by RESIPHER real-time cell analyzer (Lucid). Medium changes were performed every 3 days and pellets were collected on day 6, 9, 12, 15, 21 and 27 for gene expression by RT-qPCR and matrix deposition by histological and immunofluorescence assessments. Micromechanical testing and biochemical assays for glycosaminoglycan (GAG) matrix and DNA contents were conducted on day 27 pellets.

Results and Discussion: The real-time oxygen consumption measurements revealed that the coculture of 1:3 ratio (NC:MSC) had the highest metabolic activity (OCR) throughout the entire culture period (Figure 1), and it also had the highest mechanical strength at the end of culture. On the transcriptome level, the expression of chondrogenic markers was positively correlated with the proportion of NC and hypertrophic marker *COL10A1* is positively correlated with the proportion of MSC. On the protein level, noticeable deposition of collagen type I occurred on day 6 of culture while collagen types II and type X occurred later The group with the highest NC proportion displayed the highest collagen type II deposition and the group with the highest MSC proportion displayed the highest type X collagen deposition.

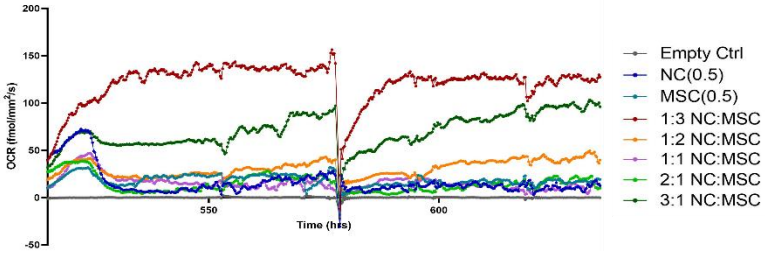


Figure 1. Real-time oxygen consumption rate of experiment groups from day 21 to day 27.

Conclusion: The OCR of the coculture pellets was influenced by the ratio of presenting NC and MSC, indicating the complex interaction between the two cell types. The adapted metabolic activity in turn affects the cell proliferation rate, chondrogenic markers expression, and matrix deposition. Detailed modeling will be conducted in the future to determine precise metabolic profiles of each cell type and to determine the cell-cell interactions.

Chondrocyte deformations during cyclic loading

Baaba S. Otoo[1,2] and Walter Herzog[1,2]
[1]Human Performance Laboratory, University of Calgary, Calgary, AB, Canada
[2]Department of Biomedical Engineering, University of Calgary, Calgary, AB, Canada

Introduction

Cartilage cells (chondrocytes) are known to respond to mechanical loading through changes of their shape and volume, which in turn produce mechanobiological responses that determine the health of the tissue [1]. Biological responses to mechanical loading have been shown to occur primarily in dynamic situations and are essentially absent for static conditions. Previous studies aimed at elucidating the cellular responses to loading were focused almost exclusively on static, steady-state conditions [2] likely due to limitations in spatial and temporal resolution of available imaging techniques. The objective of this study was to measure the instantaneous strains of chondrocytes for dynamic cartilage loading conditions. We hypothesized that the dynamic chondrocyte mechanics differ substantially from those obtained for static conditions.

Methods

6-mm diameter cartilage-bone specimens were harvested from the femoral groove of porcine knees (N=10). The cylindrical specimens were halved and mounted on a custom-designed mechanical loading device that allowed for simultaneous cell imaging and mechanical loading. Specimens were loaded cyclically (20% strain; 0.2Hz; 100 cycles) and statically (20% strain; 20 min). Image stacks were acquired at selected timepoints for the static and dynamic loading conditions. Analysis of cell volume and axial strains were performed using ImageJ and PyCell Analyst, (cyclic n=32; static n=15).

Results

Cells from statically loaded tissue samples deformed to a volumetric strain of -0.13 at 10 min and remained at steady state until 20 min. For cyclic loading, cell volumetric strain was -0.14 following the 3rd and 5th loading cycles followed by volume recovery between the 7th to the 20th cycle and steady state volume until cycle 100. For static loading cell height decreased while cell width increased. For dynamic loading cell height, width, and length all decreased.

Discussion & Conclusions

Strains in chondrocytes differ conceptually between corresponding static and dynamic loading conditions. For static conditions, chondrocytes seem to behave like a passive structure, while for dynamic conditions, cells appear to control volume and deformations in an active manner, thereby defying expected strain and deformation behaviour. Based on these results, we propose that chondrocytes in cartilage exposed to dynamic, cyclic loading try to minimize volume and shape changes after a small number of dynamic loading cycles.

References

[1] Pingguan-Murphy et al., 2005 *Arch. Biochem., 444(1), 45–51.*
[2] Guilak et al., 1995. *J. Orthop. Res. 1100130315*

Figures

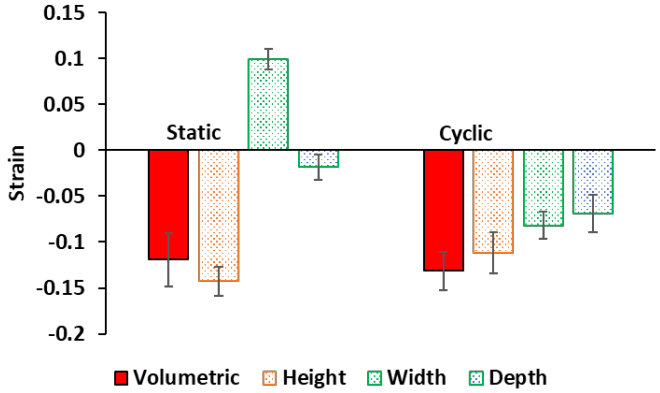


Figure: Volumetric, height, width and depth strains compared for static and cyclic loading at highest strain points.

Design And Implementation of a Smart Bicycle for Knee Osteoarthritis Rehabilitation

Seyed Hamidreza Heidary[1]*,Amin Koemili[1]
[1]Department of Biomedical Engineering, University of Calgary, AB, Canada
email: seyedhamidreza.heida@ucalgary.ca

Introduction

Annually there are approximately 86·7 million people with knee OA in 2020 worldwide. Stationary cycling is one of the effective exercises for patients with knee problems and helps to ease the movement of the joint [1]. E-bikes can help cyclists to improve knee joints health. In recent years, stationary bicycles were instrumented with biosensors to provide health performance of users. However, they are not suitable for rehabilitation due to the inability to control the amount of force exerted on the knee [2]. Using advanced control systems, the desired dynamic force can be adjusted for the healthy and injured knee during cycling based on rehabilitation programs. We anticipate that motorized rehab bicycles with an advanced control system will be a turning point for introducing smart e-bikes for knee and leg rehabilitation programs, leading to improvement of knee function in patients with knee osteoarthritis. Thus the purpose of this project was to develop a motorized stationary bicycle, capable of controlling the pedalling force during the exercise to avoid joint overloading for patients with asymmetric knee OA.

Methods

A normal electric bike is outfitted with "pedal-localizing" device, a force measurement device and microcontroller that feeds a corresponding throttle signal to the bike motor. In the advanced control system of the presented e-bike, inputs of the system are pedal torque and road slope. The outputs of the system are speed, pedal force, and motor speed. Using the auxiliary strategy and an observer, the controller can adjust the motor speed at any time. As a result, we can control the amount of force applied to each knee during cycling. The bike controller will wait until the crank is detected at a particular angular position(s) so that the motor is biasing the assistance to only one leg at a time at different throttle curves. Three subjects completed a pedaling task of 6 minutes with 50% and 80% motor torque assistance during the active cycling phase of one leg.

Results

The proposed new power assistance approach is able to dynamically switch between torque assistance and pedal force applied by the rider. By considering the relationship between torque and motor speed, the controller can adjust the auxiliary torque with minimum delay and high efficiency. In addition, the EMG of vastus lateralis muscle of the target leg was lower than the counter leg, indicating that the motor successfully assisted the target leg.

Conclusions

The result of this study showed that the developed device can provide synchronized asymmetric power to assist a potentially impaired leg while facilitating data capture. Such work has the potential to enhance patient recovery experience and open possibilities for further research to use it for outdoor activities such cross-country and trail ridings.

References

[1] Luan et al., 2021. Clinical rehabilitation 35.4: 522-533.
[2] Cheon et al., 2017. International journal of automotive technology. 18.2: 327-333.

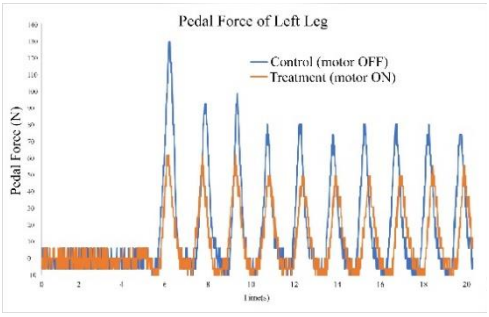


Figure 1: Pedaling force of left leg at 40 rpm and 65Watt power. Motor OFF: (Control), Motor ON: (Treatment).

Optimizing Printed Circuit Board Parameters for ACET Micropumps

Peter Luong[1,2], Stirling Cenaiko[2], Thomas Lijnse[2], Colin Dalton[2,3]
[1]Department of Mechanical and Manufacturing Engineering, [2]Department of Biomedical Engineering, [3]Department of Electrical and Software Engineering, Schulich School of Engineering, University of Calgary

Introduction

The advancement of microdevices has enabled small-scale lab functions. AC electrothermal (ACET) micropumps can manipulate highly conductive biofluids without complicated mechanical structures [1]. ACET microelectrode arrays are manufactured in a cleanroom, but this limits the affordability of the micropumps. This work investigates printed circuit boards (PCB) as an accessible alternative by examining the arrays at different parameters while maintaining PCB manufacturing standards.

Methods

2D models of a PCB ACET device were simulated using COMSOL Multiphysics. Considering the manufacturer's minimum feature size of 152.4 µm, parameters such as electrode width (W2), separation distance (G2), and channel height (H) (Fig. 1A) were optimized with respect to velocity. A PCB was then designed using EAGLE and fabricated by JLCPCB. Experiments were run using microbeads and compared to the 2D simulations to determine the simulation's validity.

Results

Setting the channel height to 250 µm, the optimized parameters were found to be 723.9 µm for W2 and approximately 506.7 µm for G2 (Fig. 1B). At these parameters, the COMSOL model calculated the average velocity as 12.3 µm/s. The simulations show that increasing H would increase the average velocity (Fig. 1B), but this would also change the optimized parameters – meaning W2 and G2 would also increase.

Discussion

Experimentation has shown that this PCB design is functional and that further experiments are needed to prove the validity of this fabrication method for ACET devices. Currently, some PCB manufacturers can produce smaller dimensions at a higher price. As more manufacturers increase PCB miniaturization, flow rate will continue to improve.

References

[1] Salari, A. et al., Micromachines 2019.

Figures

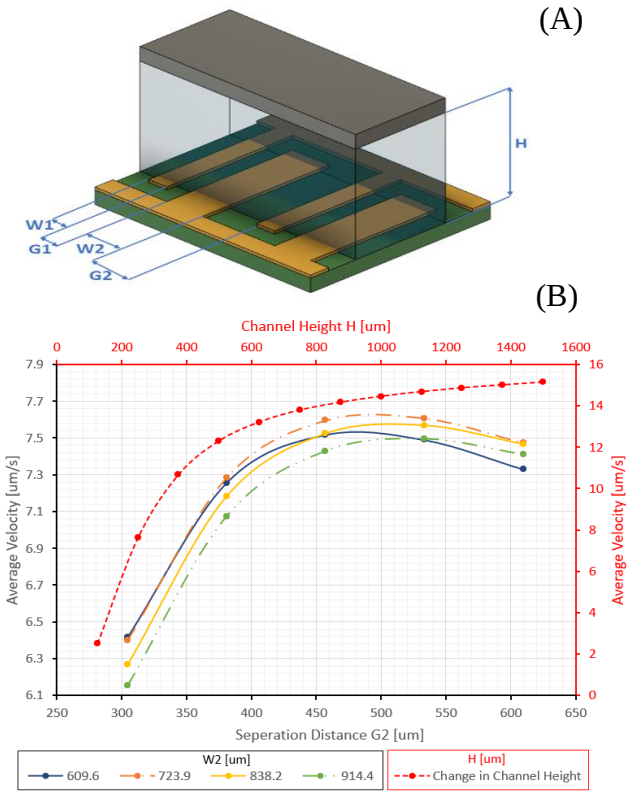


Figure 1: (A) 3D Conceptual Drawing of Array (B) Average Velocity at 7 V_{rms} for G2 and W2 at H = 250 µm (Black Axis) and for H at W2 = 723.9 µm, G2 = 506.7 µm (Red Axis).

A Validation Study of Markerless Motion Capture Using Sit-to-Stand Tests

Sumaya Soufi, Ayooluwakiitan Okesanya, Salim Soufi, Wisdom Sanouvi-Awoga, Hannah MacDuff, Kaelan Findlay, Martin Ferguson-Pell, Ph.D
Rehab Robotics Laboratory, Faculty of Rehabilitation Medicine, University of Alberta,
2-545 Edmonton Clinic Health Academy, Edmonton, AB T6G 1C9, Canada.

Introduction

Marker-less motion capture systems make use of artificial intelligence to track objects or body landmarks as they move through space. This eliminates the need for multiple cameras and markers, as is the case for Marker-based motion capture (1). The application of this technology has shown to be more accessible for patients in communities that face barriers in accessing clinicians and completing diagnostics. This study aims to validate the Kinetisense markerless motion capture system through iPad LiDAR cameras by comparing it to marker based motion capture, the current gold standard.

Methods

This study used the OptiTrack motion capture system as the marker-based gold standard and Kinetisense in tandem with iPad LiDAR sensors as the markerless motion capture system. Sit-to-stand tests were conducted on both systems simultaneously and we collected parallel body landmark data as CSV files. Matlab was then used to clean, filter and analyze the raw data obtained from the trials. From the resulting raw datasets, calculations were made to derive quantitative biometric data in the form of graphs and tables. As for the qualitative data, we used an open source animation generator.

Results

As a means to assess the quality of the Kinetisense software, we graphed the results of the filtered and analyzed Matlab code (Figure 1) which determined the lean distance, rise height, and other parameters for each participant.

Conclusions

As indicated by our study, the Kinetisense iPad version proves its similar capabilities to Optitrack in the field of motion capture. With the iPad Kinetisense version, individuals in rural communities will have the added advantages of lower cost as well as increased accessibility and portability.

References (APA7)

1. Corazza, S., Mündermann, L., Chaudhari, A. M., Demattio, T., Cobelli, C., & Andriacchi, T. P. (2006). A markerless motion capture system to study musculoskeletal biomechanics: Visual hull and simulated annealing approach. *Annals of Biomedical Engineering*, *34*(6), 1019–1029. https://doi.org/10.1007/s10439-006-9122-8

Figures

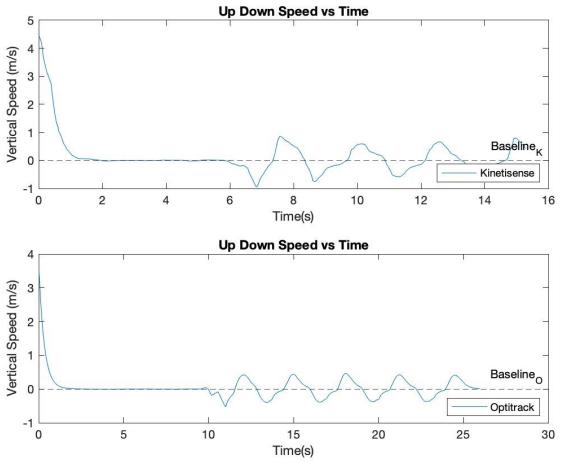


Figure 1: Sample Vertical Speed of Participant Derived Using the Optitrack and Kinetisense System

Rapid Fabrication of Metal Microneedle Arrays

Kazim Haider[1], Thomas Lijnse[1], Catherine Betancourt-Lee[1], Colin Dalton[1,2]
[1]Department of Biomedical Engineering, [2]Department of Electrical and Software Engineering

Introduction

Hypodermic needles are used to deliver many key drugs that cannot be taken orally due to degradation in the gastrointestinal tract, or topically due to the barrier properties of skin. A major drawback of hypodermic needles is tissue trauma and injection pain due to interaction with nerves located in the dermis. Microneedles are a pain free alternative to traditional hypodermic needles, owing to their small size (10-100μm diameter, 25-1000μm height) which minimizes interaction with dermal nerves. Due to their small size, microneedles are limited in their drug delivery capacity as they are either hollow to deliver drugs through a central microchannel or solid and coated with a drug to be released upon insertion. To maximize drug payload, microneedles are formed in arrays of 100s-1000s of needles, but a drawback of increasing array density is a greater skin insertion force. Larger insertion forces are correlated with greater perceived pain [1]. Furthermore, microneedles are currently made using complex multi-step microfabrication processes that require significant resources and have low yields. This greatly increases the unit cost of microneedles relative to traditional hypodermic needles and precludes their widespread adoption into clinical practice.

Methods

A high throughput method of fabricating microneedle arrays using a modified wire bonder process has previously been reported in our lab [2]. Using this process, in this work microneedle arrays were formed on rigid FR-4 printed circuit board (PCB) substrates using an HB-16 semi-automatic wire bonder. An electroless nickel electroless palladium immersion gold (ENEPIG) surface finish was applied to the substrates to provide a bondable surface. A 1 mil (25 μm) diameter gold wire was used to form microneedles in a 1 x 1 cm area. Arrays were inspected with a calibrated microscope to obtain needle height and density measurements and imaged with a scanning electron microscope (SEM) to characterize needle tip geometries. Insertion forces were tested using a Tinius Olsen H1kT universal testing machine to advance each array into porcine skin at a constant speed while measuring the force response.

Results

Overall, 16 arrays were formed with microneedle densities ranging from ~450-3100 needles/cm^2. The targeted needle height was 300 μm for 9 arrays (mean: 305 μm, S.D.: 15 μm) and 400 μm for 7 arrays (mean: 441 μm, S.D.: 16 μm). Insertion forces ranged from ~0.5N (density = 1666 needles/cm^2) to ~3N (density = 2200 needles/cm^2).

Conclusions

Preliminary results indicate that greater array densities require larger insertion forces. Future work will involve constructing and testing a larger sample size to build a more granular correlation between array density and insertion force to find ideal parameters for an array that can deliver the most drug while causing the least pain. This work will also facilitate the development of a low cost manufacturing process that reduces the barriers for adoption of microneedles into clinical practice.

References

[1] F. Aldawood *et al*. (2021). *Polymers*.
[2] T. Lijnse *et al*. (2022). *Microfluidics, BioMEMS, and Medical Microsystems XX*.

Figures

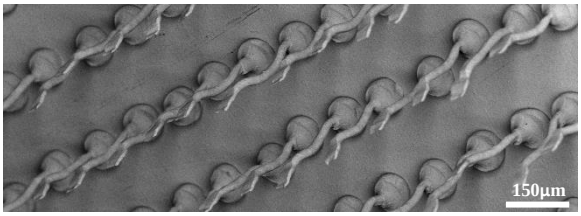


Figure 1. SEM image of a gold microneedle array formed using a semi-automatic wire bonder.

The Correlation Between Behavioural and Physiological Changes in the CNS in the EAE Mouse Model of Multiple Sclerosis

Rania Muhammed, Rehman Tariq, Uche J. Ohaezukosi, Racheal Steele, Ying Wu, Qandeel Shafqat, Jeff F Dunn
Hotchkiss Brain Institute, Dept. of Radiology, Cumming School of Medicine, University of Calgary

Introduction

Multiple sclerosis (MS) is a debilitating neurological disease. Recently, arterial spin labeling (ASL) MRI was used to show that individuals with MS experience reductions in cerebral blood flow (CBF)[1,2]. NIRS has been used to detect brain hypoxia (low tissue oxygenation) in individuals with MS[3] and in a disease model known as the experimental autoimmune encephalomyelitis (EAE)[3]. Low CBF might contribute to hypoxia in MS[4].

We propose that brain hypoxia in MS could be assessed with quantitative susceptibility imaging (R_2*) which increases with increased deoxyhemoglobin (dHb). We quantified R_2*, CBF and behaviour to determine if increased sickness scores relate to CBF and R_2*.

Methods

C57BL/6 female mice (N=30) were equally divided into three groups; the EAE group received MOG_{35-55} emulsified in complete Freund's adjuvant (CFA) and pertussis toxin (PTx); the CFA mouse group received the same injections, except MOG. Two days post-induction, EAE & CFA mice received a PTx booster injection. The Naïve group received no injections. To test for motor dysfunction, we used a 15-point scale. Open field was used to assess behavioral changes at baseline (pre-induction), 7-days post induction, and at peak sickness for EAE mice prior to sacrifice and subsequent imaging (day 17-21). All groups were imaged using a 9.4T MRI Bruker Avance console accompanied by a Bruker Cryophobe. Images were acquired through four continuous ASL (cASL) Haste sequences (matrix size = 256 x 72, field of view = 25.6 mm x 25.6 mm, repetition time = 3000 ms, time to echo = 13.5 ms). A 3D multi gradient echo sequence was used to collect T_2* relaxation, a technique sensitive to magnetic inhomogeneities including dHB which is a paramagnetic compound. The relaxation rate R_2* is the inverse of T_2*. Levels of dHB are expected to positively correlate with R_2*. A one-way ANOVA and Bonferroni post-hoc was used for the statistical analysis.

Results

Sickness behaviour onset was observed in EAE mice starting post-induction day 7, followed by a progressive increase in scoring; comparatively CFA and Naïve mice did not show an increase in behavioural scoring. Locomotion was decreased in EAE compared to controls at mid-study (p = .002) and peak disease (p < .001). There was a significant decrease in CBF in the CFA-PTx (p = .012) and EAE (p = .040) mice compared to Naïve. A significant decrease in CBF was also seen in the thalamus. Cortex R_2* increased in the EAE compared to both Naïve (p = .047) and CFA-PTx (p = .023).

Conclusions

As both CFA-PTx and EAE have inflammation, while EAE also has autoimmunity, those changes that differ between the two may relate to these relative differences. Thus, R_2* or hypoxia may relate to autoimmunity while reduced CBF may be associated with inflammation. Time course MRI of CBF and hypoxia may prove useful in understanding the physiological changes that occur in the brain in this model of MS.

References

1. Johnson et al. (2016). *PloS one, 11*(12).
2. de la Peña et al. (2019). *Acta radiologica open*, *8*(12).
3. Yang and Dunn (2019). *Multiple sclerosis Scientific reports,* 5.
4. Xu et al (2014). *Magnetic resonance in medicine,* 72(2): 438-445.